Active spectroscopy on HID lamps : exploration of various methods

Document Version:
Publisher's PDF, also known as Version of Record (includes final page, issue and volume numbers)

Please check the document version of this publication:

• A submitted manuscript is the version of the article upon submission and before peer-review. There can be important differences between the submitted version and the official published version of record. People interested in the research are advised to contact the author for the final version of the publication, or visit the DOI to the publisher's website.
• The final author version and the galley proof are versions of the publication after peer review.
• The final published version features the final layout of the paper including the volume, issue and page numbers.

Link to publication

ACTIVE SPECTROSCOPY ON HID LAMPS

EXPLORATION OF VARIOUS METHODS

PROEFSCHRIFT

ter verkrijging van de graad van doctor
aan de Technische Universiteit Eindhoven,
op gezag van de Rector Magnificus, prof.dr. R.A. van Santen,
voor een commissie aangewezen door het College voor Promoties
in het openbaar te verdedigen
op donderdag 17 februari 2005 om 16.00 uur

door

Xiaoyan Zhu

geboren te Shenyang, China

Dit proefschrift is goedgekeurd door de promotoren:

prof.dr.ir. M. Haverlag
en
prof.dr.ir. G.M.W. Kroesen

Copromotor:
dr. J.J.A.M. van der Mullen

Contents

Contents

Contents

Chapter 1

Introduction

Abstract

This study deals with the design and construction of diagnostic tools to investigate the energy balance and transport phenomena in metal halide (MH) lamps. Therefore we explored a vast range of the electromagnetic spectrum and used γ-ray photons with energies in the order of several MeV, X-ray photons of several tens of keV and photons from the visible part of the spectrum (around 2 eV). Gamma photons were used to trace radioactive nuclei, X-rays to detect inner shell electrons while the visible photons were employed to investigate the free and loosely bound outer electrons.

Metal Halide lamps are lamps for which the light is generated by plasmas of complex chemical composition. The light emitting species are metals such as Na, Tl, Dy and Ce, which are excited in a medium that predominantly consist of mercury. An essential feature of the plasma in MH lamps is that a minority of species is responsible for the majority of plasma properties. This makes these plasmas strongly non-linear and extremely sensitive to external conditions. An example of this non-linear behavior is the sensitivity of metal halide (MH) lamps to the gravitation force: turning from a horizontal to a vertical burning position can change the color of a MH lamp substantially. This is remarkable if we realize that plasmas are mainly ruled by the presence of electrical charged particles (electrons and ions) and that the electrical force on an ion is more than a billion times (10^9) larger than the gravitation force on that ion. If we are able to come to an in-depth understanding of these type of lamps, this may certainly contribute to the design of more efficient light sources.

The study on these lamps is of societal importance since the natural resources in the earth are limited and the shortage of energy might be a big future problem. Therefore, energy conservation and environment protection are important tasks for the modern society. Of the electrical energy that is consumed worldwide, about 20% is used for lighting [1]. This motivates the lighting industry to produce lamps with high efficiency and long life-time.

In this chapter we start with a brief history of various light sources used for general lighting purpose. This is followed by a description of the de-mixing phenomena in MH lamps and the role of gravitation. After that an overview will be given on various experimental techniques used in our study. Finally we conclude with a presentation of the outline of this thesis.

1.1 A brief history of electrical lighting

Even though there are many kinds of different lamps, we can divide them in three major types: incandescent lamps, gas discharge lamps and solid-state lamps (LEDs).

The first generation of electric lamps that were produced on a large scale are the incandescent lamps. They were developed separately by Thomas Edison and Joseph Swan in 1878. Discharge lamps were developed as early as 1802 (Davy), but it has to last until the 1930s before they became commercially available on a large scale. This so-called second generation consists of (low-pressure) fluorescent lamps, low-pressure sodium lamps and high-pressure mercury lamps. Since then a lot of research and development had been done to improve the efficiency, life-time, and color rendering of discharge lamps. In the 1960s, a new generation of discharge lamps was introduced, namely high-pressure sodium lamps and metal halide lamps.

This new generation yielded major improvements of efficiency and color rendering. Also in recent years substantial progress has been made and the performance of gas discharge lamps have been improved significantly. Some new products were recently introduced including electrode-less lamps with long life-time, such as the low pressure QL lamp, and a high pressure sulphur lamp. In the first case the light-emitting medium is an inductively coupled plasma and in the second example it is a microwave induced plasma. Much research efforts have been paid to remove toxic materials out of lamps. Several types of mercury-free lamps were constructed such as lamps where the buffer gas Hg was replaced by Zn or Xe. The next generation may consist of solid-state lamps, such as light emitting diodes (LEDs). However, at this moment the efficiency of LEDs is still much lower than state-of-the-art 'white' discharge lamps and their cost is much higher.

1.2 Classification of conventional lamps

In the following, a general overview will be given on conventional lamps, including incandescent lamps and gas discharge lamps. The latter can be subdivided into low-pressure and high-pressure discharge lamps.

1.2.1 Incandescent lamps

Incandescent lamps generate light from electrically heated filaments. In the first incandescent lamps these were carbon filaments that due to the high evaporation rate had a short life-time, therefore they were replaced in 1910 by tungsten filaments. However, also the

tungsten filaments suffer from evaporation. That is why the incandescent lamps of the first generation were limited in life-time, maintenance (light loss over life) and efficiency. Many developments were done on the filament design and gas filling in order to reduce the tungsten evaporation. A breakthrough was realized in 1961 by the introduction of the halogen lamps. In these lamps the blackening of the lamp wall is eliminated by means of the tungsten-halogen chemical cycle that is made possible by filling the light bulb with halogen gas. In this way, incandescent lamps are improved in efficiency, life-time, maintenance and compactness.

Due to the good color rendering and low costs (no ballast and a simple design), incandescent lamps are still widely used, such as in photography, TV-studio or stage lighting and home lighting. The halogen lamps are widely used as car headlamps and in floodlighting, projection lighting, in shops' windows, exhibitions, stage and film lighting. However, the efficacy of incandescent lamps is still rather low, namely about 15–30 lm/W[1]

The typical life-time is also limited to about 1000–3000 hours. Thus incandescent lamps are rather inefficient in energy terms.

1.2.2 Gas discharge lamps

One of the major developments in the last century within the lamp industry is realized by the introduction of gas discharge lamps. The main advantage of gas discharge lamps is that they can achieve high efficacy and long lifetime. The principle is that the electric power is converted into radiation by means of an electrical discharge in the gas medium in the lamp. In such lamps a weakly or moderate ionized plasma is created. The electrons are accelerated by an externally imposed electric field and transfer energy to heavy particles by means of elastic and inelastic collisions. The inelastic collisions are essential for chemistry processes, such as excitation, ionization and dissociation and the generation of radiation. The excited particles lose their energy by the radiative decay from higher to lower excited states. The visible radiation can be produced in two ways: directly or by down-conversion using a phosphor-coating of the tube. Depending on the pressure, gas discharge lamps can be divided into two groups: low pressure and high pressure lamps.

Low-pressure gas discharge lamps are in general large in volume, low in pressure, low in luminance and power densities and the plasma conditions in these lamps are far from equilibrium. These lamps normally contain a noble buffer gas with a pressure of a few hundred Pa and light emitting species such as Hg or Na of only a few hundred milli-Pa. Under normal working conditions, that is after ignition and warming up, the energy of the electrons is mainly transferred to the light emitting species since they have a lower excitation and ionization potential. However, there is still a need for a buffer gas since

---

[1]Efficacy of a light source is defined as the ratio of the total luminous flux and the lamp power. It can be written as $\eta = \frac{K_m \int_{380}^{780} P_\lambda V(\lambda) d\lambda}{P_l}$, where K_m is the maximum spectral efficacy of human eyes (for photopic vision) at wavelength of 555 nm which equals 683 lm/W. P_λ the spectral distribution of a lamp, $V(\lambda)$ the eye sensitivity curve and P_l the lamp power.

the collision mean free path of electrons with light emitting atoms is very large so that electrons could easily diffuse out of the plasma if buffer gas atoms were absent.

Typical low-pressure discharge lamps are the *fluorescent lamps* and the *low-pressure sodium lamps*. For fluorescent lamps, about 60 ∼ 70% of electric power is converted into UV radiation (254 nm and 185 nm resonance lines), which is subsequently converted into visible light by a phosphor coating. The well-known linear fluorescent lamps of 36 W have an efficacy of 80–100 lm/W. They are mainly used in indoor lighting such as in offices.

For low-pressure sodium lamps, the input lamp power is largely converted to the resonance line of sodium, namely the Na D line (589.0/589.6 nm), which is close to the maximum eye response in the photopic vision (555 nm). That is why these lamps have a very high efficacy (up to 200 lm/W) and do not need a fluorescent phosphor coating. However, due to the monochromaticity of the spectrum, these lamps have a very bad color rendering and very low color temperature (CCT is about 2000 K). That is why the application of these lamps is mainly restricted to road lighting where the color discrimination is less important.

High-pressure gas discharge lamps, generally have a small volume, high pressure (more than 1 atm), high luminance, a large variety in power settings (10 W–18 kW) while the plasma in these lamps are close to local thermal equilibrium (LTE). Due to their high intensity these lamps are often denoted by high intensity discharge (HID) lamps. The output light can easily be controlled by a fixture and projected over a long distance onto a surface. High power HID lamps are mainly used for outdoor applications, such as sport lighting, street lighting and floodlighting of architectural monuments. Low power HID lamps are used for indoor industrial and commercial applications. The conventional HID lamps are mainly high-pressure mercury (HPM) lamps, high-pressure sodium (HPS) lamps and metal halide (MH) lamps. In the recent years, new types of HID lamps have been developed. One example is the ultra high-pressure (UHP) mercury lamp with a Hg pressure of 150-300 bar, which is used as the main light source for video projection. Another example is the metal halide lamp filled with xenon instead of mercury, which is used as a high-quality car headlamp.

The first HID lamps produced in 1906 were high-pressure (1 atm) lamps based on pure mercury. The absence of red in the line spectra of Hg cause a bad color rendering and the bluish light output makes these lamps only suitable for outdoor lighting (such as street lighting) and industrial lighting (combined with incandescent lamps). The efficacy of these lamps is normally between 40–60 lm/W depending on the lamp power. The color-rendering index (CRI) [2] is only about 50 and this can only be realized by using a phosphor coating.

---

[2]CRI is a unit of measure that defines how well colors are rendered by different illumination conditions in comparison to a standard light source of comparable color temperature. CRI values is rated on a scale from 0–100. A CRI of 100 represents no color distortion.

For the HPS lamps, the color-rendering can be improved to more than 80 by increasing the Na pressure. However in that case the efficacy is not higher than 60 lm/W. For the more regular HPS lamps (100 - 150 lm/W), the color rendering is relatively low (about 29).

Due to the low color-rendering index (CRI), the applications of high-pressure Hg lamps and high-pressure sodium lamps are limited to mainly outdoor lighting and industrial lighting. In order to enlarge the application field the spectral performance had to be improved in the visible range. Therefore several light emitting species were added into the mercury-based discharge. This led to the birth of the *metal halide lamps* in the 1950s. They were first being marketed in 1964.

1.3 Plasma composition of metal halide lamps

The filling substances of MH lamps can be globally be divided into three categories: the starting gas, the buffer gas and the radiation emitting species.

The starting gas is a gas that is in action when the lamp is cold. It has a low ignition voltage, which facilitates the ignition of the lamp, and a low thermal conductivity so that the contribution to the heat loss is limited. Normally, noble gases such as argon and xenon are used as starting gases in MH lamps.

The buffer gas is the main constituent of the gas when the lamp (after being ignited) has reached a (quasi) steady state. It has two functions: to enhance the efficacy and to improve the electrical properties. Since the vapor pressure of a metal halide is very low (1 mbar∼ 100 mbar) the mobility of the electrons would be very high if the buffer gas were absent. This would lead to a low electric field and thus a low lamp voltage. This makes it difficult, if not impossible, to make high power MH lamps. By adding a buffer gas with a partial pressure that is much higher than that of the salt additives, we get a situation in which the lamp voltage is mainly determined by the buffer gas. The efficacy is also improved since the presence of buffer gas atoms leads to a slow-down of the dissociation and recombination processes of the additives. The most common buffer gas is mercury.

The radiation emitting species in MH lamps are mainly metals. They are brought into the discharge as constituents of the halide-salts which are less corrosive with respect to the lamp envelope and often lead to a higher vapor pressure as compared to pure metals. The excitation and ionization potentials of these metal atoms are lower than that of mercury which implies that the electrical and light technical properties of MH lamps are largely determined by the additives: the metal halides.

Since MH lamps have both a high luminance and a high CRI, they can be much more attractive than the high pressure Hg lamp and the high pressure Na lamp in both indoor and outdoor lighting. In the recent years, various new research and development activities

have been devoted to the metal halide lamps. These have led to the following improvements:
1. The burner material is made of polycrystalline alumina (PCA) instead of quartz. The reason is that the lamp with PCA burner can withstand higher (cold spot) temperatures, which results in a higher vapor pressure of the additives so that the light output increases. Therefore the efficacy of the lamp is increased. Moreover the use of PCA also allows a more precise burner dimension control (better than with quartz), so that a better lamp-to-lamp color matching is reached.
2. Rare-earth species such as Dy, Ho, Tm and Ce are added into the lamp. The efficacy, color stability and the color rendering are improved due to the rich "grass-field" line spectra in the visible range.
The main application of these lamps is for indoor lighting, such as in shops where they are more and more replacing halogen lamps.

1.4   De-mixing in metal halide lamps

The previous section has shown that metal halide lamps have many advantages over the older generation of HID lamps. However, there is still room for improvements. But due to the complexity of the plasma in such lamps, further improvements become more and more difficult and require a more in-depth study of the plasma behavior in these lamps. One of the challenges is the understanding of segregation phenomena that becomes evident when a burning MH lamp is rotated. This change in orientation leads to a difference in the color output. For a horizontal orientation, the color output is (almost) uniformly distributed along the axis. However if these lamps are operated vertically they exhibit a non-uniform color distribution along the axis. This phenomenon called axial segregation, or de-mixing is demonstrated in Fig. 1.1 showing a vertically burning lamp.
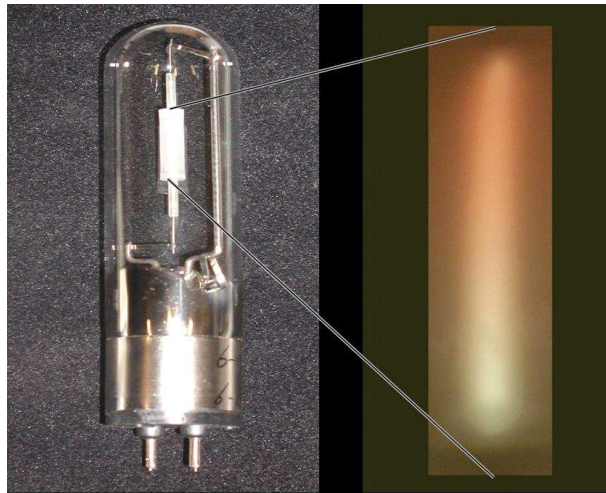
Figure 1.1: Color separation due to demixing of species in a vertically burning metal halide lamp.

Two effects are clearly visible:

6

1. The color changes along the axial direction and
2. The intensity of the light is decreasing along the axial direction from bottom to top.

Thus for such a lamp, the efficiency and color point will depend on the orientation. The underlying mechanism for this phenomena have been studied by simplified models [2–6]. However, for a better understanding the result of advanced models have to be validated by those of experiments [7].

Since it is the aim of this study to construct and apply poly-diagnostic techniques to investigate these phenomena we will give here a global interpretation of the plasma properties that are responsible for the segregation phenomena.

The complex chemical composition is the key property of MH lamps. The lamp is filled with a mixture of high pressure Hg with a small amount of metal halide salts. The partial pressure of the salt additives such as NaI, DyI_3, TlI and CeI_3 is about 1–100 mbar which is much lower than that of the mercury pressure that is in the range of 1–100 bar. However, due to the lower excitation and ionization potential these very additives are responsible for light generation and charge creation; Hg ions and (light emitting) excited Hg atoms are hardly present and the majority gas, mercury, merely acts as a buffer gas. The fact that minority species determine the plasma properties makes the plasma behavior non-linear and very sensitive to the external influences such as gravity. The basic principle is that transport processes induced by gravitation may change the spatial distribution of the light emitting easy ionizable species. This, on its turn, may change the electrical conductivity and thus the energy coupling.

The transport properties of a vertically burning lamp can be seen as the result of a competition between *convection and diffusion*; both being driven by the energy housekeeping (cf. Fig. 1.2). When the MH lamp is burning, the electric input power will be used to create heat and to generate light emission predominantly in the center of the plasma. Since the wall is kept on a relative low temperature (about 1200 K) a large temperature difference of about 4000 K will be established over a small radius of typically 2-4 mm. The salt molecules first evaporated from the salt pool (the black dot at the bottom of Fig. 1.2), enter the plasma and are carried on by a convection flow (the closed loops in Fig. 1.2). This bulk flow is mainly determined by the buffer gas (e.g. mercury) and originates from the combined action of the (internal) temperature gradient and the (external) gravitation force. Due to the large temperature gradient, the mass density of Hg atoms will be much larger in the near-wall region than in center of the discharge. Consequently the mercury in the high-density outer regions is pulled down due to gravitation. This will force the mercury atoms in the central hot (where the density is low) region to move upwards. The result is a convective circulatory motion (cf Fig. 1.2 and Fig. 1.3).

When molecules travel with the convection flow and enter the hot center, they will dissociate and release the metal atoms. Therefore density gradients of atoms and molecules will be built up in mutual opposite directions and this leads to diffusion. The metal and iodine atoms diffuse outwards to the wall where they recombine into molecules whereas
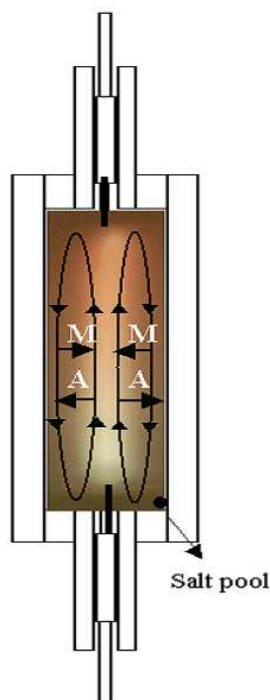
Figure 1.2: A scheme of the transport processes in a vertical burning metal halide lamp; M stands for molecules, A for atoms. Metal halide molecules diffuse from the cold wall to the hot center where they dissociate into atoms, metal atoms will be excited or ionized and generate light. Due to the density and temperature gradient, the metal and iodine atoms diffuse from the hot center to the cold outer region near the wall where they recombine again. These diffusion processes have to compete with convection, which is the result of the combination of the radial temperature gradient and the gravitation force (buoyancy)

the molecules diffuse inwards to the center where they dissociate into atoms. This set of contra-directed diffusion processes has two positive effects. First, enough metal atoms can be transported to the arc center where they contribute to the light generation. Second, the formation of metal-iodide molecules in the region close to the wall prevents the reaction of metal atoms with the wall. This will reduce the corrosion of the burner wall drastically. Thus in metal halide lamps, two main material transport processes are present: convection of the bulk flow caused by the combined action of gravitation and the temperature gradient and diffusion caused by the gradients of the partial pressure of different minority species. Apart from this, various other physical and chemical processes take place, such as (de)excitation, ionization/recombination, dissociation/association and the generation and transport of radiation.
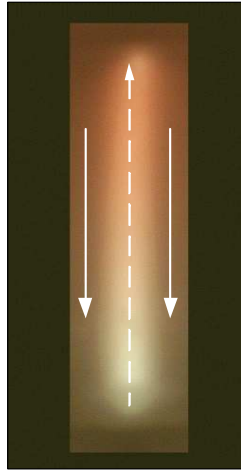
Figure 1.3: The driving force of the convection of Hg vapor in a MH lamp is gravitation, which pulls down fluid elements of high density; buoyancy.

1.5   Segregation; elemental concentration

Due to the fact that MH lamps operate under high pressure and high power density it is generally assumed that the plasmas in these lamps are close to LTE. This does not exclude that plasmas can be inhomogeneous and non-uniform along the axis. To continue the explanation of axial segregation and the color non-uniformity as seen in Fig. 1.1 we have to introduce the concept of elemental concentration.

The light emitting species (e.g. sodium) can be transported as an atom (Na), ion (Na$^+$) or as a constituent of molecules (NaI, Na$_2$, Na$_2^+$, Na$_3$ ...). However, the displacement of one Na$_2$ molecules is equivalent to that of two atoms. It is therefore useful to introduce the concept of elemental density that for the case of sodium is defined as

$$\{\mathrm{Na}\} = [\mathrm{Na}] + [\mathrm{Na}^+] + [\mathrm{NaI}] + 2[\mathrm{Na}_2] + 3[\mathrm{Na}_3] + \cdots \tag{1.1}$$

or more general

$$\{\mathrm{Na}\} = \sum_j R_{j\alpha} n_j \quad (\text{here } \alpha \equiv \mathrm{Na}), \tag{1.2}$$

where α refers to the element (in this example: sodium) and n_j to the density of species labelled by j. The stoichiometric coefficient $R_{j\alpha}$ counts the number of sodium (or more general α) nuclei in the compound or species j. For instance, for a species Na$_2^+$, α refers to sodium and j refers to Na$_2^+$, thus $R_{j\alpha} = 2$. The summation in Eq. 1.2 runs over all the species. For those compounds that do not include sodium we have $R_{j\alpha} = 0$. We adopt the notation convention as given in [5] and denote the elements with Greek symbols (α, β ...) and the species with normal Roman letters. Note that a notational distinction is made between the concentration of a species such as [Na] $= n_{\mathrm{Na}}$ or [NaI]$=n_{\mathrm{NaI}}$ and the elemental concentration $\{\mathrm{Na}\}$ (in curly brackets). In the latter case we refer to the presence

of sodium irrespective of the state of excitation or binding.

In fact the determination of {Na} is counting the number of sodium nuclei in a unit volume. This is precisely what we will do with the method of gamma spectroscopy treated in chapter 2 where the feasibility of this technique will be explored for the determination of the elemental concentration of sodium in lamps. But also in the X-ray absorption technique is based on this principle. In that case the elemental density of mercury is determined by probing the presence of inner shell electrons of Hg (chapter 3).

In an analogue way we can define the elemental pressure. In the case α refer to sodium we have $p_\alpha = n_\alpha KT = \{Na\}kT$.

The phenomena of axial demixing or segregation is closely related to that of radial segregation. The latter is present especially if convection is absent. As stated before: the large radial temperature gradient leads to diffusion of molecules from outside to inside and diffusion of atoms in the opposite direction. However, since the molecules are bigger and heavier than atoms, they have a lower diffusion coefficient. This will lead to a non-uniform distribution of the elemental densities of metals along the radius. This so-called radial segregation is always present in MH lamps.

The strong relation between radial and axial segregation can now be understood. When convection is present, the additive species in the hot center will be dragged upwards by the convection flow and pushed downwards near the cold wall region. But due to the radial segregation of the metal elements, the elemental concentration will be (extra) lower in the center than at the wall. Therefore the uprising convection stream contains less sodium than the down-falling stream. Moreover the Na-atoms are much more volatile and can easily leave the upward convection flow whereas refilling this upward axial flow due to the diffusion from of NaI molecules from outside to inside is hindered by the large molecular diffusion coefficients. This leads to a decrease in the elemental concentration in the upper part of the burner. Therefore the upper part will produce less radiation and has a different color than the bottom of the lamp.

Depending on the competition with diffusion, the convection flow can have two opposite effects on the axial segregation. For relatively small convection flows we will find that an increase in convection will cause an increase of the axial segregation. On the other hand, in case of a high convection flow, we find that a further increase reduces the axial segregation. By realizing that the convection is proportional to the pressure of the buffer gas it can be understood that there is one pressure for which the axial segregation reaches a maximum. This is clearly demonstrated by a so-called Fischer curve [2] (see Fig. 1.4) showing the dependence of axial segregation as a function of pressure.

In that figure we introduced the axial segregation parameter λ_α for the element α which is defined as [2]

$$\lambda_\alpha = \left| \frac{1}{p_\alpha} \frac{\Delta p_\alpha}{\Delta z} \right|, \tag{1.3}$$

where p_α is the partial pressure of element α whereas z is the height of the plasma column.
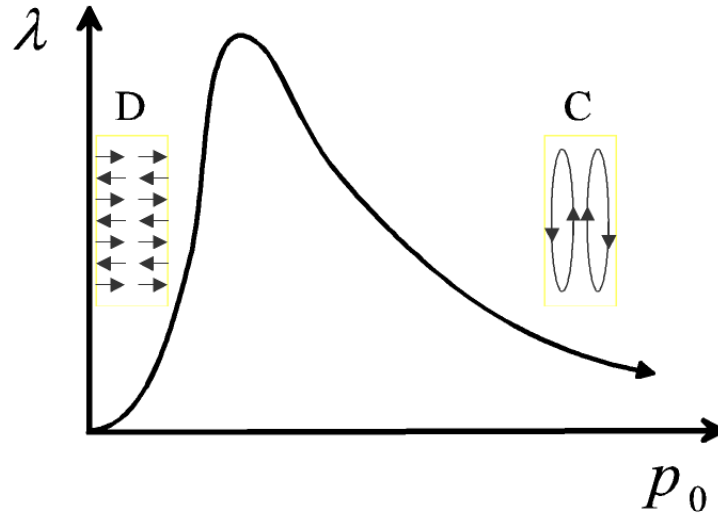
Figure 1.4: A schematic drawing of the segregation known as the Fischer curve. It shows the axial segregation parameter λ as a function of total pressure p_0. D represents the region where diffusion process is dominant; C is for the region where convection is dominant.

Fig. 1.4 shows that the axial segregation of an element α is increasing with the pressure for low pressure conditions for which diffusion is dominant, and decreasing with pressure for high pressure conditions where convection prevails.

1.6 The influence of gravity

Above we have seen that the axial segregation is caused by the combination of convection and diffusion. The convection is the result of the gravitational force and thus directly related to the value of the free fall acceleration $g = 9.8\,\mathrm{m/s^2}$. To understand the impact of gravitation more precisely, it is interesting to measure the density distribution at extreme acceleration situations: under (almost) zero-g and enhanced g conditions. This is one of the aims of the ARGES project. ARGES, an acronym for **A**tomic densities measured **R**adially in metal halide lamps under micro-**G**ravity conditions with **E**mission and absorption **S**pectroscopy, is a collaboration between Philips Lighting and Technische Universiteit Eindhoven (TU/e). Another aim of the ARGES project is to understand helical instabilities that can occur in certain types of metal halide lamps.

The ARGES lamp was designed such that the axial de-mixing attains more or less its maximum value at normal operating conditions. Thus, under normal 1 g conditions, the axial segregation in the ARGES lamp corresponds to that given by the maximum in Fig. 1.4. Two extreme conditions are created during the experiment, i.e. no convection (zero-g) and enhanced convection (g enlarged by almost a factor of two).

1. No convection. Under micro-gravity conditions, the convection velocity is very small so that diffusion is dominant. We are still able to observe radial demixing; i.e. the concentration of the radiating species will still be lower in the center of the lamp as compared to the regions near the wall.

2. High convection. Under high acceleration conditions, the convection velocity will be enlarged so that the concentration of the salt element in the lamp will become well mixed (think of a cocktail shaker); any radial de-mixing caused by diffusion will be erased (partly) by convection.

Therefore this ARGES lamp is specially designed to be sensitivity to the changes in (pseudo) gravity, i.e. from 1 g to 0 g and from 1 g to 2 g. Since the demixing is at the maximum for the 1 g case, it is expected that the de-mixing is reduced in both transitions, which have both have been realized during parabolic flights. These experiments revealed certain phenomena that can be explained qualitatively. However, the period (almost 20 s) of zero-g during parabolic flights is too short to stabilize the plasma. In order to do the experiment under stable zero-g conditions, ARGES lamps were sent to the International Space Station (ISS) where experiments were done in the week of April 24, 2004 by the Dutch astronaut André Kuipers. In the near future the ARGES lamps will also be investigated under high-g conditions (centrifuge experiment).

1.7   The scope of this thesis

The complex nature of segregation is already studied by a number of investigators. Qualitatively the mechanism is understood, but quantitatively the disagreement between theoretical models and the measured color separations is often large. Therefore more in-depth studies are needed and quantitative data from experiments are required to validate models. The final goal is to set up a complete theoretical model to fully understand the energy balance and transport processes in such chemistry-complex plasmas. This grand model can then be used to design lamps with high efficiency and good color rendering.

This Ph.D. project is part of a larger project for the understanding of the energy balance of MH lamps and the plasma transport processes that are responsible for segregation phenomena in these lamps. The primary objective of this thesis is to set up poly-diagnostic tools to study the plasma properties in HID lamps. Therefore we explored a vast range of the electromagnetic EM spectrum and used photons in the gamma range, the X-ray interval and from the visible EM region.

One of the major plasma properties is the temperature. It is assumed by most researchers that the plasmas in these high-pressure discharge lamps are in local thermodynamic equilibrium (LTE). This implies that only one temperature field is needed to describe all the processes. However the important question remains whether this LTE assumption is valid or not. If LTE is not established, this would imply that the local chemical compo-

sition, the radiation generation and transport processes are determined by a multitude of temperatures. This would make the description the system very complex.

The validation of the LTE assumption requires different temperature measurements. Therefore this Ph.D work is mainly devoted to temperature measurements in HID lamps for which basically two methods were employed: X-ray absorption (XRA) and Thomson scattering (TS).

The primary observable of the XRA is the Hg density distribution, which by means of the ideal gas law $p = nkT$ can be translated into a temperature distribution (assuming isobaric conditions).

The comparison of the gas temperature with the electron temperature gives insight on potential deviations from LTE. Therefore another diagnostic tool, namely Thomson scattering was also explored. TS is the scattering of (laser) light on electrons. From the scattered photon one can determine the electron temperature and electron density.

The second objective of this study is to explore methods to measure the distribution of species densities in these types of lamps. Apart from TS which gives the electron density distribution the feasibility of other active methods such as γ spectroscopy and X-ray fluorescence (XRF) have to be investigated as well. The reason is that standard optical techniques, such as emission spectroscopy are not adequate for the following reasons:

1. Emission spectroscopy on molecules in cooler plasma zones is due to the lack of (a sufficient amount of) electronic transitions extremely difficult, if not impossible.

2. The use of PCA as burner wall material obstructs normal optical methods so that spatial information of high resolution cannot be obtained.

Due to the reasons mentioned above it is worthwhile to investigate the feasibility of γ spectroscopy and X-ray fluorescence. By means of XRF the elemental densities of many additives such as {Dy}, {Ce} and {I} can be determined. If the plasmas in HID lamps are in LTE conditions, we can transform the information of the elemental densities into that of the different species using the well-known equilibrium statistical distribution functions. That is why XRF experiments are planned in the near future as a part of another Ph.D. project.

Although X-ray fluorescence seems to be applicable for the detection of most elements in HID lamps, we can expect that it will not be capable to measure the elemental density of sodium. The reason is that the excitation energy of the X-ray fluorescence line of sodium is low so that the radiation cannot penetrate through the wall material of HID lamps. Therefore a feasibility study of the application of γ-spectroscopy on the determination of the elemental sodium distribution has been conducted. The results will be described in chapter 2 where it turns out that such an experiment might be possible if we take advantage of the expertise developed for equipment for medical applications.

1.8   The experimental setups

As said this thesis is mainly focused on two diagnostic techniques: X-ray absorption (XRA) and Thomson scattering (TS). The XRA method is used to measure the gas temperature. Its application to various HID lamps is described in the Chapter 5. Comparing the gas temperature profiles of different lamps with each-others gives insight in the influence of the salt composition, the pressure and the power on the temperature profile.
The application of Thomson scattering, which is used to determine the electron temperature and electron density of pure Hg lamps, is described in the Chapter 7. The combination of XRA measurements and Thomson scattering performed on the same lamps gives insight on the degree of the departure from LTE.

Much effort has been paid to the construction of both the XRA and TS setups. Especially the effort for realizing a state of the art XRA setup was substantial. The fact that during XRA only a small absorption signal has to be deduced out of a large background absorption signal makes XRA experimentally difficult. Besides that, it turned out that the data handling process is very difficult. In order to isolate the Hg contribution in the absorption we had to eliminate the influence of the wall material. This was realized by subtracting (the logarithm of) lamp-off and lamp-on profiles. However, the wall material of a hot burning lamp is not the same as that of cool non-burning lamp. Therefore correction had to be performed on the individual images before subtraction could take place. Another difficulty is the Abel inversion. The noisy character of the signal will spoil the determination of the column density of Hg. Several numerical tests have been done and finally a Tikhonov regularization method was found to be the most successful.

The TS setup we used is based on an existing design originally constructed for the performance of TS on plasma for spectrochemistry. In that case the plasma-laser interaction can be arranged such that photons created is a plasma-wall interaction can not penetrate the detector (easily). However, for TS on a real lamp this is much more difficult and the setup had to be adjusted such that the negative influence of stray light generated by the laser-wall interaction, the creation of a laser induced plasma and the plasma light emission could be reduced. The adjustments were performed successfully and electron densities and electron temperatures could be obtained for a high pressure mercury discharge. Herewith a firm base is constructed for future TS measurements on MH lamps.

In this thesis, several HID lamps are used for the experiments.

Table 1.1 shows 8 different lamps that were used for the X-ray absorption experiment. The type 1 lamp is shown in Fig. 1.5(a), type 2-1 and 2-2 have the same geometry shown in Fig. 1.5(b) but with different Hg fillings, type 3-1, 3-2 and 3-3 lamps have the same geometry shown in Fig. 1.5(c) but with different fillings. The oven-lamp is shown in Fig. 1.5(d) and the type 4 lamp is shown in Fig. 1.5(e).

Type	P_{lamp} (W)	L/D	D_{in}	L_{arc}	wall thickness	m_{Hg}	Salt
type 1	142	2.13	8	17	1	10	DyI_3
type 2-1	200	2.17	18	39	1	15	-
type 2-2	200	2.17	18	39	1	50	-
type 3-1	70	4	4.5	18	0.8	4.46	-
type 3-2	70	4	4.5	18	0.8	4.46	NaI
type 3-3	70	4	4.5	18	0.8	4.46	NaI/CeI_3
Oven-lamp	50 (DC)	4	4.5	18	0.8	4.46	-
type 4	142	8	4	32	0.5	0.6	NaI/CeI_3

Table 1.1: HID lamps for this study. Here L/D is called the aspect ratio of the lamp. The dimensions of inner diameter D_{in}, arc length L_{arc}, and wall thickness are all in mm. The Hg filling in the lamp is in the unit of mg.

(a)   (b)   (c)   (d)   (e)
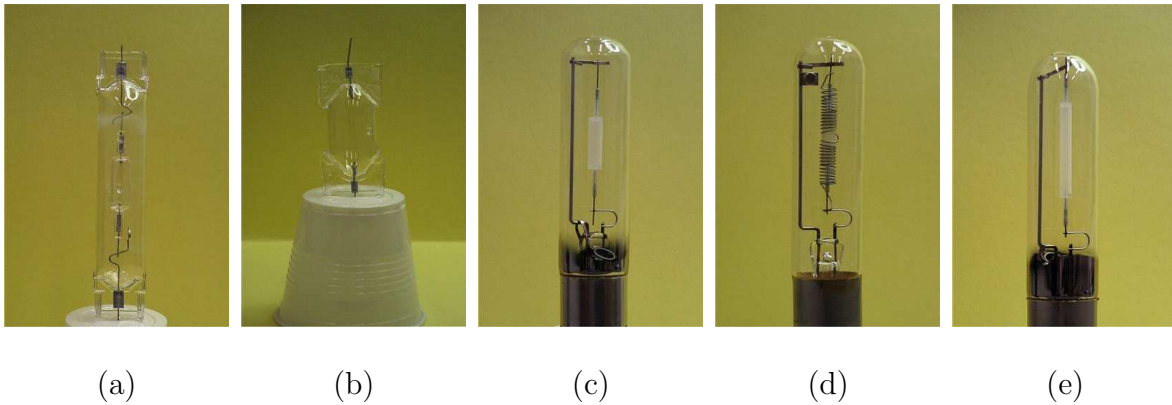
Figure 1.5: The pictures of different types of HID lamps used in the X-ray absorption experiment. **(a)**: Type 1 lamp. **(b)**: Type 2-1 and 2-2 lamp. **(c)**: Type 3-1, 3-2,3-3 lamp. **(d)**: Oven-lamp. **(e)**: Type 4 lamp.

1.9   Thesis outline

As said before we explored a vast range of the electromagnetic spectrum in order to find active spectroscopical means to investigate light generating plasmas. In presenting the results we follow the direction of decreasing photon energy. We start in chapter 2 with a feasibility study on gamma spectroscopy. This is followed by a triad of the Chapters 3, 4 and 5 on X-ray absorption spectroscopy. After that two chapters on Thomson scattering will be presented. More specifically this thesis is organized as follows:

Chapter 2 reports on a feasibility study of γ-spectroscopy. Based on several experiments, the various possibilities to detect sodium by radioactive tracer techniques are discussed.

Chapter 3 presents the design of the experimental setup for X-ray absorption that was used for the determination of the gas temperature. The discussion is focused on the requirements of an XRA experiment on HID lamps, i.e. the high flux of the X-ray beam, the monochromaticity of the X-ray spectrum, high spatial resolution and high dynamic range.

Chapter 4 deals with the complete data handling procedure of XRA measurements. It describes how multiple pairs of lamp-on and lamp-off profiles have to be measured and processed in relation with each-other. The procedure starts with the signal extraction that corrects for the dark current, offset and non-uniformity of CCD pixels (flat field). Then several influences on the image will be discussed such as blurring, beam-hardening, image magnification, thermal expansion and density decrease of the burner for the lamp-on case. After this, a fitting procedure of lamp-off and lamp-on profiles is presented. Subtraction of these profiles gives the relative column density. An Abel inversion procedure will be given for the fitting of the lateral profile. In order to reconstruct the radial profile, the numerical difficulties for this ill-posed problem are discussed and the Tikhonov regularization method is introduced to obtain the best results.

Chapter 5 presents the application of XRA on various HID lamps. This technique has been proved to be successful for the measurement of the gas temperature of HID lamps. A discussion will be given on the comparison of the temperature profiles of different lamps. Insight is obtained on the influence of the salt composition, the power and the pressure on the gas temperature profiles.

Chapter 6 is devoted to Thomson scattering (TS) experiment on a high-pressure argon DC discharge lamps. It was a pioneer experiment done together with a group of Ruhr University of Bochum to investigate the feasibility of TS on small high-pressure discharges with nearby arc tube walls or electrodes. This experiment has been successful and the electron density and temperature could be measured in regions close to the electrodes.

Chapter 7 applies the TS experiment to a high-pressure Hg lamp. The difficulties we had to face with this setup were how to deal with stray light generated by the laser-wall interaction, the laser induced plasma and the plasma light emission. Time-resolved TS measurements were done on Hg plasmas excited by square-wave ballast and useful information was obtained for lamps with different Hg pressures and power-settings. A discussion is given on the degree of the deviation from LTE.

Chapter 8 ends this study by drawing conclusions and giving recommendations for future research.

Chapter 2

Feasibility study of γ-spectroscopy on metal halide lamps

Abstract

As announced in the introduction, this chapter deals with an active spectroscopic method using photons of the highest energy; namely γ-photons. A feasibility study is carried out to detect sodium in metal halide (MH) lamps with γ-spectroscopy using radioactive Na isotopes. The reason is that the elemental density of sodium cannot be detected by X-ray fluorescence whereas optical techniques are not able to detect the outer molecular part of the plasma. Since Na is an important light emitting element we have to look for alternatives for which we investigated the feasibility of γ-spectroscopy. The emission of γ-photons is realized by "replacing" the natural sodium isotope ^{23}Na (partly) by ^{22}Na or ^{24}Na.

This feasibility study starts with an experiment in which a MH lamp containing ^{23}Na was irradiated by neutrons in the near vicinity of a production target attached to a cyclotron. The experiment was carried out at our own university. From the data analysis we found that ^{24}Na isotopes have been formed but the intensity of the γ photons created by the decay of ^{24}Na is too small for imaging Na in the MH lamp. However, considerable improvements can be realized if the irradiation time and the neutron flux can be increased and the detection volume and solid angle can be enlarged. Especially irradiation with a high neutron flux nuclear reactor seems to be promising. However, irradiating a lamp with a nuclear reactor creates a highly radioactive medium that is not easy to handle. In principle, the replacement of ^{23}Na by commercial available ^{22}Na can also provide a high γ-flux for imaging. However, given the boundary conditions imposed by the typical amount of ^{22}Na which is commercially available and tractable, this seems not a viable option.

Most promising is the method in which Na is bound with ^{123}I. Then we can use medical diagnostic methods tracing ^{123}I. Single Photon Emission Computed Tomography (SPECT) in combination with a pinhole makes it possible to reach a spatial resolution of better than 0.5 mm. Insight in the spatial distribution of NaI obtained in this way can be combined with optical observations of the Na atoms in the central region.

2.1 Introduction

Sodium (Na) is one of the most common radiative species in metal halide lamps. Its presence influences the color of lamps in a positive way and improves the efficiency considerably. Therefore, the Na density profile in the lamp is a key factor in understanding the plasma energy aspects and segregation phenomena. It is, for instance, important to know how sodium is distributed in the radial direction. If the lamp envelope is made from transparent material (such as quartz), it is possible to determine the density of *atomic* sodium in the center of the discharge using standard optical techniques such as laser induced fluorescence (LIF), diode laser absorption and/or absolute line intensities. However, a considerable part of sodium will be bound in halide *molecules* like NaI and resides in the colder regions of the lamp. That region is not easily accessible with the optical methods mentioned above. One of the reasons is that the electronic transitions of the NaI will not be (easily) excited in this cold region. One alternative could be to work with (active) IR spectroscopy, but this is not easy to perform since the radiation will be hindered severely by the nearby presence of the curved wall.

As stated above one could apply optical spectroscopy to observe the central region of the lamp. However this is only possible if special lamps are made for such experiments. Due to the high heat load of the wall material the commercial arc tube is normally made of polycrystalline alumina (PCA). This material is translucent and not transparent which means that for the visible range light can pass through the envelope, but will be scattered. As a consequence the original direction information is lost. Thus normal optical methods are not suitable for making spatially resolved measurements on plasmas embedded in PCA.

In literature [8,9], X-ray fluorescence (XRF) techniques are described which have been used to measure the elemental density distribution in lamps. The advantage of the XRF method is that the presence of the element can be detected despite its chemical state. For Na, the most important X-ray transitions have the following energies:

$$E(K_\alpha) = 1.04 \, \text{keV} \quad \text{and} \quad E(K_\beta) = 1.07 \, \text{keV} \, ,$$

so that the characteristic K-shell emission of Na is only about 1 keV. However, photons of these energies will be absorbed by the wall material. For example, for X-rays with an energy of 1.07 keV, the optical depth τ_{SiO_2} of a quartz outer bulb with a wall thickness of 1 mm, and a density of 2.2 g/cm^3 is about 500; for the PCA burner (density of 3.97 g/cm^3 and wall thickness of 0.8 mm) the same photon has an optical depth of around 700. Thus, the wall material of the lamp is opaque for 1 keV photons so that X-ray fluorescence spectroscopy (XRF) is not suitable for detecting Na. The main reason that X-ray fluorescence is suitable for the determination of many other elements is that their corresponding photon energy is much higher. Unfortunately for sodium the corresponding photon energy is too low. Therefore, it is necessary to find another method to measure the Na density distribution.

In this chapter we present a feasibility study on the detection of sodium using γ-ray spectroscopy. An experiment was performed in which various commercial lamps were irradiated by moderated neutrons in the near vicinity of a irradiation target attached to a cyclotron by which the natural isotope ^{23}Na was transformed into ^{24}Na. After being produced by irradiation, ^{24}Na decays into ^{24}Mg under the emission of γ photons of 1.369 MeV and 2.754 MeV. For these energies the lamp envelope is transparent so that these photons can be detected. The outcome of these experiments is that this technique is suitable to determine the presence of sodium as well as other elements, but the detected flux of γ ray photons is too small to use this method for a spatial resolved determination of the elemental sodium concentration. However, the insight obtained by these preliminary experiments indicates possible routes for further improvements. Most promising is the method in which the normal sodium iodide in the salt pool is replaced by NaI in which the natural isotope ^{127}I is (partly) replaced by the radioactive isotope ^{123}I. In that way we can take advantage of the rapid development in the SPECT (Single Photon Emission Computed Tomography) technique that is available for medical diagnostics. It is to be expected that in the near future the determination of the spatial resolved salt concentration in the wall region is feasible. This method should then be combined with optical techniques for the central region to detect Na-atoms. Naturally, special lamps have to be constructed for such a combination of diagnostics.

2.2 Creating and measuring radioactive Na isotopes

2.2.1 Theory

The elemental density of sodium in metal halide lamps can be investigated with radioactive tracers. Suppose that we have at time t a number of radioactive nuclei $N(t)$ present in the lamp, in a subsequent small time interval dt a part of the initial number $N(t)$ will decay with a decay rate $\lambda \, [\mathrm{s}^{-1}]$ that is defined by the equation:

$$\frac{dN}{dt} = -\lambda N. \tag{2.1}$$

Integration of Eq. 2.1 gives the following expression for the number of radioactive nuclei $N(t)$ at time t

$$N(t) = N_0 e^{-\lambda t}, \tag{2.2}$$

where N_0 is the original number of the radioactive nuclei at $t = 0$. This expression can also be written as

$$N(t) = N_0 \left(\frac{1}{2}\right)^{t/t_{1/2}}, \tag{2.3}$$

where $t_{1/2}$ is the half-life of the radioactive nucleus. By comparing Eq. 2.2 with Eq. 2.3, we get

$$\lambda = \frac{\ln 2}{t_{1/2}}. \tag{2.4}$$

The activity of the radioactive nuclei $A(t)$ is defined as

$$A(t) \equiv \lambda N(t). \tag{2.5}$$

The SI unit of A is Becquerel (Bq): 1 Bq=1 decay/s.

There are primarily three types of nuclear decay processes: the α, β and γ decay[1]. In the α, β decay processes the unstable nucleus emits an α or β particle. In γ decay an excited state decays towards the ground state without changing the nuclear composition. In most cases a decay scheme can be rather complicated involving the emission of α, β and γ particles in several competing modes or branches. In our experiment we dealt with the detection of γ solely.

In order to determine the initial number of radioactive nuclei the following procedure is used.

1). From the nuclei decay diagram, we know the decay constant and the energy of the γ photons emitted during (a branch of) the decay process. 2). By measuring ΔN_γ, the number of the γ photons during a certain time interval Δt, the initial decay activity A_0 can be determined (cf. Eq. 2.10). 3). Using equation 2.5, the initial number of radioactive isotopes at a certain (initial) time $t = 0$ can be obtained.

2.2.2 The radioactive isotopes ^{22}Na and ^{24}Na

In nature, sodium (Na) has only one stable isotope ^{23}Na. By irradiation, the radioactive isotopes, ^{22}Na and ^{24}Na can be obtained. ^{22}Na is a long-lived isotope with half-life of 2.6 year. It decays into the (2^+) [2] excited state of ^{22}Ne by β^+ emission (probability 90.5%) and electron capture (probability 9.5%) which subsequently decays into the ^{22}Ne (0^+) ground state by the emission of a γ photon with an energy of 1274.5 keV.

In contrast to ^{22}Na, ^{24}Na is a relatively short-lived isotope with a half-life of 15 hours. During the β^- decay process, ^{24}Na decays into the 4^+ excited state of ^{24}Mg with a probability larger than 99% [11] followed by the subsequent emission of two γ-photons with energies of 1368.6 keV (corresponding to the $2^+ \rightarrow 0^+$ transition) and 2754 keV (corresponding to the $4^+ \rightarrow 2^+$ transition). Simplified decay processes of ^{22}Na and ^{24}Na are given in reaction schemes presented in Table 2.1.

Generally speaking, there are three ways to detect sodium by means of radioactive methods:

1. Creating ^{24}Na by irradiation of ^{23}Na with neutrons.
2. Filling the lamp with a salt containing ^{22}Na.
3. Filling the lamp with a salt containing ^{123}I for labeling the molecular species (NaI).

The first two methods are used to measure the elemental density of sodium, and the third

---

[1] Electron capture, also indicated by ϵ [10], can be seen as a member of the larger group of β-decay together with β^- and β^+.

[2] This notation (2^+) used in nuclear physics to express the excited state of a nucleus, should not be confused with the convention in plasma physics to label the charge of the species.

$$
\begin{array}{lll}
{}^{22}_{11}\text{Na} + \text{e} \xrightarrow{9.5\%} {}^{22}_{10}\text{Ne}(2^+) & \Rightarrow {}^{22}_{10}\text{Ne}(2^+) \rightarrow {}^{22}_{10}\text{Ne}(0^+) + \gamma \,(1274.5\,\text{keV}) \\
{}^{22}_{11}\text{Na} \xrightarrow{90.5\%} {}^{22}_{10}\text{Ne}(2^+) + \text{e}^+ & \Rightarrow {}^{22}_{10}\text{Ne}(2^+) \rightarrow {}^{22}_{10}\text{Ne}(0^+) + \gamma \,(1274.5\,\text{keV}) \\
\\
{}^{24}_{11}\text{Na} \xrightarrow{99\%} {}^{24}_{12}\text{Mg}(4^+) + \text{e} & \Rightarrow {}^{24}_{12}\text{Mg}(4^+) \rightarrow {}^{24}_{12}\text{Mg}(2^+) + \gamma \,(2754\,\text{keV}) \quad \Rightarrow \\
& \Rightarrow {}^{24}_{12}\text{Mg}(2^+) \rightarrow {}^{24}_{12}\text{Mg}(0^+) + \gamma \,(1368.6\,\text{keV})
\end{array}
$$

Table 2.1: Simplified decay schemes of the radioactive isotopes ${}^{22}_{11}Na$ and ${}^{24}_{11}Na$. The decay of ${}^{24}Na$ mainly follows one chain of which 3 steps are given. Therefore the emission probability of the photons at 1368.6 keV and 2754 keV respectively is almost 100%.

method can be applied to obtain the elemental distribution of iodine which will be primarily bound in NaI molecules in the near wall region of the lamp.

We have used the first method in a series of experiments in which ^{24}Na was created by irradiating ^{23}Na with neutrons in the near vicinity of an ^{123}I production target attached to a cyclotron. By analyzing the results of this method we can establish its (non-)feasibility and discuss the possibilities of other methods.

2.2.3 Experimental procedure

The experimental procedure for the creation of radioactive ^{24}Na isotopes in a metal halide lamp containing a salt mixture of NaI/CeI$_3$ is shown in Fig. 2.1. First, the whole lamp was placed in the near vicinity of a production unit of ^{123}I attached to the 30 MeV Cyclotron at Eindhoven University of Technology (TU/e) and irradiated for a few hours Δt_1. Then, after a cooling-down period Δt_2, the lamp was taken out from the cyclotron irradiation vault and the γ spectrum emitted by the isotopes in the lamp was measured. The measurement time is denoted by Δt_3.
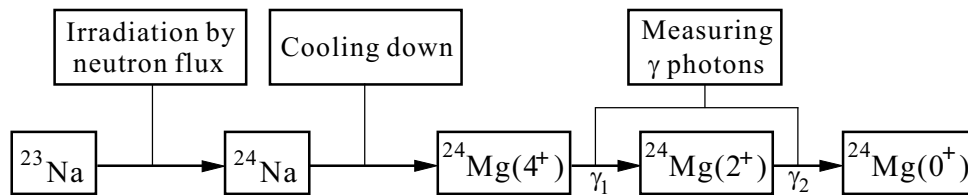
Figure 2.1: The experimental procedure of creating and detecting radioactive isotope ^{24}Na.

The time-sequence is sketched in Fig. 2.2. It is important to optimize the irradiation, cooling and measurement time in order to obtain the best results.

Now we will give a short description of the neutron irradiation process. By means of irradiation, a part of the ^{23}Na will be transformed into ^{24}Na and consequently the number
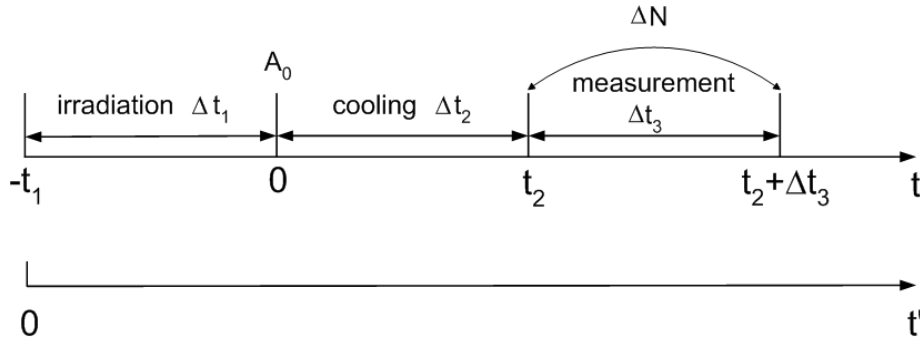
Figure 2.2: The time sequence of the experimental procedure of creating and detecting the radioactive isotope ^{24}Na.

of ^{24}Na isotopes will increase. However due to the spontaneous decay the created ^{24}Na will be transformed into Mg isotopes. The time behavior for the irradiation process can be described by the following differential equation

$$\frac{dN(t')}{dt'} = P - N(t')\lambda, \tag{2.6}$$

which expresses that the increase of the number N of radioactive nuclei per unit time is determined by the production P due to irradiation, minus the destruction by spontaneous radioactive decay $N(t')\lambda$. To describe the irradiation process a different time coordinate t' was introduced that has its origin $t' = 0$ for $t = -t_1$ such that $t' = t + t_1$. Solving this differential equation we get, for the boundary condition $N(t' = 0) = 0$:

$$N(t') = \frac{P}{\lambda}(1 - e^{-\lambda t'}). \tag{2.7}$$

Using Eq. 2.5, it is found that the activity of the decay process at time t' equals

$$A(t') = P(1 - e^{-\lambda t'}). \tag{2.8}$$

The production $P = N_0 \sigma F$, is proportional to the number of the nuclei in the target N_0, the production cross-section $\sigma \, [\text{cm}^2]$ and the neutron flux density $F \, [\text{cm}^{-2}\text{s}^{-1}]$. It has a fixed value for a given neutron flux density and a given target. The estimated flux density of thermal neutrons in the cyclotron vault is around $10^6 \, \text{neutrons}/[\text{cm}^2 \cdot \text{s}]$ [12].

A graphical representation of formula 2.8 given in Fig. 2.3 shows that $A(t')$ will approach a constant value that equals $A(t' = \infty) = P$. This can be understood realizing that in steady state the number of created radioactive nuclei by means of irradiation equals the number of decay process. Thus the larger P, the larger $A(\infty)$ will be. The characteristic time for this procedure is independent of P and equals $1/\lambda$. It gives the time duration after which the activity A will reach $63\%P$.

Produced ^{24}Na activity
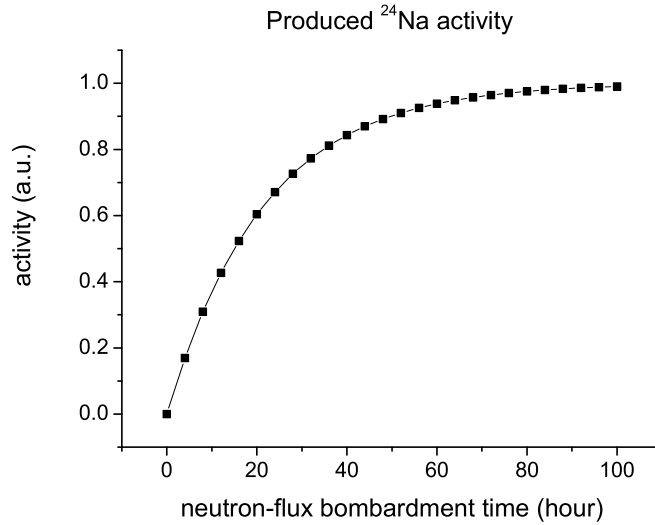
Figure 2.3: The activity of radioactive isotope ^{24}Na as a function of bombardment time t' in the neutron irradiation process(cf. eq. 2.8).

The number of ^{24}Na atoms that are created from the neutron capture process is unknown because it depends on several parameters: the initial number of ^{23}Na nuclei, the neutron flux density and the neutron energy distribution. None of these parameters is easy to measure. Therefore the activity after irradiation cannot be determined out of the irradiation parameter P. However, the activity generated by the irradiation can be determined by counting the decay process that follows after the irradiation since more than 99% of the decay processes of ^{24}Na nuclei are associated with an emission of two γ photons with energy of 1368.6 keV and 2754 keV. Therefore by counting the number of γ photons in a period after irradiation the activity can be found. Its temporal behavior is given by

$$A(t) = A_0 e^{-\lambda t}, \tag{2.9}$$

where $A_0 = A(0)$ is the activity of ^{24}Na immediately after the neutron bombardment (t=0). The activity of ^{24}Na in the whole process (irradiation plus pure decay) is illustrated in Fig. 2.4.

If the measurement starts after the cooling-off time t_2, the number of γ-photons ΔN_γ measured during the measurement time Δt_3 is a measure of the number of the decay processes ΔN of ^{24}Na. This is expressed by

$$\Delta N_\gamma = \eta \xi \frac{\Delta \Omega}{4\pi} \Delta N = \eta \xi \frac{\Delta \Omega}{4\pi} \frac{A_0}{\lambda} e^{-\lambda t_2} (1 - e^{-\lambda \Delta t_3}), \tag{2.10}$$

where η is the probability that a certain decay process generates a specific γ-photon, ξ the efficiency of the detector, and $\Delta \Omega$ the solid angle of the detection system. Therefore the
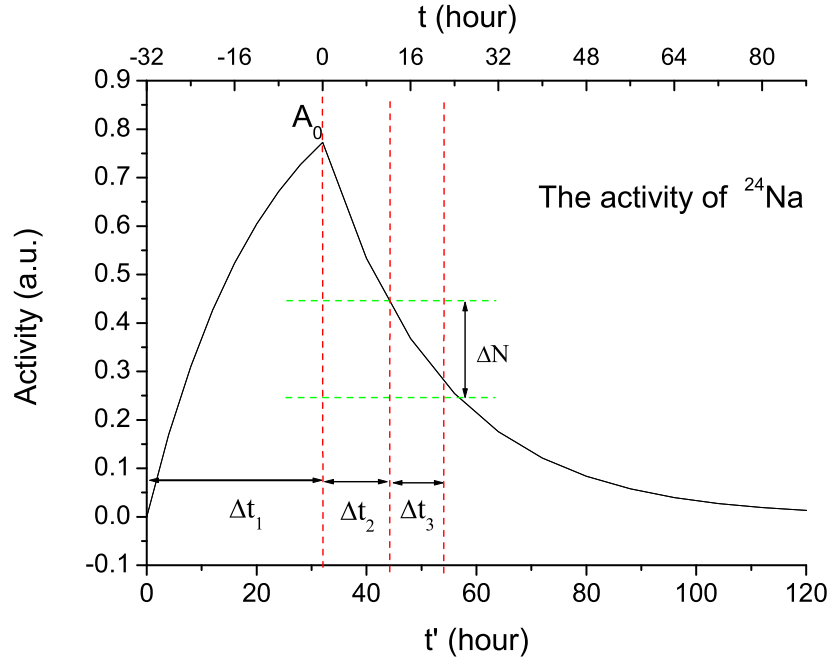
Figure 2.4: The activity of ^{24}Na during the whole process; Δt_1 is the neutron flux bombardment time, Δt_2 the cooling-down time and Δt_3 the measurement time. A_0 is the activity of ^{24}Na at the end of the neutron bombardment.

absolute activity immediately after the irradiation can be computed from the intensity of the γ photons as

$$A_0 = \frac{\Delta N_\gamma \lambda}{\eta \xi e^{-\lambda t_2}(1 - e^{-\lambda \Delta t_3})} \frac{4\pi}{\Delta \Omega}. \tag{2.11}$$

The branching ratio of the generation of 1368.6 keV photons equals almost 100%, so that $\eta(1368.6 \, \text{keV}) = 1$. This means that nearly each decay of a ^{24}Na nucleus generates one γ-photon of 1368.6 keV. Thus by counting the 1368.6 keV photons we can determine the total number ΔN of decay processes during the measurement time. The A_0-value, the absolute activity of ^{24}Na at $t = 0$, can be computed if the solid angle $\Delta \Omega$ and the absolute efficiency ξ of the detection system are known.

2.3 Experimental setup

The experimental setup of γ spectroscopy on lamps is illustrated in Fig. 2.5.
The lamps that were used in these experiments consist of a burner and an outer bulb. The burner had an inner diameter of 4 mm and an inner length (distance between two electrodes) of 32 mm. They were filled with Hg and a salt-mixture (NaI/CeI$_3$) and placed
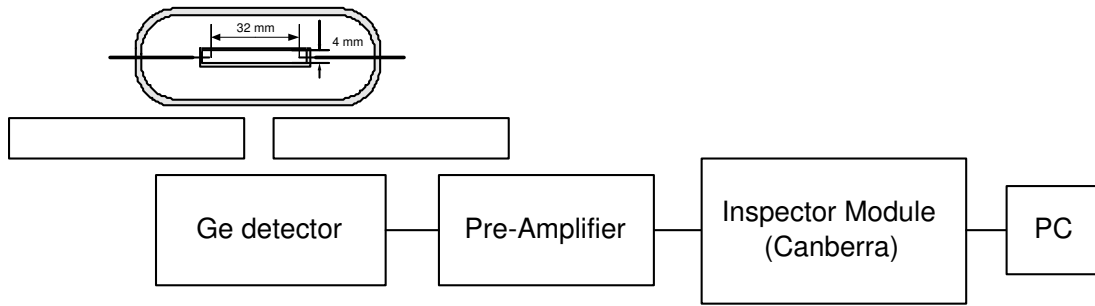
Figure 2.5: The experimental setup for γ spectroscopy on lamps. A lead shielding is placed between the lamp and the high-purity Ge detector when a spatially resolved measurement is required. The γ photons of different energies and intensities are detected by the Ge detector, the signal is amplified and analyzed by the Inspector module from Canberra. Finally the data-acquisition software GENIE-2000 (Canberra) is used to identify the isotopes using a built-in database. The lamp consists of an outer bulb and a burner (made of PCA material). The burner has an inner diameter of 4 mm and an inner length of 32 mm.

directly on top of a high-purity Ge detector. The Inspector Module contains a spectroscopy amplifier unit, an A/D converter (ADC), a multi-channel analyzer (MCA) and a high voltage supply for operating the Ge detector. The data-acquisition software used is the GENIE-2000 system (Canberra) which allows isotope identification using a built-in database.

2.4 Results

2.4.1 Exploration of the γ-spectra

To explore the possibility of detecting ^{24}Na and other elements in the lamp, four groups of experiments were done. The γ-spectra of the lamp were measured and the corresponding isotopes were identified using the known characteristic energy values of the γ-photons and the half-life of nuclei decay. The experimental results are shown in Table 2.2.

From the experimental data, it was found that due to the neutron flux irradiation, other elements than Na in the lamp are also being transformed into radioactive isotopes. The first group of experiments was done on a metal halide lamp with an *outer bulb* of *glass*. It was found that the γ-ray intensity generated by ^{24}Na has a very high peak-value that is much larger than that of other elements. This suggest that Na is not only located in the burner, but also in the outer glass bulb of the lamp. Therefore a new lamp with an (sodium-free) outer bulb made of *quartz* was constructed. All the following experiments were done with this new lamp.

From the second experiment, we found that the γ-ray intensity generated by the decay

Experiment	No.	t_{cool}	$t_{measure}$ (s)	Detected radio-active elements
1st **Experiment** 3-hours neutron flux irradiation on the HID lamp (NaI/CeI$_3$ and Hg) with glass outer bulb.	#1−1	12 hr	10,000	^{24}Na, ^{56}Mn, ^{64}Cu, ^{69m}Zn, ^{99}Mo/^{99m}Tc, ^{187}W
	#1−2	17hr 8min	3,000	^{24}Na, ^{56}Mn, ^{64}Cu, ^{69m}Zn, ^{187}W
	#1−3	43hr 5min	50,000	^{24}Na, ^{64}Cu, ^{65}Zn, ^{69m}Zn, ^{187}W
	#1−4	134hr 5min	10,000	^{24}Na, ^{65}Zn, ^{187}W
	#1−5	163hr 31min	50,000	^{24}Na, ^{65}Zn, ^{187}W
2nd **Experiment** 4-hours neutron flux on the HID lamp with quartz outer bulb and double-ends.	#2	10hr 58min	10,000	^{24}Na, ^{56}Mn, ^{99}Mo, ^{99m}Tc, ^{143}Ce, ^{165}Dy, ^{187}W
3rd **Experiment** 4-hours+3-hours flux on the HID lamp with quartz outer bulb.	#3−1	13 min	1,000	^{24}Na, ^{56}Mn, ^{99m}Tc, ^{128}I, ^{143}Ce, ^{165}Dy, ^{187}W, ^{101}Mo/^{101}Tc
	#3−2	31 min	1,000	^{24}Na, ^{56}Mn, ^{99m}Tc, ^{128}I, ^{143}Ce, ^{165}Dy, ^{187}W, ^{101}Mo/^{101}Tc
4th **Experiment** 4-hours neutron flux on the HID lamp with quartz outer bulb.	#4−1	13hr 53min	1,892	^{24}Na, ^{56}Mn, ^{99}Mo/^{99m}Tc, ^{143}Ce, ^{165}Dy, ^{187}W
	#4−2	17hr 38min	1,000	^{24}Na, ^{56}Mn, ^{99}Mo/^{99m}Tc, ^{187}W
Measure the whole lamp when it is not burning.	#4−3	18hr 12min*	1,000	^{24}Na, ^{187}W

Table 2.2: The identification of the radioactive isotopes created by the neutron bombardment process. All the experiments were measured with a Ge detector. All experiments were done with the whole lamp. In experiment #4 − 3 the outer part was shielded using a lead shield and only the burner part was measured.

of ^{24}Na drops significantly because sodium is now only present in the salt in the burner. Other radioactive isotopes than ^{24}Na were identified, such as ^{56}Mn, ^{99}Mo/^{99m}Tc, ^{143}Ce, ^{165}Dy and ^{187}W. Especially Ce is important to know since it is also one of the light emitting species. However, we didn't see any isotopes from iodine although iodine should be present as all light emitting additives (like Na and Ce) are brought into the plasma as iodine-salts. The absence of iodine generated γ- photons can be explained by the fact that ^{128}I has a short half-life of about 25 minutes. After the long cooling time of 10 hr or longer (cf. Table 2.2) the I-radioactivity has decayed almost completely. Therefore a third experiment was done in order to observe ^{128}I.

In the third experiment we measured the γ-spectra right after the irradiation (13 minutes later). This time we found the γ-emission of ^{128}I at 442.9 keV.

The fourth series of experiments has been done with a lead shielding between the lamp and the detector such that only the burner part is detected. This was done in order to

check whether the metal wires outside the burner also contain sodium. It turns out that the detected signal of sodium only comes from the burner.

A typical γ-spectra of measurement $\#3-1$ is shown in Fig. 2.6.
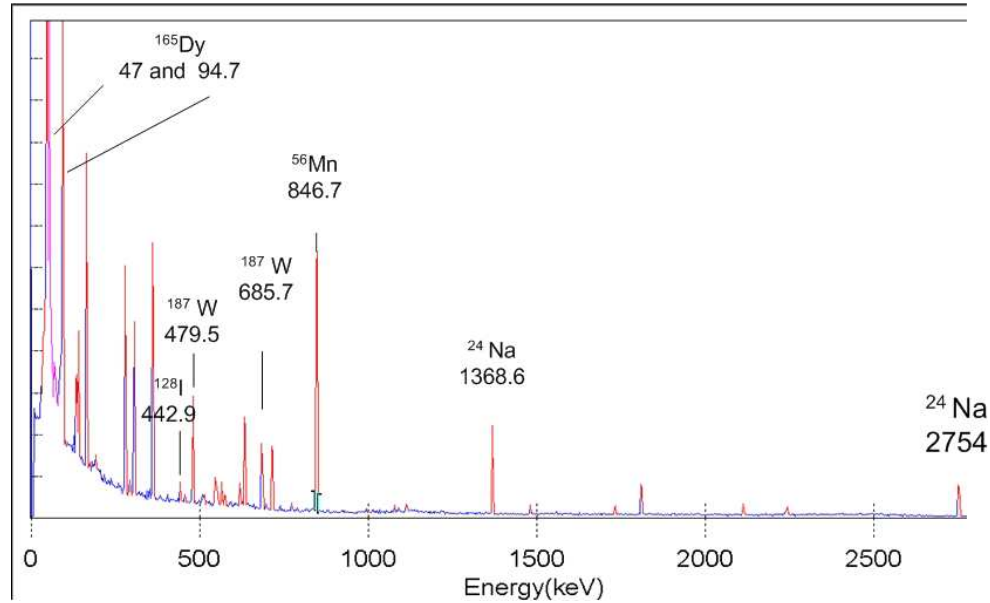
Figure 2.6: The γ spectra of measurement $\#3-1$.

From these experiments, we can conclude that

1. We can detect four elements that are related to the operation of the metal halide lamp: ^{24}Na (half-life of 15 hr), ^{143}Ce (half-life of 33 hr), ^{128}I (half-life of 25 min) and ^{187}W (half-life of 23.7 hr).

2. The γ ray peak from ^{24}Na (1368.6 keV) is well separated from other spectral lines (see Fig. 2.6) and therefore it is easy to detect Na in the lamp.

3. Other elements can also be detected such as Mn, Mo which are located in other lamp parts outside the burner.

4. If we want to detect iodine, a very short cooling time is required since ^{128}I has a very short half-life of 25 min.[3]

5. The radioactive isotopes are mainly short-lived, so that after a few weeks, almost no radioactive waste is left.

---

[3]The ^{123}I isotope (cf. section 2.6.3), that is well-known for medical applications, is not created in this irradiation process
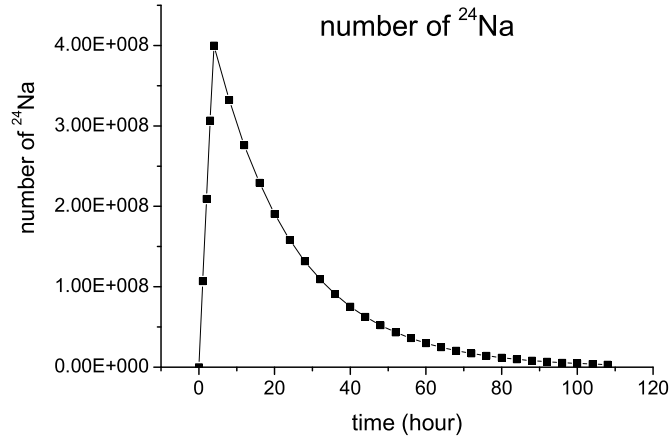
Figure 2.7: The number of ^{24}Na during the process of neutron bombardment and measurement. The peak is reached at the end of the neutron bombardment; after the peak a exponential decay takes place (cf. Fig. 2.4).

2.4.2 The number of ^{24}Na nuclei produced by irradiation

Using the GENIE 2000 software it was found that the activity of the ^{24}Na isotopes directly after irradiation equals $A_0 = 5000 \, \mathrm{Bq}$ (over 4π solid angle). This was realized by an irradiation period of 3 hours. Thus the total number of ^{24}Na atoms in the lamp directly after irradiation is

$$N_{^{24}Na}(0) = \frac{A_0}{\lambda} = \frac{5 \times 10^3}{1.28 \times 10^{-5}} = 4 \times 10^8. \tag{2.12}$$

The number of radio-active ^{24}Na atoms as a function of time during the entire process is shown in Fig. 2.7.

However, the lamp is filled with 4 mg NaI which corresponds to a total number of Na atoms of 1.6×10^{19}. Therefore only a very small fraction (2.5×10^{-11}) of the ^{23}Na atoms are converted into ^{24}Na atoms during the neutron irradiation process. Apparently the conversion efficiency is very small.

To study the distribution of Na in the plasma, we are interested in the number of Na atoms in the gas phase. This is estimated to be about 0.3% of the total amount of Na in the lamp. The rest is present in the salt pool. This implies that only 0.3% of the detected γ-photons stems from the gas phase ^{24}Na nuclei (about 1.2×10^6). Therefore the activity of ^{24}Na in the gas phase is estimated to be

$$A_{^{24}Na(gas)} = 0.3\% \times 5000 = 15 \, \mathrm{Bq} = 15 \, \mathrm{decay/s} \,. \tag{2.13}$$

The conclusion is that the production of the ^{24}Na isotopes is very low. Although the irradiation facility attached to the cyclotron is primarily producing high energy neu-

trons, the estimated flux of moderated thermal neutrons near the lamp is approximately 10^6 neutrons/(cm$^2 \cdot$ s). In order to increase the irradiation efficiency, one should look for methods to increase the P-value in Eq. 2.8. For instance, one might consider to irradiate the lamp in a high neutron flux nuclear reactor which can deliver a neutron flux of typically 10^{14} neutrons/(cm$^2 \cdot$ s) [13]. This and other possibilities will be discussed in section 2.6.

2.5 Spatial resolution

The main goal of γ-spectroscopy is to obtain the elemental distribution of sodium in the lamp, namely {Na} (cf. section 1.5). This requires a spatial resolved measurement of γ-spectra from the metal halide lamp.

The experimental setup to measure the spatially resolved density distribution of ^{24}Na is illustrated in Fig. 2.8.
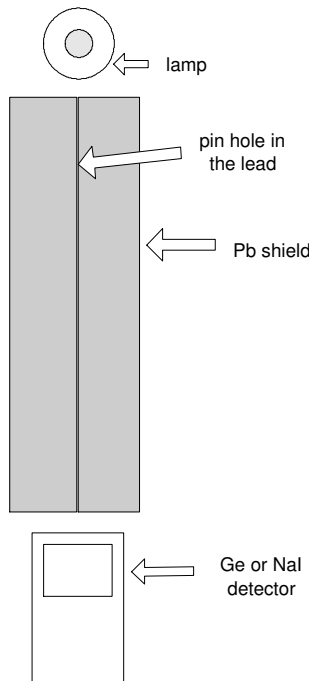
Figure 2.8: The experimental setup scheme to measure Na density profile. It includes the lamp, a thick lead plate with a pinhole and gamma ray detector.

For a measurement of the Na density distribution of such a thin lamp ($D_{in} = 4$ mm), we need a spatial resolution of at least 0.2 mm. Since there is no lens available for γ-rays we have to reduce the detection volume by confining the solid angle. This is done by making a pinhole of 0.2 mm diameter in a thick lead plate. To reduce the intensity of γ-ray with photons of 1.37 MeV by a factor of 100 from the near vicinity of the point of interest (the position observed by the pinhole), the thickness of lead shielding must be about 7 cm. Behind the pinhole a Ge or NaI detector can be placed to measure the 1.37 MeV photons.

From the pinhole diameter $d = 0.2\,\text{mm}$, the thickness of the Pb shielding $l = 7\,\text{cm}$ and the lamp outer radius $R = 1.5\,\text{cm}$ we find a solid angle of

$$\Delta\Omega = \frac{S}{(l+R)^2} = \frac{\frac{1}{4}\pi d^2}{(l+R)^2} = 4.3 \times 10^{-6}\,\text{Sr}. \tag{2.14}$$

By collecting γ-photons for various lateral positions we can, in principle, obtain information to determine the radial density distribution of ^{24}Na nuclei by means of an Abel inversion method. The smallest number of γ-photons will be obtained from the detection volume near the edge (see Fig. 2.9). Taking a path length of $1.74\,\text{mm}$ we get a detection
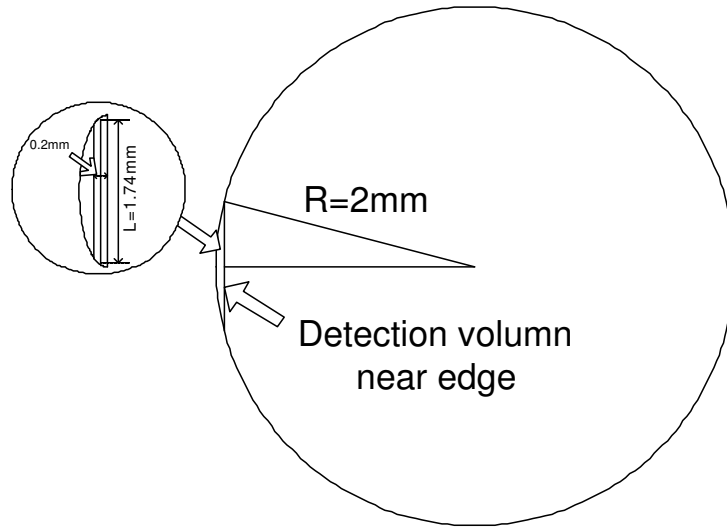
Figure 2.9: A sketch of the detection volume near the edge of a lamp for side-on experiments.

volume ΔV that only forms a small fraction of the total volume V. This small detection volume has a shape of cylinder, i.e. $\Delta V = \pi \times 0.1^2 \times 1.74 = 5.47 \times 10^{-2}\,\text{mm}^3$. Numerically the volume fraction thus equals $\Delta V/V = 1.2 \times 10^{-4}$. Assuming that ^{24}Na (in the gas phase) is homogeneously distributed and that the quantum efficiency of the detector is approximately 2% [14], we find using Eq. 2.13 that the maximum photon flux collection rate at the end of the irradiation (t=0) equals

$$C_\gamma = \eta\xi A_{^{24}Na(gas)}(0)\frac{\Delta V}{V}\frac{\Delta\Omega}{4\pi} = 1.2 \times 10^{-11}[\,\text{photons/s}\,]. \tag{2.15}$$

We have to conclude that the photon count rate of ^{24}Na, generated by the irradiation with a neutron flux in the near vicinity of an irradiation facility at a cyclotron is far too low to make spatially resolved measurements possible if the geometrical pin-hole setup of Fig. 2.8 is used.

2.6 Discussion

Now we discuss the three possible methods that were introduced in section 2.2.2 and look whether they are feasible. They are recalled here for convenience:
1. Creating ^{24}Na by irradiation of ^{23}Na with neutrons.
2. Filling the lamp with a salt composed of ^{22}Na.
3. Filling the lamp with a salt containing ^{123}I for labeling the molecular species (NaI).

Guided by the analysis given in the previous section we will introduce several factors to improve the γ-photon count rate:

1. f_t to increase the irradiation time.

2. f_P to enhance the production rate by the neutron source.

3. f_ξ to improve the detector efficiency.

4. $f_{\Delta\Omega}$ to enlarge the solid angle.

5. $f_{\Delta V}$ to increase the detection volume.

The contribution of the first two factors (f_t and f_P) leads to an enhancement of the *activity*. The last three are related to an improvement of the *detection* system.

2.6.1 Feasibility of the ^{24}Na method by irradiation

According to Eq. 2.8, the produced number of ^{24}Na can be increased by increasing the irradiation time and the production rate P. The irradiation time by the neutron flux in the experiments was about $3 \sim 4$ hours. The produced number of ^{24}Na can be increased by a factor $f_t \approx 4$ by increasing the irradiation time up to about $2t_{1/2} = 30\,\text{hours}$.
The production rate can be increased substantially by placing the lamp in a nuclear reactor. Since the neutron flux density in such a reactor is about $10^{14}\,\text{neutrons}/(\text{cm}^2 \cdot \text{s})$ instead of the $10^6\,\text{neutrons}/(\text{cm}^2 \cdot \text{s})$ found for the cyclotron, we can achieve an improvement of a factor of $f_P = 10^8$. Therefore the total number of activity of the produced ^{24}Na can be improved by a factor of $f_t f_P = 4 \times 10^8$, i.e. $2 \times 10^{12}\,\text{Bq}$.

Replacing the pinhole by a slit will lead to an increase both in the solid angle and the detection volume. This can only be done if the axial gradient of the sodium elemental density is small and negligible. If we consider a slit height of 1 mm, the increase in the solid angle and detection volume are $f_{\Delta\Omega} = 6.4$ and $f_{\Delta V} = 6.4$.

The detector efficiency of the Ge detector depends on the size of the crystal and can be increased from $\xi = 2\%$ to approximately 5% [14]. Since the ^{24}Na-line appears clearly

seperated in the energy spectrum (see Fig. 2.6) it might be possible to apply a NaI scintillation detector which would increase the detector efficiency to a maximum of approximately $\xi = 50\%$. Thus the improvements in the detection system can be as high as $f_\xi f_{\Delta\Omega} f_{\Delta V} \approx 1.0 \times 10^3$.

By realizing all these improvements simultaneously this leads to an enhancement of the photon detection with a factor of 4.0×10^{11} so that the γ-photon count rate that in our preliminary experiment was found to be 1.2×10^{-11} photons/s (cf. Eq. 2.15) can be increased to 4.8 photons/s right after the irradiation. With this initial count rate, it is possible to make spatially resolved measurement. However in practice it remains extremely difficult to handle a lamp which is so highly radioactive.

2.6.2 Feasibility of using ^{22}Na

^{22}Na is commercially available with an activity up to 10^6 Bq. This activity is approximately 6 orders of magnitude lower than that of a sample of ^{24}Na that is obtained by means of an irradiation by a nuclear reactor (cf. section 2.6.1). Then by applying the detection improvements ($f_\xi f_{\Delta\Omega} f_{\Delta V}$) discussed in the previous section this would lead to a photon count rate of about 4.8×10^{-6} photons/s. Therefore we can conclude that experiments with tractable amounts of commercially available ^{22}Na is not a favorable option.

Since ^{22}Na is a β^+ emitter, another suitable diagnostic method might be to detect the γ-photons emitted by the annihilation process (e$^+$+e$^-$=2γ). The coincident detection of the annihilation photons for imaging is known as positron emission tomography (PET). The state of the art spatial resolution of PET is approximately 1.5 mm in animal tissue. However the plasma in a metal halide lamp has a low density compared to that in a biological tissue. This low density will cause a large range of the positron and all the positron annihilation will take place at the lamp wall. Therefore PET can not give a realistic picture of the elemental density distribution in the lamp and we have to conclude that the second option, filling the lamp with a salt composed of ^{22}Na is not a promising method.

2.6.3 Feasibility of labeling NaI by tracing ^{123}I

The third possibility to measure the distribution of NaI is to put a dosis of the ^{123}I-labeled sodium iodide direct into the lamp. ^{123}I is a commonly used radionuclide in nuclear medicine diagnostics. It has a short half-life (13 hours) and generates γ radiation at 160 keV with a decay probability of 87%. ^{123}I can have a radioactivity of about 200 GBq right after production by the cyclotron, but the process of binding with Na to make the NaI salt and filling NaI into the lamp will take some time. The estimated radioactivity of ^{123}I after making NaI salt and filling into the lamp is about 50 GBq. For the gas phase of the ^{123}I labelled NaI this will be about 150 MBq. In the following we discuss the feasibility of the measurement of elemental density of iodine {I} by tracing ^{123}I using Single Photon

Emission Computed Tomography (SPECT).

Research on high-resolution pinhole SPECT [15] has shown that a spatial resolution of approximately 1.3 mm can be reached with a pinhole of 1 mm and a solid angle of 1 Sr. In reference [15], the sensitivity was investigated for the radionuclide ^{99m}Tc (γ-ray energy of 141 keV). It was demonstrated that the measured sensitivity of the detecting system is proportional to the solid angle of the detection system (cf. Eq. 2.14) and thus proportional to the square of the ratio between the pinhole diameter and the distance of the measured point from the pinhole aperture. It was found that for a pinhole aperture of 2 mm and a distance of 1.7 mm to the source, the sensitivity equals 735.4 cps/MBq. In our case we cannot work with a distance of 1.7 mm since the lamp has an envelope with an outer diameter of 30 mm. Thus the distance to the burner axis is at least 15 mm. Taking a distance of 16 mm and a pinhole diameter of 0.2 mm, the sensitivity in our case is a factor of 8.9×10^3 smaller, i.e. 0.083 cps/MBq.

The volume fraction of the lamp viewed by the SPECT system through the 0.2 mm pinhole in a 2 mm lead shielding plate is approximately 5% of the total burner volume. The estimated count rate of the SPECT system then amounts to 0.6 counts/s which should be sufficient to image the ^{123}I concentration of the lamp with a resolution < 0.5 mm. Consequently the iodine density distribution in the lamp can be obtained. The information of the elemental density of {I} can be used in combination of the gas temperature measurement from X-ray absorption to obtain the density distribution of NaI molecules at the cold outer region of the plasma. Nevertheless, the experiment remains difficult. The lamp has to be produced in a radiochemical laboratory that is equipped to handle the high radioactivity of isotopes that have to be inserted into the lamp.

2.7 Conclusion

The γ-spectroscopy technique using radioactive isotopes and a detection system with a pinhole has been investigated as a means to determine the elemental density distribution of Na. It turns out to be impossible to make spatially resolved measurements of ^{24}Na generated by the irradiation of the lamp with neutrons in the near vicinity of a production target attached to a cyclotron. The main reasons are that the neutron flux is too low, and the solid angle and volume of the detection system are too small. If the lamp could be placed for a longer period (30 hours) into a nuclear reactor, it might be possible to enhance the amount of ^{24}Na such that it is feasible to do spatially resolved measurement of elemental density of Na.

It is also found to be impossible to do spatially resolved measurement using commercial available ^{22}Na due to the following reasons:

- The activity of ^{22}Na is too low.

- The use of micro-PET in combination with ^{22}Na is not feasible since the range of the positron in the plasma is larger than the diameter (typically 4 mm) of the lamp envelope.

The SPECT technique has been applied successfully in nuclear medicine imaging by tracing the radiopharmaceutical ^{123}I labelled sodium iodide. It is a promising technique for the detection of the elemental density distribution of iodine in the lamp. By introducing ^{123}I-labelled NaI into the lamp, it is in principle feasible to do spatially resolved measurement. However in practice this would involve handling of high radioactive material during the dosing process of the lamp. This needs a further investigation and an in-depth study in order to apply this method to metal halide lamps.

Chapter 3

Experimental design of X-ray absorption on HID lamps

Abstract

In the previous section we dealt with a technique in which γ photons were used. In the following three chapters we will use photons of lower energy to perform X-ray absorption (XRA) measurements. XRA is a good diagnostic tool to determine the gas temperature in high pressure discharge lamps. It can directly produce complete 2-D maps of the elemental density distribution of the buffer gas (Hg, Xe, Zn) over the lamp. It is also suitable if apart from the buffer gas also minority species such as metal halides are present. From the ideal gas law, the relative temperature profile inside lamps can be inferred. In combination with the absolute measurement of the wall temperature, the complete temperature profile is obtained. This chapter deals with the experimental setup of XRA.

3.1 Introduction

For a proper understanding of the relation between the plasma transport phenomena and the energy coupling of high intensity discharge (HID) lamps we need insight in the temperature distribution over the plasma. That is why a reliable diagnostic has to be constructed and applied to measure the gas temperature, i.e. the temperature of the heavy particles. However, the species in the plasma that are directly heated by the external electric field are the electrons. Depending on the amount of interaction between the different species the electron temperature may differ from that of the heavy particles. In order to establish whether the plasma is in LTE, we need to measure both the electron temperature T_e and the heavy particle temperature T_h independent of each other. This must be done by using techniques for which the results are not dependent on the state of equilibrium departure. The determination of T_e will be done with Thomson scattering (TS) and the results will be given in the Chapter 6 and Chapter 7. For the determination of the T_g we use X-ray absorption (XRA). This method will be discussed in this chapter and the following two chapters 4 and 5.

The basic process of XRA is that due to the interaction with inner-shell electrons X-ray photons are removed from the beam. Since the density of the buffer gas mercury outranges that of the other species, the primary observable is the Hg density distribution n_{Hg}. Therefore we can use the ideal gas law $p = n_{Hg}kT$ to translate the n_{Hg}-field into a spatial distribution of a relative (or normalized) temperature. This is justified since the plasma is within a high degree isobaric.

In the past comparable XRA measurements have been done by several other groups; the results are reported in [16–18]. Our approach is different in the sense that the obtained relative temperature field is calibrated with an absolute measurement of the wall temperature. The application of XRA has the following advantages: Firstly, X-ray photons can penetrate all regions of the lamp, and do not suffer from refractive effects. This makes the method especially interesting for translucent (ceramic) polycrystalline alumina (PCA) burners. Secondly, the X-ray absorption cross-section depends only weakly on the electronic or chemical state of the atom. Thirdly, X-ray absorption measurements only depend on the absolute density of the detected elements. Other plasma parameters such as electron density, electron temperature, do not influence the absorption directly.

The result of XRA are presented in Chapter 5 where the application to several lamp types is reported. By comparing the results with each other we can establish how the T_h field is influenced by changing the chemical composition, the pressure and the power. These results were obtained via a data handling procedure that is treated in Chapter 4. It turns out that the data analysis must be done with some care since the effect of the various instrumental components must be eliminated. The setup and the various functions of its components are dealt with in this chapter, which shows that the design of the experimental setup is not trivial at all. The fact that during XRA only a small absorption signal (due to Hg) has to be inferred out of a large background absorption signal (due to the wall material) makes XRA experimentally difficult. Moreover the XRA experiment on HID lamps asks

for high spatial resolution, high dynamic range and a more or less monochromatic X-ray spectrum.

3.2   Experimental setup: general description

In order to measure the Hg density distribution, an X-ray absorption (XRA) experiment was constructed for which the setup is shown in Fig. 3.1.
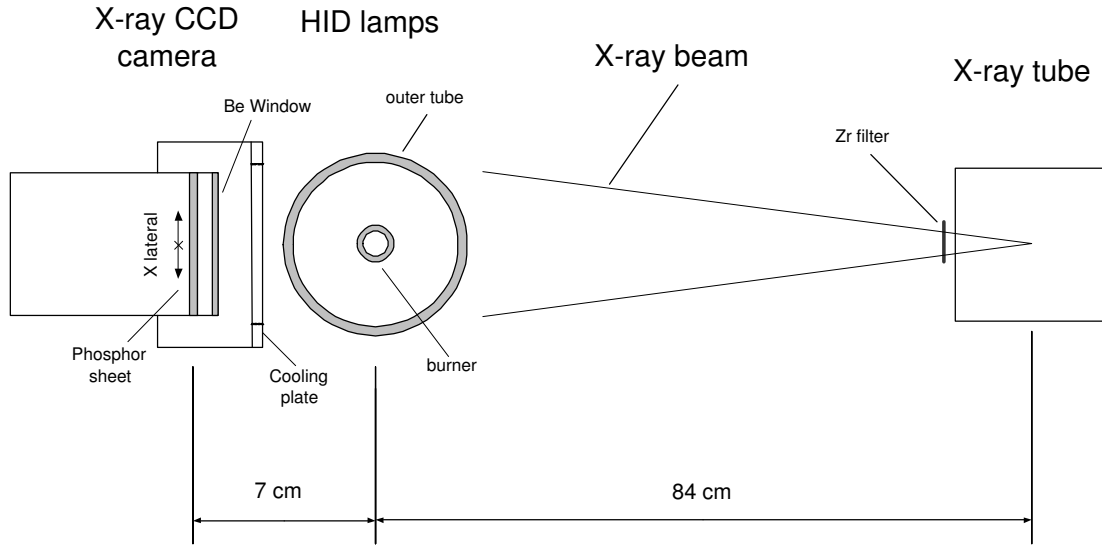
Figure 3.1: Top view of the X-ray absorption experimental setup. X-ray photons generated by a fine-focus Mo X-ray tube equipped with a Zr filter are directed through the lamp. Part of the X-ray radiation will be absorbed by the lamp, the remaining flux falls onto the X-ray CCD camera. The distance between the X-ray source and HID lamp is around 84cm. The total distance between the X-ray source and the CCD camera is about 91cm.

A quasi-monochromatic X-ray beam generated by the Mo-anode X-ray tube (equipped with a Zr filter), is directed towards the HID lamp under investigation. Part of the radiation will be absorbed while the remaining photons are detected by an X-ray CCD camera. CCD images are taken for both lamp-on and lamp-off situations. In the off-situation, the mercury is not present in the volume of the burner, but is condensed in one or two small droplets on the wall or the electrodes. When the lamp is burning, it is filled with mercury vapor. The mercury in the lamp-on situation causes an additional absorption of the X-ray photons. Therefore, the difference of the absorption signal between the lamp-on and lamp-off cases gives information on the mercury density. In the following sections we discuss the different elements of the setup. We start in section 3.3 with a discussion of the lamps and the relevant lamp components. In this way demands are set on the X-ray source and the CCD camera. These are discussed in section 3.4 and 3.5.

3.3 X-ray properties of HID lamps

The XRA technique has been applied to four different designs of HID lamps. These lamps are shown in Fig. 1.5 and their parameters are given in table 1.1. In the following 'type 3' lamp is chosen as an example to discuss the X-ray properties of essential lamp parts.

3.3.1 Optical depth of the different lamp materials

HID lamps consist of an outer bulb and an inner burner that, during operation, is filled with mercury vapor. Thus along the X-ray beam, three different types of lamp materials are encountered, i.e. the outer bulb (made of SiO_2), the inner burner (Al_2O_3 or SiO_2) and the Hg vapor inside the burner; see Fig. 3.2. In order to understand the challenges associated with the measurements, we will estimate the optical depth of these three materials. This will first be done for a beam through the center of the lamp (along path a in Fig 3.2). After that the optical depth will be estimated for a beam that passes at 20 μm distance from the inner wall of the burner (path b). For reference we also give path c, which enters the outer bulb but stays outside the burner.

   Typical values of the path lengths for path a are 2 mm for the outer bulb, 1.6 mm for the inner burner and 4.5 mm for the Hg vapor ('type 3' burner).

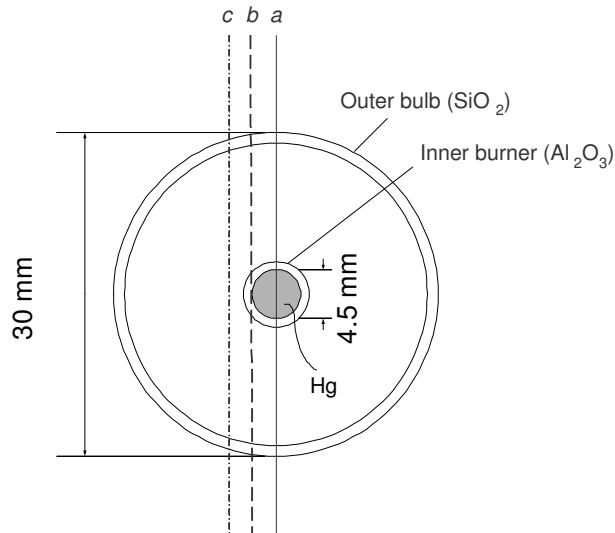*Figure 3.2: The geometry of a 'type 3' lamp. The inner diameter of the outer bulb is 28 mm; for the inner burner this equals 4.5 mm. The wall thickness of the outer burner and inner tube are 1 mm and 0.8 mm respectively. The volume-average Hg density is taken to be 0.015 g/cm^3. (This Hg density value corresponds to the Hg pressure of 19 bar at T_{eff}=3000K). Path c is the path outside the burner.*

material	$\mu_\rho(\text{cm}^2/\text{g})$	$\rho(\text{g/cm}^3)$	$l_a(\text{cm})$	$l_b(\text{cm})$	$l_c(\text{cm})$	τ_a	τ_b	τ_c
SiO_2	3.59 [19]	2.2	0.2	0.2	0.208	1.58	1.58	1.64
Al_2O_3	3.12 [19]	3.97	0.16	0.356	0	1.98	4.41	0
Hg	1.2×10^2 [19]	0.015 (a)/0.03 (b)	0.45	0.06	0	0.81	0.22	0

Table 3.1: Properties of the three different materials for 17 keV X-ray photons along the beam for three cases (Case a: path through the center of the lamp. Case b: path along the outer part of the Hg plasma, 20 μm from the inner wall. Case c: path outside the burner, 4 mm from the center.)

Table 3.1 shows the mass density ρ and the mass absorption coefficients μ_ρ for SiO_2, Al_2O_3 and Hg for a photon energy of 17 keV. One should realize that the mercury density is not constant. In fact it is this very quantity and its spatial distribution that has to be measured. However, to get insight in the order of of magnitude, we took an average density of 0.015 g/cm³ for path a. This corresponds to a pressure of 19 bar at T_{eff}=3000K. With the values of Table 3.1, the optical depth τ of the different elements can be calculated, and we find for path a

$$
\begin{aligned}
\tau_{SiO_2} &= \mu_\rho\rho l = 3.59 \times 2.2 \times 0.2 = 1.58; \\
\tau_{Al_2O_3} &= \mu_\rho\rho l = 3.12 \times 3.97 \times 0.16 = 1.98; \\
\tau_{Hg} &= \mu_\rho\rho l = 1.2 \times 10^2 \times 0.015 \times 0.45 = 0.81.
\end{aligned}
\tag{3.1}
$$

From this calculation it is clear that the optical depth of the burner is 1.98. The τ -value of the Hg gas is only 0.81 so the difference is approximately 1.17, which means that the absorption effect of Hg is only $e^{-1.17} = 31\%$ of the absorption effect of lamp wall material. The optical depth of the outer bulb gives a constant contribution over the region of the burner, i.e. $\tau_{SiO_2} = 1.58$, since it has a constant absorption length for the region in which X-ray photons pass through the burner. Therefore, the outer bulb does not influence the contrast of the signal inside the burner with respect to the outside region. However the presence of the outer bulb does influence the integration time for each single image and therefore the accuracy of the final results.

Next we consider the absorption along path b situated at $20\,\mu$m from the inner wall of the burner (see Fig. 3.2). For the burner the optical depth will increase to 4.41, while the optical depth of Hg drops to 0.22. Now the difference in τ-value between the wall material (burner) and Hg is 4.19. Therefore along path b the absorption of Hg will be 66 times smaller than that of the wall material, which implies that the absorption discrimination capability of the setup should be better than 1.5%; a value that is substantially lower than the 31% found above for path a.

Finally we consider the lamp-off case. If the signal of the region outside of the burner is considered as a constant background as 1, then the signal after the absorption of the burner for path a is $e^{-1.98} = 0.14$, and for path b it is 0.01. In the lamp-on situation, the absorption

of Hg will be 56% for path a and 20% for path b. This means that we need to discriminate a signal change of 0.08 for path a and 0.002 for path b respectively. Therefore, in order to see the absorption of Hg, the dynamic range should be at least $500 \approx 2^9$. For getting accurate results, it is preferable to go to a 14-bit or an even better 16-bit resolution system.

This case study, which compares the two paths a and b with each other, shows that changing the beam position (e.g. from path a to b) will not affect the τ value associated with the outer bulb. This is due to the fact that the outer bulb has a relatively large diameter of 30 mm. On the other hand, the absorption path through the burner (Al_2O_3) will change drastically. This is illustrated in Fig. 3.3 that shows the path length through the burner as a function of radial position. This drastic change in path length has an effect on the spectral distribution of non-monochromatic beams in such a way that the X-ray spectrum as offered to the Hg gas along path a is not the same as that along path b. Since the absorption coefficient is decreasing for increasing photon energy we find that for larger path lengths the spectrum is shifted to the more energetic ("harder") photons. This filtering effect is known as beam-hardening and it will be discussed more extensive in section 3.3.3.
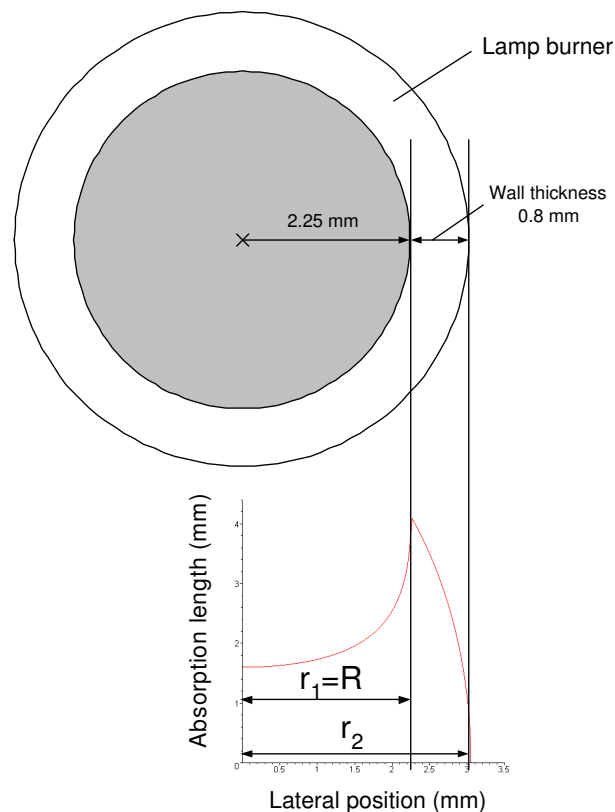

Figure 3.3: The absorption length of the burner as a function of lateral position for a "type 3" lamp with inner radius of 4.5 mm and wall thickness of 0.8 mm.

From this case study devoted to the X-ray absorption properties of the lamp constituents the following conclusions can be drawn with respect to X-ray source and the detection system.

1. For an accurate observation of the large mercury density gradient in the region close to the burner wall a spatial resolution better than 100 μm is required.

2. The low transmission of the wall materials demands a large X-ray photon flux.

3. To reduce the beam-hardening effect the X ray spectrum should be close to monochromatic.

4. It is recommended to work with an X-ray source that has a good long-term stability so that the number of photons (dose) for the lamp-on case is the same as that of the lamp-off situation. In section 4.5 we will discuss a method to correct for a possible dose-inequality so that this requirement can be considerably relaxed.

5. Due to long-term instabilities in the lamp burner position, it is preferential to use short exposure times.

6. Because the optical depth of Hg is small compared to that of the wall material, we need a detector (**CCD** array) with a high dynamic range.

The requirements for the X-ray source (high brilliance & monochromaticity) and the detector (high dynamic range) are discussed in section 3.4 and 3.5 respectively.

3.3.2 Spectral properties of the different lamp materials

The comparison of the energy dependence of the absorption effect for the different lamp materials is presented by using the linear attenuation coefficient. This quantity k with the unit of cm^{-1} is defined as

$$k(E) = \mu_\rho(E)\rho. \tag{3.2}$$

A plot of the linear attenuation coefficient for outer bulb, inner burner and Hg is given in Fig. 3.4. Taking again the case of the 'type 3' lamp, Fig. 3.4(a) shows that for X-ray energies below 15 keV, the linear attenuation coefficient of the wall material (outer bulb SiO_2 and inner burner Al_2O_3) is so high that hardly any X-ray photons will be transmitted by the wall. Moreover it is clear that the k-value of Hg is much lower than that of the wall material. Therefore the Hg contribution in the absorption is not detectable with X-ray photons with energies below 15 keV. When the photon energy is increased to above 17 keV, the k-value of Hg becomes comparable to that of the burner, that is to say, it is not much lower than 10% of the k-value of the PCA burner.

Measurements with a PCA burner can be more difficult than those with a quartz burner since $k_{Al_2O_3} > k_{SiO_2}$ for the same wall thickness. Therefore, a lamp with the lowest Hg pressure (in the order of 1 bar) and a PCA burner, such as the type 4 lamp, will be

(a) (b)
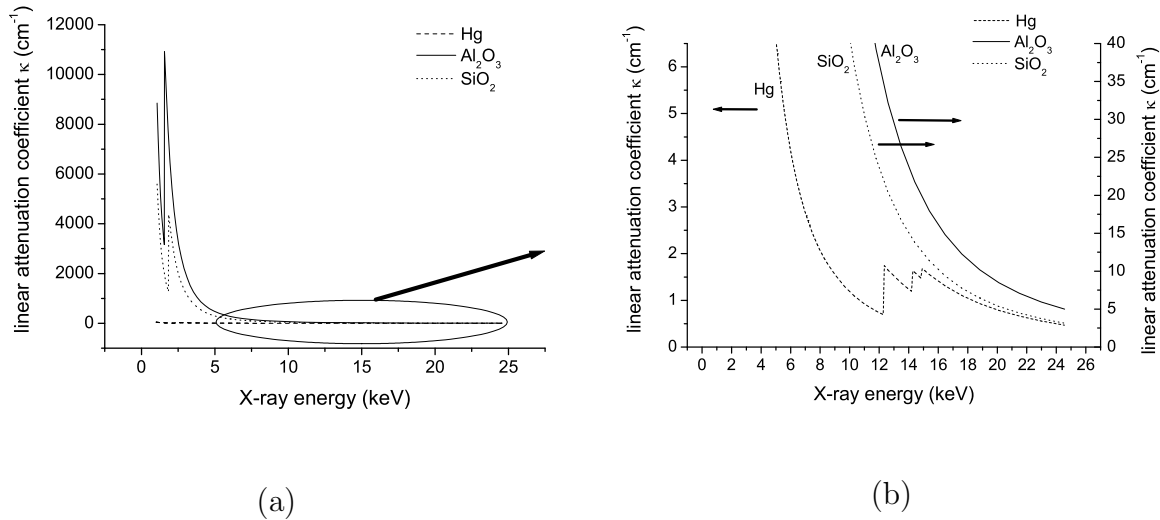
*Figure 3.4: The linear attenuation coefficient as a function of X-ray energy for the outer tube (SiO_2), inner burner (Al_2O_3) and Hg of 19 bar pressure at 3000 K. **(a)**: The total energy range plot. **(b)**: The detailed plot for the energy range between 10 keV and 25 keV. The data is coming from NIST database (see link http://physics.nist.gov/PhysRefData/FFast/html/form.html)*

unfavorable for the X-ray experiment . Nevertheless it has been investigated whether XRA measurements are possible in this worst-case scenario (see section 5.5).

3.3.3 Beam-hardening

As pointed out in section 3.3.1, it can be expected that the spectrum of a non-monochromatic X-ray beam will change during its path through a (strongly) absorbing medium for which the linear attenuation coefficient k is a function of the photon energy E. A decreasing k-value for increasing photon energy will lead to the tendency that along the absorption path the effective E-value will increase; i.e. the surviving photons are harder. This so-called beam-hardening effect will have the consequence that the spectrum along the different chords through the Hg plasma is not the same. Since the detection is not energy-selective this may degrade the Abel inversion procedure.

Figure 3.5 gives a calculation of a typical beam-hardening effect we expect for our XRA experiment on lamps. The calculation was done by multiplying the X-ray source energy spectrum [20] with the transmission of the Zr filter, lamp outer bulb (SiO_2), and the PCA burner (Al_2O_3) for paths a and b.

There are three possibilities to solve this beam hardening effect:
1. To measure the spectrum at each pixel position.
2. To use a monochromatic source.
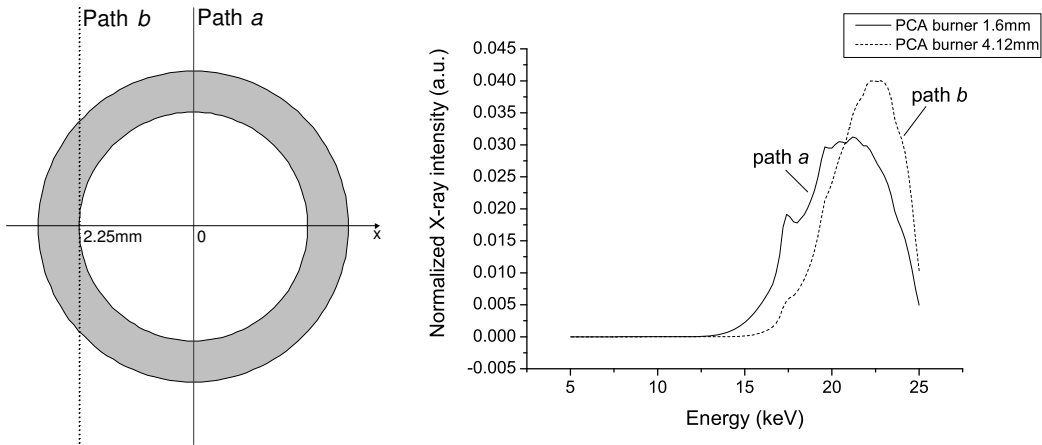
*Figure 3.5: Illustration of how the beam hardening effect changes the spectrum as function of lateral position. [**left**] Two X-ray beams; one (a) passing through the center while the other (b) is tangent to the edge of the burner. [**right**] The calculated X-ray spectrum (normalized over the area under the spectrum) corresponding to path b compared to that of path a shows a shifting towards the high energy side. The spectrum is generated by a Mo-anode X-ray tube, and the beam is attenuated by an outer tube of quartz (thickness 2 mm) and a PCA burner (1.6 mm for path a and 4.1 mm for path b).*

3. To measure the beam-hardening effect using a lamp filled with a homogeneous Hg density and to use this as a correction.

Possibility (1) turned out to be unfeasible within our limited budget, moreover such an experiment would be time-consuming. Therefore we explored options 2 and 3. This will be discussed in section 3.4 and section 4.3.4, respectively.

3.4   The X-ray source

In the previous paragraph, the X-ray absorption properties of different lamp parts were discussed. From this it was concluded that a monochromatic X-ray source is needed with a high brightness[1] and a small focal spot size. This subsection is focused on the properties of the X-ray source and presents a discussion of the choices that have been made.
A commercial X-ray source, initially designed for crystallography, was used for our X-ray absorption experiment on HID lamps. The system has a standard tube tower housing, in which different X-ray tubes can be installed. For hard X-ray generation, two different X-ray tubes can be used, employing either a molybdenum or a tungsten anode.

---

[1]High brightness means large flux generated by a small focal spot size in a narrow solid angle.

In our XRA experiment, the Mo-anode X-ray tube has been used. Since the W-anode X-ray source does not have any strong X-ray lines in the energy region below 20 keV only, a continuum spectrum is present below 20 keV which will suffer from beam hardening more than the semi-monochromatic Mo line. Typical properties and experimental settings of the X-ray source are given in table 3.2:

Table 3.2: Typical settings of the X-ray source.

properties	value
current	20 mA
voltage	25 kV
spot size	0.4 mm*8 mm
take-off angle	6°
beam angle	12°

3.4.1 Focal spot size on the anode of the X-ray source

In order to obtain a high spatial resolution, the dimensions of the X-ray emitting area (the anode) must be as small as possible, especially in the horizontal direction that is parallel to the lateral dimension x of the HID lamp under investigation. Therefore a fine focus (FF) X-ray tube has been chosen, with a focus size of 0.4 mm $\times$ 8 mm. The 8 mm refers to the depth, this dimension pointing more or less in the direction X-ray source $\rightarrow$ lamp. The 0.4 mm size is parallel to the lateral direction x. We recall that the lamp is positioned vertically. Since the beam axis is tilted down over a take-off angle of 6°, the projected size of the focus area, the anode, is 0.4 mm$\times$0.8 mm. Taking advantage of geometrical downscaling (cf. section 3.6) we can get a spatial resolution of 100 μm in the lateral direction. The schematic drawing of the X-ray source geometry is shown in Fig. 3.6.

3.4.2 Beam angle and orientation

The original X-ray source has a beam angle of 12° centered around a direction that makes an angle of $-6°$ with the horizon. Therefore in order to get a horizontal beam the (housing of the) X-ray source has been tilted up over 6°.

3.4.3 Brightness of the X-ray source

To reach a good spatial resolution (<100 μm) with an X-ray focal spot of relatively large dimensions (0.4 mm in lateral direction), the object (HID lamp) has been placed far from the source (cf. section 3.6). Moreover, since the wall material has a low X-ray transparency, a relatively small number of photons will be collected by the detector. This demands for a

(a)   (b)
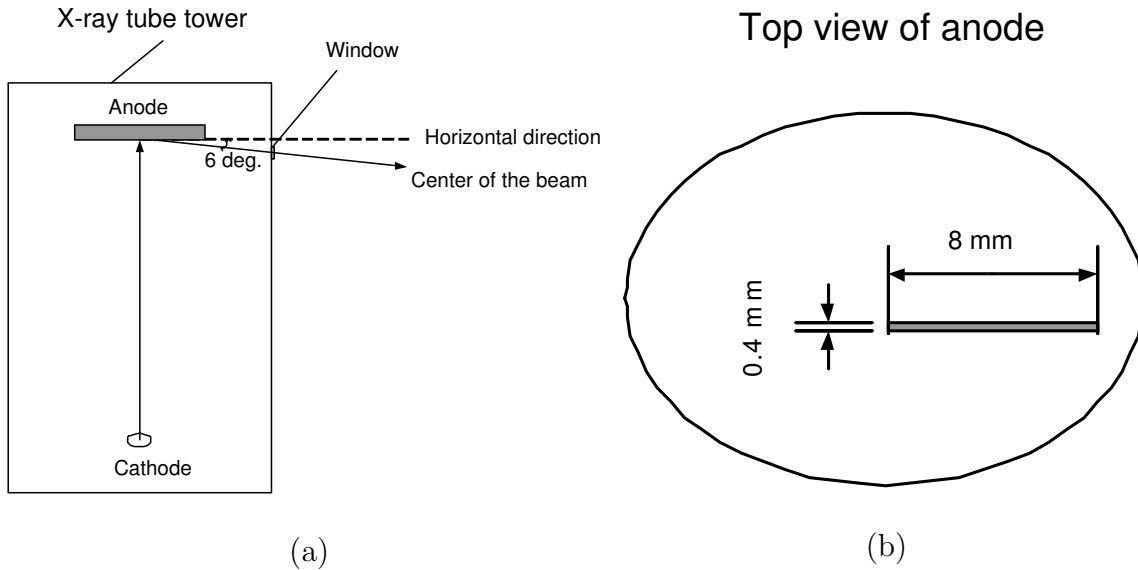
*Figure 3.6: Schematic drawing of the X-ray source geometry. (**a**): The X-ray source was initially designed for X-ray diffraction (crystallography); for that purpose the exit window was positioned such that the beam was tilted down over* $6°$*. In order to get a horizontal beam, the housing of the X-ray source has been back-rotated for* $6°$*. (**b**): The top view of the anode of the X-ray source. Both 8 mm and 0.4 mm are in the horizontal plane.*

large flux in a small solid angle.

With a high-brilliance X-ray source it is possible to take single image in a relatively short integration time (typically 60 s), multiple images (typical 50 images) can be taken within one hour. The final image can be composed by accumulation and averaging. In this way the signal to noise ratio can be increased by a factor of $\sqrt{N}$ (cf. section 3.5.2) where N is the number of images.

3.4.4 Spectrum of the X-ray source

The Mo anode X-ray tube has a spectrum that contains two typical Mo K-lines (K_α: 17.5 keV, K_β: 19.6 keV). The Zr filter has a K absorption edge at 18 keV, and therefore the X-ray spectrum above 18 keV is strongly absorbed by the Zr filter. Thus the spectrum from the X-ray source is expected to consist mainly of Mo K_α(17.5 keV) super-imposed on a continuous background of Bremsstrahlung radiation. Figure 3.7 shows the spectra of a Mo tube with and without a Zr filter, and clearly shows that the spectrum with the Zr filter is much narrower than the original spectrum of the Mo tube. The energy below 15 keV will be further attenuated by the outer bulb of the HID lamp. Therefore we can assume that the spectrum of the radiation offered to the burner is quasi-monochromatic and mainly consists of the Mo K_α line as shown in Fig. 3.8.

(a)   (b)
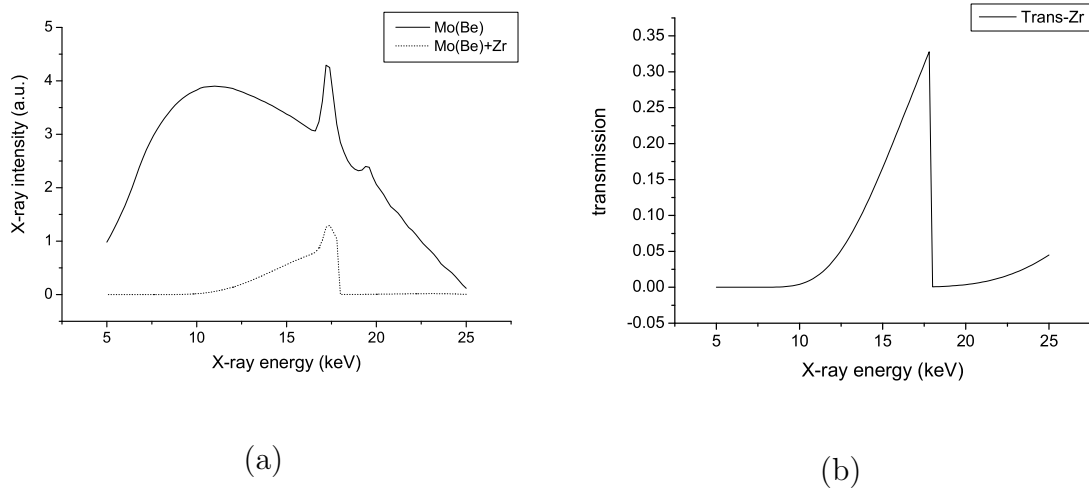
Figure 3.7: **(a)** *The X-ray spectrum of a fine focus(FF) Mo-anode X-ray tube with and without Zr filter at an acceleration voltage of 25 kV. The solid curve is the spectrum from the Mo-anode X-ray tube only. The dotted curve is the spectrum of the Mo X-ray tube with Zr filter. [20]* **(b)** *The transmission profile of the Zr filter with a thickness of 117 µm.*
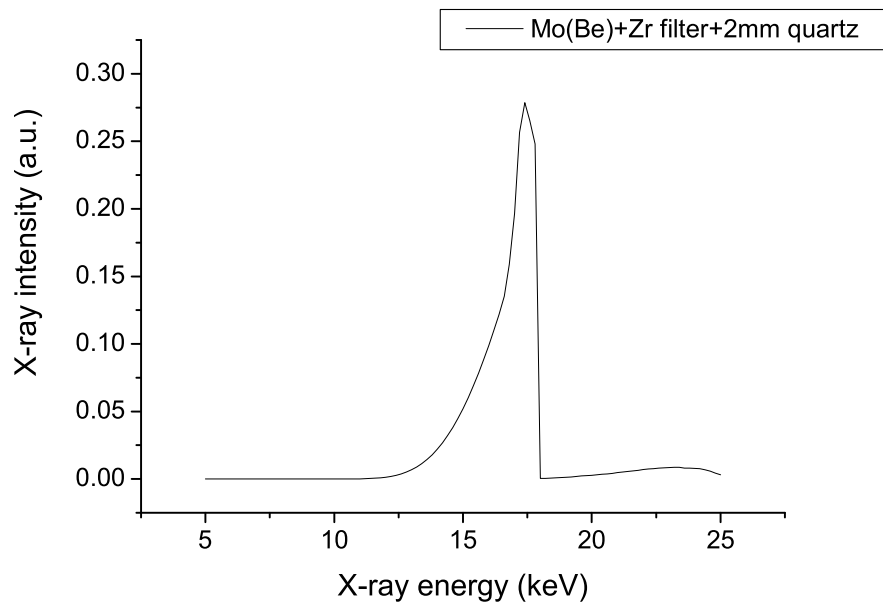
Figure 3.8: A typical X-ray spectrum through the center of a non-burning lamp. The X-ray spectrum is generated by a Mo-anode X-ray tube, filtered by a Zr filter and the quartz outer-bulb (2 mm path length).

3.5 X-ray CCD camera

3.5.1 Structure of the X-ray CCD camera

In order to detect the X-ray photons that have passed through the HID lamp we make use of an X-ray CCD camera. The crucial part of this device is a CCD-array of a type that is well-known for applications of image registration. However, since the CCD-array is not sensitive for hard X-ray radiation we have to convert the X-ray quanta into visible photons. During that conversion, effectuated by a phosphor plate, use can be made of the fact that the energy of an X-ray photon (typically 17 keV) is much larger than visible photons (typically 2 eV). For this reason one X-ray quantum generates a large number of visible photons (quantum cutting).

Fig. 3.9 shows the three-fold structure of the X-ray CCD camera: 1) a phosphor sheet, 2) fiber optics and 3) the CCD-array.
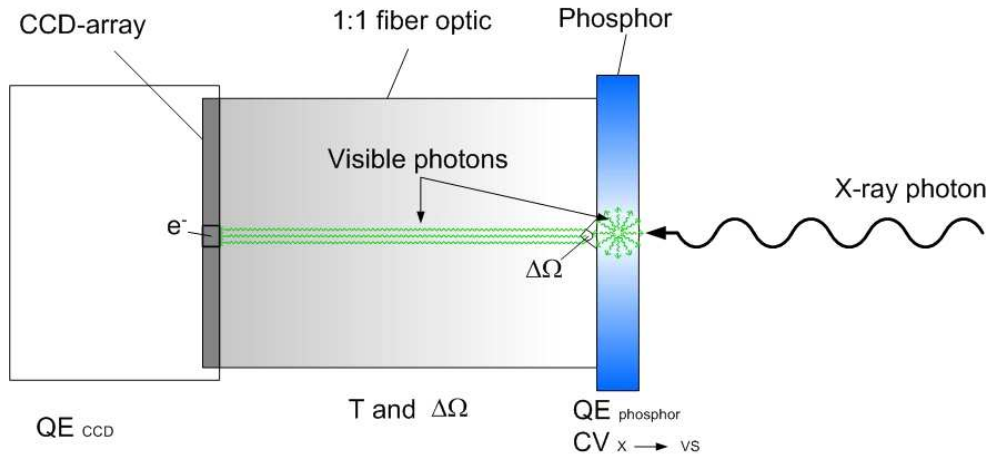
Figure 3.9: The structure of the PI-SCX1300 X-ray CCD camera with three different parts: phosphor sheet, fiber optics and CCD-array. The properties of these structure elements are: for the phosphor layer: $QE_{Phosphor}$, the quantum efficiency for detecting the x-ray photons, and $CV_{X.\rightarrow vs.}$ the number of visible photons produced per detected X-ray photon; for the fiber optics: $\Delta\Omega$, the solid angle of the visible photons that enter the fiber optic, and T the transmission; for the CCD-array: QE_{CCD}, the quantum efficiency of the CCD array.

Among these structure elements, the fiber optic and CCD-array are quite standard and their properties (cf. Table 3.3) have well known and fixed values. For the phosphor sheet different options can be selected by choosing the phosphor type, the grain size and the sheet thickness. In choosing the grain size and the thickness a trade-off is made between the quantum efficiency (QE) and the spatial resolution. A coarse grain will give a high quantum efficiency, but a poor spatial resolution. The same applies to the sheet thickness.

A very important feature of the system is the yield Y, that is the number of generated electrons (in the CCD-array) per incoming X-ray photon (at the phosphor sheet). It is

determined by the product of several factors

$$Y = \underbrace{QE_{phosphor} \times CV_{X \to vs}}_{\text{phosphor}} \times \underbrace{\frac{\Delta\Omega}{4\pi} \times T}_{\text{fiber optic}} \times \underbrace{QE_{CCD}}_{\text{CCD}} = QE_{phosphor} \times M, \qquad (3.3)$$

where $QE_{phosphor}$ is the quantum efficiency of the X-ray phosphor, which gives the probability of detecting an X-ray photon (usually expressed in %), $CV_{X \to vs.}$ the conversion factor of the phosphor, i.e. the number of visible photons per detected X-ray photon, $\frac{\Delta\Omega}{4\pi}$ the fraction of the visible photons that enter the fiber optic, T the transmission of fibre optic taper and QE_{CCD} the QE of the CCD-array which is defined as the number of photo-electrons generated per incoming visible photon. Another useful quantity is M, the X-ray photon-to-electron multiplication factor which is defined as

$$M = CV_{X \to vs} \times \frac{\Delta\Omega}{4\pi} \times T \times QE_{CCD}. \qquad (3.4)$$

Typical values of these parameters are listed in Table 3.3.

Table 3.3: Typical values of the parameters for X-ray CCD camera.

X-ray CCD structure	properties	values
Phosphor	$QE_{phosphor}$	70%@17 keV
GADOX	$CV_{X \to vs}$	1.1×10^3@17 keV
Fiber optics	$\Delta\Omega/4\pi$	$\lesssim 0.5$ (typical 40%)
	transmission T	50%
CCD sensor	QE_{CCD}	30%
	pixel size	20 μm$\times$20 μm
	readout noise	3.31 e$^-$/pix/read
	dark current	1.6 e$^-$/pix/sec@ $-$ 20°C
	linear full well depth	200,000 e$^-$
X-ray CCD	M	$\sim$ 66 e$^-$ /detected X-ray photon

In the following we will discuss the properties of the various parts of the X-ray CCD camera in more detail. This will be done following the route from X-ray, via visible photon to photo-electron.

Only a fraction of the incoming X-ray photons will be detected; this fraction $QE_{phosphor}$ largely depends on the phosphor type. Since Hg has a relatively high X-ray absorption cross-section at 15$\sim$17 keV (cf Fig. 3.4(**b**)), we selected a phosphor which has the highest quantum efficiency (i.e. 70%) at 17 keV. This was achieved with a Gadolinium Oxysulphide ($Gd_2O_2S : Tb$) phosphor, often referred as GADOX or P43.

If an incoming X-ray photon is detected by the phosphor, a large number of visible photons will be generated. The conversion factor $CV_{X \to vs}$ corresponding to this process

has an energy efficiency of typically 15%. Thus 15% of the absorbed X-ray photon energy is converted into visible photons with energies of typically 2.28 eV (equivalent to a wavelength of 545 nm). Therefore the conversion factor equals:

$$CV_{X \to vs} = \frac{E \times 0.15}{2.28}, \tag{3.5}$$

where E is the energy of the X-ray photon. For E=17 keV and the selected phosphor, we find $CV_{X \to vs} = 1.1 \times 10^3$.

The visible photons generated by the phosphor will be emitted in all directions and are equally spread out over the full 4π solid angle. Since the phosphor sheet is very thin and it is directly pressed against the front face of the fiber optics, the fraction of the visible photons $\Delta\Omega/4\pi$ entering the fiber optics is close to 50% and can be approximated by 40%. But also during the transport towards the CCD-array photons will be lost in the fiber optic. From the manufacturer's specification, we found the transmission T is typically 50%.

The visible photons collected and transmitted by the fiber optic, will finally hit the CCD sensor where a part of them will be converted into electrons. The efficiency of this process depends on the QE of the CCD (QE_{CCD}), which is specified as the effective ratio of the CCD to convert received photons into measurable electrons. The value of QE_{CCD} at 545nm is about 30%.

Substituting in these parameters into Eq. 3.3, gives for the X-ray CCD a value of $Y = 46$ electrons/incoming X-ray photon. For the M factor, this would mean $M = 46/0.7 = 66\,\mathrm{e}^-$/detected X-ray photon. For our X-ray CCD camera, a typical value of the multiplication factor M (information given by the manufacturer) is taken as 58 electrons/detected X-ray photon, which is close to our calculation. This value of $58\,\mathrm{e}^-$/detected X-ray photon has been used in the further calculation of S/N.

3.5.2   Signal to noise ratio

The estimation of S/N will be done for two types of experiments 1) a single exposure single pixel (SESP) measurement and 2) the multiple exposure multiple pixel measurements (MEMP).

We start with the SESP measurements.

The best S/N value, is reached if a maximum number of events are collected. An important parameter is the gain-setting for the CCD camera which equals the number of electrons per count. It is known that the linear pixel depth of the CCD is 200,000 electrons and that the digitization accuracy of the CCD is 16 bits which corresponds to $2^{16} = 65,536$ ADU[2].

---

[2]One ADU is a unit related to the analogue to digital conversion.

In order to match the maximum linear pixel depth to the maximum of the digitization signal, the best CCD analog gain setting will be $200,000/65,536 = 3.05$ e$^-$/ADU. However, this gain setting is not available. The closest value is 2.44 e$^-$/ADU which has been chosen for the experiment. In that way we certainly make use of the entire linear dynamic range of the CCD and it is guaranteed that the CCD pixels are not saturated before they reach the maximum of 65535 counts.

The maximum number of electrons for this gain setting is thus $2.44 \times 2^{16} = 1.6 \times 10^5$ electrons.

The maximum signal after the subtraction of a dark frame will now correspond to $1.59 \times 10^5/M = 2741$ X-ray photons ($M = 58$). If the photon statistics is the only source of noise we find S/N $= \sqrt{2741} = 52$ and N/S $= 1.9\%$. However, this S/N-value corresponds to the region with the lowest absorption, which is located out-side the lamp (path c). At the inner boundary of the burner (path b in Fig. 3.5(a)) the signal will be about 120 times less, which means that we only have 23 X-ray photons. Here the error caused by the statistical noise is about 21%. Realizing that there are other noise-sources as well, we have to conclude that the N/S of that image part will always be worse than 21%. This clearly shows that an improvement is needed, which can be obtained by binning pixels and averaging the signal of multiple exposures.

Apart from the shot noise associated with the photon statistics we also have read-out noise and noise from the dark current.

The dark-current noise and readout noise are specified in the numbers of electrons, however the noise from the photon source itself is determined by the number of the detected X-ray photons N_*, and equals $\sqrt{N_*}$ (Poisson statistics). By means of the multiplication factor M, this can be associated with a number of shot noise electrons equal to $M\sqrt{N_*}$. Therefore in the final calculation of the total noise, all the noise terms have been translated into number of electrons. The noise terms are denoted as:

$$Noise_* = \ M \times \sqrt{N_*}; \quad \text{X-ray statistics,} \tag{3.6}$$

$$Noise_D = \ \sqrt{N_D}; \quad \text{Dark current noise,} \tag{3.7}$$

$$Noise_R = \ N_R; \quad \text{Readout noise.} \tag{3.8}$$

Therefore the total noise is given by

$$N = \sqrt{Noise_*^2 + Noise_D^2 + Noise_R^2} = \sqrt{M^2 \times N_* + N_D + N_R^2} \tag{3.9}$$

So that the S/N of one SESP is given as

$$\frac{S}{N} = \frac{M \times N_*}{\sqrt{M^2 \times N_* + N_D + N_R^2}}. \tag{3.10}$$

Now comparing the noise from the different sources with each other, we find for the lowest signal that the shot noise of the signal equals $\sqrt{23} \times 58 = 278$ electrons, the noise from the dark current is 9.8 electrons and the readout noise 3.31 electrons. Therefore the noise is mainly determined by the X-ray photon statistics and we may write

$$\frac{S}{N} \approx \sqrt{N_*}. \tag{3.11}$$

The Multiple Exposure Multiple Pixel (MEMP) type experiment will now be discussed using a case study, i.e. that of the lamp-off image of a "type 3" lamp (cf. Fig. 1.5 and Table 1.1) produced by the maximum exposure time of 102 seconds.

In this case the noise of the image is mainly determined by the minimum signal (1137 electrons corresponding to 19.6 X-ray photons per pixel) in the image (the inner boundary of the burner). The noise from the X-ray photons on a SESP basis is about $\sqrt{19.6} \times 58 = 257$ electrons while the noise of the dark current is only 12.8 electrons and the readout noise is 3.31 electrons. From Eq. 3.10, the total noise of this pixel is 257 electrons. The relative error of this pixel will be 23%. By adding pixels e.g. by binning 20 rows and by adding signals of 50 images, the relative error will be reduced by factor of $\sqrt{1000}$. This means the detection limit for the Hg absorption signal for these settings becomes $\frac{23\%}{\sqrt{1000}} \approx 0.7\%$.

Since the noise of the image is determined by the signal level at the plasma boundary (inner boundary of wall), this implies that the wall thickness has a crucial influence on the accuracy of the method. For high wall thickness, a higher X-ray photon energy will be better.

3.5.3 Linearity of the X-ray CCD camera

In order to know whether the CCD pixels respond linearly to the number of incoming photons in the whole dynamic range of the CCD camera, a linearity test has been made for different exposure time until the full scale of the ADU of the CCD. The result is shown in Fig. 3.10. The camera appears to pass this test easily.

3.6 Optimization of experimental geometry

In our experimental setup, both X-ray source and X-ray CCD camera have finite dimensions, therefore the spatial resolution does not only depend on the properties of the X-ray source and X-ray detector, but also on the geometry of the experimental setup.

First let us look at blurring due to the X-ray source. If the power distribution of the X-ray focus spot has a Gaussian shape with a standard deviation σ_{Src}^S, an infinitely small pinhole in the object plane (thus within the HID lamp) will appear on the detector with a Gaussian intensity distribution which is scaled due to the geometrical magnification factor β. Therefore the width of the spot on the detector will be

$$\sigma_{Src}^D = \sigma_{Src}^S(\beta - 1) \quad \text{with} \ \ \beta = L/L_1, \tag{3.12}$$
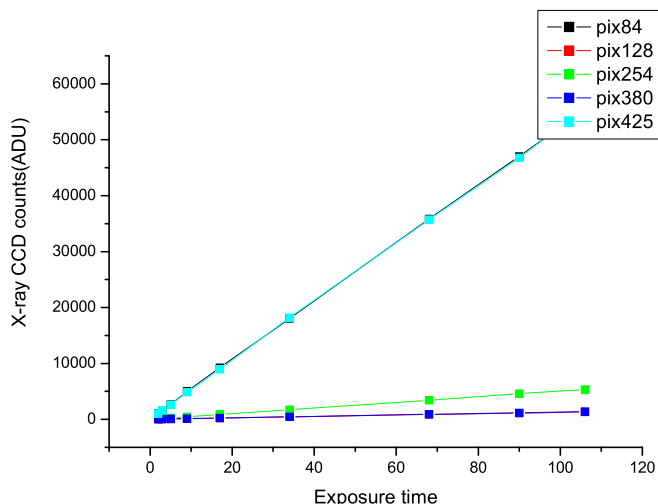
Figure 3.10: Linearity test of the CCD camera at different pixel positions for a lamp-on case.

where L and L_1 are the distances defined in Fig. 3.11. The superscripts D and S are for the position plane, i.e. detector position and source position respectively. The subscripts Src denote the X-ray source.
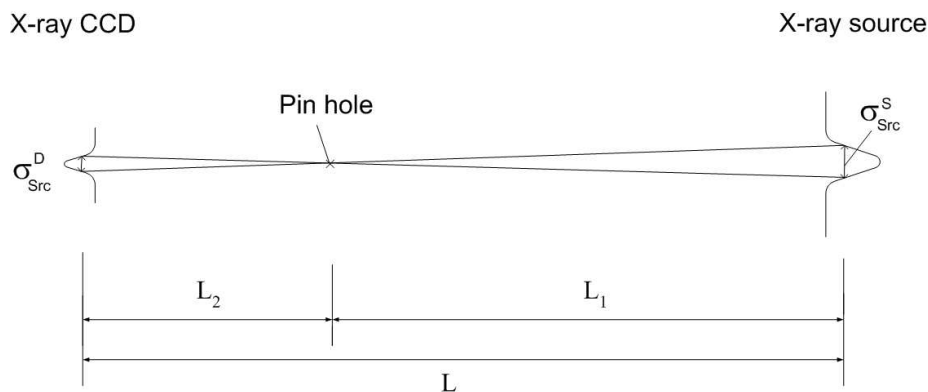
Figure 3.11: By means of imaging, the source image is reduced and leads to a small σ on the detector plane, i.e. $\sigma^D_{Src} < \sigma^S_{Src}$.

Equation 3.12 shows that if we place the object very close to the detector, i.e. if $\beta \to 1$, the blurring due to the finite dimension of the source will vanish.

Secondly, we have to take the imperfectness of the detector, X-ray CCD camera, into account. If an infinitely small point on the sensitive area of the CCD is irradiated, the CCD generally gives a spatially spread signal. Assuming that the point-spread-function of

the detector is Gaussian characterized by σ_{Det}^{D}, it is found that the total blurring of the image due to the combination of the imperfectness of the CCD and the X-ray source will be

$$\sigma_{tot}^{D} = \sqrt{\sigma_{Src}^{D}{}^{2} + \sigma_{Det}^{D}{}^{2}}. \tag{3.13}$$

In order to minimize blurring, we need to compare the X-ray source dimension (0.4 mm in the lateral direction) and the X-ray CCD spatial resolution (around 100 μm from the specification). Since we have a divergent beam, the instrumental profile on the image plane is bigger than that at the object plane. Therefore the real spatial resolution on the object plane is

$$\sigma_{tot}^{O} = \frac{\sigma_{tot}^{D}}{\beta}. \tag{3.14}$$

In order to optimize the spatial resolution with the given source (0.4 mm) and detector (100 μm), we should choose the β factor such that σ_{tot}^{O} is minimum. This happens for $\beta = 1.0625$. In our experimental setup, L=91 cm and L_1=84 cm, $\beta = 1.083$. With this setting, we can reach a spatial resolution of 0.0973 mm, which is close to the optimum 0.097 mm.

3.7   Conclusion

From the previous sections, it should be clear that the XRA experiment on lamps is not trivial. The challenges are
1. The optical depth of Hg is small compared to that of the lamp wall material.
2. The Hg density near the wall has a large gradient and the lamp has a small diameter.
3. The wall materials have a low transmission for X-ray radiation.
4. The burner has different path lengths for different lateral positions.
5. The X-ray spectrum is changed due to the 'beam hardening' effect.

To overcome these challenges, the X-ray experimental setup has been designed to fulfill as much as possible the following requirements:
1. High dynamic range.
2. High spatial resolution (50~100 μm).
3. X-ray source with high brilliance.
4. Monochromatic source spectrum.

Therefore a final experimental setup has been designed using: 1. A 2 kW fine-focus Mo-anode X-ray tube as the X-ray source operating at 20 or 25 kV with Zr filter. 2. A commercial 16-bit X-ray CCD camera with a QE of 70% at 17 keV and system gain of 58 electrons/detected X-ray photon. 3. The object distance and source distance such that the spatial resolution can reach 100 μm.

Chapter 4

XRA data handling

Abstract

This chapter deals with the data handling of the X-ray absorption (XRA) technique. The main goal is to construct a procedure by which the relative small reduction of the X-ray intensity due to the absorption of a low-density mercury gas can be separated from the large attenuation due to the high-density wall material. An essential aspect of the procedure is its two-fold structure: two (series of) CCD images are taken; one for a non-burning lamp (lamp-off), the other for corresponding lamp-on situation. The subtraction of (the logarithm of) the lamp-off and lamp-on signal in principle leads to the Hg-absorption contribution.

However, before this can be done the images have to be corrected for several disturbing instrumental effects such as an offset-value, a dark-current contribution, and the non-uniformity of the CCD array. But even then we are not ready to apply the subtraction. Due to the heat generated by the Hg plasma the lamp undergoes a shift, a rotation and an expansion. Therefore, before the subtraction of images can take place, we have to adjust them such that a proper mutual matching of the geometry of the lamp-on and lamp-off is obtained. To facilitate this matching we use analytical fit-functions of the profiles that also correct for the density decrease of the wall and the X-ray dose-inequality. After this matching-procedure the subtraction of lamp-on and corresponding lamp-off images leads to the column density of Hg as function of lateral position. Employing an Abel inversion-procedure transform these into radial Hg-density profiles.

Several topics of this chapter deserve more in-depth treatments. These are give in the appendices A, B and C. Appendix A deals with image blurring and beam divergence, appendix B treats the picture contrast as a function of X-ray energy while appendix C is devoted to the error analysis. It is demonstrated that the Tikhonov regularization method provides an optimized way to balance the different sources of errors in the Abel inversion procedure, i.e. reconstruction errors and noise propagation errors.

4.1   Introduction

Generally speaking, the X-ray absorption measurement of the mercury concentration in high intensity discharge (HID) lamps requires two images: one for the lamp-on and the other for the lamp-off situation. By subtracting these images, the absorption of Hg is obtained for each lateral line of sight. From this the radial density profile can be reconstructed by using an Abel inversion procedure. However, before the subtraction of these two images can take place, they must be corrected for all the various disturbing influences from the different parts of the setup. These are schematically listed below according to the setup part.

  The source has
1. a finite dimension that leads to a blurring of the image;
2. a divergent cone-like beam that makes the CCD image larger than the object;
3. a non-monochromatic spectrum which will cause a 'beam-hardening' effect.

  The lamp
1. has an unstable position during burning period;
2. will shift and expand due to the temperature rise in the on-situation;
3. brings an offset signal due to scattering of the X-rays.

  The X-ray CCD camera has
1. a dark current;
2. a non-uniform pixel sensitivity;
3. a finite phosphor grain size, which leads to additional blurring.

Therefore several corrections have to be made before subtraction of the on- and off-images can take place and Abel inversion can be applied.

In this chapter we discuss how the X-ray absorption data has to be handled such that the mercury concentration can be found. In this procedure we have to tackle all the imperfections listed above, and we proceed along the following route:

First the real signal is corrected for the dark current, the offset value and the non-uniformity of the CCD-array. This so-called *signal-extraction* will be dealt with in section 4.2. After that we deal with the removal of image imperfections. This *image reconstruction* is treated in section 4.3 where blurring and magnification will be discussed. In Section 4.4 and 4.5 we will present the *fitting* of the lamp-off and lamp-on image. The analytical functions obtained in this way will facilitate the correction of the *X-ray dose-inequality* and the *geometrical mismatch* between lamp-on and lamp-off images. In section 4.6 subtraction of on- and off- will be described and the result will be subjected to Abel inversion in section 4.7. After the introduction of the wall temperature measurement in section 4.8, finally an overview of the complete image process procedure will be given. More specific topics are

described in the appendices.

4.2   Signal extraction

Each X-ray image has the following components: 1. The real signal produced by the transmission of an X-ray beam through the lamp; 2. The dark current and bias of the CCD camera; 3. A variation due to the non-uniformity of the CCD-array; 4. An offset signal.

To extract the real signal from the measurement we follow a procedure that is given by the following equation:

$$\widehat{I}_{cor} = \frac{I_{meas} - I_{dark} - I_{offset}}{I_{XS}}, \tag{4.1}$$

expressing that we first eliminate the dark current (include bias) I_{dark} and the offset I_{offset} from the measured intensity I_{meas} and that the result of this subtraction will be divided by I_{XS}. Scattered radiation is responsible for some or all of I_{offset}. I_{XS} is the signal that is measured without a lamp in-between the X-ray source and the detector. By this normalization we achieve that the final result , $\widehat{I}_{cor}$, is corrected for the non-uniformities of the CCD array.

The influence of the dark current, the offset and the non-uniformity of the CCD will be discussed more in detail in the following subsections.

4.2.1   Dark current and bias

The number of the electrons in each pixel well is digitized into a number of counts (A/D units). The electrons are coming from photo-electrons and thermal electrons of the CCD array itself. The latter contribution is called the dark current and needs to be subtracted from the measured signal. Moreover, the A/D-converter adds a constant bias to this dark current value. The dark current of our X-ray CCD camera has a typical value of 0.26 e$^-$/pixel/s at $-40°$C. The typical X-ray absorption measurement time is 60 s. The temperature of the X-ray CCD camera is set at $-25°C$. From the measurements of the dark current and bias values for different CCD gain settings, the dark current is found to be 0.9 e$^-$/pixel/s@ $-25°$C, and the bias value is 302 counts for the medium gain setting (2.44 e$^-$/count). Now if we take an image of exposure time of 60 s, the dark current is only 54 electrons. The maximum signal in the image is around 3.3×10^4 counts, which corresponds to 8.1×10^4 electrons. Therefore contribution of the dark current and bias in the image is relatively small.

4.2.2   Offset correction

After the dark signal subtraction, an offset remains. Attempts have been made to remove the offset experimentally but without success.

The presence of the offset is shown by taking pictures of partially blocked lamps (see Fig. 4.1). This blocking is realized by placing a frame with brass strips of 2 mm thickness in front of the CCD. The offset values of a vertical cross-section at the center axis of the lamp-on image is shown in Fig. 4.1. We see that in the center of these strips a "signal" remains at a level of about 14% of the signal of the non-blocked image. This offset can not be caused by the transmission of the X-ray signal through the brass plate since a brass plate of 2 mm thickness reduces the X-ray radiation with a factor of at least 10^9. Another test has been done by blocking half of the CCD with a lead plate in a setup without any lamp. It turns out that the offset remains even in the "dark" area far from the lead edge. This offset might be caused by the X-ray scattering and/or the fluorescence by objects in the beam such as the metal frame and the outer tube of the lamp.

Since the cause of the offset is not completely clear and cannot be removed experimentally, we have to measure the offset and use this information to correct the images. This is done by taking a lamp image with a metal frame of thin strips with the setup described above and shown in Fig. 4.1. The offset value measured in this way is subtracted from every pixel in the lamp image.
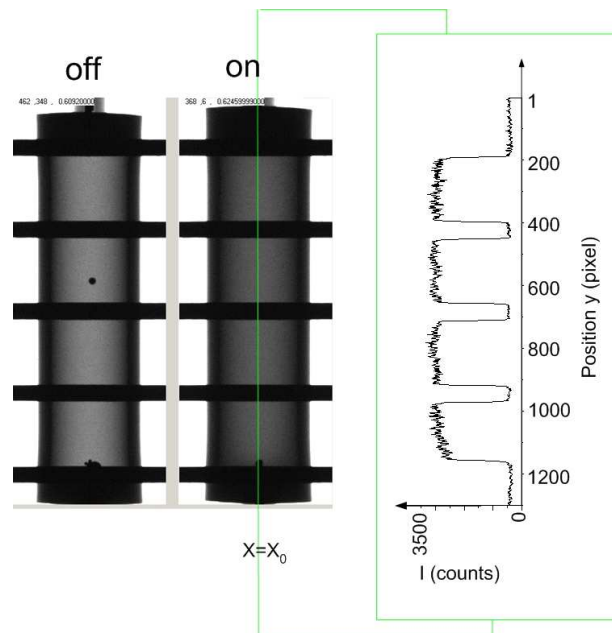
*Figure 4.1: Lamp-off (**left**) and lamp-on (**right**) images after the dark signal subtraction and flat field correction. For both images, a metal frame was installed. A vertical cross-section of lamp-on image at $x = x_0$ is shown on the right side of the image. The offset value, which remains after blocking the CCD with the frame, is around 430 counts. This is about 14% of the signal of the non-blocked image on the axis ($x = x_0$) of the burner. This offset value is used for correcting the image. Moreover, it can be seen in the picture that the lamp expands when the power is turned on.*

4.2.3   Non-uniformity(flat field) correction

The QE of the X-ray CCD camera is not the same for all the different pixels and thus depends on the 2-dimensional field position $\boldsymbol{x}$ on the CCD. We will assume that this positional dependence is independent of the X-ray photon energy which leads to the factorization

$$Q^*(E, \boldsymbol{x}) = Q(E)f(\boldsymbol{x}). \tag{4.2}$$

In this section we describe how this influence of the strongly varying non-uniform field function $f(\boldsymbol{x})$ can be eliminated. This is done by making an image of a uniform beam. This method, which leads to a uniform field distribution of the array sensitivity, is known as flat field correction.

The signal S($\boldsymbol{x}$) given by the CCD camera in general reads

$$S(\boldsymbol{x}) = f(\boldsymbol{x})\Delta t \int_0^\infty Q(E)I(\boldsymbol{x}, E)dE, \tag{4.3}$$

where Δt is the exposure time, and $I(\boldsymbol{x}, E)$ the spectral intensity of the X-ray radiation entering the CCD camera at a position $\boldsymbol{x}$. We will first apply this formula to the lamp-off situation for which we have

$$I^{off}(\boldsymbol{x}, E) = I_0(E)e^{-\tau^{off}(\boldsymbol{x}, E)}, \tag{4.4}$$

where $I_0(E)$ is the spectral intensity emitted by the X-ray source and $I^{off}(\boldsymbol{x}, E)$ the intensity which is transmitted through the non-burning lamp. The optical depth $\tau^{off}(\boldsymbol{x}, E)$ depends on the energy E and on the lateral position $\boldsymbol{x}$. We assume that $I_0(E)$ only depends on E and not on $\boldsymbol{x}$. This is justified since the energy distribution within the solid angle that emanates from the X-ray source is isotropic.

The lamp-off signal is determined by inserting Eq. 4.4 into Eq. 4.3 which leads to

$$S^{off}(\boldsymbol{x}) = f(\boldsymbol{x})\Delta t^{off} \int_0^\infty Q(E)I_0(E)e^{-\tau^{off}(\boldsymbol{x}, E)}dE. \tag{4.5}$$

The influence of the non-uniformity $f(x)$ can be eliminated by using the same setup to make a picture of the X-ray source in the absence of a lamp. This signal reads

$$S_{Src}(\boldsymbol{x}) = f(\boldsymbol{x})\Delta t_S \int_0^\infty Q(E)I_0(E)dE. \tag{4.6}$$

Dividing Eq. 4.5 by Eq. 4.6 we get a normalized lamp-off image that is corrected for the non-uniformity of the CCD array. It reads

$$\widehat{S}^{off}(x) = \frac{S^{off}(x)}{S_{Src}(x)} = B \int_0^\infty Q(E)I_0(E)e^{-\tau^{off}(\mathbf{x}, E)}dE, \tag{4.7}$$

where

$$B = \frac{\Delta t^{off}}{\Delta t_S \int_0^\infty Q(E)I_0(E)dE}, \tag{4.8}$$

is a positional independent constant.

Equation 4.7 will be used in section 4.4 where it is used to construct the fit-function of both the lamp-off and lamp-on image.

4.3 Image reconstruction

The experimental setup has two influences on the image: blurring and magnification. In this section, these two effects are discussed.

4.3.1 Blurring

The blurring of the X-ray image is caused by both the finite dimensions of the X-ray source and the spatial resolution of the X-ray CCD camera. The instrumental profile has been determined experimentally by analyzing the image of a narrow slit. As a result it is found that the intensity profile is Gaussian with $\sigma_{tot}^D = 32\mu$m at the CCD array position. Here σ is the half width at $e^{-1/2} \approx 0.6$ of the full scale. The subscript "tot" stands for total and indicates that this measured σ-value is a combination of all blurring effects.

In section 3.6, we found that the width of the X-ray source (0.4 mm) introduces a blurring with $\sigma_{Src}^D = 17 \ \mu$m. Using $\sigma_{Det}^D = \sqrt{{\sigma_{tot}^D}^2 - {\sigma_{Src}^D}^2}$ and the value of $\sigma_{tot}^D = 32 \ \mu$m, we find that $\sigma_{Det}^D = 27 \ \mu$m, so the contribution of the X-ray CCD in blurring is larger than that of the finite area of the X-ray source.

In Appendix A, we present the results of a simulation of the combination of image magnification and blurring which shows that the blurring has much less influence than the image magnification. Blurring will be eliminated by the fitting procedure whereas image magnification will be corrected by using a coordinate transformation (cf. section 4.3.2). If necessary, the influence of blurring can be removed by a deconvolution procedure.

4.3.2 Image magnification

As we have seen in the description of the experimental setup (Fig. 3.1), we can reduce the influence of the source by placing the lamp and the X-ray CCD camera at a large distance from the X-ray source. Therefore, the beam is not perfectly parallel, and thus the image will be larger than the object (cf Fig. 4.2). Since the Abel inversion is based on the subtraction of the signal collected along parallel beams for a cylindrical symmetric profile, a correction is needed that transforms the observed position value x on the CCD-array into the true value of the lateral position in the lamp at the location denoted by x_1.

From Fig. 4.2, we can deduce that

$$x_1 = \frac{L_1 \cdot x}{\sqrt{(L_1 + L_2)^2 + x^2}}, \tag{4.9}$$
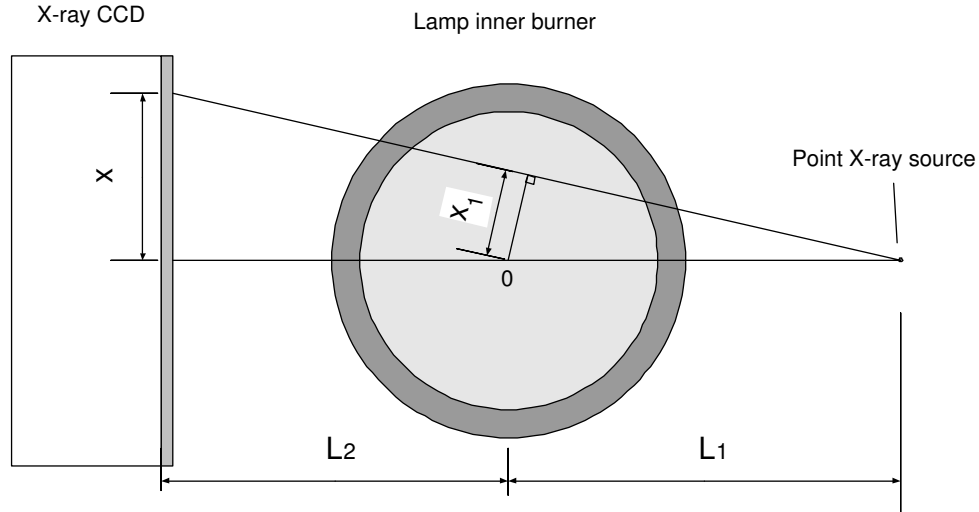
Figure 4.2: A sketch of the coordinate transformation from the position on the CCD camera x onto the lateral position in the burner x_1. The difference between x and x_1 originates from the fact that the X-ray beam is cone-like.

where L_1 is the distance between the X-ray source and the lamp, L_2 the distance between the lamp and the CCD camera, x_1 the true value of the lateral position in the burner and x the measured lateral position on the CCD array.

Using this coordinate transformation we can assign the intensity measured at the CCD position x to the corresponding true lateral lamp position x_1.

4.3.3 Thermal expansion of the burner, density decrease

When the lamp is burning, the temperature of the burner wall will reach values up to 1500 K. Due to the associated thermal expansion the burner will then be larger (see Fig. 4.1)than under non-burning conditions (room temperature) and the density of the wall material will thus be smaller. As a consequence of this density decrease, the X-ray absorption of the warm lamp envelope will be slightly smaller than that of the cold one. This means that the difference of the absorption between the lamp-off and lamp-on situation can not be attributed to the presence of Hg only.

A key quantity in this study is the thermal expansion coefficient of the burner material. This is shown in Fig. 4.3 for the case of Al_2O_3 where the linear thermal expansion coefficient $\alpha(T) = \frac{1}{L}\frac{dL}{dT}$ is found to be temperature dependent. If we average the expansion coefficients in the range from 293 K to 1500 K, we get the effective thermal expansion coefficient

$$\bar{\alpha} = \frac{1}{L_0}\frac{\Delta L}{\Delta T} \approx 8.6 \times 10^{-6}\,\mathrm{K}^{-1}. \tag{4.10}$$

61
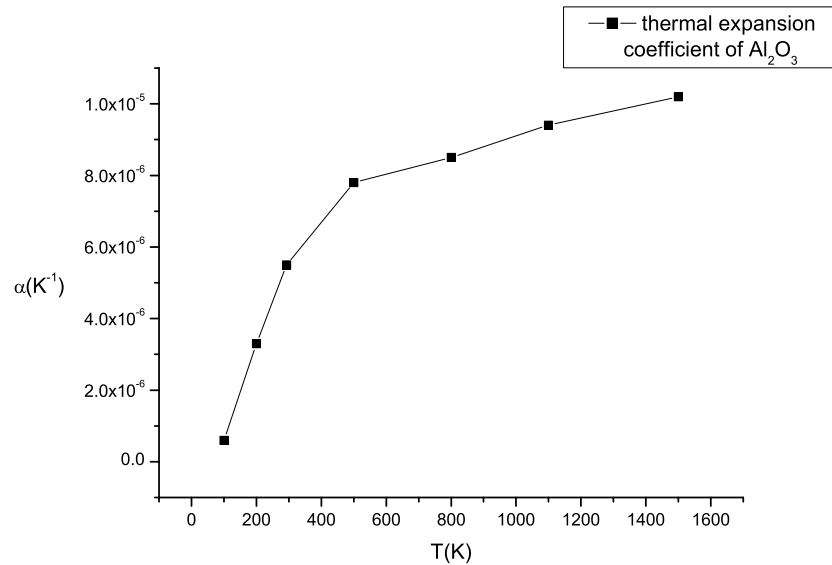
Figure 4.3: The thermal expansion coefficient of Al_2O_3 as a function of temperature.

Therefore the relative linear expansion for $\Delta T = 1207\,\mathrm{K}$ equals

$$\frac{\Delta L}{L_0} = \bar{\alpha}\Delta T = 1.04\%. \tag{4.11}$$

To study the effect of the expansion and the related density decrease of the PCA wall, we must realize that the X-ray photons are collected by the CCD array and handled per pixel. Thus we can confine ourselves to just one pixel which sets the boundaries to a beam in which X-ray photons are absorbed by the wall material or mercury atoms. We first concentrate on the interaction between X-ray and the burner. Figure 4.4 depicts the expansion of the burner material as seen by one pixel on the CCD camera.

In this figure a cubic piece of wall material was taken which, during lamp-off, has the same base-plane as a pixel. Assuming no stress in the material, in the lamp-on situation this piece will expand in all three dimensions. The X-ray beam size and the pixel size do not change. The expansion in the direction parallel to the beam does not change the number of atoms encountered by the beam. The distance between the atoms increases but this is compensated by the increase of the path length. However, the expansion in the direction perpendicular to the beam leads to a reduction of the number of atoms in the beam.

We assume that this reduction factor is the same as the 2D-expansion factor thus

$$(1 + \bar{\alpha}\Delta T)^2 \approx 1 + 2\bar{\alpha}\Delta T, \tag{4.12}$$

and that all the various pieces of the lamp as cut out by the different pixels behave all the
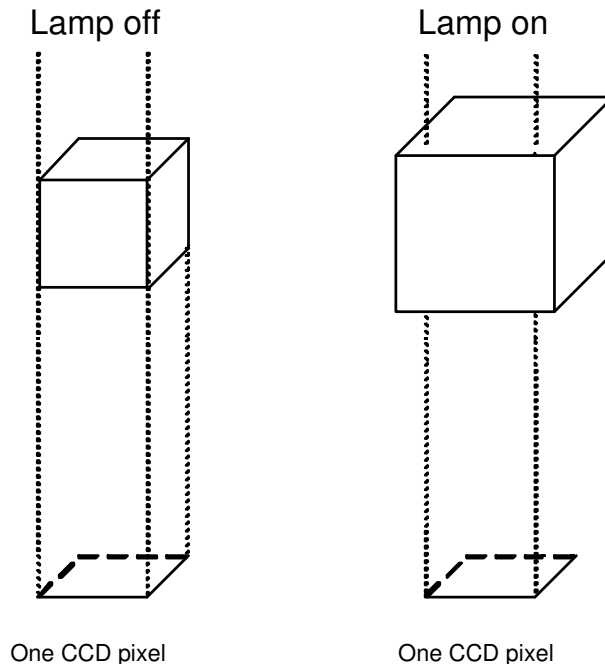
Figure 4.4: A sketch of the thermal expansion of burner viewed by one CCD pixel.

same: they are all cubes expanding with the same factor.

Taking these assumptions into account, we can state that for each path through the burner (from X-ray source towards CCD), the optical depth of the wall material $\tau_w = n\sigma L$ changes with the same factor. This factor equals $1/(1 + 2\bar{\alpha}\Delta T) = 1 - \theta$, where $\theta = 2\bar{\alpha}\Delta T$. Therefore τ_w changes into $\tau'_w = \tau_w(1 - \theta) = \tau_w - \theta\tau_w$.

If we ignore this change in τ_W and we attribute all the changes between lamp-off and lamp-on to the presence of Hg, this will cause serious errors. The results suggest that there is less Hg in the path, namely $\tau_{noncorr}(Hg) = \tau_{corr}(Hg) - \theta\tau_w$.

For example, if we take the relative linear thermal expansion of wall material as 1%, then $\theta = 2\%$. Thus we can only neglect this expansion effect if the optical depth through the plasma (Hg) is substantially larger than 2% of the optical depth through the wall. In Table. 3.1, we found that near the wall, the optical depth of Hg is 0.22 and that $\tau_w = 4.41$ for PCA. Thus, the change of 2% in the optical depth of PCA is about 0.09 which is about 41% of the Hg optical depth. In the center the optical depth of Hg is 0.81, whereas 2% of the optical depth of the burner is about 0.04, which is about 5% of the Hg optical depth. So if we do not correct for the thermal expansion, the optical depth in the center will change from 0.81 to 0.77, and at the wall from 0.22 to 0.13.

This numerical example illustrates that the thermal expansion of the burner can not be neglected and that the relative effect on the plasma edges will be larger than for paths through the center. The basic reason is that there is less Hg along paths through the edges

than along those through the center. Thus neglecting this expansion/density decrease effect will cause an apparent density drop in regions close to the edge.

A procedure to correct for this will be given in section 4.5.

4.3.4 Beam-hardening

Calibration procedure

As stated in section 3.3.3, when a non-monochromatic X-ray beam penetrates a medium for which the absorption cross-section is energy dependent, the medium will act as a non-gray filter, meaning that not only the intensity but also the spectrum of the beam will change as a function of penetration depth. Since the absorption cross-section is a decreasing function of energy, we find that the longer the absorption length, the higher the effective energy of the surviving photons will be, i.e. the X-ray beam becomes "harder". Therefore this effect is called 'beam-hardening'.

In our experimental setup, the X-ray source is not entirely monochromatic, and the burner has different absorption lengths for different lateral positions. This implies that the spectrum of the X-ray radiation passing through the Hg vapor is a function of lateral position. This will make the Abel inversion procedure extra complicated.

In order to study the beam-hardening effect, a special oven-lamp was constructed. This is a lamp for which the spatial distribution of Hg is not determined by a Hg plasma, but by an external heating source (oven).

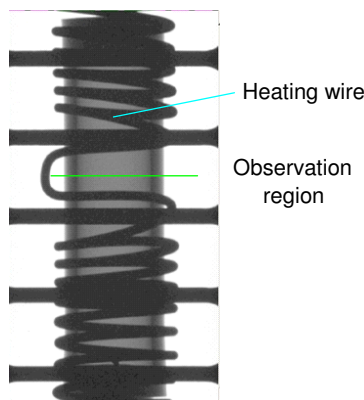*Figure 4.5: An X-ray image of an oven-lamp.*

This oven-lamp has the same geometry as that of the "type 3" lamp (cf table 1.1); the inner diameter is 4.5 mm, the wall thickness of the PCA burner is 0.8 mm and the electrode distance is 18 mm (cf Fig. 4.5). The mass of the Hg filling is 4.46 mg and the assumption is justified that the burner is homogeneously heated by the heating wire. From the geometry

and the mass of the Hg filling, the number density of Hg can be calculated as

$$n(r) = a_0 = 4.43 \times 10^{25} \, \text{m}^{-3} \,. \tag{4.13}$$

In this case, the line-integral of the density (the column-density) as function of the lateral position $F_{calc}(x)$ can be determined analytically. It is found that

$$F_{calc}(x) \equiv 2 \int_x^R \frac{n(r)r}{\sqrt{r^2 - x^2}} dr = 2 \int_x^R \frac{a_0 r}{\sqrt{r^2 - x^2}} dr = 2a_0\sqrt{R^2 - x^2}. \tag{4.14}$$

We can also determine this column-density experimentally by comparing the absorption signal of a lamp-off and lamp-on situation. It should be noted that in this case 'on' refers to 'oven-on' and 'off' refers to 'oven-off'. The experimental lateral profile of the column density is given by

$$F_{meas}(x) = \frac{1}{\bar{\sigma}(x)} \ln(\frac{I_{Off}}{I_{On}}), \tag{4.15}$$

where $\bar{\sigma}(x)$ is the mean value of the cross section, which due to the beam-hardening effect depends on the lateral position x. Its value can be found experimentally by equating $F_{calc}(x) = F_{meas}(x)$ which gives

$$\bar{\sigma}(x) = \frac{1}{2a_0\sqrt{R^2 - x^2}} \ln(\frac{I_{Off}}{I_{On}}). \tag{4.16}$$

Results

In order to investigate the beam-hardening influence, a series of experiments have been done for the oven-lamp at different acceleration voltages of the X-ray source, i.e. 20 kV, 25 kV, 30 kV and 60 kV. The results are given in Fig. 4.6 where $\bar{\sigma}(x)$ of Hg is shown as a function of lateral position x. In the ideal case of a monochromatic X-ray source and no blurring we would expect horizontal lines.

Figure 4.6 shows that there are two types of deviations from the ideal horizontal line. The most striking one is the sharp increase in the boundary region, especially for the acceleration voltages of 20 kV, 25 kV and 60 kV. This is not a beam-hardening effect, but the result of an image imperfectness as induced by blurring. At higher acceleration voltages (for example 60 kV), we can detect the beam-hardening effect. In the inner region $\bar{\sigma}$ has larger value than at the outer region (edge excluded, thus e.g. at $x \approx 0.75R$). This can be understood realizing that photons passing through the inner region are less filtered so that soft photons are better preserved and these have a large σ-value. This study suggests that 40 kV (cf Appendix B) is the most suitable acceleration voltage which will be confirmed by a study given in Appendix B. Nevertheless most of the measurements were done with acceleration voltage of 25 kV in order to get the monochromatic X-ray spectrum without beam-hardening calibration.
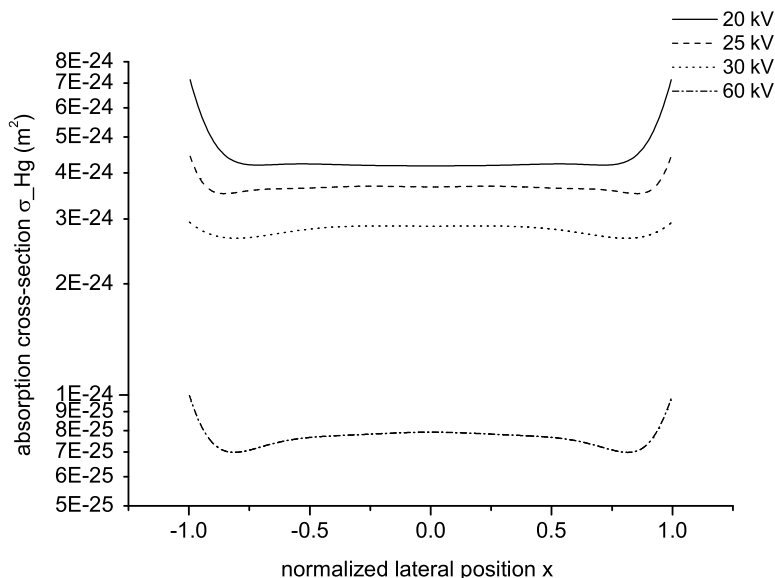
Figure 4.6: The mean value $\bar{\sigma}$ of the Hg attenuation cross-section as a function of the lateral position x as measured for different acceleration voltages of the X-ray tube, i.e. 20 kV, 25 kV, 30 kV and 60 kV. It is clearly demonstrated that $\bar{\sigma}$ decreases for increasing acceleration voltages which is based on the fact that $\sigma(E)$ is a decreasing function of energy. In the ideal case of monochromatic X-ray radiation (no beam-hardening) and perfect imaging we would find a horizontal line. The sharp increase approaching the wall points towards image imperfections (eg. blurring). For high acceleration voltages higher $\bar{\sigma}$ values are found at central lateral positions than at the outer region (x=0.75R): that is the result of beam-hardening.

4.4   Fitting the lamp-off profile

It appears quite straightforward to obtain the Hg density profile from the difference between the lamp-on and lamp-off images. However, due to the warm-up after switch-on, the burner will rotate, shift and expand, so that the geometrical position and the density of the wall material (density decrease due to expansion) will be different from that of lamp-off situation. Moreover, due to the instability of the X-ray source, the number of X-ray photons, the X-ray dose, applied in the lamp-on situation is generally not the same as that of the lamp-off case. Therefore, before the subtraction of the images can take place we have to adjust the images such that a proper matching of the geometry and the X-ray dose is obtained. This matching is largely facilitated if the images of the wall material can be cast in analytical formulas. To that end we use two fitting-procedures: one for lamp-off and the other for lamp-on. In both cases the fitting-procedure will be guided by Eq. 4.7

that is reproduced here for convenience

$$\widehat{S}^{off}(x) = B^{off} \int_0^\infty Q(E) I_0(E) e^{-\tau^{off}(\mathbf{x}, E)} dE. \tag{4.17}$$

A first step towards finding the structure of the fit function is obtained by replacing the integral by a product of the energy width ΔE and the integrand at a mean value $\bar{E}$ which leads to

$$\widehat{S}^{off}(x) = B^{off} Q(\bar{E}) I_0(\bar{E}) e^{-\tau^{off}(x, \bar{E})} \Delta E. \tag{4.18}$$

The optical depth of the lamp in the lamp-off situation can be written as

$$\tau^{off}(x, \bar{E}) = \tau_b(x, \bar{E}) + \tau_t(x, \bar{E}), \tag{4.19}$$

where $\tau_b(x, \bar{E})$ is the optical depth of the burner at lateral position x and energy $\bar{E}$ and τ_t the optical depth of the outer tube. Since the diameter of the outer tube (28mm) is much larger than that of the burner (4.5mm), we can assume that the path length through the outer tube is constant over the lateral range of interest (around 5 mm). Therefore we can simplify Eq. 4.18 to

$$\widehat{S}^{off}(x) = C^{off} e^{-\tau_b^{off}}(x, \bar{E}), \tag{4.20}$$

where $C^{off} = B^{off} Q(\bar{E}) \Delta E I_0(\bar{E}) e^{-\tau_t}$ is independent of the lateral position x.

By taking the logarithm of the lamp-off signal we get a fit function of the following structure

$$y^{off}(x) = y_0^{off} - \tau_b^{off}(x, \bar{E}) \tag{4.21}$$

$$\text{with} \quad \tau_b^{off}(x, \bar{E}) = n_b \bar{\sigma}_b(x) l_b(x). \tag{4.22}$$

Here $y^{off}(x) \equiv \ln(\widehat{S}^{off}(x))$, $y_0^{off} \equiv \ln C^{off}$ is a constant offset, n_b the density of the burner and $l_b(x)$ the path length through the burner at certain lateral position x given by (see Fig. 4.7):

$$l_b(x) = 2 \left(\sqrt{r_2^2 - (x - x_0)^2} - \sqrt{r_1^2 - (x - x_0)^2} \right), 0 \le |x - x_0| < r1;$$

$$l_b(x) = 2 \left(\sqrt{r_2^2 - (x - x_0)^2} \right), r_1 \le |x - x_0| \le r_2. \tag{4.23}$$

We will now refine the structure of the fit function by giving room to the influence of the beam- hardening. This is obtained by realizing that, due to beam-hardening, the absorption cross section $\bar{\sigma}_b(x)$ is not completely constant over the lateral position. The corresponding lateral dependence can be approximated by $\bar{\sigma}_b(x) = \sigma^* \left[\frac{l_b(x)}{l_{b\,\text{max}}} \right]^{-\beta}$, where β is expected to be a small positive number. This dependence of σ on l_b reflects that the mean cross section decreases as l_b increases; a tendency which can be expected. Therefore Eq. 4.21 can be written as

$$y^{off}(x) = y_0^{off} - k^* l_b(x)^{1-\beta}, \tag{4.24}$$
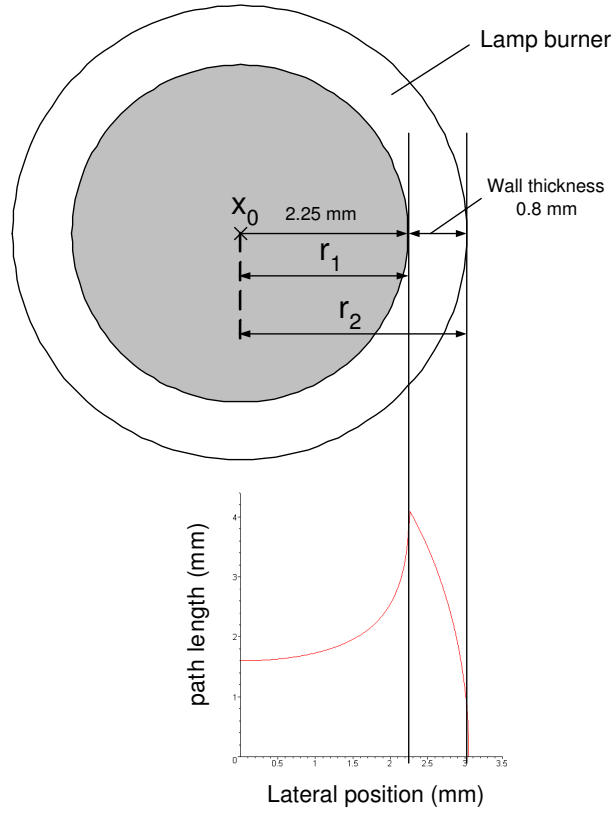
Figure 4.7: The path length through the burner as a function of lateral position.

where $k^* = n_b \sigma^* / l_{b\,\text{max}}$ is a positional independent absorption coefficient. Since $l_b(x)$ is determined by geometric formulas given above(Eq. 4.23), we can now write the fit function as

$$y^{off}(x) = y_0^{off} - k^* \times \left[2\left(\sqrt{r_2^2 - (x - x_0)^2} - \sqrt{r_1^2 - (x - x_0)^2} \right) \right]^{1-\beta}, 0 \leq |x - x_0| < r1;$$

$$y^{off}(x) = y_0^{off} - k^* \times \left[2\left(\sqrt{r_2^2 - (x - x_0)^2} \right) \right]^{1-\beta}, r_1 \leq |x - x_0| \leq r_2. \qquad (4.25)$$

Using the Levenberg-Marquardt non-linear least-square fitting method [21] to fit the experimental data, the six parameters y_0^{off}, k^*, x_0, r_1, r_2 and β can be found. An example of an experimental fit can be seen in Fig. 4.8.

A test for the influence of β on the fitting has been done by keeping $\beta = 0$ fixed in one fitting and comparing the results with those of a fit for which β was a free parameter. Figure 4.9 shows that the fit with a free β parameter is better than that of $\beta = 0$. More specifically we can express the influence of β by using the χ^2-value of the fit. For $\beta = 0$ we find that $\chi^2 = 0.14$ while for $\beta = 0.08$ a χ^2 of 0.09 is found. This strongly suggests that there is some influence of beam-hardening on the transmission profile. However the value
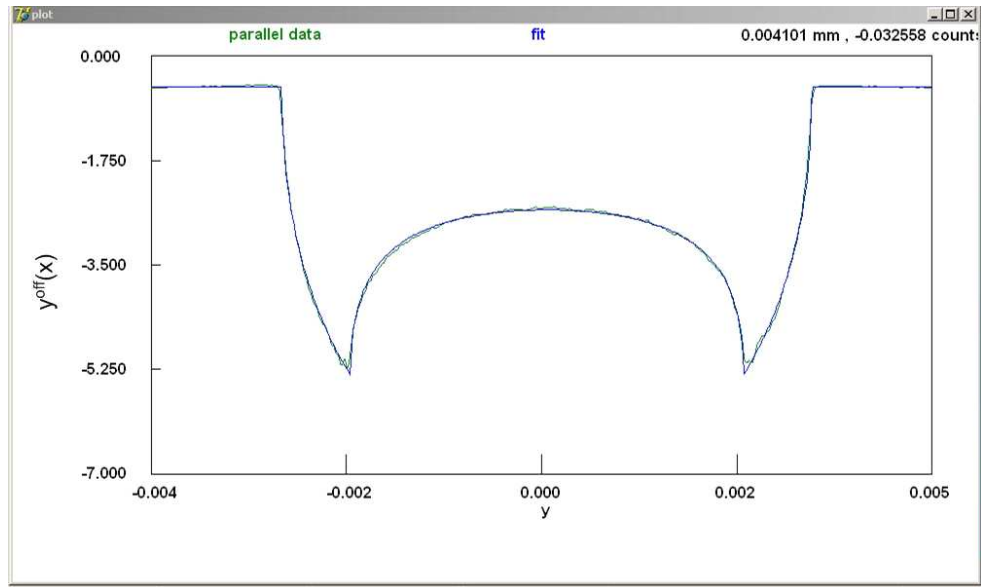
Figure 4.8: An example of the fitting of the experimental data $y^{off}(x) = \ln \widehat{S}^{off}(x)$

of β is small and typically around 0.08 for an acceleration voltage of 25 kV. This means that the beam-hardening effect is not dramatic and thus that the X-ray spectrum obtained for this acceleration voltage is close to monochromatic.

We can conclude that it is useful to allow for the beam-hardening effect by introducing a lateral dependent mean cross section of the form $\bar{\sigma}_b(x) = \sigma^* \left[\frac{l_b(x)}{l_{b\,max}} \right]^{-\beta}$.

| | |
| (a) | (b) |
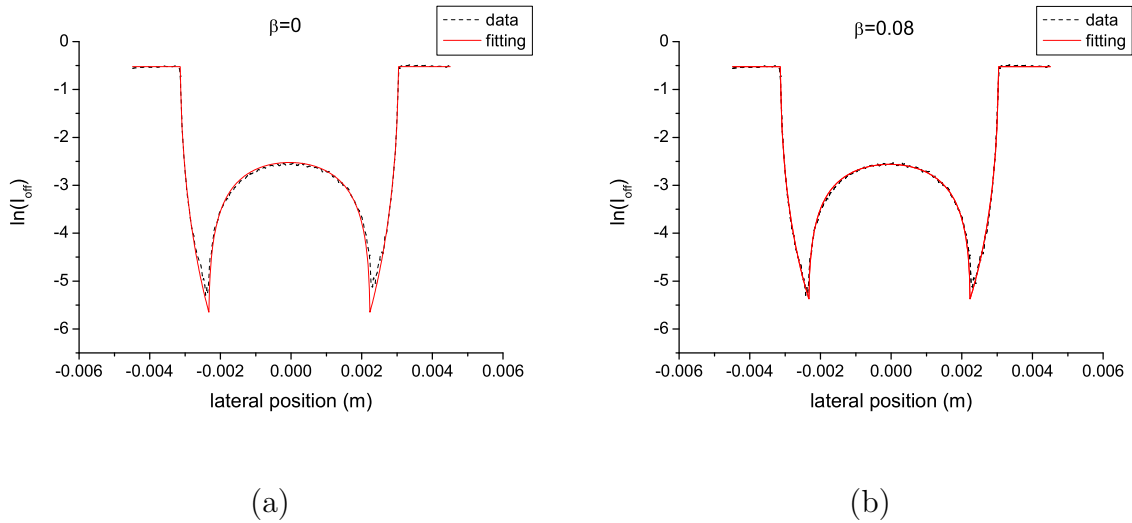
Figure 4.9: The influence of β on the fitting of lamp-off profile. **(a):** $\beta = 0$. **(b):** β is free parameter which obtains the value $\beta = 0.08$.

69

4.5   Fitting the lamp-on profile

The construction of the fitting function for the lamp-on situation is again guided by Eq. 4.7 which now reads

$$\widehat{S}^{on}(x) = B^{on} \int_0^\infty Q(E) I_0(E) e^{-\tau^{on}(\mathbf{x},E)} dE, \qquad (4.26)$$

which has the same form as Eq. 4.17 with the difference that τ^{off} and B^{off} are replaced by τ^{on} and B^{on}. We should realize that during the lamp-on measurement I_0 is not exactly the same as that for the lamp-off situation. However, this change can also be regarded as a change in a measurement time (and thus in B). What matters is the total number of photons, the X-ray dose, which is determined by the product BI_0. An important step in the final fitting procedure is to correct for the dose-inequality; i.e. to bring the number of photons for the on-case in accordance to that in the off-case.

Following the same procedure as in the lamp-off case we replace the integral by the product of energy interval and a mean value of the integrand:

$$\widehat{S}^{on}(x) = B^{on} Q(\bar{E}) I_0(\bar{E}) e^{-\tau^{on}(x,\bar{E})} \Delta E = C^{on} e^{-\tau^{on}(x,\bar{E})}, \qquad (4.27)$$

where C^{on} is defined in analogy with C^{off} and the optical depth is described as

$$\tau^{on}(x, \bar{E}) = \tau_b^{on}(x, \bar{E}) + \tau_{Hg}(x, \bar{E}), \qquad (4.28)$$

where $\tau_{Hg}(x, \bar{E})$ the optical depth of Hg at lateral position x and energy $\bar{E}$.

If we take the logarithm of the lamp-on signal, we get

$$y^{on}(x) = y_0^{on} - \tau_b^{on}(x, \bar{E}) - \tau_{Hg}(x, \bar{E}) \qquad (4.29)$$

with $y = \ln(\widehat{S}_{on}(x))$ and $y_0 = (\ln C^{on})$.

If we compare this with the corresponding equation for the lamp-off situation

$$y^{off}(x) = y_0^{off} - \tau_b^{off}(x, \bar{E}), \qquad (4.30)$$

it is tempting to think that $\tau_{Hg}(x, \bar{E})$ can be obtained by means of a simple subtraction of Eq. 4.30 and Eq. 4.29. However, there are two reasons why such a simple operation is not correct. First, due the warm-up of the burner after switch-on, a rotation, shift and expansion (and thus density decrease) will take place, so that the geometrical position and the density of the wall material will be different from that of the lamp-off situation; therefore $\tau_b^{on} \neq \tau_b^{off}$. Second, the number of photons for the on- and off-case are not exactly the same, so that we in general have $y_0^{on} \neq y_0^{off}$. Therefore, the $y^{on}(x)$ has to be corrected by means of a fitting-procedure which corrects for the geometrical miss-match and the dose-inequality. The corresponding fit-function reads

$$y^{*on}(x, \boldsymbol{a}) = \{y^{on}(x \cdot a_1 + a_2)\} \cdot a_3 + a_4, \qquad (4.31)$$

in which $\boldsymbol{a}$ stands for a fit-vector which consists of the elements a_1, a_2, a_3 and a_4 that correct for expansion a_1, shift a_2, density decrease a_3 and offset a_4. This last parameter corrects for both dose-inequality and density decrease operation.

The method that was used to find the structure of this fit-function will now be explained.

First, we must correct for the density decrease of the wall (cf. section 4.3.3) by introducing the parameter $\Delta y = y - y_0$ which isolates the offset y_0 from the expressions(4.29) and (4.30):

$$\Delta y^{off} = y^{off} - y_0^{off} = \begin{cases} 0, & |x - x_0| > r_2 \\ -\tau_b^{off}(x, \bar{E}), & |x - x_0| \leq r_2 \end{cases}$$

and

$$\Delta y^{on} = y^{on} - y_0^{on} = \begin{cases} 0, & |x - x_0| > r_2 \\ -\tau_b^{on}(x, \bar{E}), & r_1 \leq |x - x_0| \leq r_2 \\ -\tau_b^{on}(x, \bar{E}) - \tau_{Hg}(x, \bar{E}), & |x - x_0| \leq r_1. \end{cases}$$

For the X-ray beam which passes through the burner wall region ($r_1 \leq |x - x_0| \leq r_2$), only τ_b (*on* or *off*) matters and the difference between Δy^{on} and Δy^{off} is caused by the density-decrease effect of the wall material, which is described as

$$\frac{\Delta y^{off}}{\Delta y^{on}} = \frac{\tau_b^{off}(x, \bar{E})}{\tau_b^{on}(x, \bar{E})} = \frac{1}{1 - \theta} = a_3. \tag{4.32}$$

Thus

$$\Delta y^{off} = a_3 \Delta y^{on} \quad \text{for} \quad r_1 \leq |x - x_0| \leq r_2. \tag{4.33}$$

Second we have to correct for the shift and expansion of the burner material. This is done by re-assigning the Δy -value measured at the lateral position x to the new position $(x \cdot a_1 + a_2)$, where a_1 takes care for the expansion and a_2 for the shift. Thus, if we may assume that expansion of the burner wall material is linear, we get the following transformation:

$$\Delta y^{*on}(x, \mathbf{a}) = \{\Delta y^{on}(x \cdot a_1 + a_2)\} \cdot a_3. \tag{4.34}$$

Third, in order to correct for the dose-inequality we introduce $a_4 = y_0^{off} - a_3 \cdot y_0^{on}$. Combining these three operations we get the expression for the fit-function for the on-case as stated above (cf. Eq. 4.31[1]).

$$y^{*on}(x, \mathbf{a}) = y^{on}(x \cdot a_1 + a_2) \cdot a_3 + a_4. \tag{4.35}$$

Since this fitting function is non-linear, we again apply the Levenberg-Marquardt fitting procedure [21] to find a_1,a_2,a_3 and a_4. The fit is made for all data points in the range of $|x - x_0| > r_1$ where r_1 is the inner radius of the burner(cf Fig. 4.7).

---

[1]Since strictly spoken the function $y^{on}(x)$ is only known at the measurement points x_i, it is made continuous by linear interpolation between measurement points.

The overall fitting procedure has two steps:
The first step is to apply Eq. 4.25 to fit for the lamp-off case. Then the lamp-on measurement is fitted for the region which does not contain the Hg vapor (the region $|x - x_0| \geq r_1$). Due to the presence of the Hg for the lamp-on case, the inner radius of the burner r_1 cannot be determined accurately for the lamp-on measurement. However, from the fit, the outer radius r_2 and the center x_0 can be found. By assuming that the expansion of the burner is linear, i.e. that the inner wall and outer wall have the same expansion factor, we can determine a good estimate for r_1. Now by applying Eq. 4.25 on both the full profile of the lamp-off image and the wall-part of the lamp-on, we can, by comparing the results determine a first guess of a_1 and a_2.

The second step is that based on the initial value of a_1 and a_2, we apply Eq. 4.34 to fit the on-profile onto the off-profile for the Hg free region ($r_1 < |x - x_0| < r_2$). In this way the shift, expansion and density decrease of the burner are corrected.

An example of the fitting procedure of lamp-on profile is shown in Fig. 4.10.
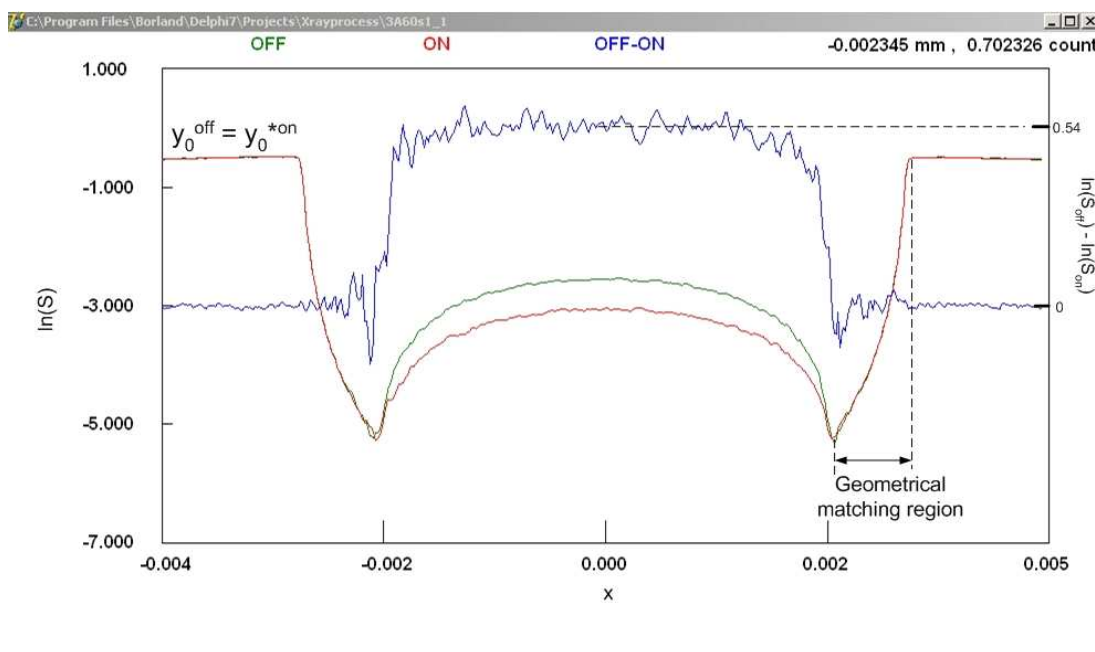
Figure 4.10: An example of the results of fitting the lamp-on and lamp-off images such that the difference in dose is corrected for: $y_0^{*on} = y_0^{off}$ in the outside region and the geometry of the wall part for lamp-on matches with that for lamp-off. The difference between the fitted lamp-on and lamp-off images provides the absorption contribution of mercury which is also given.

By fitting the lamp-on profile onto the lamp-off profile, parameters a_1, a_2, a_3 and a_4 are found. The values of a_2 and a_4 are typically 1.7×10^{-4} and 1.4×10^{-3} for a type 3-1 lamp. However there is much scatter between different images. This can be understood since the dose-inequality between the off- and on-cases can be positive or negative. The

same applies to the change in the central position. The typical values for a_1 and a_3 for "type 3-1" lamp is 1.012 and 1.02. It is interesting to see that the values of a_1 for all the lamps are larger than 1. This means that when the lamp is burning, the inner diameter is smaller than that of the lamp-off case. Theoretically a_1 should be less than 1 if the PCA burner expands outwards and it should be 0.99 for a 1% linear expansion. However since the lamp is a closed vessel subjected to tension during heating, it is possible that the lamp does not expand outwards only but both inwards and outwards. Nonuniform heating leads to nonuniform expansion. There are clear indications that stresses build up in the ceramic during operation; after a number of starts these lamps often fail due to crack formation. The value of a_3 is as we expected. If the linear thermal expansion is 1%, then the density-decrease factor of the PCA will be $1 - \theta = 0.98$. Therefore a_3 can be obtained by Eq. 4.32 which is 1.02.

4.6 Subtraction

After the geometrical correction of the lamp-on profile, the two profiles can be subtracted directly. Then we get the optical depth of the Hg vapor as:

$$
\begin{aligned}
\tau_{Hg}(x) &= \frac{1}{a_3}(\ln \widehat{S}^{off}(x) - \ln \widehat{S}^{oncor}(x)); \text{ or} \\
\tau_{Hg}(x) &= \frac{1}{a_3}(y^{off}(x) - y^{*on}(x)).
\end{aligned}
\tag{4.36}
$$

If we select the acceleration voltage of the source such that the X-ray beam entering the plasma is nearly monochromatic, the beam hardening effect by the burner at different lateral position x is negligible. Therefore $\sigma_{Hg}(x)$ is a constant and the line-integrated density profile can be obtained as

$$
\begin{aligned}
F_{exp}(x) &= \frac{\ln \widehat{S}^{off}(x) - \ln \widehat{S}^{onCor}(x)}{a_3 \bar{\sigma}_{Hg}}; \text{ or} \\
F_{exp}(x) &= \frac{y^{off}(x) - y^{*on}(x)}{a_3 \bar{\sigma}_{Hg}}.
\end{aligned}
\tag{4.37}
$$

4.7 Abel inversion

In this section, the Abel inversion procedure will be described. Since the Hg distribution in the lamp is cylindrical symmetric, the column density of Hg along each chord of the burner can be described through the Abel transform as

$$
F(x) \equiv 2 \int_x^R \left\{ n(r) \cdot \frac{r}{\sqrt{r^2 - x^2}} \right\} dr.
\tag{4.38}
$$

In order to describe the radial density profile of Hg, even-order polynomial functions are chosen as base functions in the radial domain. This leads to

$$n(r) = \sum_{i=0}^{n} a_{2i} r^{2i}. \tag{4.39}$$

Then the column density of Hg can be expressed using the base function in the forward projection space as

$$F(x) = 2 \int_{x}^{R} \frac{\sum_{i=0}^{n} a_{2i} r^{2i+1}}{\sqrt{r^2 - x^2}} dr = 2 \sum_{i=0}^{n} a_{2i} \int_{x}^{R} \frac{r^{2i+1}}{\sqrt{r^2 - x^2}} dr = 2 \sum_{i=0}^{n} a_{2i} F_{2i}(x), \tag{4.40}$$

where

$$F_{2i}(x) = \int_{x}^{R} \frac{r^{2i+1}}{\sqrt{r^2 - x^2}} dr. \tag{4.41}$$

For each value of i, an analytical form of $F_{2i}(x)$ is obtained. Examples are listed below for $i = 0 \cdots 3$.

$$\begin{aligned}
F_0(x) &= \sqrt{R^2 - x^2}; \tag{4.42}\\
F_2(x) &= \frac{R^2\sqrt{R^2 - x^2}}{3} + \frac{2x^2\sqrt{R^2 - x^2}}{3};\\
F_4(x) &= \frac{R^4\sqrt{R^2 - x^2}}{5} + \frac{4x^2 R^2\sqrt{R^2 - x^2}}{15} + \frac{8x^4\sqrt{R^2 - x^2}}{15};\\
F_6(x) &= \frac{R^6\sqrt{R^2 - x^2}}{7} + \frac{6x^2 R^4\sqrt{R^2 - x^2}}{35} + \frac{8x^4 R^2\sqrt{R^2 - x^2}}{35} + \frac{16x^6\sqrt{R^2 - x^2}}{35}.\\
&\cdots
\end{aligned}$$

After a decision on the order of the expansion is made, the structure of the fit function in the forward projection space $F(x)$ is known. By applying Eq. 4.40 to fit the lateral profile of the Hg density, the coefficients a_{2i} will be found. After that the radial profile can be reconstructed.

The choice of the dimension of the projection space (i.e. the order of the polynomial) is not trivial. A demand for accuracy would suggest to add many higher orders. However, by increasing the order of the polynomial, we also give room to noise. The noise may "excite" finer structures and structures that are not present in reality. Thus the decision of the order of the polynomial has to be guided by an error/noise analysis. This is described in Appendix C. There we will find that the Tikhonov regularization method in the least square fitting for the lateral profile is the best solution for this problem.

Since we do not know the mean energy, the mean cross-section of Hg is not known *a priori*. By assuming $\bar{\sigma}$ as a constant, the relative radial density profile of Hg at each axial position z can be derived using the Abel inversion procedure. Since the total pressure in

the lamp is constant and the buffer gas is the dominant species, we can apply the relation $p_{Hg} \approx p_{tot} = const$. From the ideal gas law $p = nkT$, the local gas temperature $T(r)$ at each axial position z is proportional to the inverse of the mercury density $n(r)$, i.e.

$$T(r) = \frac{p}{n(r)k} \propto \frac{1}{n(r)}. \tag{4.43}$$

Then if we know the wall temperature T_w at a certain axial position z, the absolute temperature profile can be determined as

$$T(r) = \frac{n_w}{n(r)}T_w. \tag{4.44}$$

4.8 Wall temperature measurements

Wall temperature measurements were performed at Philips CDL Eindhoven. The burner of a lamp has been taken out and installed into a vacuum or pure N_2 environment depending on the filling in the outer tube of the original lamps. Then the hot burner is imaged using the infrared pyrometer AGEMA THERMOVISION 900. The measured infrared spectrum is located in the far infrared region, i.e. $8 \sim 12$ μm for PCA material and $7.5 \sim 8.3$ μm for quartz. In this infrared spectral region, the quartz or PCA burner material is not transparent anymore. Therefore the intensity of the signal can be related to the temperature of the wall provided that the emissivity of the material is known.

A typical example of the wall temperature measurement is shown in Fig. 4.11.

Since we know the wall temperature, the absolute temperature can be found by scaling the relative temperature profile to the wall temperature using Eq. 4.44.

4.9 The complete image process procedure

From the analysis of all possible error sources, a complete image process procedure has been established to determine an accurate Hg radial density. Here the procedure is given as a recipe.

1. Take two series of lamp-on and lamp-off images.

2. Correct these two images for dark current, offset and flat field of the CCD pixel array (Eq. 4.1).

3. Transform these point source images to a parallel beam system (Eq. 4.9).

4. Fit the theoretical curve to the logarithm of the lamp-off and lamp-on profiles at certain axial position z for each pair of lamp-off and lamp-on images, and subsequently scale the lamp-on profile to match the lamp-off profile for the burner material region ($r_1 < |x-x_0| < r_2$) to find the correction for geometrical mismatch, density decrease of the wall material and X-ray dose inequality. (Eq. 4.25 and Eq. 4.35).
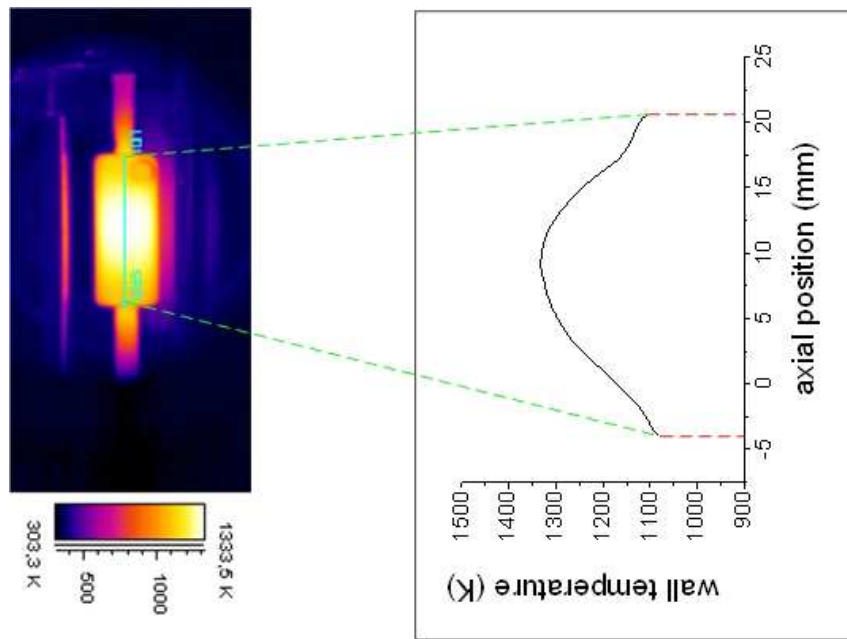
Figure 4.11: **(a)**: *The infrared pyrometry image of the wall temperature of the ARGES lamp ("type 1") operating with 142 W square-wave ballast of 83 Hz. The zero axial position is chosen at the tip of the bottom electrode.* **(b)**: *The wall temperature of ARGES lamp at different axial position.*

5. Subtract the logarithmic lamp-off and lamp-on profiles such that the correct column density profile of Hg is obtained (Eq. 4.37).

6. Accumulate and average all pairs of images, applying step 1-5 on each pair of them, to get the final column density of Hg.

7. Apply Abel inversion to get the relative radial density profile of Hg.

8. Apply the ideal gas law and measure the boundary value of the temperature to get the absolute gas temperature profile (Eq. 4.44).

Chapter 5

XRA experimental results

Abstract

Chapter 3 was devoted to the design and construction of an X-ray absorption (XRA) facility. Chapter 4 dealt with the data analysis procedure obtained by this setup. Here we will discuss the experimental results.

XRA experiments were done on several lamps. Apart from using lamps with burners of different geometrical structures we also varied the salt filling of these lamps, the Hg-pressure, and the electrical power. In this way we could establish the influence of the various external settings on the gas-temperature profile. It is found for instance, that the chemical composition has an important impact. The addition of easy ionizable elements, such as Na, Dy and Ce lead to constricted temperature profiles. Especially the region close to the bottom electrode of a vertically burning lamp exhibit slim temperature-profiles.

It was found that even for a worst-case scenario of the application of XRA on a low pressure Hg lamp with a small diameter, reliable results can be obtained. It was found that for this Hg+NaI/CeI$_3$ lamp with a pressure of 1.7 bar the increase of the power leads to a constriction of the temperature-profile.

In order to place the results in a broader perspective, XRA experiments were applied to the ARGES lamp, a lamp that was operated by the Dutch astronaut André Kuipers under zero-g conditions in the International Space Station. For these lamps temperatures were measured using data from emission spectroscopy. The XRA setup was also used for lamps that were investigated with Thomson Scattering TS (cf. Chapter 7). For both the ARGES and TS lamp it was found that the gas-temperature obtained by XRA gives lower values than those obtained with TS and atomic emission spectroscopy (AES).

In comparing our results with those of other groups one should realize that in contrast to other studies our method is more self-contained, i.e. free from data obtained by AES. The gas-temperature is not calibrated using atomic radiation emitted by the central plasma but the wall temperature obtained by pyrometry. This gives a solid bases to the comparison of XRA results with those of TS and emission spectroscopy and highlights the found discrepancies.

5.1   Introduction

After the design of the experimental setup and the establishment of the data handling procedure, we performed several X-ray absorption experiments on different HID lamps. Although all the XRA experiments were done on lamps containing Hg to determine the gas temperature, this technique can also be performed to Hg-free lamps such as metal halide lamps using Xe or Zn as a buffer gas.

All the X-ray absorption experiments were done with the 2kW fine-focus Mo-anode X-ray tube and with a Zr filter with a thickness of 0.1 mm$\pm$ 0.01 mm. The acceleration voltage was set at 25 kV. The lamp was placed around 7.0 ± 0.1 cm from the X-ray CCD imaging plane and around 84 ± 0.1 cm from the X-ray source. All the lamps were driven by a square-wave ballast which keeps the power of the lamp constant with time. This yields a quasi-DC situation. The geometry and the fillings of the different lamps are listed in table 5.1. The experimental settings for all the measurements are listed in table. 5.2.

Type	l_{arc}	D_{in}	l_{arc}/D_{in}	δ	Lamp fillings
type 1	17	8	2.13	1	10 mg Hg+DyI$_3$
type 2-1	39	18	2.17	1	15 mg Hg
type 2-2	39	18	2.17	1	50 mg Hg
type 3-1	18	4.5	4	0.8	4.46 mg Hg
type 3-2	18	4.5	4	0.8	4.46 mg Hg+NaI
type 3-3	18	4.5	4	0.8	4.46 mg Hg+NaI/CeI$_3$
type 4	32	4	8	0.5	0.6 mg Hg+NaI/CeI$_3$

Table 5.1: The designs and filling of the different HID lamps used in the XRA experiments. Here l_{arc} is the arc length, D_{in} the inner diameter of the burner, and δ is the wall thickness; all given in mm.

In section 5.2, the typical results are presented for a "type 3-1" lamp. The fitting of the lateral profile and the reconstructed radial profile are presented. The shape of the temperature profile for different axial position is discussed, and also an error analysis is given. In section 5.3, the results of "type 3" series lamps are shown, and the influence of the salt additives on the temperature profiles is discussed. In section 5.4, the XRA results are presented on two lamps which were also used for the TS study, and the influence of the pressure on the gas temperature profile is discussed. In section 5.5, the results of a 'worst case' low Hg-content metal halide lamp with small diameter are presented and discussed. In section 5.6, the results of XRA experiments on a 'type 1' ARGES lamp is shown and compared with Absolute Line Intensity (ALI) measurements. Finally, some conclusions are drawn from the results of different HID lamps in section 5.7.

Type	P_{lamp}(W)	p (bar)	τ_{Hg}	V_{acc}(kV)	I_{acc}(mA)	N_{img}	t_{expo}(s)
type 1	142	~ 10	0.55	25	35	20	100
type 2-1	200	$\sim 1.6^1$	0.16	25	35	20	67
type 2-2	200	$\sim 4.9^1$	0.26	25	35	40	67
type 3-1	70	~ 19	0.54	25	20	50	60
type 3-2	70	~ 19	0.54	25	20	30	60
type 3-3	70	~ 19	0.54	25	20	20	60
type 4	70, 90, 120, 142	~ 1.7	0.048	25	35	50	60

Table 5.2: The operation settings of the different lamps. Here P_{lamp} is the lamp power, p the estimated Hg pressure[1], τ_{Hg} the estimated diametral optical depth of Hg, V_{acc} and I_{acc} are the acceleration voltage and the current of the X-ray generator, N_{img} is the number of the pairs of lamp-on and lamp-off images, and t_{expo} is the exposure time of each image.

5.2 Typical results of XRA experiments

X-ray absorption experiments were performed on different kinds of HID lamps. The construction and operation specifications of these lamps are given in the table 5.1 and 5.2. We will start with the presentation of the results obtained with lamp "3-1". The lamp was operated in a vertical orientation at 70 W with a square-wave ballast of 81 Hz. The X-ray CCD camera was cooled down to $-20°C$.

The fitting procedure presented in chapter 4 was performed on all pairs of the lamp-on and lamp-off images to correct for the X-ray dose-inequality, the geometrical mismatch and the density-decrease effect. Then after substraction of each pair of the corrected logarithms of lamp-off and lamp-on profiles, the column density profile of Hg are obtained assuming that $\bar{\sigma}_{Hg}(x)$ is constant. The 50 lateral profiles of Hg are accumulated and averaged. Finally by applying the general structure of the lateral fitting function $F(x) = \Sigma_{i=0}^{i=30} a_{2i} F_{2i}$ (cf. Eq. 4.40) with an optimized Tikhonov regularization parameter ($\mu = 1 \times 10^{-6}$) to fit the lateral Hg density profile, the coefficients a_{2i} are found. This determines the relative radial profile of the Hg density.

The fitting of the line-integrated lateral profile of Hg density and the reconstructed radial profile of Hg density are shown in Fig. 5.1. From this relative density distribution, we can deduce a relative temperature distribution using the ideal gas law $p = nkT$. By using wall temperature measurements, we can construct the absolute temperature profile. This is done for different axial positions and the results are shown in Fig. 5.2.

Figure 5.2 clearly shows that the arc shape is similar for different axial positions with some constriction close to the top electrode (95%). Since the arc is asymmetrical close to

---

[1]The p-value is determined assuming that the Hg is unsaturated which turned out later to be not true (cf.section 5.4.2).
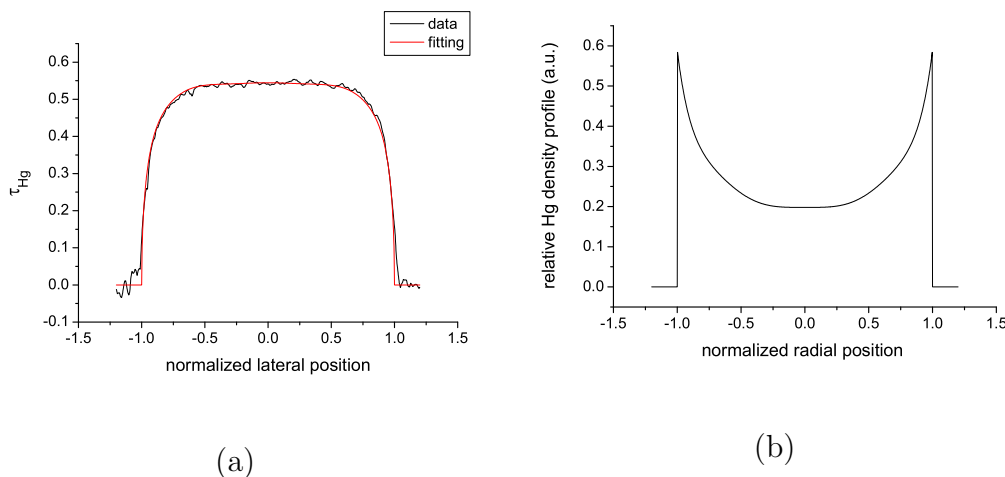
(a)

(b)

Figure 5.1: **(a)** The lateral profile of the line-integrated Hg density for a "type 3-1" lamp at 9.9 mm from the bottom electrode (55% of the arc-length). The lamp is filled with 4.46 mg Hg and operating with a 70 W square-wave ballast of 81 Hz. The burner has an inner diameter of 4.5 mm. The arc length is 18 mm and the wall thickness is 0.8 mm. The pressure in the lamp is about 19 bar (cf.table 5.1 and 5.2). **(b)** The reconstructed relative radial density profile at the same axial position (9.9 mm from the bottom electrode).

the electrodes and Abel inversion is only suitable for the cylindrical symmetric profile, we cannot obtain the temperature profile for the region very close to the electrodes.

Figure 5.2(b) gives the radial temperature for 5 different axial positions that are presented as a function of the normalized distance to the bottom electrode such that the electrode distance l_{arc} corresponds to 100%. The normalized temperature profiles are shown in Fig. 5.2(c). They show if and how far the arc is constricted. They clearly demonstrate that in the pure Hg case, the temperature profiles are broad and quite similar for different axial positions.

The dependence of the temperature along the axis of the arc in the "type 3-1" lamp are given in Fig. 5.2(a). It clearly shows that, in this case of a pure Hg filling, the axis temperature is high in the region close to the electrodes. The axis gas temperature in the middle of the lamp (at 9.9 mm corresponding to 55% l_{arc} to the bottom electrode) is about 4656 K. The wall temperature at the same axial position is 1763 K. So the ratio of the center temperature and the wall temperature T_0/T_R is 2.6, i.e. $n_R/n_0 = 2.6$. The n_R/n_0 ratio for positions close to the electrodes are 3.4 at 0.9 mm (95%) to the top electrode, and 3.6 at 1.8 mm (10%) to the bottom electrode.

The n_R/n_0 ratio of Hg density at different axial positions as published by Curry [17] are about 2.9 at the mid-plane, 4.0 at 1 mm distance to the top electrode and 2.8 at 1 mm

(a)

(b)

(c)

(d)
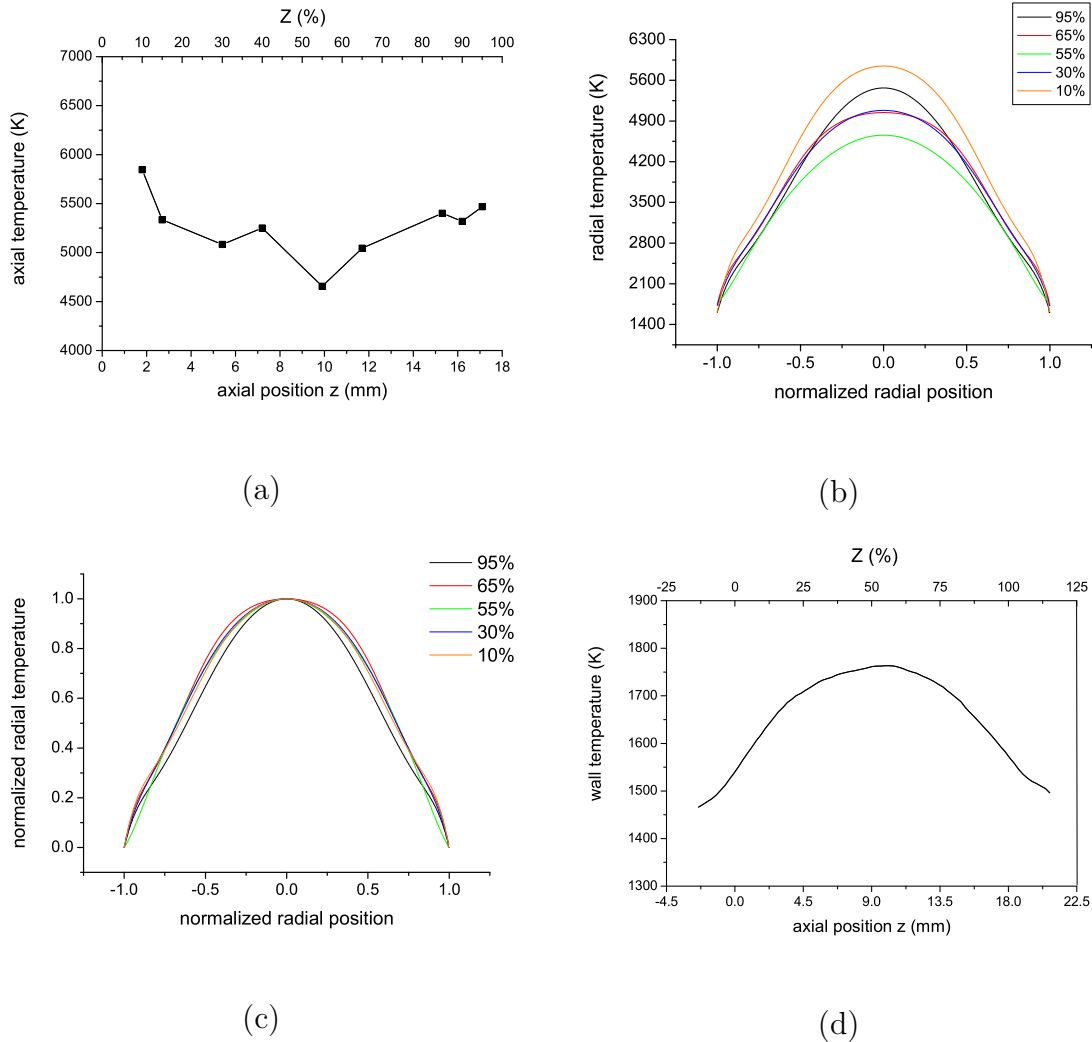
Figure 5.2: **(a)** The axial temperature profile of "type 3-1" lamp (pure Hg) burning in vertical orientation. **(b)** The radial temperature profiles of "type 3-1" lamp (pure Hg) for different axial positions expressed in the dimensionless quantity $Z = z/l$. The position $Z = 0\%$ is that of the tip of the bottom electrode. **(c)** The normalized temperature profiles of "type 3-1" lamp (pure Hg) as function of radial position for different axial positions. **(d)** The wall temperature of "type 3-1" lamp as a function of axial position.

to the bottom electrode. That lamp has a different geometry: an inner diameter of 2.15 cm and arc length of 5.3 cm. Moreover it was operated with a conventional inductive ballast at 60 Hz. In the mid-plane and close to the top electrode, our n_R/n_0 values are similar to those found by Curry. But at the position close to the bottom electrode, our results are different. It should be noted that Curry did not calibrate the T-profiles by means of a T_{wall} measurement, but by an information on the central temperature T_0. This T_0 value was found by analyzing the spectral line shape of self-absorbed lines (modified Bartels' emission method) of Hg (546.1 nm, 435.8 nm, 404.7 nm and 365.0 nm). This implies that an excitation temperature was used which might be close to the electron temperature. In order to verify the presence of LTE we followed a different route in which the gas temperature profile is determined free from influence of the electron temperature. Nevertheless, comparing his results with our results we find that the central T found by Curry is larger than the value we obtained: 5570 K instead of 5250 K. Apart from the difference in the nature of the temperature (excitation temperature instead of gas temperature) we should however realize that the lamps are different.

In the rest of this chapter, several other vertical burning lamps will be discussed. In order to facilitate the comparison between different experiments, the following parameters are used: 1. The ratio of the densities at the wall and in the center $n_R/n_0 = T_0/T_R$; 2. wall temperature T_W; 3. The value of full-width at half maximum (FWHM) of the radial temperature profile.

All these three quantities are given as functions of axial position. These are presented both in an absolute scale z given in mm, and in a relative scale $Z = z/l_{arc}$ expressed in %. The zero axial position is chosen at the tip of the bottom electrode.

5.3 The influence of salt additives

In this section, we present the results of an experimental study to the influence of the salt additives on the gas temperature. For this study we used lamps of the same geometry, namely "type 3" as discussed in the previous section. Lamp 3-1 is without salt (pure Hg), lamp 3-2 has a single salt component (NaI), and lamp 3-3 has a salt-mixture filling (NaI/CeI$_3$). The experimental settings are given in table 5.2.

The results for lamp "3-2" (Hg+NaI) and lamp "3-3" (Hg+NaI/CeI$_3$) are shown in Fig. 5.3 and Fig. 5.4. They should be compared with each other and with Fig. 5.2.

Figure 5.3 shows that addition of NaI leads to a reduction of the axial gas temperature: the axis temperature of 5083 K near the bottom electrode (30%) for the pure Hg case drops to 4729 K. Moreover, the temperature profile near the bottom electrode is more constricted than that of the pure Hg case.
Figure 5.4 shows that the degree of constriction of the temperature profiles of lamp
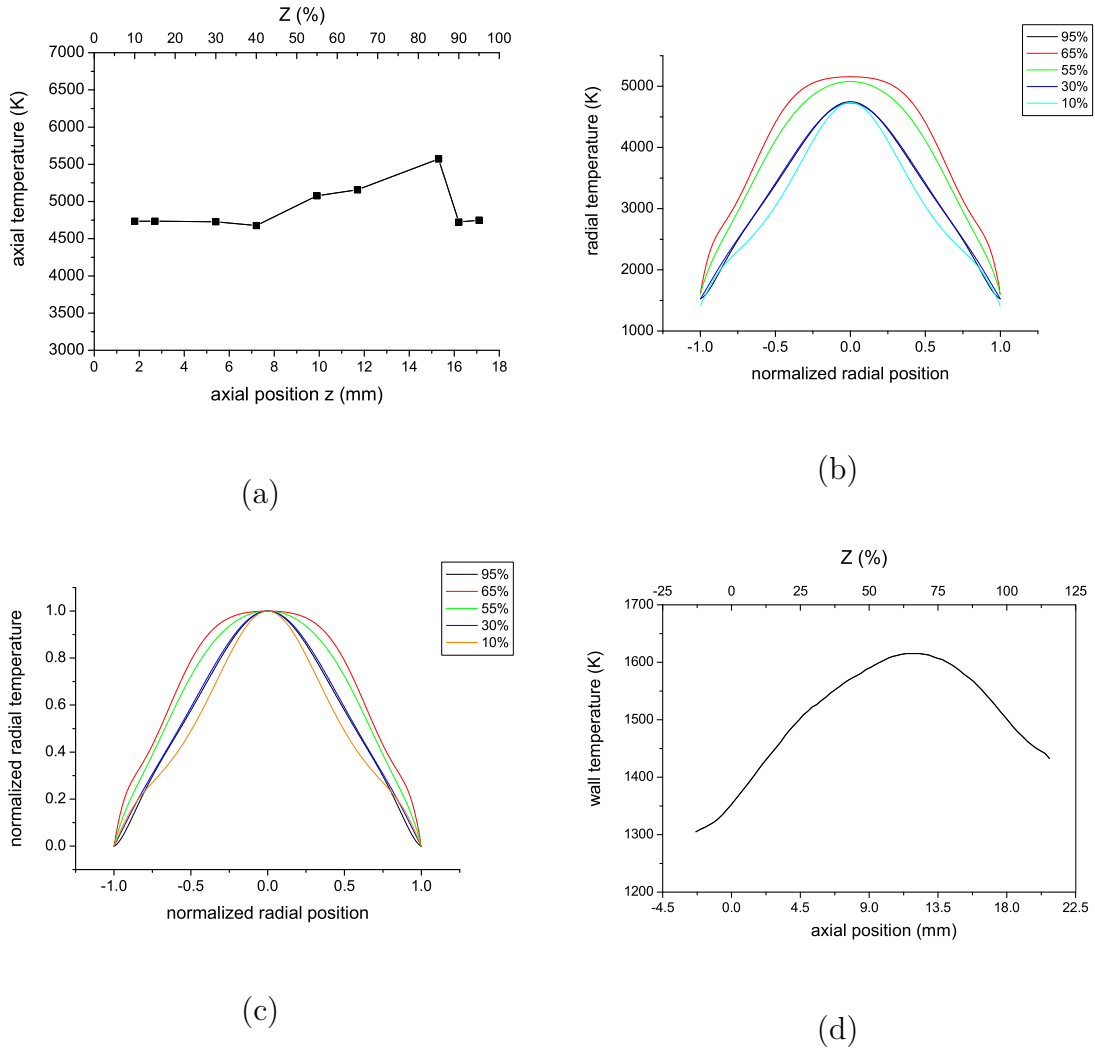
Figure 5.3: **(a)**: The axial temperature profile of type 3-2 lamp (Hg+NaI) operating with a 70 W square-wave ballast of 81 Hz (cf.Fig. 5.2). **(b)**: The radial temperature profile of type 3-2 lamp for different axial positions. **(c)**: The normalized temperature profile of type 3-2 lamp as function of radial position for different axial positions.**(d)**: The wall temperature of type 3-2 lamp.

(a)

(b)

(c)

(d)
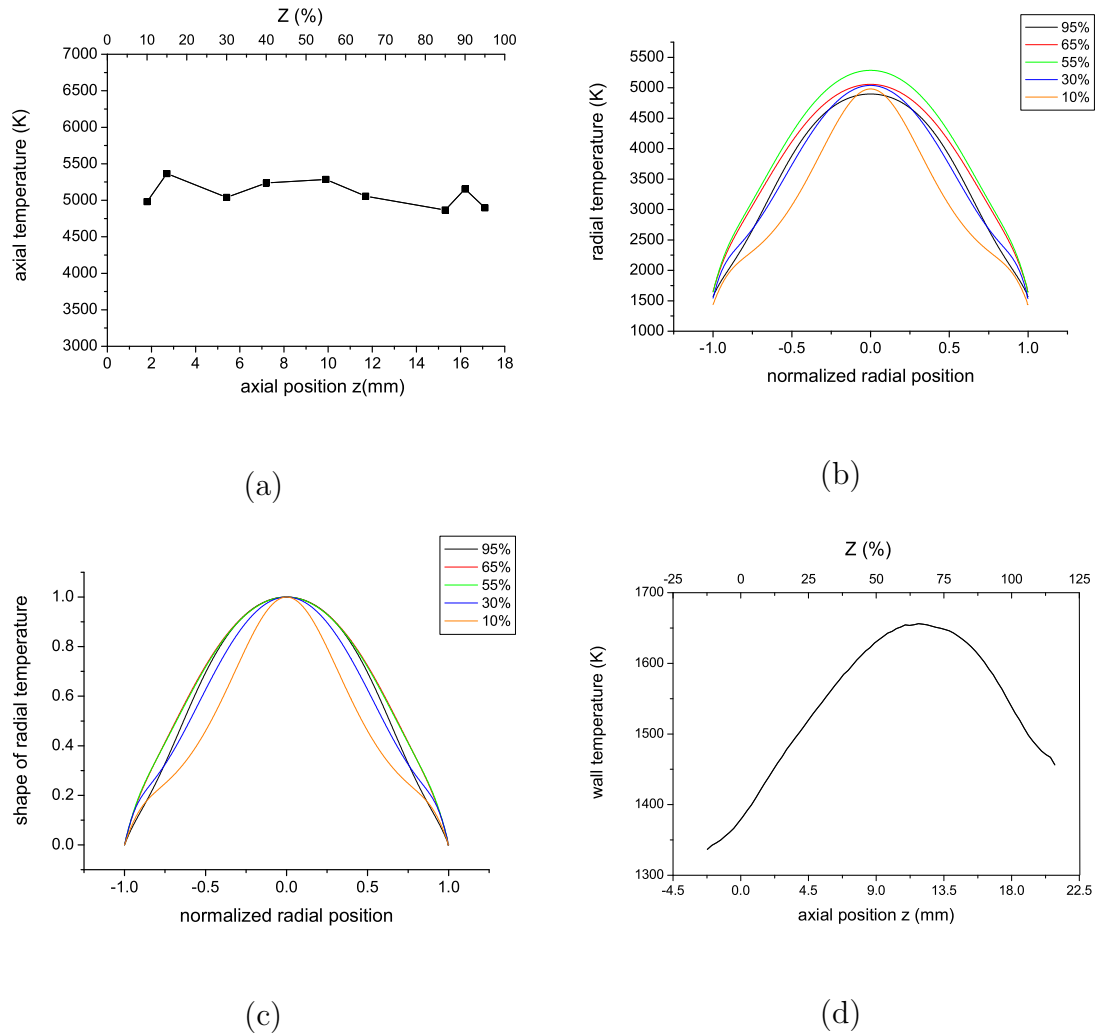
Figure 5.4: *(a): The axial temperature profile of lamp 3-3 ($Hg+NaI/CeI_3$) operated with a 70 W square-wave ballast of 81 Hz. (b): The radial temperature profile of lamp 3-3 for different axial positions. (c): The normalized temperature profile of lamp 3-3 as a function of radial position for different axial positions. (d): The wall temperature of lamp 3-3.*
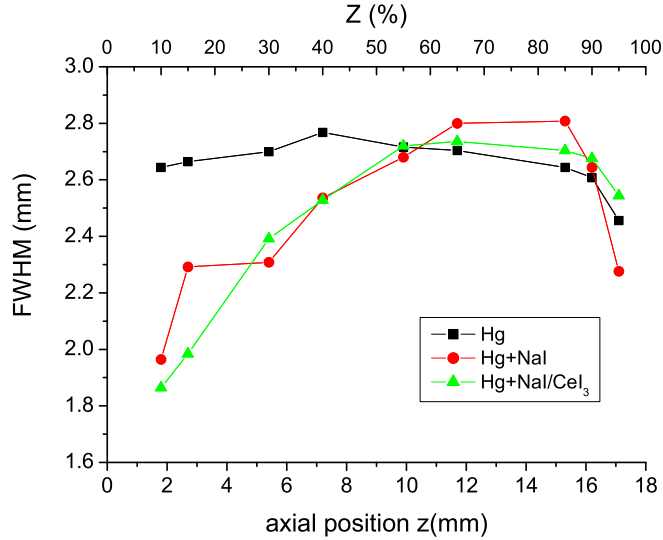
Figure 5.5: The FWHM in mm of the temperature profile as function of the axial position (z=0 is chosen at the tip of the bottom electrode) for three lamps, i.e. type 3-1(pure Hg), type 3-2(Hg+NaI) and type 3-3 (Hg+NaI/CeI$_3$). These three lamps have the same geometry but different fillings. They are all operated at 70 W with a square-wave ballast of 81 Hz.

3-3(Hg+NaI/CeI$_3$) is larger than both that of the pure Hg case and the single salt(NaI) case, especially at the bottom of the lamp.

In order to make the study of the influence of the additive chemistry on the radial temperature more quantitative we study the $Z-$dependence of the FWHM by means of Fig. 5.5, where the three lamps of the same geometry but with different lamp fillings are compared to each other.

This figure shows that the presence of the metal halide has a large influence on the temperature profile, especially in the lower part of the lamp. The temperature profile of lamp 3-3 with salt-mixture NaI/CeI$_3$ is more constricted than that of lamp 3-2 with a single salt(NaI), and the difference with lamp 3-1 (pure Hg) is even larger, especially in the lower part of the lamp. This indicates a demixing of the salt additives along the axial direction. It also indicates that the presence of the efficient radiator Ce in the lower part of the lamp leads to an additional constriction. One should realize that the atomic Ce-system has many optically thin lines so that the enhanced emission of radiation will lead to additional cooling. This leads to constriction of the discharge provided that the averaged upper level energy of the radiation transitions is low as compared to the effective ionization energy in the plasma [22]. At higher axial positions, the Ce elemental density is lower and Na becomes relatively more dominant. Therefore the FWHM of the gas temperature of the

(a)

(b)

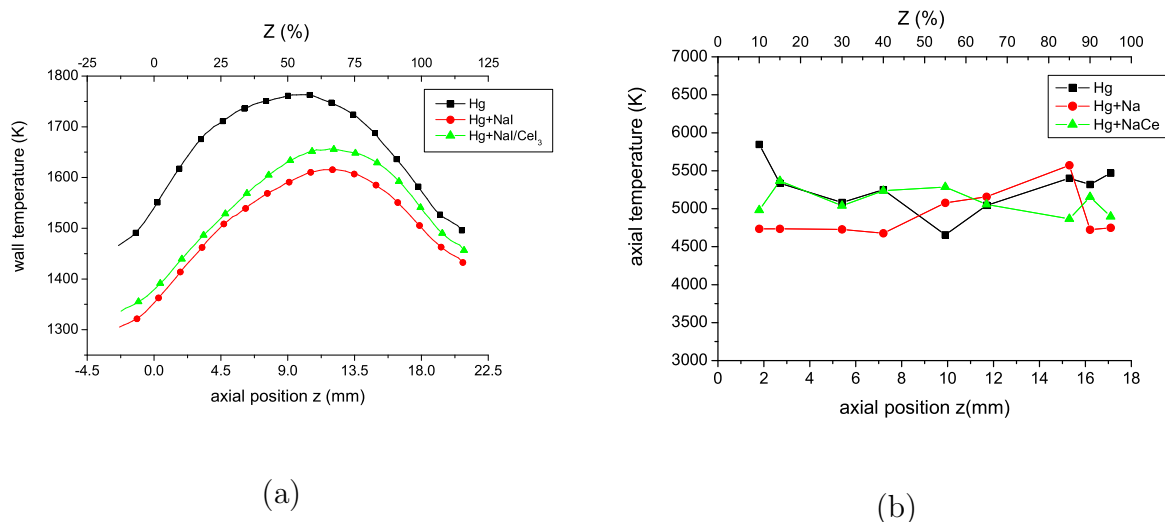*Figure 5.6:* **(a)** *Comparison of the wall temperature of three lamps (type 3-1, 3-2 and 3-3) as a function of the axial position.* **(b)**: *Comparison of the axis temperature of three lamps (type 3-1, 3-2 and 3-3) as function of axial position.*

NaI/CeI_3 lamp approaches that of the single salt(NaI) lamp. At about the middle of the lamp (55% of the arc length from the bottom electrode), the width of the temperature of all the three lamps are the same. This points towards the fact that mainly Hg is left at the top of the lamp. This phenomenon is well-known from the spectral studies and can be related to the fact that due to demixing and therefore depletion of the salt at the top, the lamp is burning on Hg, meaning that the temperature profile is determined by Hg solely. Thus, the presence of the salt (NaI and/or CeI_3) mainly influences the temperature profile near the bottom electrode. It makes the arc more constricted in the region below the axial position of $Z = 50\%$ from the bottom electrode.

Additional insight is obtained by comparing the axis and wall temperatures of these three lamps with each other. This is done in Fig. 5.6 where T_W and T_0 are shown as a function of axial position. It shows that the presence of the metal halides changes not only the center temperature but also the wall temperature. The axis temperature of lamp 3-2(Hg+NaI) is lower than that of lamp 3-1(pure Hg) in the lower part of the lamp. In contrast there is not much difference between the axis temperature of lamp 3-3(Hg+NaI/CeI$_3$) and that of lamp 3-1(pure Hg). The wall temperature is always relatively low near the top or bottom of the lamp since the end constructions provide an additional cooling to the burner vessel. For the pure Hg case, the maximum wall temperature is located at about $Z = 50\%$. However for the lamp containing salt additives, the maximum wall temperature is shifted upwards since the salt additives are dominant near the bottom electrode and provide an extra radiation cooling to the plasma in the lower region.

5.4 XRA measurements on Thomson lamps: comparing different Hg doses

In this section, we will present the XRA results on two high pressure Hg lamps: lamp "2-1" and lamp "2-2" (see table 1.1). They have the same geometry (inner diameter of 18 mm, arc length of 39 mm, wall thickness of 1mm) but different Hg filling. Lamp 2-1 is filled with 15 mg Hg and lamp 2-2 with 50 mg Hg.

These two lamps were operating at 200 W with a square-wave ballast. The experimental settings are shown in table 5.2. Since these two lamps were specially made for Thomson Scattering (TS) measurements, the outer bulb was removed. In order to retain the monochromaticity of the X-ray beam, a quartz plate with a thickness of 2.3 mm was placed in front of the X-ray source as a filter to block the lower energy part of the spectrum.

As said these two lamps were also used for TS measurements to determine the electron temperature and electron density. A comparison of the results from XRA and TS measurements is presented and discussed in chapter 7. This study was done to get insight on the validity of the LTE assumption that is often used for this type of high pressure Hg discharges.

5.4.1 Determination of the optimum μ value for the least square fitting

In Appendix C, a description is given of the Tikhonov regularization method that was used to ensure the stability of the Abel inversion fitting procedure. In this section, it is shown how the optical value of the regularization parameter μ was established.

The resulting temperature profiles (after Abel inversion) at the same axial position, but with different values of the Tikhonov regularization parameter μ are given in Fig. 5.7 showing that the temperature value is quite stable and independent of μ as long as μ is not too large or too small. When $1 \times 10^{-6} \leq \mu \leq 1 \times 10^{-4}$, the temperature profiles for different μ values are quite similar and the difference of the axis temperature is within 1%. At higher μ values such as $\mu > 1 \times 10^{-2}$, the reconstruction errors become dominant. For very low μ value such as $\mu = 1 \times 10^{-8}$, the noise propagation error becomes dominant and oscillations are observed (see Fig. 5.7(a)). Therefore the optimum μ value for the least square fitting of type 2 lamps is chosen at 1×10^{-4}.

5.4.2 Results of XRA measurements

For lamp 2-1 (15 mg Hg filling), 20 images were taken for both the lamp-on and lamp-off situations. Each image was taken with an exposure time of 67s. The total measurements were done within 100 minutes. For lamp 2-2 (50 mg Hg filling), 40 images were taken for the on- and off-situation. The absolute distribution of gas temperature profiles were obtained from the XRA measurement and the wall temperature measurement. The results
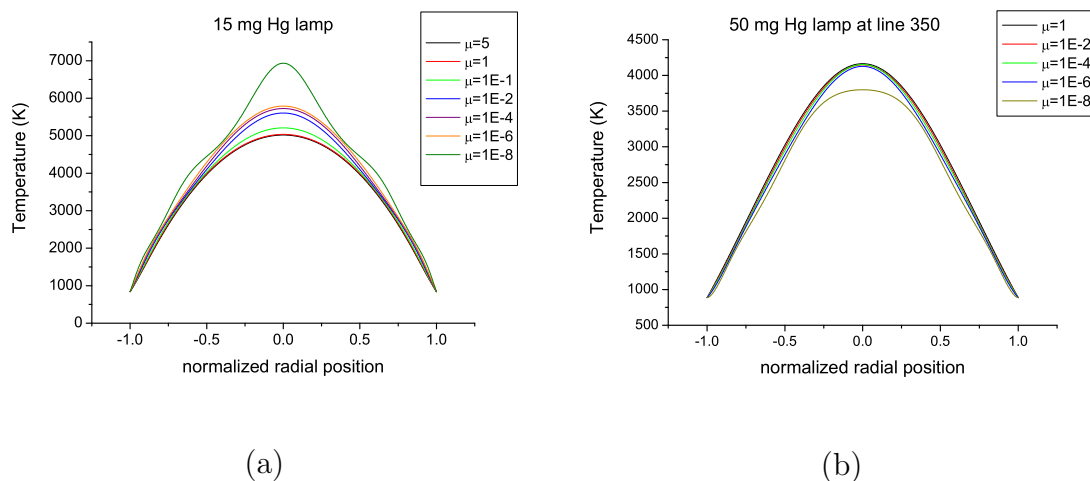
Figure 5.7: *Temperature profiles of a type 2-1 lamp (15 mg Hg) and a type 2-2 lamp (50 mg Hg) operating at 200 W as found by fitting with different μ values.*

of the measurement on these two Hg lamps are given in Fig. 5.8.

It shows that the axis temperature for lamp 2-1 (15 mg Hg) at $z = 60\%L$ equals $T_0 = 5726$ K whereas the T_0 value of lamp 2-2 (50 mg Hg) at $z = 65\%L$ was found to be substantially lower, namely 4153 K. Since the lateral profile of the 15 mg lamp has a little asymmetry, it will introduce an error in the reconstructed temperature profile. Therefore the temperature results of the 50 mg lamp are believed to be more reliable.

An interesting check of the validity of the experiments involves calculating the absolute Hg density in the HID lamps provided that the X-ray absorption cross-section is known. This cross-section can be found by means of the oven-lamp experiment. If we assume that the mean X-ray photon energy which is absorbed by Hg is about 17.6 keV, then the absorption cross-section of Hg is found to be $3.58 \times 10^{-24} \, \mathrm{m^2}$. The absolute density profile of Hg can then be obtained from the Abel inversion procedure. The Hg density is about $2.2 \times 10^{24} \, \mathrm{m^{-3}}$ at the center and $1.0 \times 10^{25} \, \mathrm{m^{-3}}$ at the wall for the 50 mg lamp. For the 15 mg lamp, it is found to be $1.4 \times 10^{24} \, \mathrm{m^{-3}}$ at the center and 9.5×10^{24} at the wall. From the Hg dose, the volume-averaged density can be calculated provided that Hg is unsaturated . It is about $4.5 \times 10^{24} \, \mathrm{m^{-3}}$ for the 15 mg lamp and $1.5 \times 10^{25} \, \mathrm{m^{-3}}$ for the 50 mg lamp. From this calculation, we can deduce that the lamp with 50 mg Hg dose is saturated since the maximum density at the wall is already lower than the calculated average density value. From the absolute Hg density profile and absolute gas temperature profile, the pressure is found to be 1.1 bar for the 15 mg lamp and 1.26 bar for the 50 mg lamp. From the wall temperature measurement, the cold spot temperature is found to be 640 K for which the saturation pressure of Hg is about 1.26 bar. This is in agreement with the XRA result. Therefore the Hg vapor is saturated for the 50 mg Hg lamp operating at 200 W.
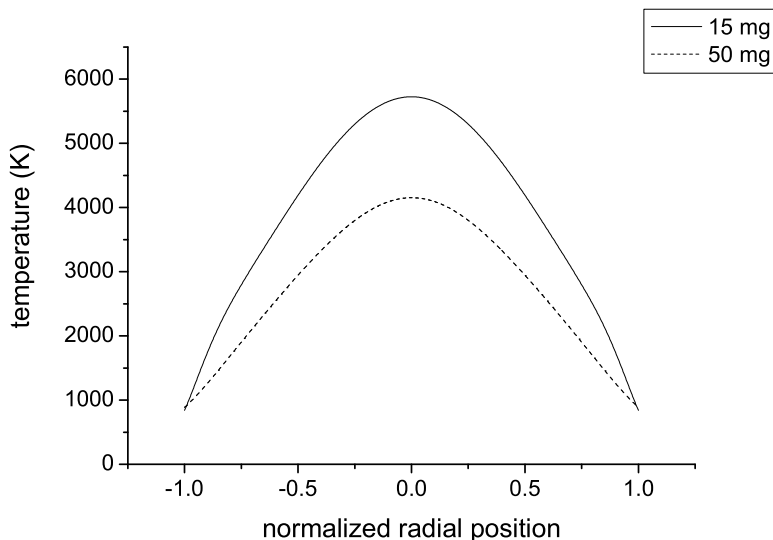
Figure 5.8: Comparison of the temperature profile between type 2-1 (15 mg of Hg) and type 2-2 (50 mg of Hg) lamps at the same axial position (25.5 mm from the bottom electrode) operating at the same power 200W with square-wave ballast.

5.5 Low Hg content metal halide lamp

Until now the XRA methods were successfully applied to HID lamps with relatively high Hg pressures or large diameters. Now a lamp with low pressure and small diameter was selected in order to determine the validity region of the XRA method.

To that end a special lamp was constructed, hereafter denoted as "type 4" lamp. From table 5.1, we can see that for this type of lamp, the optical depth is about as low as it gets for any HID lamp. Type 4 lamp has a Hg pressure of around 1 bar and a diameter of 4 mm. Therefore, the line-integrated absorption signal of Hg is very small.

A series of experiments were done on this lamp for four different power settings: 70 W, 90 W, 120 W and 142 W. The acceleration voltage of the X-ray generator was 25 kV and the current was 35 mA. Initially 50 images were taken for the on- and off-situation respectively. The measurement time for each power setting is around 2 hours. Since the absorption signal of Hg is very weak in this lamp, the noise in the data is quite high. After accumulation of these 50 images and binning over 40 rows, the noise in the center of the lateral profile is about 6%. To increase the signal to noise ratio even further, more images are required.
Advantage can be gained from our image processing procedure which is based on the treatment of pairs of lamp-on and lamp-off images for which the on-profile is subsequently
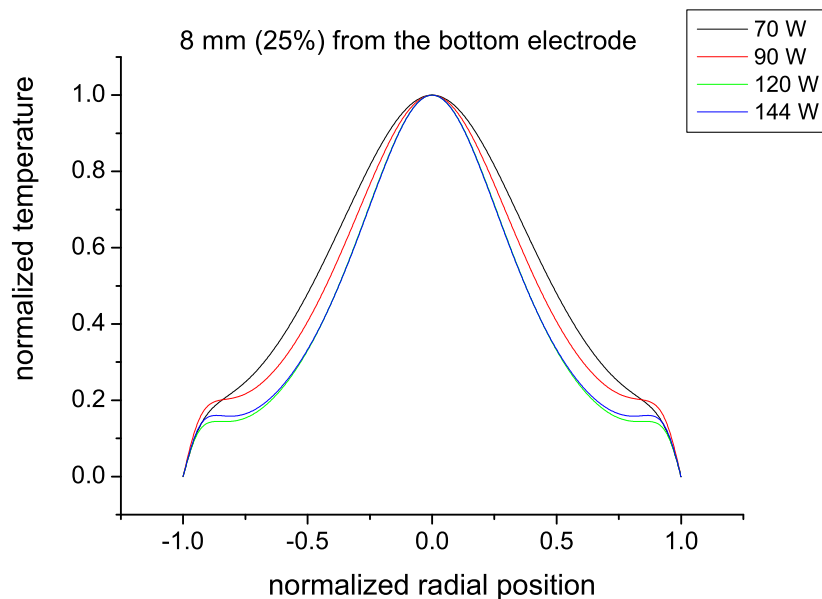
Figure 5.9: Normalized temperature profiles of a type-4 lamp for different power settings, 70 W, 90 W, 120 W and 144 W. The burner of the lamp is made of PCA with a wall thickness of 0.5 mm. The burner has an inner diameter of 4 mm, arc length of 32 mm. The lamp is filled with 0.6 mg Hg and the salt mixture NaI/CeI$_3$ (cf.table 5.1)

fitted on top of the off-profile. The pairs of images can be taken on different days and accumulated. For example, if in a 3-day-experiment 150 pairs of images for on and off-situations are taken on each day, thus in total 450 pairs of images, the signal to noise ratio will be then 3 times better than the situation mentioned above (50 images). In this way the noise will be reduced to 2% in the center of the lateral profile. For this type 4 lamp, the wall temperature was not measured. Therefore only the normalized temperature profile was obtained and is given in Fig. 5.9 for different power settings. This figure shows that the temperature profile becomes more constricted when the lamp power is increased.

To conclude, it is still possible to measure a HID lamp with a low Hg dose and a small diameter, with τ value as low as 0.05. However, in order to obtain more accurate results, more images need to be taken and therefore the measurement time involved is a few days.

5.6   XRA measurement on a ARGES lamp

ARGES, an acronym for **A**tomic densities measured **R**adially in metal halide lamps under micro-**G**ravity conditions with **E**mission and absorption **S**pectroscopy, is a collaboration between Philips CDL and Eindhoven University of Technology(TU/e). The aim of the

ARGES project is to understand two phenomena (demixing and helical instabilities) occurring in certain types of metal halide lamps under different gravity conditions. Both demixing and helical instabilities are strongly influenced by gravity. The ARGES lamp (filled with 10 mg Hg and 4 mg DyI_3 salt) is designed such that the axial demixing is most pronounced at the normal operating conditions of $1g$ ($= 9.8\,\mathrm{m/s^2}$). Therefore it was decided to study this lamp with XRA so that the gas temperature profile is known.

5.6.1 Comparison with absolute line intensity measurement

The wall temperature as a function of the axial position was obtained by an infrared pyrometer measurement (see Fig. 5.10(d)). The absolute temperature profiles as a function of the radial position are shown in Fig. 5.10(b) for different axial positions. The normalized temperature profiles at different axial positions are shown in Fig. 5.10(c).

From Fig. 5.10(a), we can see that the maximum axis temperature is around 5050 K at 38% of the arc length from the bottom electrode and that the temperature decreases approaching the top or the bottom. Another interesting result is that the temperature profile is strongly constricted at the bottom and that this degree of constriction decreases for increasing Z-values. The top electrode region has the broadest temperature profile. This means that the plasma at the top of the lamp is not much different from a pure Hg discharge which makes the temperature profile broadened. The axis temperatures were also determined from the Atomic State Distribution Function (ASDF) plot of atomic Dy. That was done by means of absolute line intensity measurement as reported by T. Nimalasuriya [23]. This procedure yields a temperature value around 5524 K at about 1.7 mm (10%) from the bottom electrode. However the axis temperature determined from XRA measurement is about 4239 K which is 1285 K (23%) lower! This means that the temperature determined from ASDF, presumably the electron temperature T_e, is higher than the temperature (T_g) from XRA. This might indicate that the LTE condition is not valid in this lamp. Another interesting result is that the FWHM plot in Fig. 5.11(b) shows that the temperature shape becomes the same when the axial position is above 55% distance from the bottom electrode. This can also be clarified in the study of laser absorption spectroscopy by A.J. Flikweert [24] which is shown in Fig. 5.11(a).

It shows that the Dy column density decreases about factor of 5 at axial position of about 10 mm (59%) from the bottom electrode. This is in agreement with the FWHM found in XRA measurement (see Fig. 5.11(b)).

5.7 Conclusion

X-ray absorption experiments have been successfully applied to different types of HID lamps. Even for the worst case situation (type 4), related to a lamp with a low Hg pressure (1.7 bar) and small diameter (4 mm), it is demonstrated that it is possible to use the XRA method to determine the gas temperature. Therefore this technique can in principle be applied to measure the gas temperature for the whole family of HID lamps. It can also

(a)

(b)

(c)

(d)
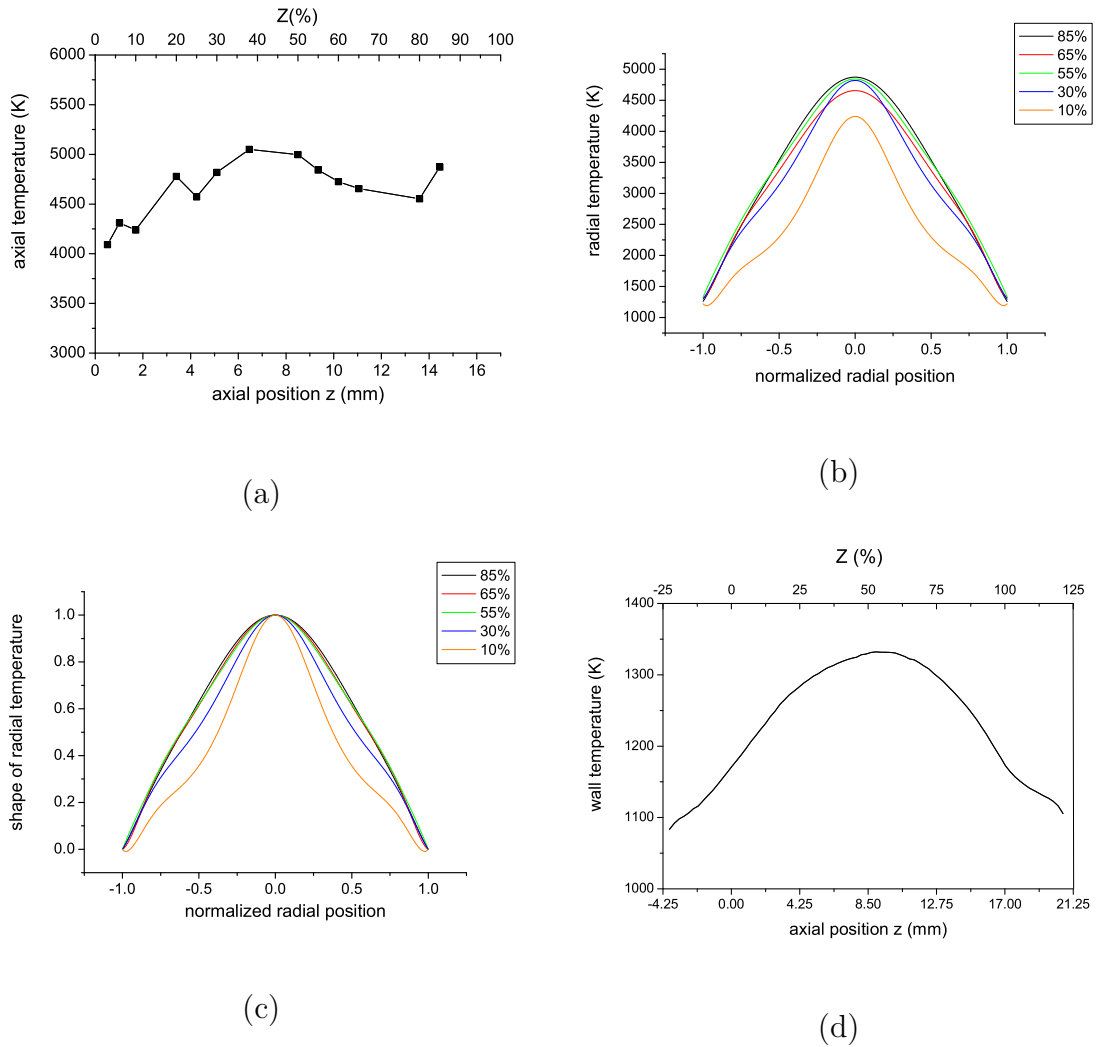
Figure 5.10: **(a)**: The axial center temperature of type 1 lamp (DyI$_3$ and 10 mg of Hg) operating at 142 W as function of axial position. **(b)**: The radial temperature profile of type 1 lamp operating at 142 W at different axial positions.**(c)**: The normalized radial temperature profile at different axial positions. **(d)**: The wall temperature of type 1 lamp.
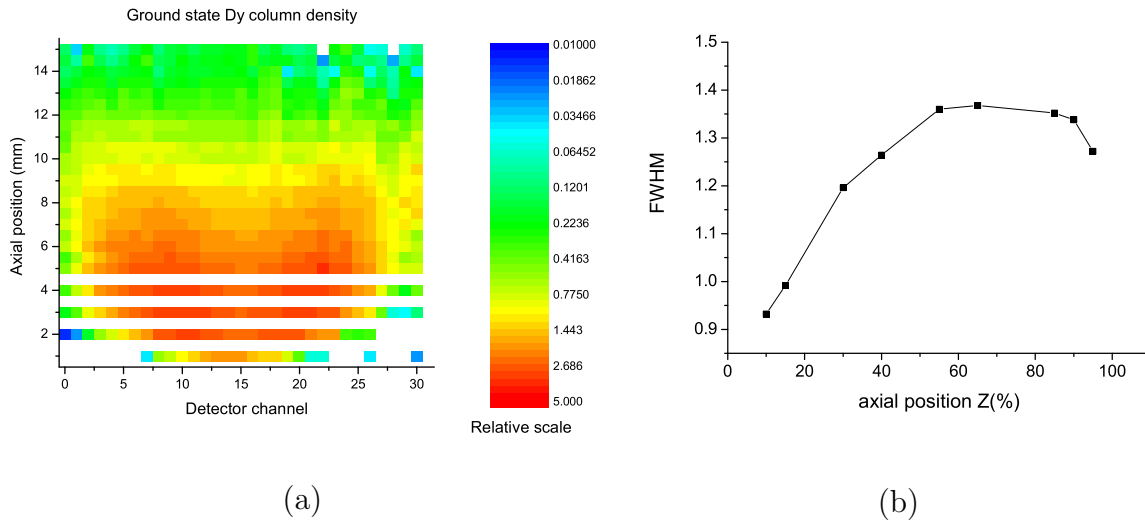
Figure 5.11: **(a)**A 2D map of the column density of the ground state Dy measured from laser absorption measurement. The horizontal axis is the radial direction and the vertical axis is the axial direction.**(b)**The FWHM of the temperature profile as function of the axial position for type 1 lamp.

be applied to other buffer gases than Hg, such as Xe or Zn provided that the buffer gas pressure is large enough. The X-ray attenuation cross-section of (Hg-free) Xe is about 21% of that of Hg at the X-ray energy of 17.6 keV. Therefore the total optical depth of Xe for the X-ray beam is about 5 times smaller than in the case of Hg for the same geometry and the same density of buffer gas. In the case of Zn, the X-ray attenuation cross-section of Zn is about 6.5 times smaller than that of Hg. This means that for the same geometry lamp, the pressure of Zn should be at least 6.5 times higher than the Hg case. Therefore X-ray absorption technique can be applied to (Hg-free) HID lamp (with Xe or Zn as the buffer gas) successfully if the buffer gas pressure is at least 9 bar for Xe and 11 bar for Zn for the same geometry ($d = 4$ mm) as 'type 4' lamp.

Some recommendations for this technique are given below:

1. To improve the accuracy of the result, the lamp design should be chosen such that the wall thickness of the burner is as small as possible.

2. A higher effective energy is favorable for the Hg contrast but in that case a monochromatic source at higher energy is required. Otherwise, a good calibration method is needed, especially for the burner wall region.

3. To increase the accuracy, multiple pairs of images are required.

4. The lamp design, construction and operation should be done with great care. For instance, the electrode design and the power of the lamp should be such that the arc

is symmetric (a 'light' electrode design which favors diffuse electrode attachment is therefore better) since the Abel-inversion cannot be applied to asymmetric profiles.

Chapter 6

Thomson scattering measurements on an Ar DC discharge lamp

Abstract

In the exploration of various active spectroscopical means to get insight in light generating plasmas we follow the route of decreasing photon energy. Chapter 2 was devoted to gamma spectroscopy (employing photons of around 1 MeV), the subsequent chapters 3, 4 and 5 were devoted to X-ray spectroscopy (and hν around 20 keV). Here we will discuss the application of photons in the visible range (around 2 eV). This chapter is the first one of the two studies on Thomson scattering (TS), i.e. the scattering of photons on the free electrons in a plasma by which the electron density and temperature can be determined. Chapter 7 deals with TS on mercury lamps and here we will discuss its application to a model lamp in argon.

Thomson scattering (TS) experiments have been performed in the region near the electrodes of a DC powered model lamp filled with 1-2 bar argon gas. In order to suppress the false stray light and Rayleigh scattered photons, a triple grating spectrograph (TGS) was used. In this way the electron density and electron temperature could be measured in the near electrode region for different arc currents. In order to get the electron density and electron temperature out of the TS spectrum, both coherent and incoherent Thomson scattering fitting procedures were used for the data processing. It was found that the radial profile of the electron temperature is more or less flat in the anode region with a value of about 1 eV. The electron density increases with arc current and is in the order of $10^{21} \, \mathrm{m}^{-3}$. From the result, we can see that the investigated plasma regions are not in LTE in the sense that locally the rate of ionization is much larger than that of recombination.

6.1 Introduction

To fully understand the plasma inside a gas discharge lamp, it is important to measure as many plasma parameters as possible. Among these parameters, the electron density and electron temperature play an important role. The reason is that the electron gas is the plasma component which directly receives energy from the external electric field. By means of elastic and inelastic collisions, this energy is used for the heating of heavy particles and the excitation and ionization of molecules, atoms and ions. The inelastic processes will finally lead to light production and the creation of electron-ion pairs. The most straightforward way to measure n_e and T_e is by means of Thomson Scattering (TS). Especially under relatively low n_e conditions, the results are easy to interpret. The frequency distribution of the scattered photons gives insight in the electron energy distribution function (and therefore T_e), whereas the number of scattered photons gives the electron density(n_e). However, there are severe limitations related to Thomson scattering. The cross section of TS is extremely low which implies that the TS photons are easily lost in the false stray light which is generated by the reflection of the laser beam on wall or electrode material. Especially for lamps, this is a severe problem. To reduce the role of false stray light, we will employ the triple grating spectrograph (TGS) setup as described in [25] where it was used to measure n_e and T_e in a QL lamp [26]. Such a lamp burns on 0.95 Pa mercury in a background of 133 Pa Argon. The same setup was also used for the study of a capacitively coupled He RF discharge [27] which was almost completely encapsulated by quartz. Although it was found that the TGS gives a substantial reduction of stray light, one still had to avoid the interaction of the laser with wall material in the direct neighborhood of the detection volume. Therefore the QL lamp was extended with two side "ears" as described in [26].

In the present study we continue our route from academic to more technological plasmas and apply the TS system to study the plasma properties in regions close to the electrodes. Therefore we selected the model lamp as constructed in Bochum. In the model lamp electrodes made of pure or doped tungsten can be operated under well-defined and reproducible conditions. It was developed with the intention to obtain experimental data to verify models describing the electrodes and the near-electrode regions in high intensity discharge lamps (HID lamps). For this purpose the operating parameters should be as close to real lamps as possible. But the model lamp also has to overcome the problems occurring with measurements at real lamps. For example, in real lamps the strong plasma radiation as well as the small and complex geometry make optical investigations of the electrodes exceptionally difficult. Changing various parameters like pressure, arc current and arc length, electrode material and geometry, is essential for the understanding of modelling results which is also difficult to achieve with real lamps. The main advantage of the model lamp is that many parameters can be changed easily. However, the real lamp is filled with vapors of metals or metal halides, whereas the model lamp is operated with pure noble gases such as argon and xenon so that the plasma radiation is much lower than the real lamp. This makes optical investigations of the electrodes much easier. In addition, important data for modelling are known for these gases, e.g. cross-sections for fundamental

plasma processes. The model lamp is described in more detail in section 2. Just as in the case of the QL lamp, we used extension tubes to place the laser–glass interaction far away from the detection volume in order to avoid that the focused laser beam would damage the glass wall (see Fig. 6.1). The model lamp was filled with 1-2 bar argon and due to this relatively high pressure, the electron density was found to be large, especially in front of the electrodes. This implies that collective scattering becomes important so that the determination of n_e and T_e is less straightforward than in the case of the low electron density plasmas we used in the past. Therefore attention must be paid to the interpretation of the TS spectrum. We will discuss how the values of n_e and T_e can be deduced for the plasma conditions close to the electrodes and whether the plasma is in LTE.

This chapter is organized as follows. In section 2 (Experimental arrangement), we will describe the model lamp geometry and the experimental setup. Extensive attention will be drawn to the TGS system which is the crucial part for recording the TS spectrum. In section 3, attention will be paid to the fitting functions for both collective and non-collective TS spectra. In sections 4 and 5, the experimental results and discussions will be given. Finally, conclusions will be drawn in section 6.

6.2   Experimental arrangement

6.2.1   The model lamp

The model lamp was designed in the university of Bochum [28–32]with the aim to study the behavior of electrodes and interaction between electrodes and plasma in order to verify models describing the near-electrode regions of HID lamps [33–37]. The gas filling of the model lamp can be adjusted but until now mainly consists of inert gasses such as Ar or Xe. It was designed such that many parameters can be easily changed, e.g. the arc length, the electrode positions, filling gas type and pressure. Electrodes made of pure or doped tungsten with different shapes can be inserted. The model lamp can be operated with DC or AC currents between 0.4A ... 10A. Furthermore the design of the quartz discharge tube can be adopted to special measurement requirements. Thus, the model lamp allows for high accessibility, flexibility and reproducibility for quantitative measurements.

The schematic drawing of the model lamp as used for Thomson scattering is shown in Fig. 6.1. In our experiment, we use a discharge tube with inner diameter of 9 mm and the arc length is set to 20 mm. The lamp is filled with pure argon at a pressure in the range of 1–2 bar. There are two horizontal extension tubes with Brewster angle connected to the mid plane of the tube in order to reduce the amount of the false stray light and to prevent that the high intensity in the region near the focus will damage the quartz wall. At each side of the lamp tube, there is a small hole which allows the laser beam to pass through the plasma without damaging the quartz tube and also to reduce the generation of false stray light at the vicinity of the detection volume. The laser beam enters the quartz discharge tube through a Brewster window far from the focal volume, focuses at the plasma inside the lamp tube, and leaves the plasma through the hole on the other side of the lamp
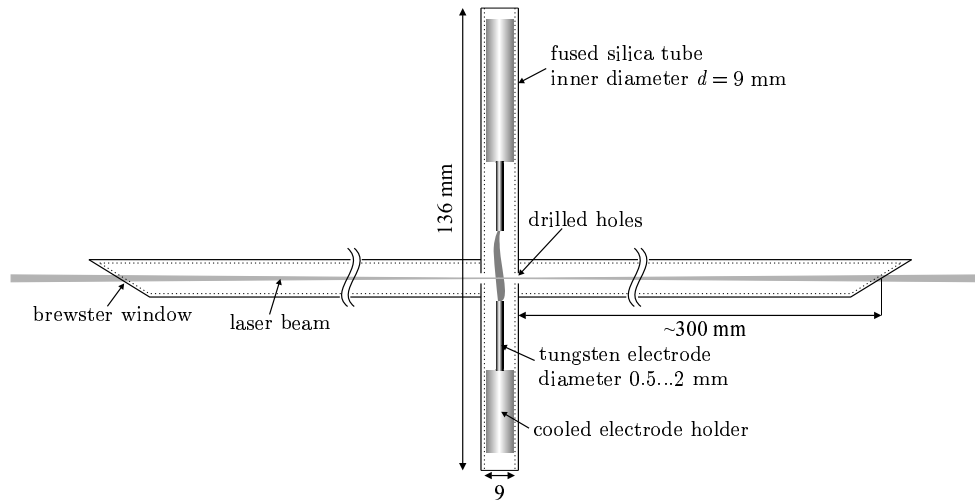
Figure 6.1: Schematic drawing of the model lamp. The lamp is burning vertically. It has an inner diameter of 9 mm, and the adjustable distance between the electrodes is set at 20 mm. The lamp is filled with Ar by a pressure control device at 1–2 bar. There are two horizontal extension tubes connected to the mid plane of the tube in order to reduce the amount of the false stray light. In our experiment, the position of the electrodes is chosen such that the cathode is at the top and anode is at the bottom.

tube.Via the Brewster window, it finally ends in a beam-dump.

6.2.2   Experimental setup

A Triple Grating Spectrograph(TGS) is used to detect the Thomson scattering signal and to offer an excellent rejection of false stray light and Rayleigh scattered photons in the Thomson spectrum.

The aim of the TGS is to get spectral information for several positions along the plasma-beam interaction region. Therefore the detection system must be two-dimensional, one dimension for the position and the other for the wavelength. Since the dispersion by the gratings is done in the horizontal direction, the vertical direction will be used for the spatial information. However, the laser beam is horizontal so that a 90° image rotator is needed. An important role is played by the notch filter which is used to reduce the stray light and Rayleigh scattered photons. It consists of the first two spectrographs in subtractive configuration forming the Double Grating Filter (DGF). Finally the third grating is used for the dispersion and the two-dimensional iCCD is used to record the spectrum both spatially and spectrally.

The experimental setup is shown in Fig. 6.2. A frequency doubled Nd:YAG laser produces 100 mJ, 7 ns laser pulses at a wavelength of $\lambda_i = 532\,\text{nm}$. The laser beam is focused by a plano-convex lens ($f = 1$ m) to a diameter of approximately 200 μm in the plasma where Thomson scattering takes place. The laser beam leaves the plasma through a Brew-
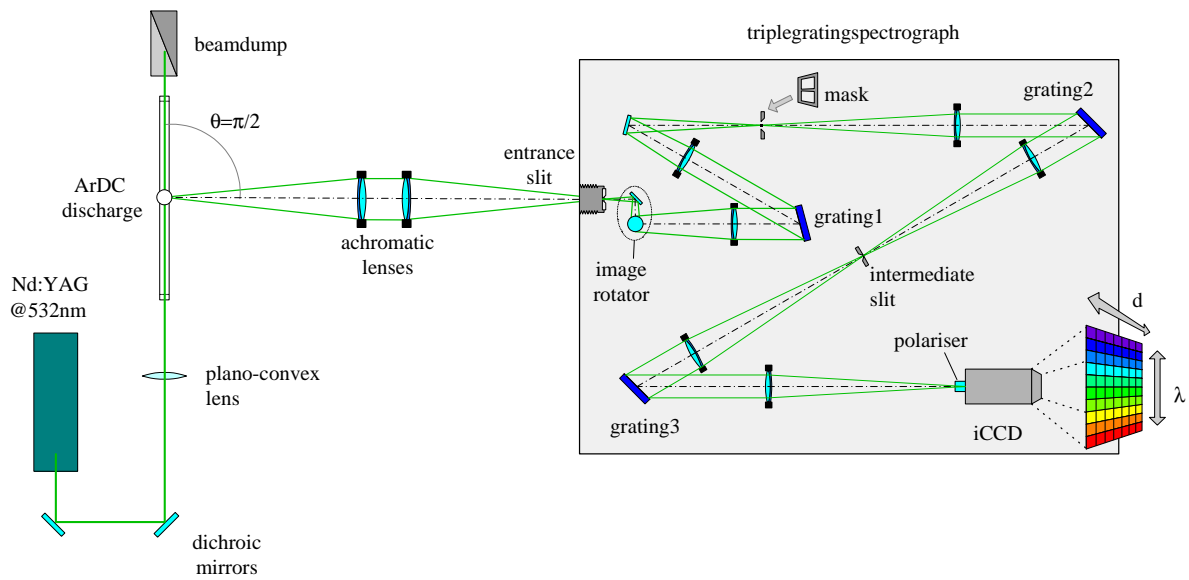
Figure 6.2: The experimental system for Thomson scattering. A frequency doubled laser beam generated by a Nd:YAG crystal is scattered by electrons in the plasma. Scattered light is collected by two achromatic doublet lenses and dispersed by a triple grating spectrograph. The first two gratings and the mask in between serve as a notch filter to suppress stray light. An intensified CCD camera records the scattering spectrum.

ster window and finally reaches the beam dump. Scattered photons are collected at 90° by a pair of achromatic doublet lenses and imaged onto the entrance slit of the Triple Grating Spectrograph (TGS). The signal which enters the entrance slit of the TGS is first rotated to vertical direction by the image rotator and is subsequently filtered by a notch filter (the first two gratings plus the mask in between) to reduce the stray light. After that it is dispersed by the third grating and imaged onto a two-dimensional iCCD camera.

In the experimental setup, several measures are taken to reduce the stray light and plasma background radiation. Firstly, the scattering angle of the system is 90° and the laser beam is polarized perpendicular to the scattering plane so that only the scattered radiation with the same polarization direction will be detected, i.e. the partially unpolarized light from the plasma and background will be reduced. Secondly, the intensity of the plasma radiation can also be reduced by shortening the gate time such that only during the laser pulse the iCCD is open to record the signal. The combination of linear polarized laser beam, the extension tubes with Brewster angle , the TGS and the short gate time helps to suppress stray light and plasma background light significantly so we can get a very good Thomson scattering signal for this model lamp.

Figure 6.3: The scattering geometry. Here θ is the scattering angle between the incident and the scattered wave vectors $\mathbf{k}_i$ and $\mathbf{k}_s$, and ϕ the angle between the inci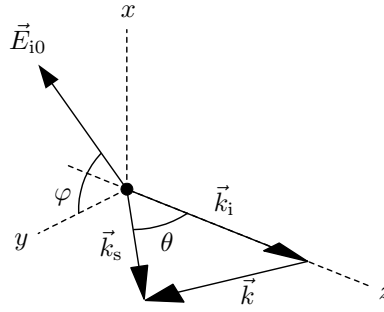dent-scattering plane and the polarization of the laser beam. In our experimental setup, $\theta = 90°$ and $\phi = 90°$.

6.3   Thomson scattering

Thomson scattering i.e. the scattering of photons by free electrons, can be used to measure the electron density and the electron energy distribution from which the electron temperature can be derived. In Fig. 6.3, a diagram is given of the wave vectors of the scattering process, most important is the so-called scattering vector $\mathbf{k}$ which equals

$$\mathbf{k} \equiv \mathbf{k}_s - \mathbf{k}_i, \tag{6.1}$$

where $\mathbf{k}_s$ and $\mathbf{k}_i$ are the wave vectors of the scattered and incident light respectively.

The equation which describes how the intensity of the scattered photons $P_s(\omega)$ at a certain frequency ω depends on the solid angle Ω is given by

$$\frac{dP_s(\omega)}{d\Omega} = \frac{d\sigma}{d\Omega} P_L L_s n_e S(\mathbf{k}, \omega), \tag{6.2}$$

where P_L the incident laser intensity, L_s the length over which scattered light is collected and $\frac{d\sigma}{d\Omega}$ the differential cross-section for the single electron scattering process; The dynamic form factor $S(\mathbf{k}, \omega)$, which gives the frequency shift resulting from the electron motion as well as the effect of correlations between the electrons, describes the spectral distribution of the TS spectrum as function of ω. When the ratio of T_e/T_i is close to unity, the dependence of Thomson scattered photons on the frequency is given by the Salpeter approximation [38, 39], which can be written as the sum of two terms: an electron spectrum whose frequency scale is kv_e, the characteristic Doppler shift at the electron thermal speed, and an ion spectrum whose frequency scale is kv_i, the characteristic Doppler shift at the ion thermal speed; v_e and v_i are the electron and ion mean thermal velocity respectively which are defined as

$$v_e = \left(\frac{2\pi k T_e}{m_e} \right)^{1/2}, \quad v_i = \left(\frac{2\pi k T_i}{m_i} \right)^{1/2}. \tag{6.3}$$

This leads to the following structure of the form factor

$$S(\mathbf{k}, \omega)\mathrm{d}\omega = \Gamma_\alpha(x_e)\mathrm{d}x_e + Z\left(\frac{\alpha^2}{1+\alpha^2}\right)^2 \Gamma_\beta(x_i)\mathrm{d}x_i, \tag{6.4}$$

where $\Gamma_\alpha(x_e)$ and $\Gamma_\beta(x_i)$ are the expression of the electron and ion contribution defined as

$$\Gamma_\alpha(x_e) = \frac{\pi^{-1/2}\mathrm{e}^{-x_e^2}}{|1 + \alpha^2 W(x_e)|^2};$$

$$\Gamma_\beta(x_i) = \frac{\pi^{-1/2}\mathrm{e}^{-x_i^2}}{|1 + \beta^2 W(x_i)|^2}.$$

Here β and W are defined as

$$\beta^2 = Z\left(\frac{\alpha^2}{1+\alpha^2}\right)\frac{T_e}{T_i};$$

$$W(x) = 1 - i\pi^{1/2}x\mathrm{e}^{-x^2} - 2x\mathrm{e}^{-x^2}\int_0^x \mathrm{e}^{p^2}dp.$$

The dimensionless frequency variables x_e and x_i are defined as $x_e = \omega/(kv_e)$ and $x_i = \omega/(kv_i)$.

Depending on the properties of the electron gas, we can distinguish between two extreme situations: non-collective and collective Thomson scattering. The degree of collectiveness depends on the value of scattering parameter α,

$$\alpha \equiv \frac{1}{k\lambda_\mathrm{D}} \approx \frac{1}{4\pi\sin(\theta/2)}\frac{\lambda_\mathrm{i}}{\lambda_\mathrm{D}}, \tag{6.5}$$

where λ_i is the wavelength of incident light, θ the scattering angle and λ_D the Debye length given as

$$\lambda_\mathrm{D} = \sqrt{\frac{\epsilon_0 k_\mathrm{B} T_e}{e^2 n_e}}. \tag{6.6}$$

The dependence of the Thomson scattering shape on the α value is shown in Fig. 6.4.

When $\alpha \ll 1$, the scale of the scattered wave length ($1/k$ scale) is much less than the Debye length and the scattering takes place within the Debye sphere where electrons are randomly distributed. In this case we get a phase-unrelated TS spectrum since the scattered waves by different individual electrons are random in phase. This leads to so-called non-collective Thomson scattering.

When $\alpha \gg 1.0$, collective effects are dominant. Since the scale of scattered wavelength is larger than the Debye length, the motion of the individual electrons as a response to the laser field is no longer uncorrelated so that a more collective behavior becomes manifest. This is denoted by collective Thomson Scattering. In practice, the Debye length can be written as

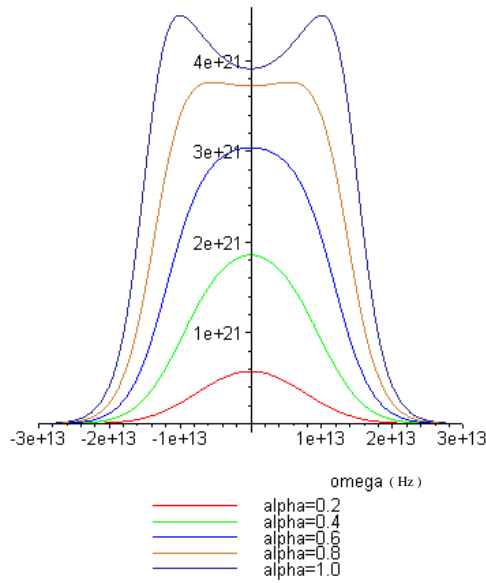$$\lambda_\mathrm{D} = 745[\mathrm{nm}]\sqrt{\frac{\hat{T}_e}{\hat{n}_e}}, \tag{6.7}$$

Figure 6.4: Thomson scattering spectrum (intensity as a function of $\Delta\omega$ (Hz) with respect to the incident laser frequency) at $T_e = 1\,\mathrm{eV}$ for different α value.

where $\hat{T}_e$ is given in eV and $\hat{n}_e$ in $10^{20}\,\mathrm{m}^{-3}$. Thus in our experimental setup, where scattering angle is $90°$ and $\lambda_i = 532\,\mathrm{nm}$, the scattering parameter is given numerically by

$$\alpha_\perp = 0.08\sqrt{\frac{\hat{n}_e}{\hat{T}_e}}. \tag{6.8}$$

Since in this high pressure model lamp, the electron temperature is expected to be more or less invariant at $T_e \approx 1\,\mathrm{eV}$, we see that $\alpha_\perp$ mainly depends on $\sqrt{n_e}$. In the center of the plasma, it is expected that $n_e \approx 10^{22}\,\mathrm{m}^{-3}$, i.e. $\hat{n}_e \approx 10^2 [10^{20}\,\mathrm{m}^{-3}]$, so that we get $\alpha_\perp = 0.8$. Thus the scattering spectrum shape is already quite collective which implies that we can't use a non-collective fitting procedure. However, at the plasma edges, where the electron density is smaller, we may expect lower α values and thus more non-collective scattering. Therefore we have to use a procedure which can deal with both collective and non-collective scattering. In both cases, the measured spectrum is fitted only to the electron contribution of the Salpeter function since the ion contribution is located in the center of the spectrum which is filtered and it is too narrow to be detected by the TGS system.

We start with a description of the fitting procedure for non-collective scattering. Non-collective Thomson scattering is based on the scattering of the photons on individual electrons in a plasma. When a photon is scattered by an electron, the scattered photon frequency has a shift which is proportional to the velocity of the electron in the direction of the scattering vector. When the electrons are in a state of local thermal equilibrium, they have a Maxwellian distribution and the electron velocity distribution has a Gaussian profile. In that case the Thomson scattering spectrum also has a Gaussian profile and

102
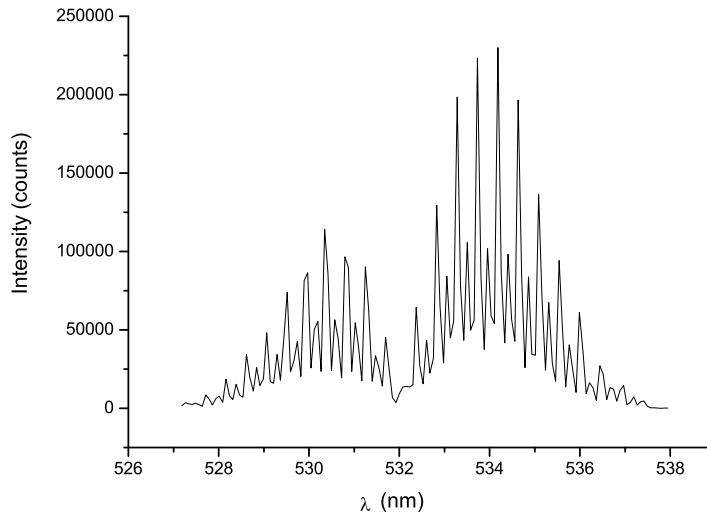
Figure 6.5: A typical Raman spectrum.

the electron temperature can be directly derived from the width of the fitted Gaussian spectrum using the equation

$$T_e = \left[\frac{m_e c^2}{8 k_B \lambda_i^2 \sin^2(\theta/2)} \right] \cdot \Delta\lambda_{1/e}^2. \tag{6.9}$$

Here m_e is the electron rest mass, c the light speed, k_B the Boltzmann constant, and $\Delta\lambda_{1/e}$ the half $1/e$ width of Thomson scattering spectrum which is given in nm. In our experiment, $\theta = 90°$ and $\lambda_i = 532$ nm, so that $T_e = 5238 \cdot \Delta\lambda_{1/e}^2 [\mathrm{K}]$.

By absolute calibration of the laser power with rotational Raman spectrum from nitrogen [25], the electron density is directly proportional to the intensity of the Thomson scattering spectrum and we get

$$n_e = n_{N_2} \cdot \frac{P_{\mathrm{T}}}{P_{RM}} \cdot \Gamma_{RM}, \tag{6.10}$$

where n_{N_2} is the density of nitrogen gas, P_T is the total Thomson scattering intensity, P_{RM} the total Raman scattering intensity and Γ_{RM} the calibration factor for the total cross-section of the rotational Raman spectrum ($\Delta J = \pm 2$) with respect to Thomson scattering. A typical Raman spectrum is given in Fig. 6.5.

For $\alpha \gg 1$, the width of the spectrum is just the distance between two satellite peaks, which is equal to twice of the plasma frequency ($\omega_p = \sqrt{\frac{e^2 n_e}{\epsilon_0 m_e}}$) which gives n_e; α is determined by fitting the exact shape of the spectrum, so that the Debye length and electron temperature can be derived as well.

For the intermediate range of α value, i.e. $0.3 < \alpha < 1$, collective effects have already influence on the spectrum. Although it can be fitted without calibration, the problem is the

values of n_e and T_e depend quite sensitively on the exact shape of the spectrum. Therefore the fitting result is relatively inaccurate. A good calibration of Raman scattering spectrum will give additional information and will improve the accuracy of the fitting result.

6.4   Results

A series of Thomson scattering experiments have been done for the regions close to cathode and anode.
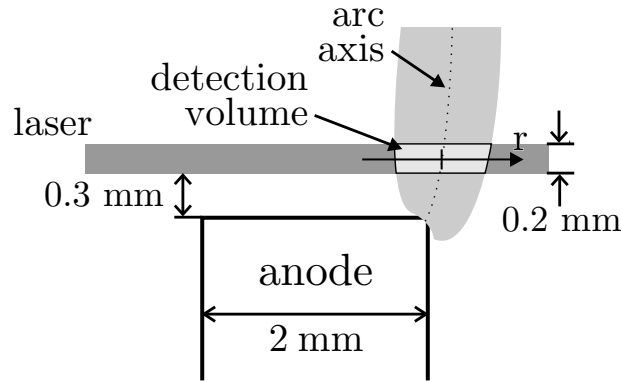
Figure 6.6: A sketch of the detection volume near the anode. For an anode with 2mm diameter and relatively low currents, the arc attachment is constricted and bent. The detection volume is located at 300 μm in front of the anode. The origin (r=0) of the radial position is chosen at the maximum of the Thomson scattering signal.

The schematic drawing of the detection volume close to the anode is shown in Fig. 6.6. The arc length is 20 mm and the Ar pressure is 1.5 bar. We used a pure tungsten cathode with 0.6 mm diameter and a pure tungsten anode with 2.0 mm diameter. A typical collective spectrum is shown in Fig. 6.7. The shape of the spectrum is not Gausian, so it has to be fitted with a collective TS fitting procedure which was described in section 6.3. Fig. 6.8 shows the radial profile of electron temperature and electron density near the anode (300 μm in front of anode) of an Ar discharge for different DC currents. It is clearly shown in Fig. 6.6 that the arc attachment near the anode was constricted and bent for the chosen parameters. Since it is difficult to determine the absolute position with respect to the anode, the center position (r=0) is chosen at the maximum of the Thomson signal. In general this does not coincide with the center axis of the anode. Since the plasma axis is not perpendicular to the electrode surface, the left and right region with respect to the center position (r=0) are not of equal size. From Fig. 6.8, it can be seen that the electron temperature distribution in the radial direction is more or less independent of the arc current and has a value between 10000 K and 12000 K. The electron density is found to be dependent on the arc conditions. It has a maximum in the arc center and is 2.6×10^{21} m^{-3}, 4.6×10^{21} m^{-3} and 8.6×10^{21} m^{-3} respectively for current of 1 A, 2 A and 3 A.
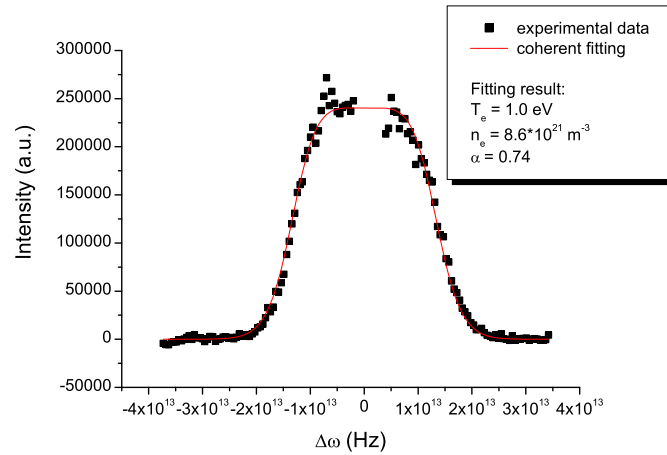
Figure 6.7: The typical collective Thomson scattering spectrum at 300 µm distance to the anode at 3 A arc current. It is clear that this is not a Gaussian so that collective effects are important apparently.
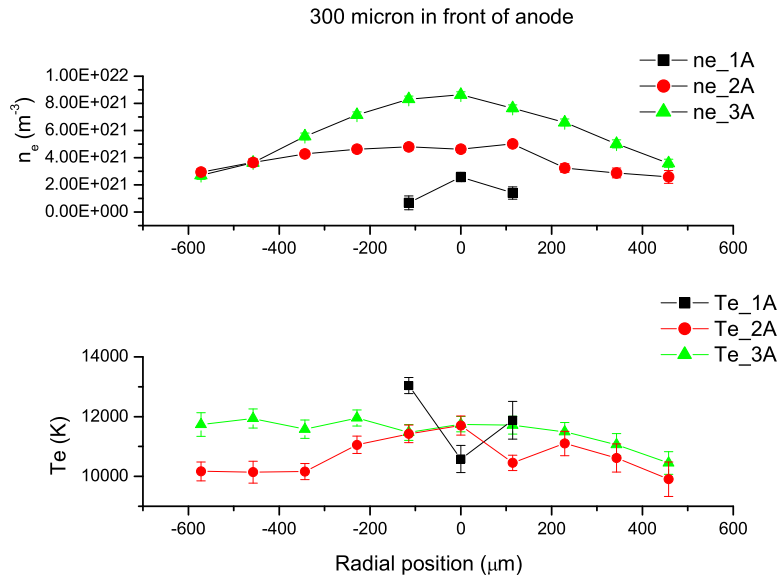
Figure 6.8: Radial profiles of the electron density and temperature at 300 µm in front of the anode for different arc currents(1 A, 2 A and 3 A).The lamp is filled with pure Ar with a pressure of 1.5 bar. Note that the electron temperature is more or less constant and that the electron density increases with increasing arc current. Here the origin of the radial position(r=0) is chosen at the highest intensity of TS signal.
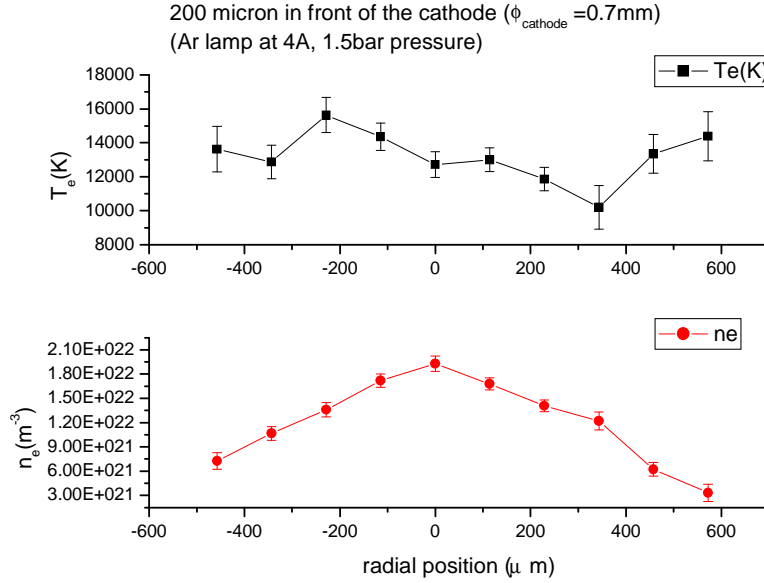
Figure 6.9: The radial profile of electron density and temperature at 200 μm in front of cathode. The lamp is burning at 4A and filled with pure Ar of 1.5 bar. Note that again T_e is more or less constant whereas n_e has a parabolic shape.

Fig. 6.9 shows electron temperature and density profiles close to the cathode (around 200 μm to cathode). It shows that in the center, $n_e \approx 1.9 \cdot 10^{22} \, \mathrm{m}^{-3}$ and $T_e \approx 13000 \, \mathrm{K}$. Here the Ar pressure is 1.5 bar. Again n_e is highest in the center of the plasma whereas T_e is again more or less constant but the value is larger than that found in the anode region.

6.5   Discussion

From the results of Thomson scattering experiments on the model lamp, we found that T_e does not change much for different arc currents at the region close to the anode whereas n_e increases with the arc current. This implies that the degree of the collectivity of the TS spectrum also increases with current. The α value is plotted in Fig. 6.10 for different currents at 300 μm in front of the anode. From Eq. 6.8, we can see that the higher electron density, the higher α value since T_e is more or less constant and equals to 1 eV.

If the plasma in the electrode regions were in LTE, then the density of the electrons n_e, ions n_+ and ground state atoms n_1 would be related to each other by means of the Saha equation

$$\frac{n_1^S}{g_1} = \frac{n_e n_+}{2g_+} \left[\frac{h}{\sqrt{2\pi m_e k T_e}} \right]^3 \exp\left(\frac{I_1}{k T_e} \right), \qquad (6.11)$$

where n_1^S and $g_1 = 1$ are the density and statistical weight of the atomic ground state
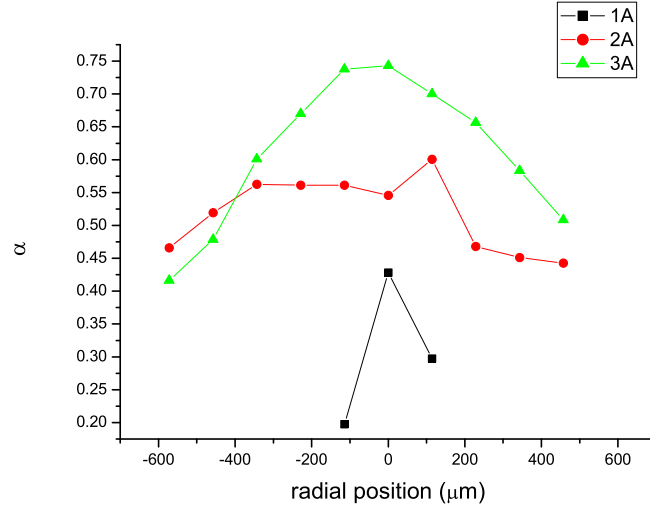
Figure 6.10: The α-value for different arc currents at 300 µm in front of anode.

respectively, n_+ the argon ion ground state density and $g_+ = 6$ is the statistical weight of argon ion ground state. Furthermore h is Plank's constant, m_e the electron mass, and $I_1 = 15.76$ eV is the ionization energy of atomic ground state for argon .

The departure from Saha equilibrium can be characterized by the dimensionless quantity $b_1 = n_1/n_1^S$ [40]. Here n_1 is the density of the atomic ground state. In order to determine the degree of equilibrium departure for the near anode region, we can take the central values of electron density and the average electron temperature of 11000 K from Fig. 6.8 and calculate the corresponding n_1^S value. For the currents of 1 A, 2 A and 3 A, this leads to the following results: n_1^S is 3.4×10^{21} m^{-3}, 1.1×10^{22} m^{-3} and 3.7×10^{22} m^{-3} for arc current of 1A, 2A and 3A respectively.

The actual value of the ground state density can be determined from the gas temperature in the Ar lamp. Since we did not measure the gas temperature in this model lamp, we estimated the gas temperature of about 5000 K. This value of 5000K, which is between the temperature of the electrodes and the temperature of the electrons, is used to estimate the b_1 factor later on. From the ideal gas law $p = nkT$ and the known Ar pressure of 1.5 bar, a ground state density of atomic Ar is estimated to be $n_1 \approx n_{total} = p/kT = 2.2 \times 10^{24}$m^{-3}. This value will be taken for all currents. Note that this approximation $p = p_{Ar(1)}$ is justified because the plasma is only partially ionized: the pressure of atomic Ar is more or less the same as the total pressure, since the Ar ion density is much lower than the atomic Ar density. Comparing n_1^S with n_1 gives a b-factor of 6.5×10^2, 2.0×10^2 and 59 for 1 A, 2 A and 3 A respectively.

6.5.1 The steady-state electron particle balance

In the previous subsection it was found that the plasma regions in front of the anode are characterized by large b_1 values. It was found that the lower the current, the lower n_e and consequently the higher the corresponding b_1 value is. The departure from equilibrium is also manifest in the region of the cathode. If we take the center point in front of cathode, $n_e = 1.9 \times 10^{22}\,\mathrm{m^{-3}}$ and $T_e = 1.3 \times 10^4\,\mathrm{K}$, the calculated ground state Saha density is $n_1^S = 1.1 \times 10^{22}\,\mathrm{m^{-3}}$, so we get $b_1 \approx 200$. This means that the plasma regions are strongly ionizing. In order to investigate how this strongly ionizing behavior is related to other plasma properties we will use the electron balance equation which is given by

$$n_e n_1 S_{\mathrm{ion}} - n_e n_+ \alpha_{\mathrm{rec}} = \nabla \cdot (n_e \mathbf{w}_e), \tag{6.12}$$

where S_{ion} and α_{rec} are the effective rate coefficients for ionization and recombination respectively, and $\mathbf{w}_e$ is the electron velocity.

In fact this equation expresses that the net ionization, i.e. ionization minus recombination, has to be compensated by the efflux of electrons. We will first investigate the ionization term which is mainly determined by the effective rate coefficient S_{ion}. Since the ionization energy of argon is relatively high (15.76 eV), the ionization is mainly step-wise. And due to the high n_e value, the escape of radiation will be relatively unimportant so that each excitation step from the ground state to the first excitation state $1 \to 2$ will lead to ionization [40–42]. Therefore we may equate S_{ion} to the rate coefficient $K_{1,2}$ for the excitation from the ground state to the first excited state which for argon can be given by [40–42],

$$S_{\mathrm{ion}}(T_e) \approx K_{1,2} \approx 6.81 \cdot 10^{-17} \sqrt{T_e} \exp\left(-\frac{E_{1,2}^*}{k_B T_e}\right) [\mathrm{m^3 s^{-1}}], \tag{6.13}$$

where $E_{1,2}^* = 12.06$ eV is the *effective* excitation energy of the first excited state.

Now we will first study the electron particle balance in the anode region(300 μm in front of the anode) for the case that the current equals 3A. In that situation we found $n_e = 8.6 \times 10^{21}\,\mathrm{m^{-3}}$ and the average $T_e = 1.1 \times 10^4$ K which corresponds to an ionization rate coefficient $S_{ion} = 2.1 \times 10^{-20}\,\mathrm{m^3 s^{-1}}$. This gives an ionization rate of $4.0 \times 10^{26}\,\mathrm{m^{-3} s^{-1}}$.

For the recombination process we will assume that only three particle recombination will be of importance. The corresponding rate coefficient α_{rec}^{3P} can be estimated from the overpopulation of argon ground state density with respect to the Saha density. If the plasma were in Saha equilibrium, the ionization process would be balanced by the recombination process, $n_e n_1^S S_{\mathrm{ion}} \approx n_e n_+ \alpha_{\mathrm{rec}}^{3P}$. However, since the plasma is not in Saha equilibrium, the ratio of ionization and recombination rates is not unity but equals

$$\frac{n_e n_1 S_{\mathrm{ion}}}{n_e n_+ \alpha_{\mathrm{rec}}^{3P}} \approx \frac{n_1}{n_1^S} \equiv b_1, \tag{6.14}$$

where b_1 is the ground state overpopulation with respect to Saha equilibrium. Therefore the recombination rate will be 59 times smaller than the ionization rate and can thus be neglected.

For the electron flux we use the following expression

$$n_e \mathbf{w}_e = -D_a \nabla n_e + \frac{\mathbf{j}_e}{e}, \tag{6.15}$$

where $\mathbf{j}_e = e n_e \mu_e \mathbf{E}$.

Here D_a is the ambipolar diffusion coefficient and μ_e the electron mobility: a negative quantity. Since the plasma convection flow is very small, we neglect the contribution of the convection term.

The divergence in the electron flux, that is the right hand side of Eq. 6.12, can now be written as

$$\nabla \cdot (n_e \mathbf{w}_e) = -\nabla \cdot (D_a \nabla n_e) + \nabla \cdot \left(\frac{\mathbf{j}_e}{e} \right), \tag{6.16}$$

and we assume that the last term can be neglected in the near anode region.

The diffusion term can be approximately written as [40, 41, 43]

$$|\nabla \cdot (D_a \nabla n_e)| \equiv n_e \frac{D_a}{\Lambda_{n_e}^2}, \tag{6.17}$$

where Λ_{n_e} is the gradient length of electron density. When 5400 K $< T_e <$ 13800 K and 2000 K $< T_h <$ 7000 K, D_a can be approximated by using the following equation [44, 45]

$$D_a \approx 1.81 \cdot 10^{-11} \cdot (5864 + T_e) \cdot T_h \quad [\text{m}^2\text{s}^{-1}]. \tag{6.18}$$

In the anode case, the average electron temperature is given by $T_e = 1.1 \times 10^4$ K and $T_h \approx 5000$ K, so $D_a = 1.5 \times 10^{-3} \, \text{m}^2\text{s}^{-1}$. Λ_{n_e} is approximated by fitting the radial profile n_e with a parabola function around the central position. This gives a value of $\Lambda = 0.3mm$ which is in the same order as the distance to the anode. Therefore the diffusion rate is about $1.4 \times 10^{26} \, \text{m}^{-3}\text{s}^{-1}$ which is 20 times larger than the recombination rate but in the same order of the magnitude of the ionization rate.

This means that due to contraction in the neighborhood of anode as introduced by the plasma-electrode attachment, a large gradient will be created which generates a large diffusive efflux of electron-ion pairs.

In the case of the near cathode region, we find a temperature of 1.3×10^4 K which is larger than the value found in the near-anode region. Thus the efflux must be larger. An estimation shows that the increase from $T_e = 1.1 \times 10^4$ K to 1.3×10^4 K leads to an enhancement of a factor of 8 in the generation of electron-ion pairs. On the other hand, the gradient length is not much different so that the diffusive efflux will not be capable to balance the ionization. Thus we have to look for other effects and investigate the last term in Eq. 6.16: the divergence of the electron current density. For the total current density $\mathbf{j} = \mathbf{j}_e + \mathbf{j}_+$, we have in steady state $\nabla \cdot \mathbf{j} = 0$, but this does not exclude the possibility that $\nabla \cdot \mathbf{j}_e = -\nabla \cdot \mathbf{j}_+ \neq 0$. This is indeed what happens in front of the cathode. It is known from literature that by approaching the cathode the ion current gets more and more the task to carry the arc current, a behavior which is depicted in Fig. 6.11 [46].
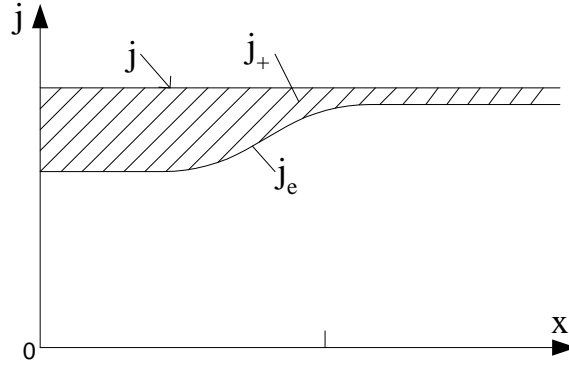
Figure 6.11: Distribution of current density in the cathode layer of an arc discharge (From Yuri P. Raizer [46]).

In order to establish whether this change in the nature of the current density is indeed capable to explain the large deviation from Saha equilibrium, we need to estimate $\nabla \cdot \frac{\mathbf{j_e}}{e}$.

Taking an arc current of 4 A and the plasma radius of 0.3 mm in front of cathode, the current density can be calculated to be equal to $1.4 \times 10^7 \, \mathrm{Cs^{-1}m^{-2}}$. So the electron flux is

$$\frac{j_e}{e} = 8.75 \times 10^{25} \mathrm{m^{-2}s^{-1}}$$

and

$$\nabla \cdot \frac{j_e}{e} \approx \frac{j}{e h_p}, \tag{6.19}$$

where h_p is the gradient length associated with the change in the nature of the current density at the location where TS were done.

It is not clear whether this change is already in action at the distance of 0.2mm from the cathode but it can be seen that we do not need a steep gradient to get $\nabla \cdot \frac{\mathbf{j_e}}{e}$ the same value as the ionization rate. Therefore it might be possible that the mechanism responsible for the large deviation from LTE has indeed to be searched for in this $\nabla \cdot \frac{\mathbf{j_e}}{e}$.

6.6   Conclusion

As far as we know, it is the first time that the Thomson scattering (TS) technique is successfully applied to study the plasma region close to the electrodes of a small lamp. In this study, the TS spectrum is partly collective. We applied the collective Thomson scattering fitting procedure to the spectrum and get a very good result. If the scattering parameter α value is in the range of [0.3,1.0], we need a very good Thomson spectrum with high signal to noise ratio and very accurate Raman scattering calibration to achieve reliable results.

From the result, we can see that the plasma is far from LTE near electrode region. It is ionizing both in the near-cathode and near-anode regions.

Chapter 7

Thomson scattering on high pressure Hg discharge lamps

Abstract

Thomson scattering (TS) experiments have been performed on high pressure Hg discharge lamps. These lamps were filled with different amounts of Hg (15 mg, 30 mg, 50 mg and 70 mg) and were operating at different powers (150 W, 200 W and 240 W) with a square wave ballast. As in the previous studies [47], a triple grating spectrograph (TGS) was used to suppress the false stray light and Rayleigh scattered photons. This setup had to be modified for this special application. The collective TS spectra have been fitted using both a calibration based on Raman scattering on N_2 and a form fitting procedure. In this way we could determine radial profiles of electron temperature and electron density in the central region. We found that the electron temperature values in the center region fluctuate around a certain value. The values of T_e varies between 5500 K ad 7600 K in the center region $r \leq 0.3R$. The spatial-averaged T_e value increases with the lamp power. The electron density was found to be in the order of $10^{21} \, \mathrm{m}^{-3}$. It is high in the center and decreases as r increases. The n_e-value also increases with the lamp power. Moreover the results of TS are compared with those from X-ray absorption (XRA) measurement. The comparison shows that the plasma in such lamps is not in LTE in the sense that $T_e \neq T_g$. Moreover it is found that on each location the rate of ionization is much larger than that of three particle recombination.

7.1 Introduction

Since the electrons in a plasma are responsible for the processes ruling the energy balance and the particle balances (chemistry), it is important to know the properties of the electron gas such as the electron density (n_e) and the electron temperature (T_e). In the past various spectroscopic techniques have been used to obtain information on n_e and T_e. They can mainly be divided into two types: passive and active diagnostics. The passive diagnostics such as absolute line intensity (ALI) spectroscopy or line-shape determination are relatively easy from an experimental point of view. However, the interpretation of the results is in most cases not straightforward and models are needed to deduce basic plasma properties out of the spectra. Examples of active spectroscopy are X-ray absorption (XRA) and Thomson scattering (TS), which are direct methods that can be used to obtain the gas temperature (XRA) and the properties of the electron gas (TS). In this chapter, we will discuss the Thomson scattering technique as applied to high-pressure mercury discharges.

There are several difficulties associated with the application of the Thomson scattering technique to high pressure mercury lamps. These are:

1. The plasma is confined in a small vessel and thus closely surrounded by a wall. It is difficult to make extension tubes such as those presented in chapter 6 since Hg will condense at the cold outer area. Therefore the laser power must be limited in order to avoid damage of the quartz wall by laser 'drilling'. This lower laser power reduces the amount of detectable Thomson signal.

2. The excitation and ionization potential of mercury is relatively low so that the creation of a laser induced plasma (LIP) by multi-photon ionization is relatively easy. This gives another reason why the laser power must be limited.

3. Most high power pulsed lasers become unstable and suffer from a deterioration of the beam quality at lower powers.

4. Since the plasma surroundings (wall) are very close to the plasma, a substantial amount of false stray light will be generated.

5. The strong plasma radiation from HID lamps can obscure the Thomson scattering signal. Therefore the TS spectrum region should be free of the plasma radiation.

6. Due to the low T_e values and the wide range of n_e conditions we can expect both collective and non-collective Thomson scattering spectra.

In this chapter we will present the methods that were used to adjust our existing TS setup to the application of TS technique to high pressure Hg lamps. These lamps, being far from academic, are used in lighting industry. The only model aspect we used is that the lamps are operated without an outer bulb [1], an envelope that is used to screen the UV light

---

[1]To be more precise, these lamps are not used as high pressure mercury lamps. The burners are Na/Sc metal halide lamps, where the salt and the outer tube were left out.

generated by the plasma to prevent the production of ozone and to keep the high cold-spot temperature such that all the liquid Hg is vaporized. Results of TS on four types of lamps operated at three different power levels will be presented. The types differ from each other with respect to the mercury filling.

An important goal of this study is to validate the assumption of the presence of Local Thermodynamic Equilibrium (LTE) for these types of lamps. If these plasmas are close to LTE this will facilitate the modelling for these plasmas considerably.

This is, as far as we know, the first time that TS is applied to a real technology plasma of such a small size and high pressure, and it can be seen as a crucial step for the application of TS technique on metal halide (MH) lamps. For the MH lamps we will be faced with even less favorable situations since metal halide lamps produce much more radiation that might overrule the TS light.

7.2 Experimental arrangement

7.2.1 The high pressure Hg lamps

Geometry

In this study, a group of high pressure Hg discharge lamps is chosen. To facilitate the experiments, we have chosen for a lamp-geometry with a relatively large diameter. In this way a reasonable distance can be retained between the wall and the focal spot so that the breaking of the wall by laser drilling can be prevented. The geometry of the burner can be summarized as follows: an inner diameter of 18 mm, an arc length of 39 mm and a wall thickness of 1 mm. Figure 7.1 shows the burner of the lamp which contains Hg and the starting gas of Ar/^{85}Kr mixture (300 mbar). The radioactive isotope ^{85}Kr is subjected to β^- decay by which, during the start-up procedure of the lamp, some initial free electrons can be generated. This facilitates the ignition of the lamp.

Pressure

Four lamps with different mercury fillings were used, respectively 15, 30, 50 and 70 mg. The mercury vapor pressure can be estimated using the empirical formula [48] which is given as

$$p = 0.75 \frac{P'^{1/4} m'^{0.9}}{d^{2.1}}, \tag{7.1}$$

where P' is the lamp power per arc length in [W/cm], m' the Hg mass per unit length in [mg/cm], and d the inner diameter in [cm]. The pressures obtained by formula 7.1 are shown in table 7.1 for different Hg fillings and powers, and can only be used when the
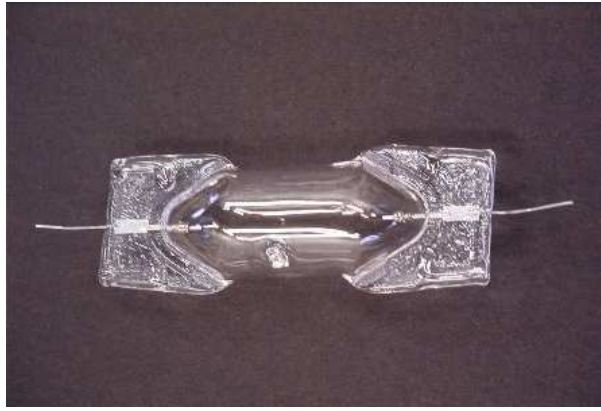
Figure 7.1: Picture of the high pressure Hg lamp for the Thomson scattering experiment.

power(W)\ mass(mg)	15	30	50	70
150	1.5	2.9	4.5	6.1
200	1.6/1.1*	3.1	4.9/1.3*	6.6
240	1.7	3.2	5.1	6.9

Table 7.1: Lamp pressures (bar) estimated using Eq. 7.1 for different gas fillings and lamp powers. In the table, the pressure values for 15 mg and 50 mg lamps with '*' are based on the XRA measurement (cf. section 5.4). It has been found that the Hg pressure in the 50 mg lamp is saturated at power of 200 W. That means that the factual pressure is smaller than the pressure found by distributing all the mercury over the lamp volume. It should be noted that also the other pressures should be corrected, especially at power of 150 W and 200 W, the Hg gas in these lamps is saturated.

calculated pressure is lower than the saturation pressure. The saturation pressure was based on the cold spot temperature.

Electrical properties

The lamps were operated with two different ballasts: a square-wave ballast at a frequency of 123.5 Hz and an inductive coil (AC) ballast alternating at a frequency of 50 Hz. The square-wave ballast can be regulated at different powers. In this chapter we will treat the results of TS on lamps operated with the square-wave ballast. A future paper will present the TS results of lamps driven by an inductive coil (AC) ballast.

7.2.2   Basic system

The main structure of the experimental setup used in this study is the same as that described in chapter 6 to which we refer for more detailed information. Here we give a brief
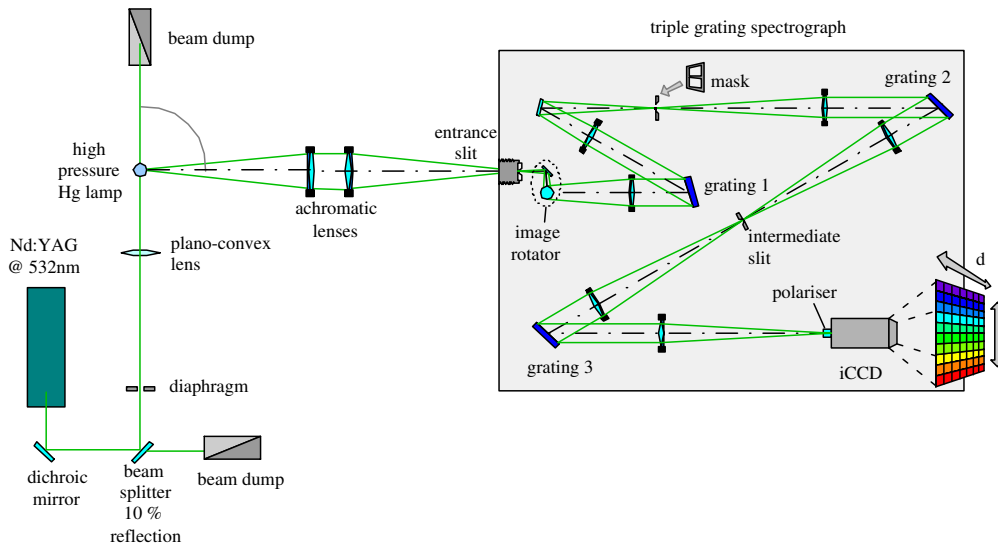
Figure 7.2: The experimental system for Thomson scattering on high pressure Hg lamps. A frequency doubled laser beam generated by a Nd:YAG crystal is scattered by electrons in the plasma. Scattered light is collected by two achromatic doublet lenses and dispersed by a triple grating spectrograph. The first two gratings and the mask in between serve as a notch filter to suppress stray light. An intensified CCD camera records the scattered spectra at different positions along the laser-plasma interaction zone.

description that is mainly intended to explain the changes that had to be made for this specific application.

The experimental setup for TS measurements on a Hg lamp is shown in Fig. 7.2. A frequency-doubled Nd:YAG laser produces 10 mJ, 7 ns laser pulses (repetition rate 10 Hz) at a wavelength of $\lambda_i = 532\,\text{nm}$. The laser beam is guided by a dichroic mirror and a beam splitter (10% reflection), confined by a diaphragm and focused by a plano-convex lens ($f = 25$ cm) into a diameter of approximately 400 μm [2] in the plasma where Thomson scattering takes place. The laser beam leaves the plasma and finally ends in the second beam dump. Scattered photons are collected by two achromatic doublet lenses at 90° and imaged onto the entrance slit of the Triple Grating Spectrograph (TGS), which rejects the stray light and disperses the scattered light. Finally the image is recorded by a 2-dimensional iCCD camera.

Several changes have been made in the experimental setup in order to reach the optimum situation for the application of TS to high-pressure Hg lamps.

- Firstly, a beam splitter with 10% reflection has been installed. The reason is that we need small energy pulses of around 1 mJ/pulse. These cannot be obtained by simply reducing the power input of the laser since the laser is constructed and optimized

---

[2]The size of the laser focus is estimated with an error bar of ±20%. The more accurate value should be measured by experiments.

for 400 mJ/pulse @532 nm. A direct reduction would lead to instabilities and severe deteriorations of the laser beam quality. Therefore a two-step approach was used. By direct reduction 10 mJ/pulses were created and these were further reduced by a factor of 10 by the beam splitter.

- Secondly, a diaphragm is placed after the beam splitter to block the reflected light from the mounting of the beam splitter.

- Thirdly, the original laser focusing lens with a focal length of $f=1$ m has been replaced by a lens with $f=25$ cm. This is done to prevent laser 'drilling' of the quartz wall.

- Fourthly, the entrance slit is partly blocked. The advantage is that the intense stray light created by scattering of the beam on the quartz wall is reduced substantially. The disadvantage is that only a minor part of the plasma can be observed.

- Finally, the mask inside the TGS has been redesigned to reduce the influence of plasma radiation.

By all these measures, we succeeded to perform Thomson scattering on high- pressure Hg lamps.

7.3   Comparison with the Ar model lamp results

7.3.1   The iCCD images
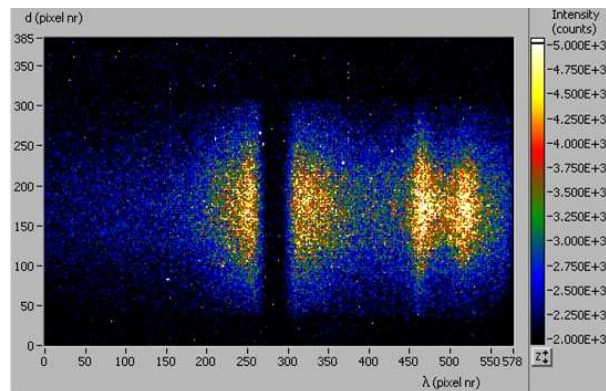
Figure 7.3: An iCCD image created by the Thomson scattering on a Hg lamp with 15 mg Hg filling, operated at 160 W with a square-wave ballast. The integration time is 600 s (6000 shots). Spectral (λ) and spatial (d) information is obtained along the horizontal and vertical directions respectively. The center of the spectrum is blocked in order to reduce the intense Rayleigh scattering and stray light signal. At the right hand side we see two spectral lines emitted by Hg and W.

Figure 7.3 shows a typical example of a 2D-iCCD image created by a TS measurement on a Hg lamp. This image is obtained by the accumulation of the scattered photons of 6000 subsequent laser shots. The vertical direction reflects the spatial dimension, i.e. the length along the laser-plasma interaction zone. The horizontal direction gives the wavelength dimension. The black central vertical band is the result of blocking the central wavelength λ_i by the Double Grating Spectrograph (DGS). Apart from the Thomson spectrum, that is present in the region close to the black central part (on both sides), we also observe at the right hand side two plasma lines. They have been identified as the 535.40 nm line of Hg and the 536.28 nm transition of W from the electrodes.

7.3.2 Typical TS spectrum

In order to clarify the difficulties associated to the current TS experiments on high-pressure Hg lamps we compare the experiment with that of our previous study: TS on the Ar model lamp. The specifications of TS measurements on two different lamps, the Ar model lamp and the Hg lamp, are shown in Table 7.2.

lamp	p (bar)	D_{in}	l_{arc}	l_{arc}/D_{in}	extension tube	t_{meas}	binning
Ar lamp	1.5	9	20	2.2	yes	5 min	4×4
Hg lamp	1.1	18	39	2.2	no	15 min	4×20

Table 7.2: Comparison of the Hg lamp (15 mg operating at 200 W square-wave ballast) with the Ar model lamp; apart from the design properties typical settings for the TS measurements are given as well. Here D_{in} (mm) is the inner diameter of the arc tube and l_{arc} (mm) the arc length.

There are several differences between these experimental setups:

1. In contrast to the Ar model lamp, we could not use extension tubes with windows at Brewster angle. Therefore the false stray light created by the quartz wall in the current Hg experiment is much larger, and to avoid that false stray light spoils the image the outer part of the the laser-plasma interaction zone could not be observed.

2. The electron temperature in a Hg plasma is lower than that in an Ar lamp. This means that the spectrum is narrower. Typical Thomson spectra of the Ar model lamp and the high pressure Hg lamp are compared in Fig. 7.4.

3. The laser power used for the Ar model lamp was about 100 mJ/pulse and the lens had a focal length of 1 m. For Hg lamps, a laser power of 1.4 mJ/pulse and a focal length of 25 cm was used in order to avoid laser drilling of the wall and the creation of LIPs. This implies that the TS experiments on Hg took a much longer time than those on Ar.

4. The Ar model lamp is designed such that the gas filling can be changed easily. This largely facilitates the Raman calibration procedure since the plasma gas Ar can easily
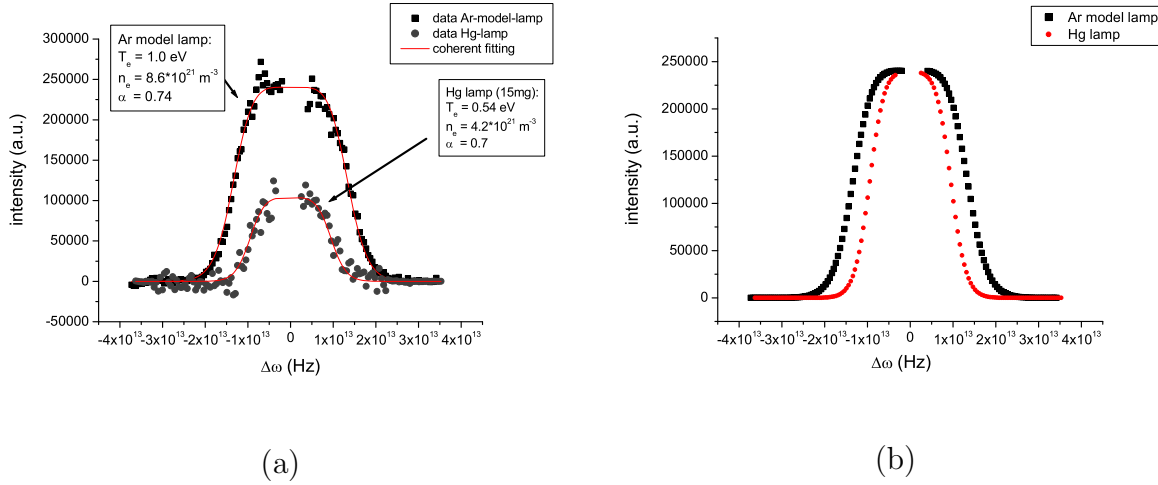
Figure 7.4: **(a)** *A typical collective TS spectra obtained from a Hg lamp compared with that of the Ar model lamp. Both spectra are measured in the center of the discharge. The signal to noise ratio of the Ar model lamp is much better than that of the Hg lamp. The scattering parameter α is similar. However both the electron temperature and electron density are lower in the Hg case (6300 K versus 11600 K and $4.2 \times 10^{21}\,\mathrm{m}^{-3}$ versus $8.6 \times 10^{21}\,\mathrm{m}^{-3}$). **(b)** The width of the TS spectrum of the Hg lamp compared with that of the Ar model lamp. The intensity of the TS spectrum for the Hg lamp is scaled such that both spectra have the same height. This is done to facilitate the comparison of the width and the influence of the mask.*

be changed by the calibration gas N_2. However in the case of a Hg lamp, the calibration can only be done by replacing the Hg lamp with a comparable tube filled with N_2. This procedure will introduce an uncertainty which will be discussed in section 7.6.1.

A typical Thomson spectrum of the high pressure Hg lamp is compared with one obtained for the Ar model lamp in Fig. 7.4. One should realize that even after 4×20 binning the intensity of the TS spectrum of the Hg lamp is lower than that of the Ar model lamp (4×4 binning). For the same integration time and binning, the intensity of Hg case is about 45 times smaller. The main reason is that the laser power is much lower than in the case of the Ar lamp case (The power density is about 20 times less). The electron density for Hg lamp is about $4.2 \times 10^{21}\,\mathrm{m}^{-3}$ which is about 50% of that of the Ar lamp ($8.6 \times 10^{21}\,\mathrm{m}^{-3}$). Also the value of the electron temperature is about half of that found for Ar model lamp (6300 K versus 11600 K). The fact that both the electron density and electron temperature are a factor of 2 smaller than in the Ar experiment implies that the degree of the collectiveness is more or less the same. This can be understood by using the expression for α given by

$$\alpha_\perp = 0.08\sqrt{\frac{\hat{n}_e}{\hat{T}_e}}, \tag{7.2}$$

in which $\hat{n}_e$ is in $10^{20}\,\text{m}^{-3}$ and $\hat{T}_e$ is given in eV (cf. Eq. 6.8). The α-values for both cases given in Fig. 7.4 are similar, 0.74 for the Ar model lamp and 0.70 for the Hg lamp. This means that just as in the Ar experiment, the Thomson scattering spectra on the high-pressure Hg is partly collective.

Figure 7.4 clearly shows that the width of Thomson spectrum for the Hg lamp is narrower than that of the Ar lamp case. This is mainly due to the fact that the T_e is lower in the Hg case.

7.4   Experimental procedure

The recorded iCCD image not only contains a TS signal (the scattering of photons by free electrons), but also a contribution of the dark current of the iCCD, Rayleigh scattering (scattering on atoms), false stray light (scattering on the plasma surroundings) and the plasma radiation from the lamp. To correct for these signals, three more images with the same integration time as the TS signal are taken, namely a dark image (lamp-off, laser-off), a stray light image (lamp-off, laser-on), and a plasma radiation image (lamp-on, laser-off). The real TS image is obtained as

$$\phi_{TS_{cor}} = \phi_{TS} - \phi_{stray} - \phi_{plasma} + \phi_{dark}. \tag{7.3}$$

Since the images of TS, stray-light and the plasma-background all contain the same amount of dark current we get a double subtraction of the dark current in the expression $\phi_{TS} - \phi_{stray} - \phi_{plasma}$. That is why ϕ_{dark} has to be added.

Due to the fact that the α-value is in the range of $0.2 < \alpha < 1.1$, the determination of n_e and T_e by the shape fitting is not accurate enough. Therefore Raman scattering experiments were done to get a reference for the calibration of the incident laser power.

7.4.1   Calibration methods for Thomson scattering

For a scattered volume ΔV and a local electron density n_e, the total Thomson scattered power within a solid angle $\Delta \Omega$ is generally described as

$$P_T = P_i n_e L_{det} \frac{d\sigma_T}{d\Omega} \Delta \Omega \int S(\mathbf{k}, \omega) d\omega, \tag{7.4}$$

where P_i is the incident laser power, L_{det} the length of the detection volume along the incident laser beam, $\frac{d\sigma_T}{d\Omega}$ the differential cross-section for TS, and $\int S(\mathbf{k}, \omega) d\omega$ the spectral distribution function integrated over all scattered frequency.

It is difficult to measure the incident laser power absolutely since the measured signal depends not only on the laser power itself, but is also influenced by the complete optical system, its transmission and the solid angle. Therefore we need a medium with a known density to calibrate the detection system. We selected Rotational Raman scattering, i.e.

the inelastic scattering of radiation on molecules. In our study, a quartz tube was used that has the same geometry as the lamp. This calibration tube was filled with 950 mbar N_2 gas and placed at the same position as the Hg lamp to do the Raman scattering experiment. In the case of collective Thomson scattering, when the electron temperature is close to the ion temperature, i.e. $\frac{T_e}{T_i} \approx 1$, the spectral distribution function $S(\mathbf{k}, \omega)$ can be simplified using the Salpeter approximation (see Eq. 6.4) [47]. Then by integrating the Salpeter function over all frequencies we get

$$\int S_e(\mathbf{k}, \omega) d\omega = \frac{1}{1 + \alpha^2}. \tag{7.5}$$

Here the subscript 'e' means the electron contribution in the Salpeter function. Since the ion contribution is located at the central frequency that is filtered by the TGS, it will not contribute to the measured TS spectral shape. Therefore only the electron contribution of the Salpeter function will be present in the measured spectrum.

For a non-collective TS spectrum, we have $\alpha = 0$ so that $\int S(\mathbf{k}, \omega) d\omega = 1$. In that case the electron density is obtained as (cf. Eq. 6.10).

$$n_e = n_{N_2} \cdot \frac{P_T}{P_{RM}} \cdot \Gamma_{RM}, \tag{7.6}$$

where n_{N_2} is the density of nitrogen gas, P_T the total TS power, P_{RM} the total Raman scattered power and $\Gamma_{RM} = \frac{\frac{d\sigma_{RM}}{d\Omega}}{\frac{d\sigma_T}{d\Omega}}$, the calibration factor for the differential cross-section of the rotational Raman spectrum ($\Delta J = \pm 2$) with respect to TS.

Combining Eq. 7.4, Eq. 7.5 and Eq. 7.6, we find for the general case including both collective and non-collective Thomson scattering that the electron density for the collective TS spectrum can be written as [25]

$$n_e = n_{N_2}(1 + \alpha^2)\frac{P_T}{P_{RM}} \cdot \Gamma_{RM}. \tag{7.7}$$

In our experimental setup, the scattering geometry is chosen perpendicular, i.e. the angles θ and ϕ both equal to 90° (cf.Fig. 6.3). The value of Γ_{Rm} is calculated for N_2 gas and equals 8.15×10^{-5} [25]. Typical iCCD images for TS and Raman scattering are shown in Fig. 7.5. The total intensity is given by the total area under the spectrum.

7.5 Results

Thomson scattering measurements have been performed on various high pressure Hg discharge lamps with different Hg doses (cf. Table 7.1) operated at different powers using the square-wave ballast. All the measurements were performed with a laser energy of about
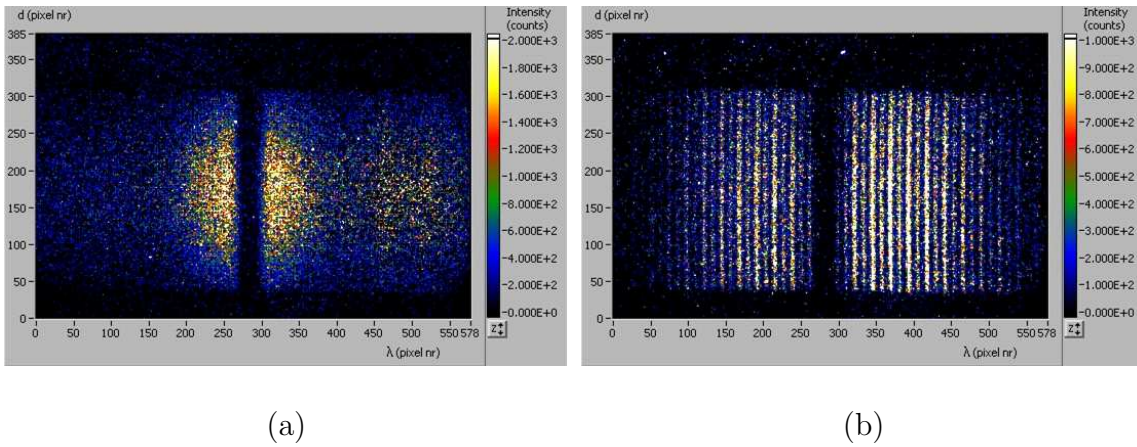
(a)   (b)

*Figure 7.5: **(a)** A typical spectrum of Thomson scattering measurement on a high pressure Hg lamp with pressure of about 1.1 bar. **(b)** A typical Raman spectrum of a nitrogen tube filled with 950 mbar nitrogen.*

1.4 mJ/pulse. The gain of the iCCD is set at the maximum value (gain 9). The integration time of each image was between 5 and 20 minutes. The electric properties of the lamp, such as I_{rms}, V_{rms} and P_{rms} were measured by a power meter (Norma 3000-PP30). The driving frequency of the power supply equals 123.5 Hz. Due to the square wave form of the current and voltage we get a situation that is comparable to a DC operation. Therefore we do not need to make a phase resolved measurement. Nevertheless the measurements were done by synchronizing the laser shots with the phase of midway between two zero crossings ($\phi = 1/4$) in order to avoid any effect from re-ignition spikes.

The results for the 15 mg Hg lamp are shown in Fig. 7.6. It shows that the electron density is high in the center of the discharge ($r = 0$) and decreases as r increases. We can also see that n_e measured at a lamp power of 150 W is lower than for 200 W and 240 W, but the profiles are similar. Figure 7.6(b) shows that T_e fluctuates around a certain value for different radial positions. If we average the value of T_e over different positions, we will find that the averaged value of T_e is increasing with lamp power, these are given in table 7.3.

Power (W)	Averaged T_e (K)
150	6576
200	6735
240	6912

Table 7.3: The averaged value for T_e at different lamp powers (150, 200, 240 W) for the 15 mg Hg lamp operating with square-wave ballast.

Thomson scattering measurements were also performed on lamps with Hg fillings of 30
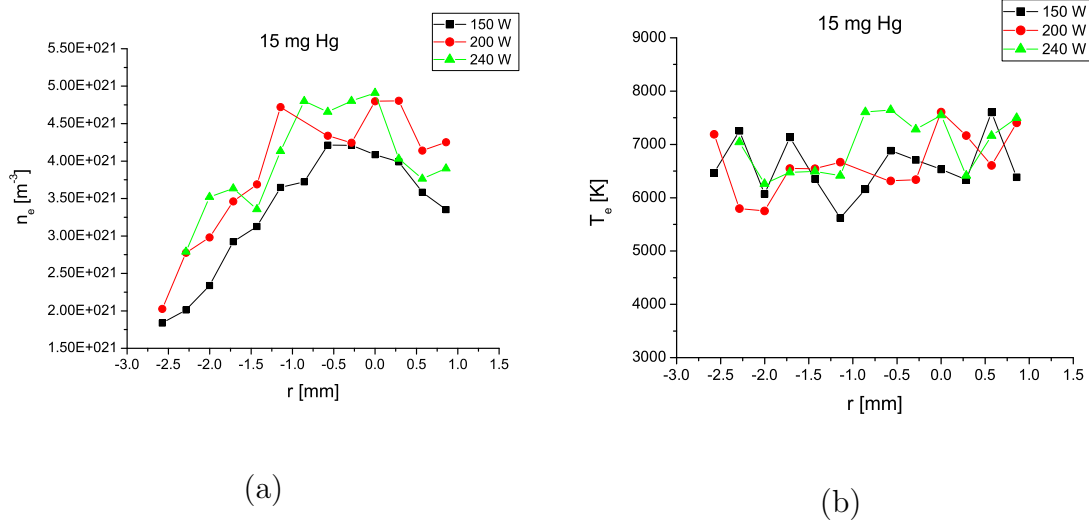
(a)

(b)

*Figure 7.6: Results of TS measurements on a lamp filled with 15 mg Hg operating with a square-wave ballast at three different power settings (150 W, 200 W and 240 W). (**a**) Electron density n_e as a function of radial position r in the middle plane of the lamp. (**b**) Electron temperature T_e as a function of radial position in the middle plane of the lamp.*

mg, 50 mg and 70 mg at different power settings, 150 W, 200 W and 240 W. It turned out later from XRA measurements that at a power level of 200 W mercury condensation was observed. Therefore only a comparison of electron density and electron temperature has been made for different Hg fillings at 240W (cf. Fig. 7.7). All these three measurements clearly show that the electron density of the 15 mg Hg lamp is the highest, whereas the electron density of the 30 mg Hg lamp is the lowest. The reason behind it might be that the alignment of the Raman calibration procedure is not always perfect. This might indicate towards a systematic error, as the same trend was also observed for the other power settings. One might expect that the electron density should increase by increasing the Hg filling of the lamp, but this trend is not observed in Fig. 7.7. The reason is that for higher fillings (and lower powers) the Hg vapor is saturated as shown in table 7.1. Therefore the pressure of Hg does not increase for higher fillings and the plasma condition is more or less the same for these lamps at low power settings (150 W, 200 W).

7.6 Discussion

In this section, two main issues will be discussed. The first one is the error analysis of TS experiments on high-pressure Hg lamps. Different sources of errors will be given and discussed. The second part will be devoted to equilibrium departure. The Saha density n_1^S of the ground-state Hg will be calculated from the measurement results. By comparing the Saha value of ground state density with the density obtained from XRA, the degree of
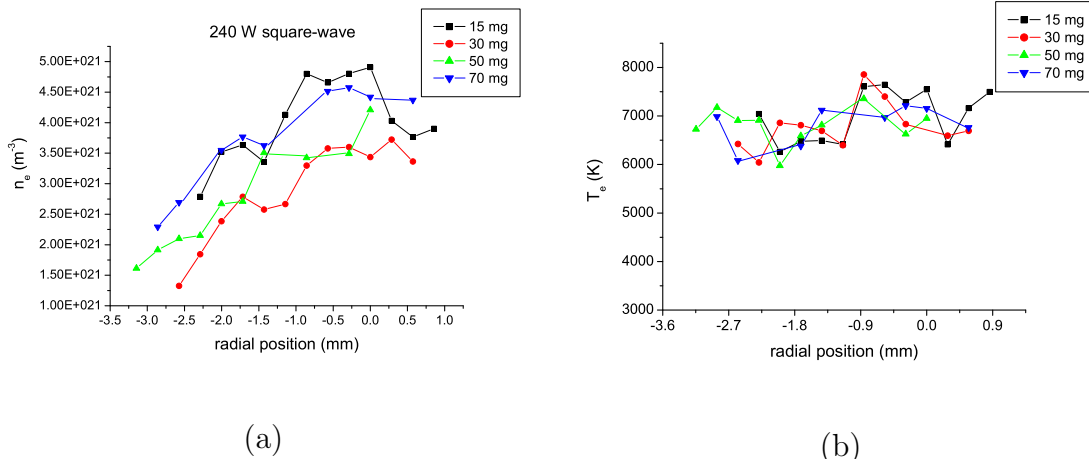
(a)

(b)

*Figure 7.7: Comparison of the n_e and T_e as obtained by TS for high pressure Hg lamps with different Hg fillings. The lamp power is fixed to 240 W. (**a**) Electron density n_e as function of radial position r in the mid-plane of the lamp. (**b**) Electron temperature T_e as function of radial position in the mid-plane of the lamp.*

the departure from LTE will be discussed using the b_1 factor.

7.6.1 Error analysis in n_e and T_e

There are two types of errors in the final results of n_e and T_e: a random error and a systematic error. The random error is caused by the fitting, the accuracy of the cross-section data (i.e. 8%) and the laser intensity drift. The systematic error is mainly introduced by the calibration procedure. In this section, an error analysis will be given.

The fitting error

To understand the fitting error one should realize that the values of n_e and T_e are determined by a procedure that is based on a combination of Raman calibration and form fitting. Another important aspect is that the center of the TS spectrum (cf. section 7.3.1) is blocked in order to suppress the false stray light. But if the spectral interval that is blocked is too large, this will influence the form fitting. Especially for the TS experiments on Hg plasmas we must be careful since we know that the width of the TS is rather small (cf. Fig. 7.4). In this section we will give an analysis of the error that can be made due to the missing (blocked) central area.

In a worst case scenario we will assume a T_e-value that is extra low; namely $T_e = 5000\,\mathrm{K}$. This value has been chosen for the simulation of a TS spectra for different α values. The results are given in Fig. 7.8. The number of pixels in the center of the TS spectrum that are blocked by the TGS system is about 56. The TGS system has a dispersion of about 0.01881 nm/pix. Therefore the half width of the blocked area $\Delta\lambda$ is about 0.53 nm. This
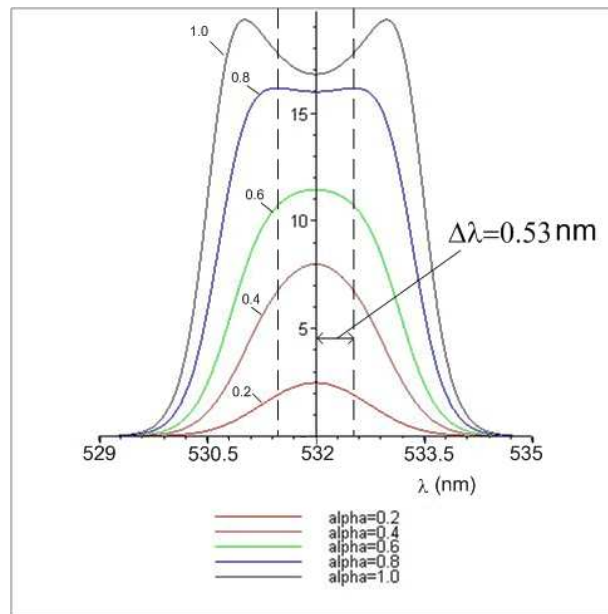
123

Figure 7.8: Simulated TS spectra for different α-values for the worst- case scenario of an electron temperature of $T_e = 5000\,\mathrm{K}$.

width is also shown in Fig. 7.8. It clearly shows that the influence of the blocking width in the TS spectrum largely depends on the α-value. For higher α-values such as $\alpha > 0.8$, the influence is limited; the shape of the TS spectrum is still easily recognizable. However, for small α-values such as $\alpha < 0.6$, the central blocking will have an influence on the accuracy of the fitting.

In reality, the electron temperature is higher, therefore the TS spectra are wider than that presented in Fig. 7.8. From this study, we can conclude that the mask width of 1 mm in the TGS system has some influence on the accuracy of the fitting, especially for the low α-values. However we may assume that this effect has not much impact on the determination of the central T_e value. In the central region α is close to 0.8 and we estimated the error due to the uncertainty of the pixels near the mask to be around 300 K.

Systematic error caused by the calibration procedure

The experimental system is aligned every day by optimizing the intensity of Raman scattering spectrum on an identical N_2-filled burner. The optimum situation is achieved by adjusting the delay and gate time of the iCCD and the height of the lens in front of the TGS system until the intensity of the Raman spectrum is at maximum. After the measurement of the Raman scattering spectrum, the N_2 tube is replaced by the Hg lamp. If the position of the Hg lamp is different from that of the N_2 tube, this will lead to a reduction of the TS signal. Therefore the measured intensity of the TS spectrum is always lower than what it should be. We will show that this underestimation of the total intensity of TS spectrum
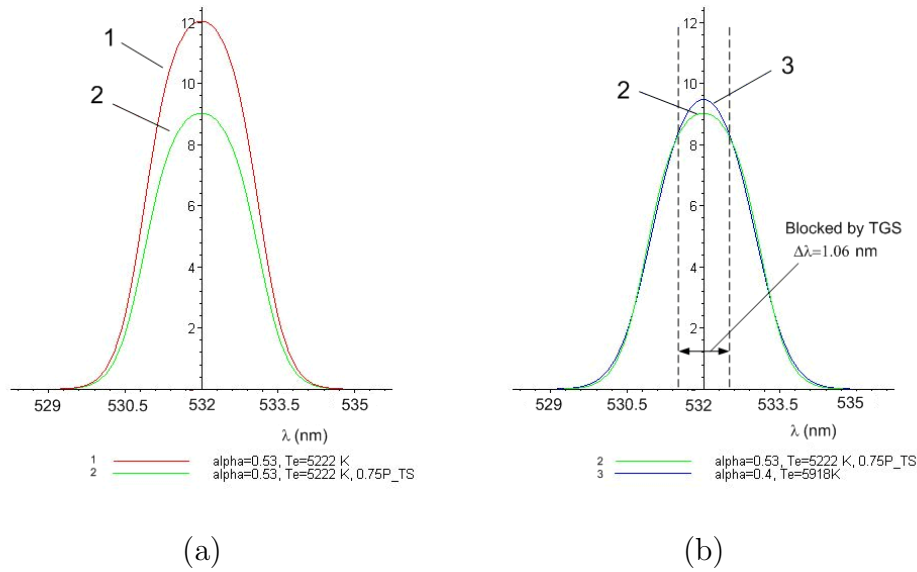
(a)   (b)

Figure 7.9: A simulation of the fitting of a Thomson spectrum with an underestimated intensity. **(a)** *Curve 1 represent the TS shape with* $T_e = 5222\,\mathrm{K}$, $n_e = 2.0 \times 10^{21}\,\mathrm{m}^{-3}$ *and* $\alpha = 0.53$. *Curve 2 is the underestimated TS spectrum which is about* 75% *of the original signal.* **(b)** *Curve 2 is the same as that under (a). Curve 3 is the fitted spectrum for curve 2 with the result* $n_e = 1.3 \times 10^{21}\,\mathrm{m}^{-3}$, $T_e = 5918K$ *and* $\alpha = 0.4$.

will not only lead to an underestimation in n_e but also to an overestimation of the T_e-value.

A demonstration of the impact of the calibration error is given by a simulation of the results which is visualized in Fig. 7.9. Figure 7.9(**a**) shows curve 1 of the "true" TS spectrum with $n_e = 2 \times 10^{21}\,\mathrm{m}^{-3}$, $T_e = 5222K$ and $\alpha = 0.53$. By simulating the experimental error due to which less photons are collected, we get a TS intensity that is lower than should be (cf. curve 2 in Fig 7.9(**a**)). Here we assume an intensity reduction of 25%. In order to fit this modified spectrum, different values of n_e and T_e are found which are shown in curve 3 in Fig. 7.9(**b**). Instead of the real value of $n_e = 2 \times 10^{21}\,\mathrm{m}^{-3}$ and $T_e = 5222K$, the fitted values of the reduced spectrum are found to be $n_e = 1.3 \times 10^{21}\,\mathrm{m}^{-3}$, $T_e = 5918K$. Thus n_e is decreased by a factor of 35% and T_e is increased for almost 700 K which is 13%.

This simulation shows that the calibration-fitting procedure will attribute to this Thomson spectrum (that is lower in height but not altered in form) an n_e value that is too low and a T_e that is too high. This can be understood by realizing that this procedure can be seen as consisting of two parts: the absolute calibration via Raman scattering and a form fitting of the shape. The Raman component prescribes a value of $\frac{n_e}{1+\alpha^2}$. The form fitting determines a value of a function between α and T_e. Now if the height of the profile is lower than in reality this primarily leads to a low n_e value, which by means of Eq. 7.2 gives a small α value. Since the form is not altered by the error in the height, the fitting procedure

will search for a higher T-value.

From the analysis above, we draw several conclusions:

1. Due to the underestimation of the intensity of the TS spectrum caused by the Raman scattering calibration procedure, errors will be introduced in n_e and T_e. This will cause a decrease of n_e, and an increase of T_e. This error can vary from measurement to measurement. Therefore it is a random distributed systematic error and the absolute value of this error is not known.

2. In order to increase the accuracy of the fitting, the following solution is recommended: Replace the grating with another one with a higher dispersion so that the TS spectrum will be broader. The blocking area by the mask will be relatively smaller than it is now and the form-fitting will be more accurate. Moreover for cases with an intermediate α value ($0.4 < \alpha < 0.7$), we can confine ourselves to the form fitting solely and get more reliable results. But for very small α-value in the case of non-collective TS, electron density can not be determined by the form fitting anymore and it can only be determined by the Raman calibration procedure.

As said before, in the results of TS the electron density of the 30 mg Hg lamp was found to be significantly lower than that of the other lamps. This might be caused by the fact that the intensity of the TS spectrum is underestimated significantly and points towards an error of 30%. It is not yet clear whether this error can be regarded as being typical.

Other error sources

Besides the two errors mentioned above, there are also other error sources, such as the accuracy of the Raman scattering cross-section which is 8% [49] and the drift of the laser pulse energy of about 3%.

Therefore for the Thomson scattering measurement, the total random error in the result is about 10%. Besides this, there is still a systematic error caused by the calibration method, it is an unknown systematic error. As seen from the simulation, it can have an error of 13% in the T_e value at an intensity error of 25%.

The laser influence on n_e and T_e

When a laser enters a plasma with an absorption coefficient κ $[\mathrm{m}^{-1}]$ at this wavelength, we find that the laser flux density F $[\mathrm{W/m^2}]$ will decrease along the path according to

$$\frac{dF}{dx} = -\kappa F. \tag{7.8}$$

In order to get an impression of the effect of the absorption of the laser power on the electron density and electron temperature, we assume that all the absorbed laser power

126

is used for ionization. Therefore the maximum change of the electron density can be estimated as

$$\Delta n_e = \frac{\kappa F \tau}{I}, \tag{7.9}$$

where τ is the laser pulse duration which is 7 ns. For a laser pulse energy of 1.4 mJ and focal spot size of $r = 0.2\,\text{mm}$, the laser beam energy flux in the focus is

$$F\tau = \frac{1.4\,\text{mJ}}{\pi (0.2\,\text{mm})^2} = 1.1 \times 10^4\,\text{J/m}^2. \tag{7.10}$$

The absorption coefficient κ (m^{-1}) is given by

$$\kappa = \frac{\omega_{pe}^2}{c} \cdot \frac{\nu_{eh}}{\nu_{eh}^2 + \omega_i^2} \approx \frac{\omega_{pe}^2}{c} \cdot \frac{\nu_{eh}}{\omega_i^2}, \tag{7.11}$$

where $\omega_{pe} = \sqrt{\frac{n_e e^2}{m_e \epsilon_0}}$ is the electron plasma frequency in $[\,\text{s}^{-1}\,]$, ν_{eh} the electron-heavy particle collision frequency, ω_i the angular frequency of the incident laser beam. The approximation in Eq. 7.11 is justified since ω_i (3.5×10^{15} Hz) is much larger than ν_{eh} ($\approx 2.2 \times 10^{12}$ Hz). A simple estimation shows that the electron-ion collision frequency is much smaller than the electron-atom interaction frequency so that the electron-heavy particle collision frequency can be written as

$$\nu_{eh} \approx \nu_{ea} = n_a \sigma_{ea}^{Hg} \bar{v}_e, \tag{7.12}$$

where n_a is the atomic Hg density in $[\,\text{m}^{-3}\,]$, σ_{ea} the cross-section for electron-Hg atoms collisions (about $1.8 \times 10^{-18}\,\text{m}^2$ [50] for $T_e = 6600\,\text{K}$), and $\bar{v}_e$ the mean thermal velocity of electrons, i.e. $\bar{v}_e = \sqrt{\frac{3 k_B T_e}{m_e}}$.

For the lamp with 50 mg Hg operating at a power of 200 W, we found in the center an n_e value of $4.0 \times 10^{21}\,\text{m}^{-3}$. The atomic density of Hg of about $2.2 \times 10^{24}\,\text{m}^{-3}$ can be obtained from the XRA measurement (cf. section 5.4). Assuming the electron temperature is 6600 K, the value of ν_{eh} can be calculated using Eq. 7.12 which gives $\nu_{eh} \approx 2.2 \times 10^{12}\,\text{Hz}$. Inserting the values into Eq. 7.11 gives the absorption coefficient of $\kappa = 7.8 \times 10^{-3}\,\text{m}^{-1}$.

Inserting these values in Eq. 7.9 and taking $I = 10.44\,\text{eV}$ we find the maximum increase of the electron density by the laser $\Delta n_e = 5.1 \times 10^{19}\,\text{m}^{-3}$.

The assumption that multi-photon and threshold ionization are not important implies that the increase in n_e must be realized by an increase of the electron temperature. This can be computed via the rate of electron creation for which we use the expression

$$\frac{\Delta n_e}{\Delta t} = n_e n_a K(1, +), \tag{7.13}$$

where $K(1, +)$ is the rate coefficient for ionization. Since the ionization process in these high density plasmas is mainly stepwise, we can use the approximation $K(1, +) \approx K(1, 2)$ where the rate coefficient for the $1 \to 2$ transition $K(1, 2)$ is given in [41] as

$$K(1, 2) = 4.36 \times 10^{-12} C_s(Hg) \hat{E}_{12}^{-2} \sqrt{\hat{T}_e} \exp(-\hat{E}_{12}/k_B T_e). \tag{7.14}$$

127

Here $\hat{E}_{12}$ is an effective energy value (in eV) of the first excitation step $1 \rightarrow 2$, which corresponds to the 253.7 nm transition with an energy of 4.9 eV. C_s is a scaling factor, which equals to 0.79 for Hg. Inserting these values into Eq. 7.14, we get

$$K(1,2) = 1.43 \times 10^{-13}\sqrt{\hat{T}_e}\exp(-4.9/k_BT_e). \tag{7.15}$$

Inserting Eq. 7.15 into Eq. 7.13, a T_e value is obtained of 4890 K which is substantially lower than the T_e value found by Thomson scattering which is about 6600 K. This implies that the laser heating will lead to an increase of the T_e value that can be neglected. Detailed calculations show that ΔT_e is about 60 K.

To conclude, the laser has little influence on the results of electron density and electron temperature in the situation sketched above.
However the influence of the laser on the plasma strongly depends on the power density of the laser in the focus. If the focus size would be very small, it will have a large influence. For example, for a very well coherent laser beam (perfect Gaussian beam), the focusing size of the laser is about $r=0.03$ mm. For this case, the increase of the electron temperature ΔT_e can attain values up to 2667 K. The maximum increase of the electron density will then be $2.3 \times 10^{21}\,\mathrm{m}^{-3}$. Therefore the main influence of the laser heating depends on the beam size in the focus and the laser power.

In the future, it is necessary to test the laser influence by the following methods:

1. Measuring the laser beam profile.

2. Performing simultaneous measurement on the continuum and line emission to check whether there are any changes in the plasma radiation due to the laser irradiation.

7.6.2 Equilibrium departure

It is often assumed that high pressure Hg discharge lamps are in Local Thermal Equilibrium (LTE). This assumption implies that for each location all material particles are both in thermal equilibrium and chemical equilibrium. Thermal equilibrium implies that there is only one kinetic temperature for the material particles and that all the particles have a Maxwell energy distribution. The presence of chemical equilibrium implies that the excitation and de-excitation balances result in a Boltzmann distribution whereas the degree of ionization is given by the Saha equation.
In the following, the equilibrium departure will be discussed in two aspects: firstly, the thermal equilibrium departure in the sense that electron temperature might be different from the gas temperature; secondly the chemical equilibrium departure concerning the deviation from Saha equilibrium.
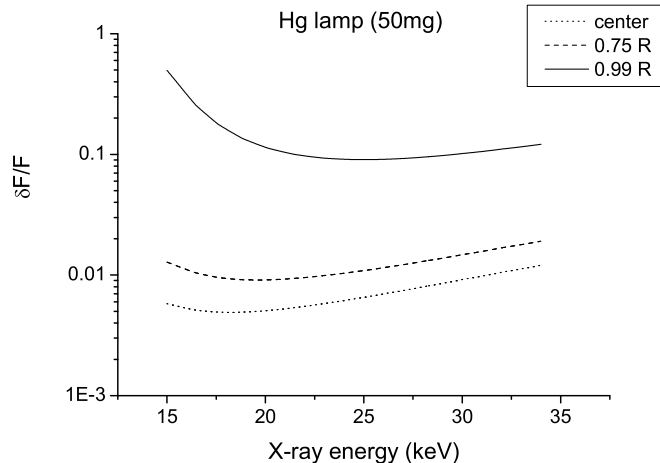
Figure 7.10: The relative error of the column density of Hg as a function of the X-ray photon energy for different lateral positions x for type 2-2 lamp (50 mg Hg filling).

Deviation from thermal equilibrium: $T_e \neq T_g$

In order to validate the presence of LTE, the electron temperature from the TS measurement has to be compared with the gas temperature obtained from the XRA measurement. Therefore two lamps, the 15 mg and 50 mg Hg lamps, operating with a 200 W square-wave ballast, are selected for both TS and XRA measurements.

From Thomson scattering experiment, it has been found that for a power of 200 W the center axis temperature is around $7600 \pm 760\,\text{K}$ for the 15 mg lamp and $6600\,\text{K} \pm 660\,\text{K}$ for the 50 mg lamp. Moreover the XRA measurements show that the center axis temperature is 5700 K for the 15 mg lamp and 4200 K for the 50 mg lamp. Thus the temperature difference is 1900 K for the 15 mg case and 2400 K for the 50 mg Hg lamp. However, since the lateral profile of XRA measurement was asymmetric for the 15 mg lamp, the result of the gas temperature is not reliable since Abel inversion is only valid for a cylindrical symmetric profile. Therefore we are going to discuss the case of the 50 mg lamp only.

For the 50 mg Hg lamp, the value of T_e can be as low as 5900 K taking into account the margin of the random error discussed above. Since the effective energy for the acceleration voltage of 25 kV is estimated to be 17.6 keV (cf. Fig. B.2), the relative error in the XRA measurement near the edge for this 50 mg Hg lamp at the lateral position close to the wall ($x = 0.99R$) is shown in Fig. 7.10. It shows that the relative error near the wall at 17.6 keV is about 18% which determines the relative error in the gas temperature since the gas temperature profile is determined from the wall temperature. Therefore the error in the gas temperature of lamp 2-2 (cf. Table 1.1) with 50 mg Hg filling is about 760 K. Taking this error into account, the gas temperature may be as high as 4960 K. So even accounting

for all possible errors in both measurements, there is still a temperature difference of about 1000 K between T_g from XRA and T_e from TS. From this comparison, the conclusion can be drawn that the high pressure Hg lamp with 50 mg Hg filling is not in LTE condition since $T_e > T_h$. The comparison of T_e and T_g is shown in Fig. 7.11.
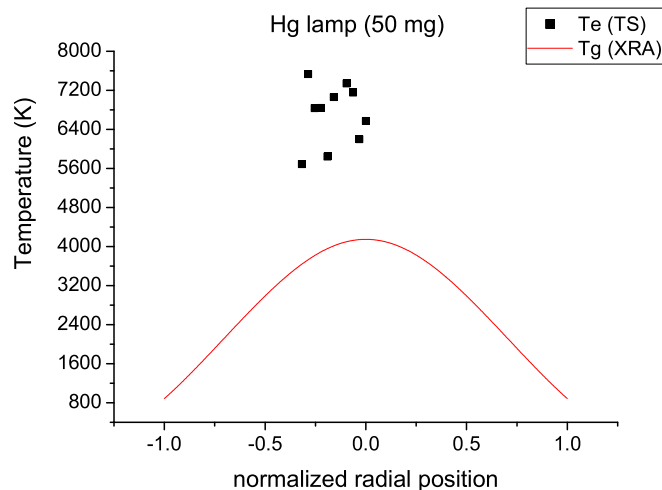

Figure 7.11: Comparison of the electron temperature obtained from TS measurement with the gas temperature obtained from XRA measurement for type 2-2 lamp (50 mg Hg filling).

Departure from Saha equilibrium comparing with XRA result

The deviation from local Saha equilibrium (LSE) is described by the b_1-factor, which gives the overpopulation of the ground state. The b_1-factor is determined by the ratio between n_1 and n_1^S, i.e. $b_1 = \frac{n_1}{n_1^S}$ (cf. Eq. 6.14). For $0.1 < b_1 < 10$, the atomic system is said to be still close to LSE, whereas for $b_1 > 10$, the atomic system is strongly ionizing and far from LSE [40].

Now we are going to analyse the deviation from LSE for the 15 mg and 50 mg Hg lamp operating with a square-wave ballast of 200 W. The Saha densities of the ground state can be determined from the measured electron density and electron temperature assuming LTE conditions. The ground state density of Hg is obtained from the XRA measurement (cf. section 5.4). Typical values of n_{Hg} in the center at the mid-plane of the lamp are $1.4 \times 10^{24} \, \text{m}^{-3}$ for the 15 mg lamp and $2.2 \times 10^{24} \, \text{m}^{-3}$ for the 50 mg lamp.

The Saha densities and the b_1-factors are plotted in Fig. 7.12. Fig. 7.12(b) shows that the b_1-factor for the 50 mg lamp is higher than that of the 15 mg lamp. The b_1-values for the 15 mg lamp are between 5 ($r = 0$) and 31 ($r = 0.29R$) whereas for the 50 mg lamp these are between 8 ($r = 0.03R$) and 75 ($r = 0.32R$). It also shows that the value of b_1
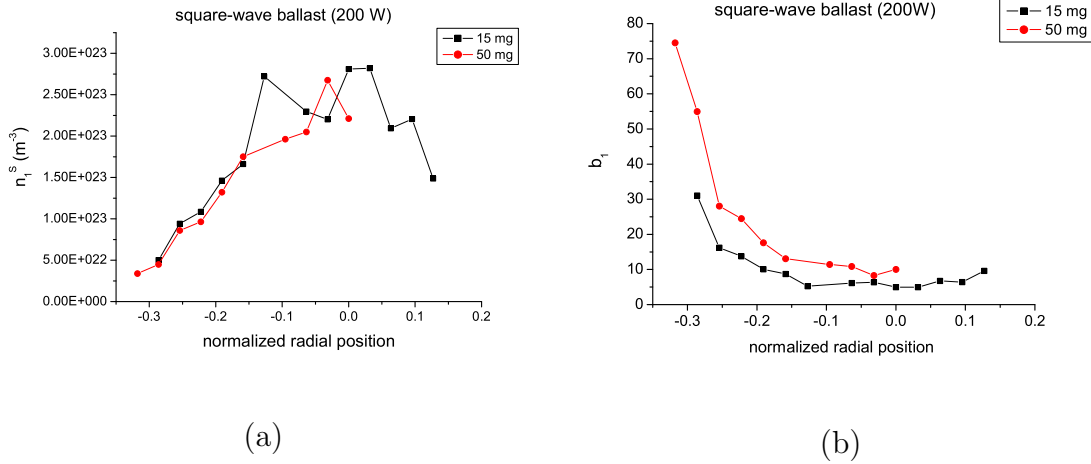
(a)   (b)

Figure 7.12: (**a**) *The calculated ground-state density of the Hg atoms according to the Saha equation as a function of the radial positions for the 15 mg and 50 mg Hg lamps. A spatially averaged electron temperature T_e is used for the Saha density calculation, which is 6730 K for the 15 mg lamp and 6700 K for the 50 mg lamp. (**b**) The calculated b_1-factor as a function of the radial positions for the 15 mg and 50 mg Hg lamp. Here the lamp was operated with a square-wave ballast of 200 W. The ground state density of Hg atoms is obtained by XRA measurement with the absorption cross-section of Hg of $3.58 \times 10^{-24} \, \mathrm{m}^2$ by assuming the mean X-ray energy is 17.6 keV.*

is increasing with the radius. When $r > 0.19R$ ($r > 1.7 \, \mathrm{mm}$), the b_1-values for the 15 mg lamp are more than 10. This means that in the center ($r < 0.19R$) of the lamp, the plasma is close to local Saha equilibrium. However for the 50 mg lamp, it is found that almost for all regions b_1 is larger than 10 which indicates that for this lamp the plasma is ionizing and deviates from LSE.

The increase of b_1-value with radius means that the plasma is more ionizing at higher r-values. This means that in the center the ionization process is almost balanced by the recombination process, while in the outer region of the discharge, the ionization process is much faster than the three particle recombination process. However this can not be balanced by diffusion. Therefore another recombination process must compensate for this net-ionization rate. One possibility might be associated with the formation and destruction of molecular ions. It is well known that the molecular ion recombination is a fast process that in many conditions was found to be responsible for the enhanced recombination.

7.7   Conclusions

As far as we know, it is the first time that Thomson scattering measurements have been performed on high pressure Hg discharge lamps. The electron gas properties, such as n_e and T_e are obtained for the lamps with Hg fillings of 15 mg, 30 mg, 50 mg and 70 mg,

131

operating with a square-wave ballast at different powers (150 W, 200 W and 240 W). From the results, we can draw several conclusions:

1. The electron density has a maximum in the center and decreases rapidly in the radial direction towards the wall in a parabola-like curve shape.

2. The electron temperature found by TS is relatively constant over the radial positions.

3. Due to the fitting error, the electron temperature can not be determined accurately. It has a relative random error of 10%. Moreover, an unknown systematic error is present due to the calibration method.

4. The electron density and the average electron temperature were found to increase slightly with lamp power.

5. Deviation from LTE is present in the 50 mg lamp in the sense that $T_e \neq T_g$. For this lamp the difference between the electron temperature (6600 K) and gas temperature (4200 K) is significant.

6. Deviation from Saha equilibrium is also present. It appears to be more severe in the 50 mg lamp than in the 15 mg lamp. The deviation from Saha increases with the distance from the center.

Further investigations are required in order to improve the accuracy of the TS technique towards other HID lamps. The following suggestions can be made

1. A higher dispersion of the TS spectrum will increase the accuracy in the fitting.

2. More images are required in order to increase the S/N ratio.

3. The competition of the plasma radiation and TS signal requires a higher laser energy in a short pulse time and short gate time. On the other hand, the laser power should stay in a safe region which does not disturb the plasma. Therefore a shorter gate time and hence a smaller laser pulse energy might be the solution for HID lamps, especially for the intense metal halide lamps.

4. A solution might be to replace the current Nd:YAG laser by a laser with a better beam quality, shorter pulse and high repetition rate.

Chapter 8

Conclusions

With the aim of understanding the segregation phenomena and the validation of the presence of LTE conditions in HID lamps, several active diagnostic methods were explored on HID lamps, i.e. γ spectroscopy, X-ray absorption (XRA) and Thomson Scattering (TS). A feasibility study on $\gamma-$ spectroscopy was carried out in order to investigate whether it is possible to detect the elemental density of Na (chapter 2). Moreover, an X-ray absorption setup was constructed and data handling procedures were developed to interpret the data in terms of the radial temperature profile. For the X-ray absorption technique, three aspects had to be dealt with: the experimental setup design (chapter 3), the data handling process (chapter 4) and the Abel inversion (chapter 4 and appendix C). Several XRA measurements have been performed on different types of HID lamps and the results give a solid proof that this XRA technique is suitable for the gas temperature measurements on HID lamps (chapter 5). The results indicate that the radial temperature profiles are significantly influenced by the presence of axial segregation in metal halide lamps and the power settings.

Furthermore a Thomson scattering technique has been successfully applied to two different types of high pressure plasmas: an Ar model lamp (chapter 6) and high pressure Hg discharge lamps (chapter 7). For the Ar model lamp, TS was applied to measure the electron properties at the region close to the electrodes. It was found that the plasma is far from LTE in the near-electrode region. In chapter 7 the results of Thomson scattering measurements show that LTE conditions are not present in the studied high pressure Hg lamp in two aspects: 1. $T_e \neq T_g$; 2. The b_1 factor indicates a deviation from Saha equilibrium, that is to say the (local) number of ionization processes largely exceeds that of atomic recombination processes.

In the following, the most important conclusions are presented for each chapter:

- *Chapter 2: Feasibility study of γ-spectroscopy on metal halide lamps.*
  In order to detect the elemental distribution of salt-additives in metal halide lamps, a γ-spectroscopy technique using radioactive isotopes and a detection system based on a pinhole has been investigated. Three radioactive isotopes ^{24}Na, ^{22}Na and ^{123}I

were studied. In the experiment, ^{24}Na nuclei were created by irradiating the lamp with neutrons in the near vicinity of cyclotron. It turns out to be impossible to do spatially resolved measurements on ^{24}Na with this method due to the low neutron flux, the small detection volume and small solid angle. Moreover, a feasibility study was carried out for other possibilities based on the experimental results. If the lamp could be placed for a longer period into a nuclear reactor, the amount of ^{24}Na might be increased such that it is feasible to do spatially resolved measurement.

It is found to be impossible to do spatially resolved measurement using commercial available ^{22}Na mainly due to the low photon count rate.

A promising method is the SPECT technique which has been successfully applied in nuclear medicine imaging. By introducing ^{123}I-labelled NaI into the lamp, it is in principle feasible to obtain the spatial distribution of iodine. However in practice it would involve handling of high radioactive material during the dosing process of the lamp. It requires a further investigation and an in-depth study in order to apply this method to metal halide lamps.

- *Chapter 3: Experimental design of X-ray absorption on HID lamps*
  The design of the XRA experiment on lamps is not trivial due to the characteristics of HID lamps:
  1. Hg is in the gas phase therefore the contrast between the absorption signal of Hg with respect to the wall material is low.
  2. The Hg density has a large gradient over a small radius (typically 2 mm).
  3. The burner has different path lengths at different lateral positions.

  Therefore, the XRA measurement system has been designed such that a high dynamic range, high brilliance, high spatial resolution (50~100 μm) and a monochromatic X-ray spectrum are reached.

- *Chapter 4: XRA data handling*
  The data handling procedure of X-ray absorption measurements is rather complex. Two main challenges are present: How to obtain a correct lateral density profile of Hg and how to perform Abel inversion properly. The first difficulty is solved by four major steps:
  1. The real signal is extracted by correcting the signal for dark current, flat field and the (scattering) offset.
  2. Each image is reconstructed to correct for image magnification.
  3. The lamp-off profile is directly fitted to find the plasma boundary properly with a theoretical function correcting for the beam hardening.
  4. The lamp-on profile is corrected for the geometrical mismatch, thermal expansion (density decrease) of the burner and the X-ray dose inequality to match the off-profile

for the burner wall and outside region.

After all these corrections the subtraction of the logarithm of off- and on-profiles yields the proper optical depth of Hg. This preludes the second difficult task, i.e. the Abel inversion process which is non-trivial due to the fact that the radial density profile has a minimum in the center. In order to reconstruct the original profile with minimum error and maximum physical meaning, the Tikhonov regularization method has been used in the Abel inversion process. To get the best result, the choice of the value of the Tikhonov regularization parameter μ is important.

In the future, it is necessary to deconvolute the raw XRA-profiles in order to avoid systematic errors on the temperature profile.

- *Chapter 5: XRA experimental results*
  The XRA method has been proved to be suitable for the measurement of the gas temperature field in HID lamps. Although not tested in the context of this study, it is also applicable to HID lamps with a different buffer gas than Hg, such as Xe or Zn.

  The results of the XRA measurements on the HID lamps with different fillings (pure Hg, single salt, salt mixture) show that axial segregation is present and influences the degree of constriction of the temperature profile. A 'worst case' scenario was chosen to test the detection capability of XRA and it turns out that it is successful even for the most unfavorable case in the family of HID lamps. The measurements on metal halide lamps at different power settings show that the higher the power, the more arc-constriction is observed.

- *Chapter 6: Thomson scattering measurements on an Ar DC discharge lamp*
  Thomson scattering has been successfully applied to study the plasma region close to the electrodes of an Ar model lamp in order to detect the electron gas properties in the near-electrode region. In this study the TS spectrum is partly collective. The results show that the plasma is ionizing and far from LTE near the electrode region.

- *Chapter 7: Thomson scattering on high pressure Hg discharge lamps*
  For the first time TS has been applied to high pressure Hg lamps. The deviation from LTE is present in lamps with a relatively large Hg filling dose in two different aspects: 1. The electron temperature is much higher than the gas temperature. 2. The plasma deviates from Saha equilibrium and this deviation increases with the distance to the center.

Bibliography

[1] Lister G G, Lawler J E, Lapatovich W P and Godyak V A 2004 *Rev Mod Phys* **76** 541–598

[2] Fischer E 1976 *J Appl Phys* **47** 2954–2960

[3] H.P.Stormberg 1981 *J Appl Phys* **52** 3233–3237

[4] Zollweg R J 1975 *Journal of the Illuminating Engineering Society* **5** 12–19

[5] Heijden H 2002 *Modelling of radiative transfer in light sources* Ph.D. thesis Eindhoven University of Technology, The Netherlands

[6] Stijfs A 2003 *Modelling segregation phenomena in metal halide lamps*

[7] Curry J J, Adler H G, Lee W K and Shastri S D 2003 *J Phys D Appl Phys* **36** 1529–1534

[8] Curry J J, Adler H G, Shastri S D and Lawler J E 2001 *Appl Phys Lett* **79** 1974–1976

[9] Curry J J, Adler H G, Shastri S D and Lee W K 2003 *J Appl Phys* **93** 2359–2368

[10] Krane K S 1988 *Introductory Nuclear Physics* (John Wiley & Sons, Inc.)

[11] Lederer C M and Shirley V S 1978 *Table of Isotopes, 7th edition* (John Wiley & Sons, Inc.)

[12] Moerdijk G and Franken Y *private communication*

[13] Moerdijk G *private communication*

[14] Keyser R M, Twomey T R and Sangsingkeow P 1998 *The 1998 Winter Meeting of the American Nuclear Society* Http://www.ortec-online.com/pdf/onefitall.pdf

[15] Habraken J B A, de Bruin K, Shehata M, Booij J, Bennink R, van Eck Smit B L F and Sokole E B 2001 *J Nucl Med* **42** 1863–1869

[16] Fohl T, Kramer J M and Lester J E 1993 *J Appl Phys* **73** 46

[17] Curry J J, Sakai M and Lawler J E 1998 *J Appl Phys* **84** 3066–3072

Bibliography

[18] Curry J J, Adler H G, MacPhee A, Narayanan S and Wang J 2004 *Plasma Sources Sci Technol* **13** 403–408

[19] Chantler C 1995 *J Phys Chem Ref Data* **24** 71–643

[20] B.D.Cullity 1978 *Elements of X-ray diffraction* (California: Addison-Wesley Publishing Company,Inc)

[21] William H. Press Saul A. Teukolsky W T V and Flannery B P 1992 *Numerical Recipes in C, The Art of Scientific Computing, Second Edition* (Cambridge University Press)

[22] Waymouth J F 1971 *X-Ray data booklet* (Massachussets: The M.I.T. Press)

[23] Nimalasuriya T Future papar in preparition

[24] Flikweert A J Future papar in preparition

[25] van de Sande M J 2002 *Laser scattering on low temperature plasmas — High resolution and stray light rejection* Ph.D. thesis Eindhoven University of Technology, The Netherlands `http://alexandria.tue.nl/extra2/200210414.pdf`

[26] van de Sande M J and van der Mullen J J A M 2002 *J Phys D Appl Phys* **35** 1381–1391

[27] van de Sande M J, Deckers R H M, Lepkojus F, Buscher W and van der Mullen J J A M 2002 *Plasma Sources Sci Technol* **11** 466–475

[28] Nandelstädt D, Redwitz M, Dabringhausen L, Luhmann J, lichtenberg S and Mentel J 2002 *J Phys D Appl Phys* **35** 1639–1647

[29] L.Dabringhausen, Nandelstädt D, Luhmann J and Mentel J 2002 *J Phys D Appl Phys* **35** 1621–1630

[30] Luhmann J, Lichtenberg S, Langenscheidt O, Benilov M S and Mentel J 2002 *J Phys D Appl Phys* **35** 1631–1638

[31] Lichtenberg S, Nandelstädt D, Dabringhausen L, Redwitz M, Luhmann J and Mentel J 2002 *J Phys D Appl Phys* **35** 1648–1656

[32] Hartmann T, Günther K, Lichtenberg S, Nandelstädt D, Dabringhausen L, Redwitz M and Mentel J 2002 *J Phys D Appl Phys* **35** 1657–1667

[33] H.Schmitz and K.U.Riemann 2001 *J Phys D Appl Phys* **34** 1193–1202

[34] H.Schmitz and K.U.Riemann 2002 *J Phys D Appl Phys* **35** lighting cluster

[35] Benilov M S and Marotta A 1995 *J Phys D Appl Phys* **28** 1869–1882

[36] Bötticher R and Bötticher W 2000 *J Phys D Appl Phys* **33** 367–374

[37] Flesch P and Neiger M 2002 *J Phys D Appl Phys* **35** 1681–1694

[38] Evans D E and Katzenstein J 1969 *Rep Prog Phys* **32** 207–271

[39] Salpeter E E 1960 *Phys Rev* **120** 1528

[40] Jonkers J, van de Sande M, Sola A, Gamero A and van der Mullen J 2003 *Plasma Sources Sci Technol* **12** 30–38

[41] van der Mullen J A M and Jonkers J 1999 *Spectrochim Acta B* **54** 1017

[42] Hartgers A and van der Mullen J A M 2001 *J Phys D* **34** 1907

[43] Jonkers J 1998 *Excitation and transport in small scale plasmas* Ph.D. thesis Eindhoven University of Technology, The Netherlands `http://alexandria.tue.nl/extra2/9800212.pdf`

[44] Devoto R S 1973 *Phys Fluids* **16** 616

[45] McDaniel E W 1964 *Collision phenomena in ionized gases* (New York: John Wiley & Sons)

[46] Raizer Y P 1991 *Gas Discharge Physics* (Springer-Verlag)

[47] Zhu X, Redwitz M, Kieft E R, van de Sande M J and van der Mullen J J A M 2004 *J Phys D Appl Phys* **37** 736–743

[48] Elenbaas W 1951 *The High-pressure Mercury-vapour Discharge* (Amsterdam: North Holland)

[49] Penney C M, Peters R S and Lapp M 1974 *Journ Opt Soc Am* **64** 712

[50] England J P and Elford M 1991 *Aust J Phys* **44** 647–675

[51] M.Bertero and Boccacci P 1998 *Introduction to inverse problems in imaging* (Bristol and Philadelphia: Institute of Physics Publishing)

[52] Henke B L, Gullikson E M and Davis J C 1993 *Atomic Data and Nuclear Data Tables* **54** 181–342

Appendix A

Numerical simulation of blurring and beam divergence

A.1 Blurring test

In order to test the effect of blurring on the X-ray profile, numerical simulations have been done for a lamp of type 3 (cf. Table 5.1). A normalized Gauss function has been used to simulate the instrumental profile, i.e.

$$K(x) = \frac{1}{\sigma\sqrt{2\pi}}e^{-x^2/2\sigma^2}. \tag{A.1}$$

The standard deviation is the result of the combination of the finite source dimension and the spatial resolution of the CCD camera. A typical value that can be selected is $\sigma = 30$ μm. The transmission profile can be simulated by convoluting the real transmission profile with the Gauss function as

$$g^{(0)}(x) = \int K(x - x')f^{(0)}(x')dx', \tag{A.2}$$

where $f^{(0)}(x)$ represents the original object, $K(x - x')$ is the point spread function (PSF) of the linear system, $g^{(0)}(x)$ is the resulting (noise-free) image which is also called a blurred version of the object $f^{(0)}(x)$.

   In order to see the effect of blurring on the optical depth, two profiles are shown in Fig. A.1, one with and the other without blurring. It is clearly shown that the instrumental profile only has influence in the region close to the inner and outer boundary of the burner. This blurring effect could have been corrected by a deconvolution procedure. However, such a deconvolution procedure will also introduce oscillations. One of the methods to solve the problem of these oscillations is to introduce the Tikhonov regularization method [51]. Since the influence of the instrumental profile (as shown in Fig. A.1) is not very big, a direct fitting procedure (cf. section 4.4) was employed instead.
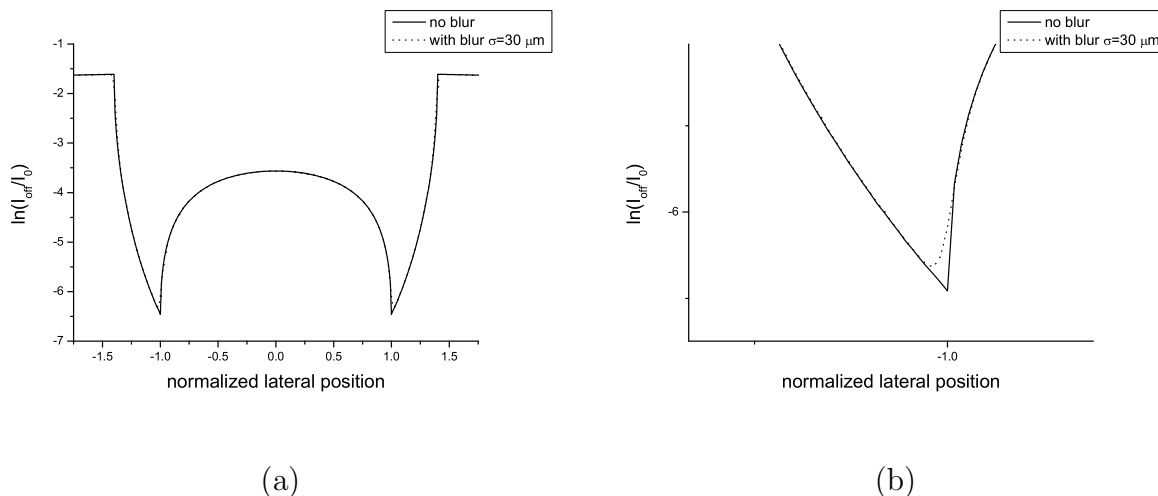
(a)   (b)

Figure A.1: ***(a)*** *The logarithm of the transmission profile of a lamp-off case with and without blurring. The solid line is the calculated lamp-off profile without blurring. The dotted line is the calculated blurred image for which* $\sigma = 30\,\mu\mathrm{m}$ *.* ***(b)*** *Result of the zooming-in profiles of* ***(a)*** *for the region near the inner boundary of the burner.*

A.2   Non-parallel beam test

In the previous section, the blurring effect has been simulated with an instrumental profile of $\sigma = 30\,\mu\mathrm{m}$. The blurring effect can only be noticed near the inner and outer boundary of the burner. In this subsection, we will apply a numerical simulation to determine the influence of the beam divergence. This has been done for a typical experimental geometry, i.e. $L_1 = 84\,\mathrm{cm}$ and $L_2 = 7\,\mathrm{cm}$ (cf. Fig. 3.1) for a type 3 lamp (cf. Fig. 1.5). The transmission profiles are calculated for three different beams: a parallel beam, a point-source beam and a divergent beam with an instrumental profile of 96 $\mu\mathrm{m}$[1]. The results are shown in Fig. A.2.

Fig. A.2 clearly shows that the beam divergence has much more influence on the transmission profile than the blurring caused by a non-point source. Therefore, the following conclusions can be drawn: 1. the influence of the dimension of the X-ray source is moderate. 2. a translation of the coordinate from point source beam to parallel beam is needed.

---

[1]This is 3 times bigger (for purpose of demonstration) than that of the real measured instrumental profile. The instrumental profile is determined experimentally, i.e. $\sigma = 32\,\mu\mathrm{m}$.
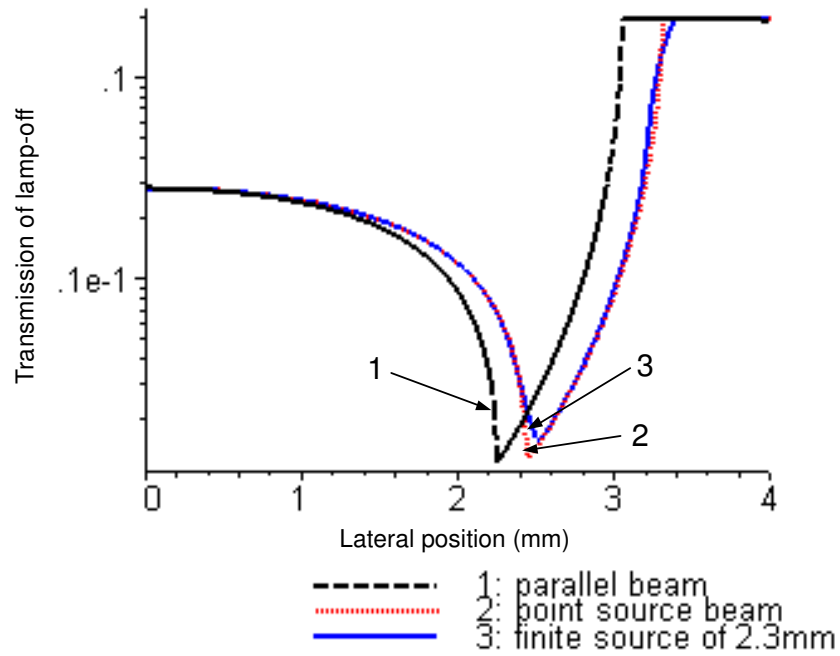
Figure A.2: The transmission profile of the type IV lamp irradiated by 3 different beams: a parallel beam 1, a point source beam 2 and a finite source beam 3 with a lateral dimension of 2.3 mm (equivalent with an instrumental profile of 96 μm). Case 3 is equivalent to a measurement done with an instrumental profile that is 3 times larger than what we found experimentally for our setup. Nevertheless we see that this influence of blurring is rather limited.

Appendix B

Optimum Hg contrast and calibration of X-ray energy

The column density of mercury is determined by means of a subtraction procedure in which the contribution of the absorption of the wall material, PCA (Al_2O_3), is eliminated. It is evident that the accuracy of this procedure is poor if the optical depth ($\tau = n\sigma l_x$) of the wall material is much larger than that of Hg. In this appendix we will search for the optimum conditions, that is to say, for the conditions for which the contrast of Hg is relatively large. Therefore we have to optimize the ratio

$$\frac{\tau_{Hg}(x)}{\tau_b(x)} = \frac{n_{Hg}\sigma_{Hg}(E)l_{Hg}(x)}{n_b\sigma_b(E)l_b(x)}. \tag{B.1}$$

In this study we confine ourselves to the oven-lamp for which the density of Hg is constant. Since the ratio of the geometrical distance $l_{Hg}(x)/l_b(x)$ has a fixed dependence on x, we have to determine the optimum E value for which $\sigma_{Hg}(E)/\sigma_b(E)$ is at maximum. Since the accuracy of the density profile is determined by the accuracy near the wall, we are especially in search for the E-value for which the contrast of Hg is large in the wall vicinity.

B.1   Hg contrast

The investigation towards the optimum Hg-contrast will be guided by an error analysis of the column density of mercury. We will assume that this error only depends on the noise of the data which is dominated by Poisson statistics (cf. section 3.5.2). An essential quantity in such a noise analysis is the initial number of X-ray photons (X-ray dose) ϕ_0. After being filtered by means of Zr and the outer tube, the X-ray photons will transverse through the burner wall and the Hg cloud, and are collected by the CCD. Finally it gives rise to a measured number of counts. In this case study we deal with a dose of $\phi_0 = 5.6 \times 10^5$ photons which corresponds to a Multiple-Exposures-Multiple-Pixels (MEMP) measurement of an accumulation of 20 images and a vertical binning of 20 pixels.

Appendix B

The measured signal $\phi_{ovenOff}$ and ϕ_{ovenOn} correspond to $\phi_0 t_b$ and $\phi_0 t_b t_{Hg}$ X-ray photons, where $t_b = e^{-\tau_b}$ and $t_{Hg} = e^{-\tau_{Hg}}$ are the transmission of the burner and Hg respectively. Using Poisson statistics, we find that the relative uncertainties of $\phi_{ovenOff}$ and ϕ_{ovenOn} are

$$\frac{\delta\phi_{ovenOff}}{\phi_{ovenOff}} = \frac{1}{\sqrt{\phi_0 t_b}} \; ; \; \frac{\delta\phi_{ovenOn}}{\phi_{ovenOn}} = \frac{1}{\sqrt{\phi_0 t_b t_{Hg}}}. \tag{B.2}$$

Applying the error propagation formula to

$$F = \frac{\tau_{Hg}}{\bar{\sigma}} = \frac{\ln\phi_{ovenoff} - \ln\phi_{ovenon}}{\bar{\sigma}} \tag{B.3}$$

we find

$$\begin{aligned}
\delta F &= \sqrt{\frac{1}{\bar{\sigma}^2}[(\delta\ln\phi_{ovenOff})^2 + (\delta\ln\phi_{ovenOn})^2]}; \tag{B.4} \\
&= \frac{1}{\bar{\sigma}}\sqrt{\frac{1}{\phi_0 t_b}\left(1 + \frac{1}{t_{Hg}}\right)},
\end{aligned}$$

so that the relative uncertainty of column density equals

$$\frac{\delta F}{F} = \frac{1}{\tau_{Hg}}\sqrt{\frac{1}{\phi_0 t_b}\left(1 + \frac{1}{t_{Hg}}\right)}. \tag{B.5}$$

The role of the various quantities in equation B.5 becomes more clear if we may assume that the absorption of Hg is so small that the term in between the brackets in Eq. B.5 can be approached by 2. In that case equation B.5 can be simplified to

$$\frac{\delta F}{F} = \frac{e^{\tau_b/2}}{\tau_{Hg}}\sqrt{\frac{2}{\phi_0}}, \tag{B.6}$$

demonstrating that the relative error in the column density decreases with $\sqrt{\phi_0}$ (Poisson statistics) and will be smaller if Hg is more absorbing while τ_b is smaller. By comparing Eq. B.6 with Eq. B.1 we see that τ_b has much more influence in the value of $\delta F/F$ since it appears as the argument of an exponent. Therefore a reduction of τ_b is especially worthwhile.

We will study the Hg contrast for three lateral positions, namely for $x = 0$, $x = 0.75R$ and $x = 0.99R$ where R is the inner radius of the burner. Since the Hg density in the oven-lamp equals $4.43 \times 10^{25}\,\mathrm{m}^{-3}$ (cf. section 4.3.4), we can determine the Hg column density for these three lateral positions since the path lengths are known.

The mass density of the burner (PCA) is $3.97\,\mathrm{g/cm^3}$ and the length of the paths through the wall can easily be found (cf. Eq. 4.23). Finally, by inserting the values of the absorption cross-section of Hg and Al_2O_3 for different X-ray energy values as found in literature [52], we can calculate the transmission $t = e^{-n\sigma l}$ of the burner and Hg. Using Eq. B.5 we can
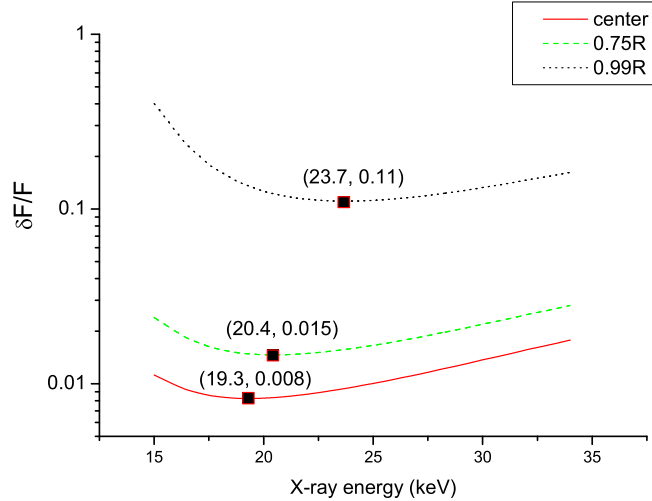
Figure B.1: The relative error of the column density of Hg as a function of the X-ray photon energy for different lateral positions x of the oven-lamp. Each curve has a minimum; the $\delta F/F$ value and the corresponding E value for that minimum is given. The initial X-ray dose after filtering by the outer bulb ϕ_0 is taken as 5.6×10^5 X-ray photons which corresponds with a Multiple-Exposures-Multiple-Pixels (MEMP) of 20 images accumulation and 20 pixels binning; each image has an exposure time of 60 s.

determine the relative errors of the column density of Hg as a function of X-ray energy for different lateral positions.

The results are given in Fig B.1, which demonstrates that there is an optimum energy value for which $\delta F/F$ is the lowest, and that this optimum energy changes with lateral position.

It also shows that the highest relative error $\delta F/F$ is attained at the boundary ($x = 0.99R$) for which $\delta F/F$ turns out to be 0.11, while the corresponding X-ray energy equals $E = 23.7$ keV. This optimum E-value for the edge region is the most suitable energy value for the experiment as a whole, that is, for all path lengths. The reason is that an accurate Abel procedure of a hollow profile needs a well-defined value for the outer part.

In order to find the acceleration voltage that creates photons with an (averaged) energy of 23.7 keV we constructed figure B.2. It gives the cross section as a function of energy as known from literature (solid curve) together with the measured mean cross-sections $\bar{\sigma}$ as found experimentally with our oven-lamp setup. These experimental values are put on the curve so that the corresponding (mean) photon energy can be found. From Fig. B.2(a), a plot of the mean X-ray energy versus acceleration voltage can be deduced, which is shown in Fig. B.2(b). Using this graph the required acceleration voltage for the optimum X-ray energy of 23.7 keV can be estimated. It turns out to be around 40 kV for this case. For other geometries and wall materials this analysis has to be re-evaluated.
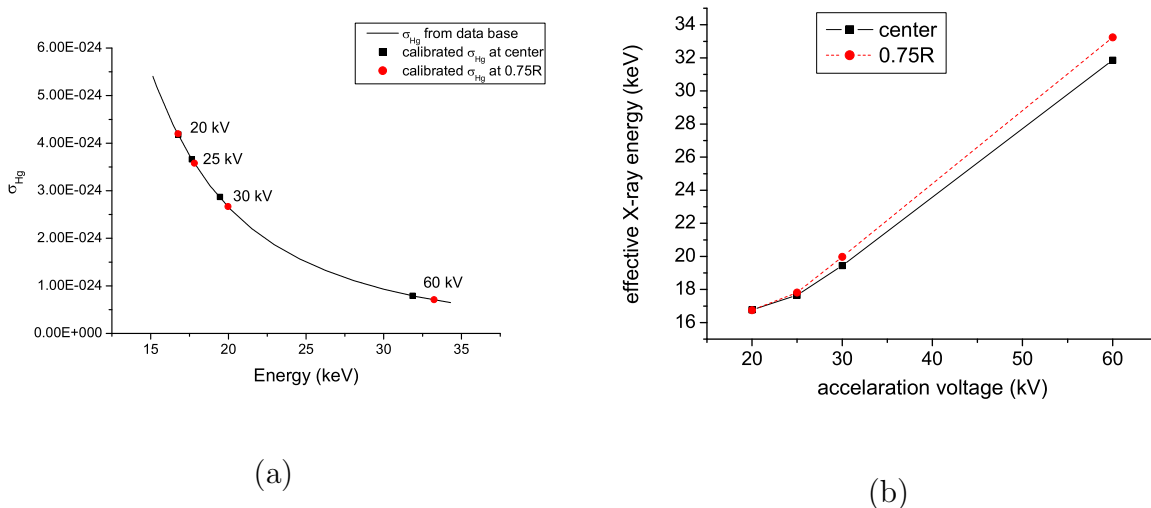
(a)

(b)

Figure B.2: **(a)**: *The cross section as a function of energy as known from literature (solid curve). The measured mean cross sections $\bar{\sigma}$ as found experimentally are also given for two lateral positions: $x = 0$ and $x = 0.75R$. These are given with the corresponding acceleration voltages and located on the cross section curve so that the corresponding (mean) photon energy can be found. This is found to be lower than the acceleration energy.* **(b)**: *The effective energy plot versus acceleration voltage for oven-lamp geometry.*

Some more information can be deduced from Fig. B.2:

Firstly, it is evident that we can trust our oven-lamp experiments; the $\bar{\sigma}$-values that are found are in good agreement with the literature values, especially if we realize that the values of the acceleration voltages should always be (somewhat) larger than the corresponding mean photon energy values.

Secondly, it is also demonstrated that the effective energy in the outer region ($x = 0.75R$) is in all cases higher than that of the center. This points towards beam-hardening.

Thirdly we find that the higher the acceleration voltage, the larger the separation is between the $\bar{\sigma}$-value for two lateral positions $x = 0$ and $x = 0.75R$. This means that for higher acceleration voltages, the beam-hardening is much more important; or to state it differently, that the beam is more monochromatic for low acceleration voltages.

We may conclude that:

1. In practice, the Hg contrast of a burning lamp will be somewhat better since in contrast to the oven-lamp for which this study was done, we have a larger Hg concentration at the wall of a burning lamp. The reason is that Hg forms an unsaturated vapor for typical HID lamp on Hg filling dosage, so for the same Hg dose the density of Hg in a burning lamp will be lower in the center ($n = p/(kT)$) and higher near

the wall as the average density must stay the same as that of the oven lamp.

2. There is a trade-off between the monochromaticity of the beam and the Hg contrast of the image. For low E-values, we are not limited by beam-hardening but the Hg contrast is poor. On the other hand at optimum contrast condition, i.e. at 40 kV, the beam will not be monochromatic anymore.

3. Finally one could consider to reduce the wall thickness, but this has its limitations as thin envelopes can easily explode due to the gas pressure in the burner during operation,

Appendix C

Numerical test of Abel inversion

The final result of Abel inversion depends on two factors: the noise in the column density and the order of the fitting function. In order to see how these two factors influence the final result, several numerical tests have been done.

C.1 Noise and error analysis

There is always noise on the measurement data, and this noise will have an influence on the Abel inversion results. In order to determine this effect, we need a procedure to simulate the noise. This is based on the following considerations.

If the measured signal in a pixel expressed in the number of X-ray photons equals ϕ, then the noise $\delta\phi$ in ϕ is given by $\delta\phi = \sqrt{\phi}$. This is justified since the noise of detected X-ray photons is governed by Poisson statistics. Therefore the noise in the logarithm of the signal ($\delta \ln \phi$) can be written as

$$\delta \ln \phi = \frac{\partial \ln \phi}{\partial \phi} \times \delta\phi = \frac{1}{\sqrt{\phi}}. \tag{C.1}$$

Using Eq. 4.15, the noise in the column density of Hg will be

$$\delta F(x) = \frac{1}{\sigma_{Hg}}\sqrt{(\delta \ln \phi_{off})^2 + (\delta \ln \phi_{on})^2} \approx \frac{\sqrt{2}}{\sigma_{Hg}} \times \delta \ln \phi_{off} = \frac{\sqrt{2}}{\sigma_{Hg}} \times \frac{1}{\sqrt{\phi_{off}}}. \tag{C.2}$$

The approximation which leads to the second (near) equality is justified if the absorption of Hg is low so that the difference between ϕ_{off} and ϕ_{on} is very small and consequently $\delta\phi_{off} \approx \delta\phi_{on}$.

Based on Eq. C.2, a formula is derived to create the noise numerically as

$$\delta F(x) = N_{rand}(x) \times \frac{A}{\sqrt{\phi_{off}}}, \tag{C.3}$$

where N_{rand} is the random noise, created by the computer in the range of [-0.5, 0.5], and A a number by which the amplitude of the noise can be manipulated. This noise generator will be used in section C.3.

C.2   Least square fitting

As described in section 4.7, the unknown density distribution of Hg $f(r)$ is expanded to a polynomial series:

$$f(r) = \sum_{i=1}^{N} a_{2(i-1)} f_{2(i-1)}(r), \tag{C.4}$$

where the polynomial functions are

$$f_{2i}(r) = r^{2i}. \tag{C.5}$$

Inserting this in the Abel integral, the lateral profile in the projection space is obtained as

$$G(x) = 2 \sum_{i=1}^{N} a_{2(i-1)} \int_{x}^{R} f_{2(i-1)}(r) \frac{r}{\sqrt{r^2 - x^2}} dr, \tag{C.6}$$

where the integrals

$$g_{2i}(x) = 2 \int_{x}^{R} f_{2i}(r) \frac{r}{\sqrt{r^2 - x^2}} dr \tag{C.7}$$

can be solved analytically. The coefficients a_{2i} are evaluated from the data $g_{meas}(y_k)$ that is measured at M points. After least square fitting we get

$$\sum_{k=1}^{M} (G(x_k) - g_{meas}(x_k))^2 \rightarrow \min. \tag{C.8}$$

The partial derivative of this condition to the unknown coefficients a_{2i} yields a system of equations:

$$\sum_{i=1}^{N} a_{2(i-1)} \sum_{k=1}^{M} g_{2(m-1)}(x_k) g_{2(i-1)}(x_k) = \sum_{k=1}^{M} g_{2(m-1)}(x_k) g_{meas}(x_k), \ m = 1 \cdots N. \tag{C.9}$$

In a matrix notation, this can be written as

$$\mathbf{M} \cdot \vec{a} = \vec{b}, \tag{C.10}$$

where $\mathbf{M}$ is a square and symmetric $N \times N$ matrix with

$$M_{mi} = \sum_{k=1}^{M} g_{2(m-1)}(x_k) g_{2(i-1)}(x_k), \quad for \ 1 \leq m \leq N, \ 1 \leq i \leq N. \tag{C.11}$$

The column vectors are given by

$$\vec{a} = (a_0 \ \cdots \ a_{2(i-1)} \ \cdots \ a_{2(N-1)})^T \tag{C.12}$$

and

$$\vec{b} = (b_1 \ \cdots \ b_m \ \cdots \ b_N)^T, \ \ with \ b_m = \sum_{k=1}^{M} g_{2(m-1)}(x_k) g_{meas}(x_k). \tag{C.13}$$

Therefore the unknown coefficients $a_{2(i-1)}$ can be obtained by inverting the matrix $\mathbf{M}$:

$$\vec{a} = \mathbf{M}^{-1} \cdot \vec{b}. \tag{C.14}$$

For each lateral position x_k, $g_{2(i-1)}(x_k)$ are the base function values calculated from Eq. C.7, while $g_{meas}(x_k)$ represent the measured data. Solving this system yields the coefficients $a_{2(i-1)}$. After that the unknown radial distribution can be obtained by Eq. C.4.

C.3 Influence of the dimension of the projection space

In order to test the influence of the noise and the dimension of the projection space, an analysis of the noise propagation in the fitting procedure was performed for a density profile given by $n(r) = 0.2 + 0.8r^2$. The corresponding noise-free lateral profile is given by

$$F(x) = \frac{14}{15}\sqrt{1 - x^2} + \frac{16}{15}x^2\sqrt{1 - x^2}. \tag{C.15}$$

Therefore the following recipe is followed: 1. The radial density profile $n(r) = 0.2 + 0.8r^2$ is projected to the "lateral space" which is given in Eq. C.15. 2. Noise with different amplitude is added to the lateral profile (cf. Eq. C.15). 3. The noisy lateral profile is fitted with $F(x) = \sum_{i=0}^{n} a_{2i}F_{2i}$ of different dimensions n.

Fig. C.1 shows the different noise amplitudes that have been superimposed onto the column density profile of Hg. With the least square fitting in the projection space, new values of a_{2i} are determined. This provides a new radial profile. The reconstructed radial profile depends on: 1. The dimensions of the base function in projection space. 2. The numerical error of the least square fitting procedure itself. 3. The noise in the data.

In the following, two examples are given for the reconstructed radial profile with two different base functions: the first of order 2 and the second of order 8. The reconstructed radial profiles of order 2 corresponding to the lateral base function $F(x) = 2(a_0F_0 + a_2F_2)$ are shown in Fig. C.2(a)(b)(c). The 8-order radial profiles corresponding to lateral base function of $F(x) = 2(a_0F_0 + a_2F_2 + a_4F_4 + a_6F_6 + a_8F_8)$ are shown in Fig. C.2(d)(e)(f).

Fig. C.2 shows that fitting with a higher order function introduces a larger error on the reconstructed results. The more noise on the Hg column density profile, the larger the error in the final results. Therefore, a conclusion can be drawn that the orders of the
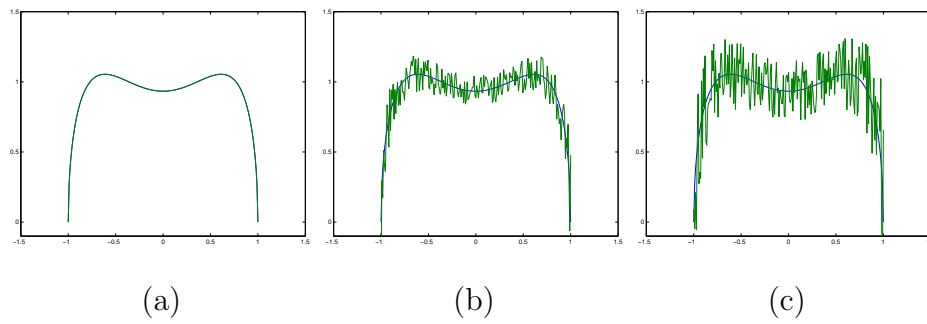
Figure C.1: *Three cases of lateral profiles obtained by adding noise to the lateral profile given by Eq. C.15.* **(a)** *Noise-free lateral profile with A=0.* **(b)**: *A random noise with A=3.* **(c)**: *A random noise with A=6. The smooth curve is the noise-free lateral profile given by Eq. C.15.*
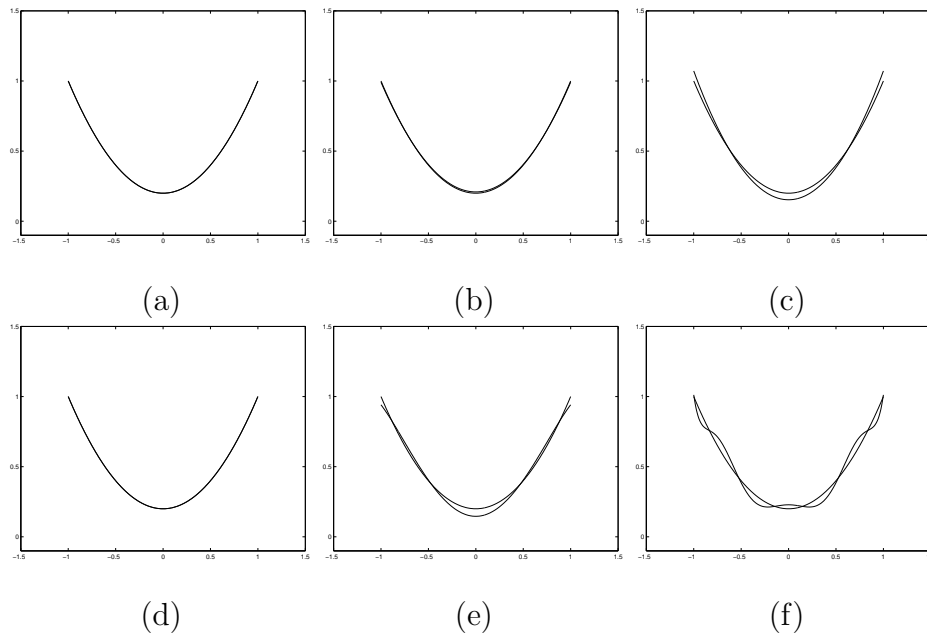

Figure C.2: *The reconstructed radial profiles after fitting of the lateral profiles given in Fig. C.1 (where noise was superimposed with different amplitudes). Here an initial radial density profile was chosen of form $n(r) = 0.2 + 0.8r^2$. The lateral base function is chosen as $F(x) = 2(a_0F_0 + a_2F_2)$ for (a)(b)(c).* **(a)** *Noise-free (A=0).* **(b)** *A=3.* **(c)** *A=6. For (d)(e)(f) the base function is chosen as $F(x) = 2(a_0F_0 + a_2F_2 + a_4F_4 + a_6F_6 + a_8F_8)$* .**(d)** *Noise-free (A=0).* **(e)** *A=3.* **(f)** *A=6.*

fitting function should be chosen such that it is just enough to get a good fit. The reason is that higher orders of the fitting function can be "excited" by the noise in the signal so that an erroneous result is obtained. If the data itself is noise-free, then the orders of the fitting function do not influence the result.

(a)   (b)   (c)
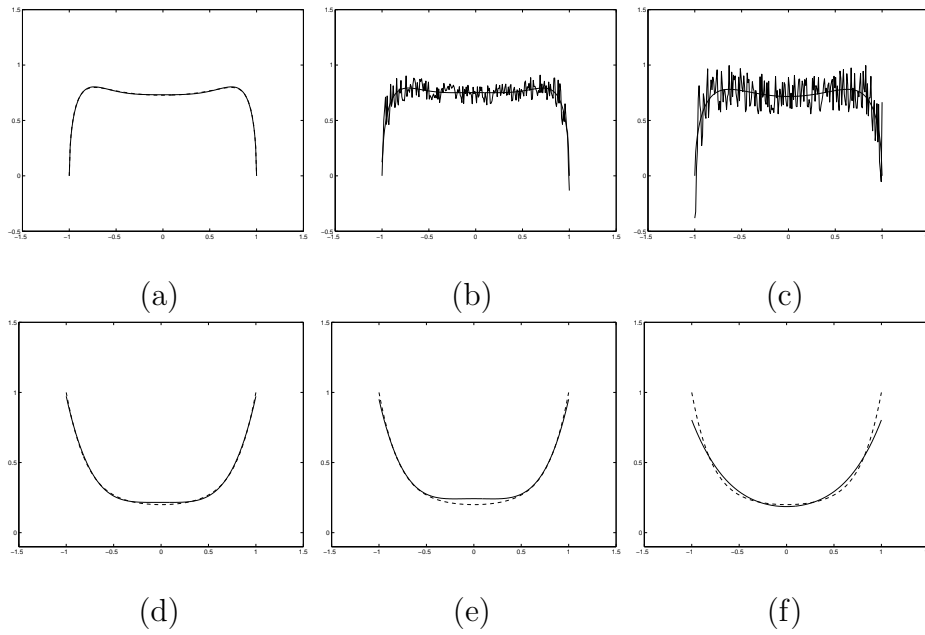
(d)   (e)   (f)

Figure C.3: The fitting of the lateral profile (a,b,c) and the reconstructed radial profile (d,e,f) with different amplitudes of the superimposed noise. Here a radial density profile was given as $n(r) = 0.2 + 0.2r^2 + 0.2r^4 + 0.4r^6$. The lateral base function was chosen as $F(x) = 2(a_0 F_0 + a_2 F_2 + a_4 F_4)$. (a) Noise-free lateral profile. (b) Lateral profile with a noise with A=2.5. (c) Lateral profile with a noise with A=5. (d) Radial profile for noise-free case. (e) Radial profile for a random noise with A=2.5. (f) Radial profile for a random noise with A=5.

However, since the radial profile of the Hg density is not known a priori, it is difficult to know how many orders of the fitting function are needed for an appropriate fitting. Therefore, it is not always good to choose a low order fitting function since it may not be a suitable representation of the original profile.

This is illustrated by the following example for which the radial density profile is given by $n(r) = 0.2 + 0.2r^2 + 0.2r^4 + 0.4r^6$, that is of order 6. We constructed three lateral profiles with different noise levels: A=0 (noise free), A=2.5 and A=5. To reconstruct the original radial function, the lateral base function $F(x) = 2(a_0 F_0 + a_2 F_2 + a_4 F_4)$ was chosen; thus of lower order than the initial radial function. The reconstructed profiles for these three different noise level are given in Fig. C.3. In this figure, (d), (e) and (f) show the reconstructed radial profiles; they correspond to the fit of (a), (b), (c) respectively.

It is clearly shown that the low order fitting function does not reconstruct the original profile very well, especially for the high noise case. Therefore the low order fitting function can work to a certain extent, but for high noise levels it will also introduce large errors in the reconstructed profiles and it will not represent the original profile properly. From this we have to conclude that the reduction of the order of the fitting function does not always work and that we need to find another solution for the fitting with higher order base functions that is not sensitive to the noise in the data. This method is called the

Tikhonov regularization method [51].

C.4 Tikhonov regularization method

The linear inverse problem of reconstruction of the original object from the projected profile is an example of an ill-posed problem that is characterized by instability to small variations (noise) in the data. The thorough mathematical formulation of the ill-posed problem is given in [51]. Abel-inversion is also a typical ill-posed problem. In the presence of noise, the exact solution of such a problem will be unstable and have no physical meaning. Therefore, the exact solution is not the best solution. In order to deal with this, we should not look for the exact solution, but try to find such approximate solution (reconstructed object) that satisfactorily approximates the true solution and at the same time is stable to the noise. To find this optimal solution, we need to make use of some additional properties of the solution, which can be given in the form of mathematical constraints having a physical meaning. The Tikhonov regularization is a method that allows us to do so. The Tikhinov regularization is used to stabilize the solution of the least square fitting by restricting all possible solutions to the solutions with minimum norm. Instead of conventional least square minimization, it is called penalized least square minimization in which the fitting parameters are found by

$$\vec{a} = (\mathbf{M}^*\mathbf{M} + \mu\mathbf{I})^{-1}M^* \cdot \vec{b}, \tag{C.16}$$

where μ is the regularization parameter, $\mathbf{M}^*$ the transposed matrix of $\mathbf{M}$ and $\mathbf{I}$ the identity matrix.

In the inverse procedure, two types of errors are introduced, the approximation error and the noise-propagation error. Since the approximation error increases with μ, whereas the noise-propagation error decreases with μ, there is an optimum value of μ for the inverse problem. A numerical test has to be made for each case in order to get an optimum μ value. With this method, even higher order lateral base functions can be chosen which can reconstruct the profile as close as possible to the original one, provided that an optimum value of the Tikhonov regularization parameter μ is used.

To show the effect of the Tikhonov regularization method, it was applied to the same profile as that of Fig. C.3, by fitting with a higher order of lateral base function $F(x) = 2(a_0F_0 + a_2F_2 + a_4F_4 + a_6F_6 + a_8F_8)$, the reconstructed radial profiles are shown for different noise levels in Fig C.4. The results of the fitting without Tiknonov regularization will be shown in Fig. C.5.

From the noise analysis, we can draw some conclusions:

1. The fitting result is sensitive to the noise in the signal. A larger noise will introduce larger errors in the result.

2. For noise-free data, the fitting will give the same result as the original if a higher order polynomial fitting function is chosen.

3. For the same noise level data, a higher order of the fitting function will be more sensitive
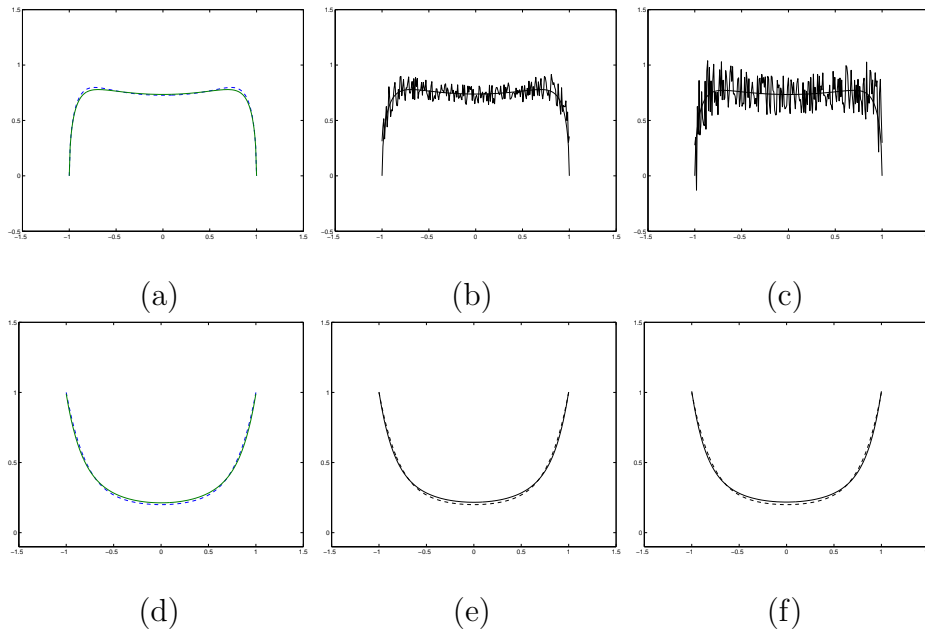
(a) (b) (c)

(d) (e) (f)

Figure C.4: The fitting of the lateral profile (a,b,c) and the reconstructed radial profile (d,e,f) with different amplitude of the superimposed noise. Here a radial density profile was given as $n(r) = 0.2 + 0.2r^2 + 0.2r^4 + 0.4r^6$. The lateral base function was chosen as $F(x) = 2(a_0 F_0 + a_2 F_2 + a_4 F_4 + a_6 F_6 + a_8 F_8)$. In this fitting procedure, a Tikhonov regularization method has been used with a regularization parameter $\mu = 5$. (a) Noise-free lateral profile. (b) Lateral profile with a noise with A=2.5. (c) Lateral profile with a noise with A=5. (d) Reconstructed radial profile for noise-free case. (e) Reconstructed radial profile for a random noise with A=2.5. (f) Reconstructed radial profile for a random noise with A=5.

to the noise and produce oscillations in the final result.

4. In order to get the best result with a minimum error, both the selection of the orders of the lateral base function and the choice of the value of Tikhonov regularization parameter μ are important. Since the original radial density profile is not known a priori, the base function should contain enough terms to describe the radial profile. Then the numerical test has to be done for each case to find the optimum value of the regularization parameter μ.
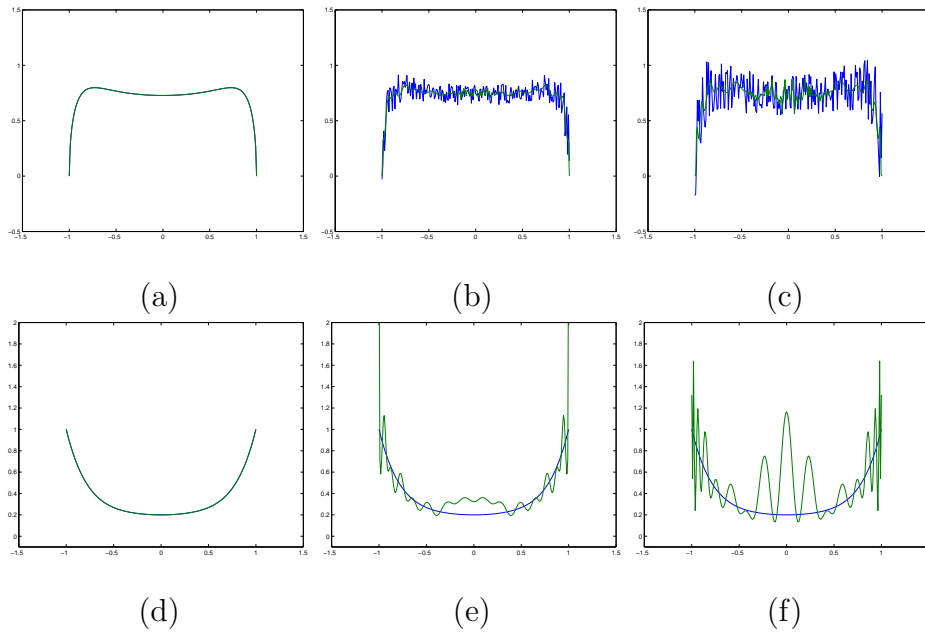
Figure C.5: *The fitting of the lateral profile (a,b,c) and the reconstructed radial profile (d,e,f) with different amplitudes of the superimposed noise. Here a radial density profile was given as* $n(r) = 0.2 + 0.2r^2 + 0.2r^4 + 0.4r^6$. *The base function of the radial profile was chosen as* $F(x) = a_0 F_0 + a_2 F_2 + a_4 F_4 + a_6 F_6 + a_8 F_8$. *In this fitting procedure, the Tikhonov regularization method has not been used, i.e. the regularization parameter* $\mu = 0$. **(a)** *Noise-free lateral profile.* **(b)** *Lateral profile with a noise with A=2.5.* **(c)** *Lateral profile with a noise with A=5.* **(d)** *Radial profile for noise-free case.* **(e)** *Radial profile for a random noise with A=2.5.* **(f)** *Radial profile for a random noise with A=5.*

Summary

In order to improve our understanding of plasma processes in metal halide (MH) lamps, numerical models are under construction. Verification of these models requires quantitative data of the species density distributions inside these lamps. Since density profiles are dictated to local chemical processes and transport mechanisms, both strongly depending on the temperature, accurate temperature information is of great importance. Therefore the first goal of this thesis is to develop diagnostic techniques and to employ these techniques to determine two different temperatures, namely the gas temperature and the electron temperature. Based on the temperature data, the presence of LTE can be verified. This validation of the LTE-assumption will have a significant impact on modelling.

To achieve the first goal, two main diagnostic tools have been designed and explored, namely X-ray absorption (XRA) and Thomson scattering (TS). XRA gives the gas temperature while TS provides data on the electron temperature and electron density. In a sidetrack we also did a feasibility study to determine the elemental density of sodium or iodine by means of γ-spectroscopy. However, by tracing radioactive isotope ^{24}Na generated by the irradiation of the natural isotope ^{23}Na, it was found that it is impossible to obtain the elemental density distribution unless the lamp could be placed in a nuclear reactor. Moreover, a simple calculation shows that filling the lamp with a salt containing ^{22}Na is not an option to obtain the spatial distribution of sodium. One promising method would be the SPECT technique which has been successfully applied in nuclear medicine diagnostics to trace radioactive nuclei. By introducing ^{123}I-labelled NaI into the lamp, it is in principle possible to obtain the spatial distribution of iodine with the SPECT system with a spatial resolution of 0.5 mm. It requires further investigation and an in-depth study in order to apply this method to metal halide lamps.

Both XRA and TS measurements were performed on the same lamps, high pressure Hg lamps with 15 mg and 50 mg Hg fillings. The results show that the electron temperature is higher than the gas temperature. This means that the LTE-assumption in these lamps is not valid. Moreover, a deviation from Saha equilibrium was found by comparing the ground state Hg density using the XRA results and the ground state Saha density using the results from TS. It has been found that the deviation from Saha equilibrium is increasing with the distance to the center.

Summary

TS has also been performed on an Ar model lamp in order to investigate the plasma properties in front of the electrodes. It has been found that the plasma is strongly ionizing in front of the electrodes and thus not in LTE.

There are several challenges when TS is performed on the high pressure Hg lamps. Firstly, the TS signal has to compete with the substantial signal of stray light which is introduced by the plasma surroundings: the lamp envelope. Secondly, the TS signal has to compete with the strong plasma radiation in the Hg lamp. Thirdly, the TS signal is limited by the laser power since the laser should not break the quartz tube and not create a laser-induced plasma. If one can not meet these three requirements at the same time, then it is impossible to do TS measurements. Fortunately, by means of several adjustments on the existing TS-setup we have successfully obtained the clear TS signal on high pressure Hg lamps.

The results obtained in this way on pure Hg plasmas may offer a firm platform from which TS on metal halide lamps can be conducted in the near future. However, it should be realized that the presence of metal halides will lead to an increase of the plasma background radiation so that the application of TS will be increasingly difficult.

The execution of XRA measurements on HID lamps is found to be far from trivial, but possible. The experimental setup required covers a high dynamic range CCD camera, a high flux X-ray source and a near monochromatic source. After lamp-on and lamp-off images are taken, a simple subtraction of the logarithm of lamp-off and lamp-on image intensities will not bring us automatically the correct temperature profile. The final temperature profile depends on correct procedures for signal extraction, image process procedures and Abel inversion. To demonstrate the capabilities of this technique, XRA measurements were performed on various kinds of HID lamps. It was shown that this method is well suited for gas temperature measurements on HID lamps.

It was also shown that the presence of the metal additives in the arc leads to constriction of the temperature profile. Moreover, the constriction of temperature profile indicates the presence of axial segregation effects. Even for the worst scenario, a PCA HID lamp with low Hg pressure and small diameter, it has been proven that this method can yield reliable results.

To conclude, the XRA method is a reliable and sensitive diagnostic method for gas temperature measurement in HID lamps. TS is another important technique for the electron gas properties. By combining these two methods, we have obtained a better insight in the plasma conditions.

Samenvatting

Om het begrip van plasmaprocessen in metaal-halide-lampen (MH) te vergroten, zijn er numerieke modellen in ontwikkeling. Verificatie van deze modellen vereist kwantitatieve gegevens over de dichtheidsverdelingen van de diverse deeltjessoorten in deze lampen. Omdat dichtheidsprofielen worden gedicteerd door de lokale chemische processen en transportmechanismen, beide sterk afhankelijk van de temperatuur, is een nauwkeurige temperatuurbepaling van groot belang. Daarom is het eerste doel van dit proefschrift om diagnostische technieken te ontwikkelen en deze toe te passen ter bepaling van twee verschillende temperaturen, namelijk de gastemperatuur en de elektronentemperatuur. Met deze temperatuurmetingen kan de aanwezigheid van LTE (Lokaal Thermisch Evenwicht) worden geverifieerd. Deze validatie van de LTE-aanname is van grote betekenis voor de modelvorming.

Om het eerste doel te bereiken zijn er twee diagnostische methoden ontwikkeld en onderzocht, namelijk X-ray absorptie (XRA) en Thomson-verstrooiing (TS). XRA geeft de gastemperatuurverdeling terwijl TS de gegevens betreffende de elektronentemperatuur en elektronendichtheid verschaft. Als zijspoor is ook een haalbaarheidsstudie gedaan naar het bepalen van de dichtheid van Na met behulp van gammaspectroscopie. Daartoe is een experiment opgezet waarbij radioactief ^{24}Na wordt gegenereerd in een lamp door de bestraling van het aanwezige natuurlijke isotoop ^{23}Na. Echter, het bleek dat de intensiteit van de gammastraling die daarmee wordt opgewekt te klein is om plaatsopgeloste dichtheids metingen mogelijk te maken. Een studie wijst uit dat er wellicht mogelijkheden zijn als we (in de toekomst) gebruik gaan maken van de ontwikkelingen in de medische technologie. Door Na te binden aan het radioactief jodium-isotoop ^{123}I kan men, gebruikmakend van computer-tomografie (CT), in principe tot een plaatsopgeloste meting van het NaI-molecuul komen die tot op 0.5 mm nauwkeurig is.

Zowel de XRA- als de TS-metingen zijn gedaan op dezelfde lampen, te weten hogedruk-kwiklampen. De resultaten laten zien dat de elektronentemperatuur hoger is dan de gastemperatuur. Dit wijst er op dat voor het plasma in dit soort lampen de aanname van LTE niet geldig is. Bovendien is er een afwijking van Saha-evenwicht gevonden door de grondtoestand van Hg verkregen met behulp van XRA te vergelijken met de waarde die volgt uit de Saha formule. De afwijking van Saha is substantieel en neemt toe in de richting van de wand.

Thomson-verstrooiing is ook toegepast op een Ar-modellamp waarvan de plasma eigenschappen vlak voor de elektroden onderzocht zijn. Er is gevonden dat vooral voor de

kathode het plasma sterk ioniserend is en dat daar dus geen LTE heerst.

Er zijn verschillende uitdagingen wanneer TS wordt toegepast op hogedruk-kwiklampen. Ten eerste moet het TS-signaal concurreren met het valse strooilicht dat gegenereerd wordt door de interactie van de laser met de plasmaomgeving. In de tweede plaats moet het TS-signaal concurreren met de sterke plasmastraling van de lamp. In de derde plaats is het TS-signaal sterk begrensd omdat de laser maar op een fractie van het vol vermogen kan worden bedreven. Dit, om te voorkomen dat de ballon beschadigd raakt of dat er een laser-geïnduceerd plasma ontstaat. Indien er niet gelijktijdig aan deze drie eisen wordt voldaan is het onmogelijk om TS-metingen te doen. Ondanks het feit dat dit overlapgebied zeer klein is, zijn we er in geslaagd om door middel van verscheidene aanpassingen aan de bestaande TS-opstelling een duidelijk TS-signaal te verkrijgen. De resultaten verkregen met kwiklampen verschaffen een stevige basis waarop in de toekomst TS op MH-lampen kan worden bedreven. Men moet zich wel realiseren dat de aanwezigheid van metaal-haliden zal leiden tot een toename van de plasma-achtergrondstraling zodat de toepassing van TS niet eenvoudig zal worden.

De uitvoering van XRA-metingen op HID-lampen ter bepaling van de gastemperatuur blijkt mogelijk maar buitengewoon ingewikkeld. De experimentele opstelling vereist een hoog dynamisch bereik van de CCD-camera, een hoge X-ray-flux en een bijna monochromatische X-ray-bron. Omdat de lamp tijdens het bedrijf (lamp-aan) door de thermische belasting van vorm verandert, zal een simpele subtractie van de (logaritme van de) lamp-uit en lamp-aan beeldintensiteiten niet automatisch het correcte temperatuurprofiel van het Hg in de (brandende) ontlading verschaffen. Het uiteindelijke temperatuurprofiel is afhankelijk van correctieprocedures voor signaalextractie, beeldverwerking en de Abel-inversie. Om de mogelijkheden van deze techniek aan te tonen zijn er XRA-metingen gedaan op verschillende HID-lampen. Het is aangetoond dat met de juiste procedures voor meting en data-analyse deze methode zeer geschikt is voor het bepalen van de gastemperatuurverdeling in HID-lampen.

Gebruikmakend van de XRA-methode is aangetoond dat de aanwezigheid van metaal-haliden in het plasma leidt tot constrictie van het temperatuurprofiel. Bovendien duidt de constrictie van het temperatuurprofiel op de aanwezigheid van axiale segregatieverschijnselen. Om de grenzen van de XRA-methode te verkennen is de methode ook toegepast op een zeer ongunstig scenario, namelijk een keramische HID-lamp met een lage kwikdruk en een kleine diameter. Het is bewezen dat deze methode zelfs onder deze moeilijke omstandigheden betrouwbare resultaten kan opleveren.

Concluderend mag men stellen dat de XRA-methode een betrouwbare en gevoelige diagnostische methode is om de gastemperatuur te bepalen in HID-lampen. TS is een belangrijke techniek voor het bepalen van de eigenschappen van het elektronengas. Door deze twee technieken te combineren hebben we beter inzicht verkregen in plasmacondities.

摘要

为了完善对金属卤化物灯中等离子体过程的了解，需要建构用于描述金属卤化物灯中等离子体过程的数值模型。验证这些模型的正确与否，需要有关于灯中各种粒子密度分布类型的定量数据。由于决定粒子密度分布特征的两种基本因素，即局部的化学过程和等离子体的输运机制，都受到温度的强烈影响，因此，对温度的精确测量就显得非常重要。本论文的首要目标就是建立各种用于诊断等离子体温度的方法，并用这些方法来测定两种不同的温度，即气体温度和电子温度。根据这些温度数据，即可验证在高强度放电灯中是否存在局部热平衡（LTE）。对高强度气体放电灯的模型而言，局部热平衡假说的正确与否，将会产生巨大的影响。

为了实现这个目标，论文作者主要设计和研究了两种温度诊断方法：X 射线吸收法（XRA）和汤生散射法（TS）。X射线吸收法向我们揭示了灯中等离子体的气体温度分布方面的数据，而汤生散射法则提供了电子温度和电子密度分布方面的数据。此外，本文还对用 γ 射线法来追踪钠的放射性同位素 ^{24}Na 从而得到灯中钠元素的密度分布进行了可行性研究。研究结果证明，希图通过对钠的天然同位素 ^{23}Na 进行中子束照射而产生的放射性同位素 ^{24}Na 进行追踪，来得到钠元素的空间密度分布，在实践上是很困难的。原因在于回旋加速器设施中的中子束辐射通量很低，以致 γ 光子的采集速率无法满足空间测量的要求。除非把灯放到核反应堆进行中子束照射，这在理论上是可以达到空间密度测量的要求，然而由此产生的高辐射剂量的 ^{24}Na 在实际操作中是很难操作的。然而当代先进的辐射医学诊断上采用通过追踪放射性 ^{123}I 来诊断癌症的方法非常成功。如果在灯中加入金属碘化物，其中部分碘化物用 ^{123}I 来制成，通过追踪 ^{123}I，我们可以得到碘元素的密度分布，进而得到灯的管壁附近的碘化物分子的分布。这将会成为另一个重要的研究方向。

论文作者对两种分别充有15 mg 汞和50 mg 汞的高压汞灯进行了两种不同诊断方法（即X射线吸收法和汤生散射法）的实验。实验结果表明，电子温度高于气体温度。这说明在高压汞灯中并不存在局部热平衡。此外，通过比较由X射线吸收法实验得到的基态汞原子密度值与由汤生实验结果得到的电子温度和电子密度算得的基态汞原子的沙哈密度，发现高压汞灯中的汞原子基态密度值偏离沙哈平衡，并且这种偏离随着径向距离的增大而增大。

为了研究高强度放电灯中等离子体在近电极区域的特性，论文作者还对一种充氩气的模型灯进行了汤生散射实验。实验发现等离子体在电极附近强烈电离，偏离局部热平衡（LTE）。

在对高压汞灯进行汤生散射实验时，有几个难题需要解决。首先，汤生散射的信号必须战胜由灯的管壁引起的很强的杂散光；第二，汤生散射的信号必须战胜高压汞灯中强烈的等离子体辐射；第三，汤生散射的信号还受到激光功率的限制，原因在于激光不

得击穿石英管壁和产生激光诱导的等离子体。如果以上三个要求不能同时满足，那么汤生散射实验就不可能进行。幸运的是，通过对现有的汤生散射实验装置所作的某些调整，论文作者成功地测量到了清晰的高压汞灯中的汤生散射信号。汤生散射实验在高压汞灯的纯汞等离子体上的成功应用为其将来在金属卤化物灯上的应用提供了坚实的实验基础。然而，必须认识到的是，金属卤化物的存在将导致等离子体背景辐射的增强以及激光对等离子体影响的增强。因此，汤生散射实验在金属卤化物灯上的应用的难度将会更大。

对高强度气体放电灯进行X射线吸收实验比想象的要困难的多，但还是可行的。进行该实验所要求的实验设备包括一台高动态量程范围的X射线CCD 相机，一台高辐射通量的X射线源和一个近似单色的X射线谱。在实验中，首先对灯燃点和灯熄灭的情况拍摄了许多幅X射线照片，然后针对某一轴向位置，取灯燃点和灯熄灭的X射线强度的对数曲线。如果我们直接对这两条曲线取差值并进行阿贝转换，所得到的气体温度的结果是不正确的。要想得到正确的结果，我们必须要考虑以下几个因素：如何从原始测量的图象中提炼出正确的信号（例如暗电流的修正，CCD像素的非均匀性修正，X射线图象中偏置信号的修正），正确的图象处理和阿贝转换过程。为了演示X射线吸收实验的可行性和适用范围，论文作者对不同种类的高强度放电灯进行了X 射线吸收实验。实验结果证明，X射线吸收方法非常适用于高强度气体放电灯。

实验还发现，存在于电弧中的金属添加物会引起温度曲线的收缩。并且，温度曲线的收缩显示了等离子体中的金属添加物的密度分布存在着轴向分层效应。实验结果证明，即使在最差的情况下，即在用多晶氧化铝（PCA）作为管壁材料的低汞蒸气压（1大气压）和细管径（4 mm）的高强度放电灯的情况下，X射线吸收方法也可以产生可靠的结果。

总而言之，X射线吸收法是一种可靠而灵敏的测量高强度放电灯内气体温度的方法。汤生散射方法是一种重要的测量电子气体特性的方法。综合应用这两种方法，可以使我们对高强度放电灯内等离子体的特性有了更透彻的了解。

Acknowledgement

This manuscript draws a definitive end for my four-year-period of doctoral study in the group of Elementary Processes in Gas discharges (EPG) at Technische Universiteit Eindhoven (TU/e). A long list of thanks is due to all the people who have supported me for one of the most important periods in my life.

First of all, I would like to express my gratitude to my direct supervisor, Joost van der Mullen, who offered me the opportunity to pursue a three-month training project and later on a four-year's PhD study. During my PhD period, you gave me tremendous inspiration and encouragement, answered countless questions, held numerous discussions and provided comprehensive remarks and revisions, which formed the solid base of this thesis.

Special thanks to my first promotor, Marco Haverlag, for your generous help on my PhD work, sharing your knowledge on lamp physics, the XRA data handling procedure and the help on the program which leads to the success of the XRA diagnostic method.

I am deeply indebted to those,
- Gerrit Kroesen, my second promotor, for sharing your extensive knowledge on how to solve physics and experimental problems and nice comments on my stellingen.
- Gilles Moerdijk, for your great help and cooperation in the experiments of γ-spectroscopy.
- Leo van IJzendoorn, core committee member, for the intensive discussion and knowledge on γ spectroscopy methods.
- James Lawler, core committee member, who was busy working at Kitt Peak Observatory at the time to read and comment on this manuscript.
- Evert Ridderhof, for your tremendous help in building and testing the X-ray absorption setup, and working together to solve the experimental problems.
- Andrei Bronnikov, who led me to understand the ill-posed problem and the Tikhonov regularization method.
- Erik Kieft, for your help and discussions on TS experiments on Hg lamps.
- Marco van de Sande, you helped me to understand and grasp the TS technique.
- Marco Redwitz, for the nice cooperation with you on TS on Ar model lamp.
- Nienke de Vries, my student, who has done a great work to further improve the TS setup and the TS measurements on the high pressure Hg lamps.
- Wouter Brok, Jean-Charles Cigal and Bram Visser, for your great help and discussions in physics, lamps and Latex problems etc.
- Huib Schouten, for your design of the electronic system in both TS and XRA setups.
- Loek Baede, for the discussions and knowledge on the CCD and optical systems and the

165

nice lamp pictures for the cover of my thesis.

- Charlotte Groothuis, for your help on simulations with optical ray-tracing program.
- Erik Kieft, Tanya Nimalasuriya, Maxime Gendre, Nienke de Vries, Ingrid Kieft, Tanja Briels, and Arjan Flikweert, for your time spent on reading this manuscript and made many useful suggestions.
- Mark Bowden, Gabriela Paeva, Misha Sorokin, Jérôme Remy, Charlotte Groothuis for the nice suggestions on my stellingen.
- PLASIMO modelling group, Harm van der Heijden, Jan van Dijk, Bart Hartgers, Bart Broks and Mark Beks for your helps on the plasma simulations and Latex problems.
- Virgil Tromp, Yuri Franken, Piet Thijssen, Wim Kok from SBD, providing support for the radiation protection of XRA setup.
- Bert Koopmans, for providing the X-ray setup and Hans Dalderop for the instructions on how to operate the X-ray setup.
- Team of Marius Bogers of our faculty workshop and members of central workshop (GTD) involved in the design and construction of the XRA setup.
- Wim Hellebrekers for your recommendation for my Ph.D study.
- Paul Harvey for your help on the XRA data analysis using X-ray tomography program.
- Xisheng Luo for the nice discussions on XRA problems and the thesis compilation.
- John Curry, for the nice discussions with you on XRA techniques.
- Tao Jiang, for your kind help on several nice graphs in my thesis.
- Tarik Gammoun, Willem Sukkel and Arjeh Tal, for your helps on software problems.

Once again, I'm deeply grateful for the many valuable discussions and insights provided me by the people from Philips Research Laboratories in Aachen and Philips CDL in Eindhoven. Many thanks to Ulrich Hechtfischer, Folke Noertemann, Jens Pollmann, Rob Keijser, Joop Geijtenbeek and Joost van der Eyden.

Also thanks to all other members of EPG group who are not mentioned above, it was a great pleasure for me to work with you in the past four years. Special thanks to the secretary of our group, Rina Boom, offered her generous help all the time.

Members of the sister group of EPG, ETP, my sincere thanks to Herman de Jong, Bertus Husken, Reis van de Sande, Karine Letourneur for your help during my training period at the ETP group.

Thanks to all the members in the BuEx China study trip. It is such a good memory in my life. Thanks to my friends in the Chinese student association in TU/e for the spirit support. Thanks to the teachers of "Teigetjes" in Tuimelaar for taking care of my daughter and all the friends who helped me for picking up my daughter from school. Especially, thanks to Igna Topff, my Belgian friend and godmother of my daughter, who has spent so much time with us in sharing the European culture and its beautiful landscape.

Last but not least, I'm deeply grateful to my parents, Wengao Zhu and Feiying Wei, for their love, education, encouragement and support. My brother, Xiaosong Zhu, for his help and love. My husband Wei Cheng, who has encouraged my independence, helped me to face the difficult problem, and my lovely daughter, Siyan (Caroline), who cheered me up and brought me new energy to face every new day.

Curriculum vitae

January 20, 1971	Born in Shenyang, Liaoning Province, China
September 1989 - July 1993	Bachelor of science in physics, Dept. of Light Sources and Illumination Engineering, Fudan University, Shanghai, China
September 1993 - July 1996	Master of science in physical electronics, Dept. of Light Sources and Illuminating Engineering, Fudan University, Shanghai, China
July 1996 - April 1999	Teacher in Illuminating Design, Dept. of Light Sources and Illuminating Engineering, Fudan University, Shanghai, China
August 2000 - December 2004	Ph.D. research in the group: Elementary Processes in Gas Discharges, "Active spectroscopy on HID lamps - exploration of various methods" Eindhoven University of Technology, the Netherlands